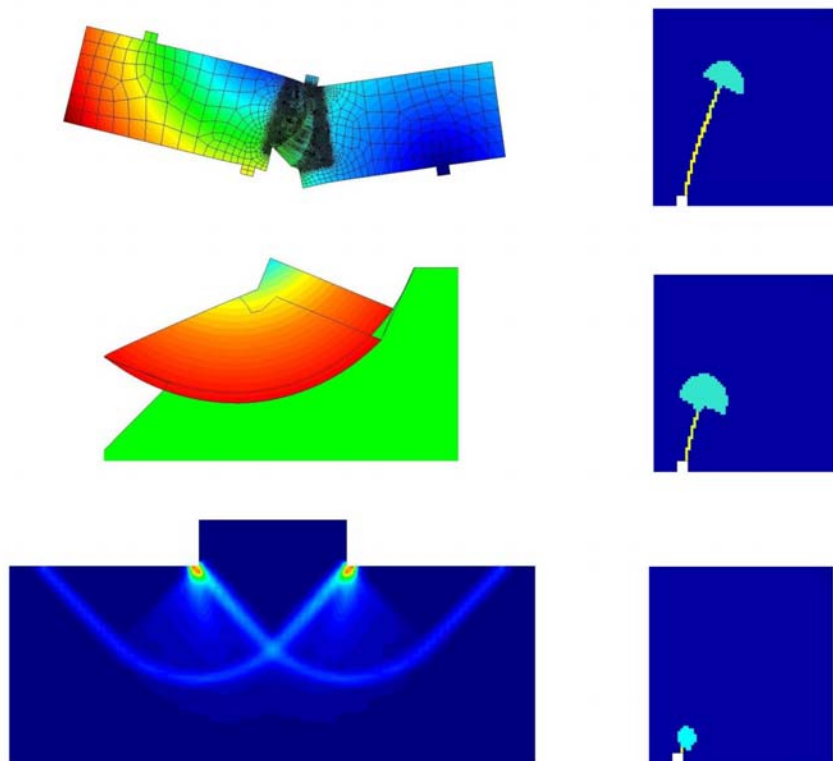


Strain Injection Techniques in Numerical Modeling of Propagating Material Failure

I.F. Dias
J. Oliver
A.E. Huespe



Strain Injection Techniques in Numerical Modeling of Propagating Material Failure

**I.F. Dias
J. Oliver
A.E. Huespe**

Monograph CIMNE N°-134, October 2012

INTERNATIONAL CENTER FOR NUMERICAL METHODS IN ENGINEERING
Edificio C1, Campus Norte UPC
Gran Capitán s/n
08034 Barcelona, Spain
www.cimne.com

First edition: October 2012

STRAIN INJECTION TECHNIQUES IN NUMERICAL MODELING OF PROPAGATING MATERIAL FAILURE
Monograph CIMNE M134
© The authors

ISBN: 978-84-940243-7-5

Depósito legal: B-31890-2012

Acknowledgments

The first author acknowledges to the Fundação para a Ciência e a Tecnologia (FCT) and to the Laboratório Nacional de Engenharia Civil (LNEC) for their financial support to this research.

The second author acknowledges to the Spanish Ministry of Science and Innovation, and to the Catalan Government Research Department, for their financial support to this research under Grants BIA2011-24258 and 2009 SGR 1510, respectively.

Summary

The methodology proposed in this research work explores the use of the strain injection concept in a combination of classical strain localization methods and embedded strong discontinuities, to remove the flaws (stress locking and mesh bias dependence) of the former, and simultaneously abdicate of the global tracking algorithms usually required by the later. The basic idea is to use, after the bifurcation instant, *i.e.* after the time that elements are amenable to develop discontinuities, a mixed continuous displacements - discontinuous constant strains condensable finite element formulation ($Q1/\epsilon 0$) for quadrilaterals in 2D. This formulation provides improved behavior results, specially, in avoiding mesh bias dependence. In a first, very short, stage after the bifurcation the concept of strong discontinuity is then left aside, and the apparent displacement jump is captured across the finite element length (smeared) like in classical strain localization settings. Immediately after, in a second stage, the kinematics of those finite elements that have developed deep enough strain localization is enriched with the injection of a weak/strong discontinuity mode that minimizes the stress locking defects. The necessary data to inject the discontinuity (the discontinuity direction and its position inside the finite element) is obtained by a post process of the strain-like internal variable field obtained in the first stage, this giving rise to a local (elemental based) tracking algorithm (the crack propagation problem) that can be locally and straightforwardly implemented in a finite element code in a non invasive manner. The obtained approach enjoys the benefits of embedded strong discontinuity methods (stress locking free, mesh bias independence and low computational cost), at a complexity similar to the classical, and simpler, though less accurate, strain localization methods. Moreover, the methodology is applicable to any constitutive model (damage, elasto-plasticity, etc.) without apparent limitations. Representative numerical simulations validate the proposed approach.

Table of contents

Chapter 1 Introduction	1
1.1. State of the art	1
1.2. Adopted approach	4
1.3. Objectives	5
1.4. Outline	6
Chapter 2 Strain Localization	7
2.1. The initial boundary value problem in nonlinear solid mechanics ..	10
2.2. Material nonlinearity - continuum constitutive models	12
2.2.1. Plasticity models.....	12
2.2.2. Damage models	20
2.3. Material bifurcation - localization analysis.....	24
2.4. Classical strain localization methods –Standard (irreducible) finite element formulations.....	27
2.4.1. Weak formulation of the boundary value problem.....	28
2.4.2. Finite element approximation.....	29
2.4.3. Lack of objectivity and regularization.....	30
2.4.4. Mesh bias dependence.....	34
2.4.5. Stress locking	37
2.5. Integration of the constitutive equation - IMPL-EX scheme	40
Chapter 3 Mixed Finite Element Formulations and Localized Strain Injection	43
3.1. Mixed strain-displacement formulation.....	43
3.1.1. Using mixed $(\mathbf{u}, \boldsymbol{\varepsilon})$ formulations for strain localization problems: motivation	45
3.1.2. Mixed constant strain linear displacement variational formulation	46
3.1.3. Finite element approximation.....	47
3.1.4. Stabilization.....	50
3.1.5. Matrix equations.....	51
3.1.6. A first set of representative numerical examples.....	52

3.2.	Constant strain mode injection. Domain restricted mixed $(\mathbf{u}, \varepsilon)$ formulation	59
3.2.1.	The mixed injection domain	60
3.2.2.	Variational formulation	61
3.2.3.	Isochoric constitutive model – special treatment.....	62
3.2.4.	Implementation aspects	63
3.2.5.	Total vs. incremental time formulations	63
3.2.6.	Matrix equations	65
3.2.7.	A second set of representative numerical examples - Numerical assessment of the injection procedure	65
3.3.	Summary and conclusions	71
 Chapter 4 Strain localization, strong discontinuities and material fracture.....		73
4.1.	The continuum strong discontinuity approach.....	74
4.1.1.	Strong discontinuity kinematics	75
4.1.2.	Regularized strong discontinuities kinematics.....	77
4.2.	Strain localization and strong discontinuities	78
4.3.	Strain localization mismatch indicators	80
4.3.1.	Local mismatch indicator	81
4.3.2.	Global Mismatch indicators.....	82
4.4.	The localization domain.....	84
4.5.	Numerical simulations	85
4.5.1.	Strip in homogeneous uniaxial tensile stress state – Mode I fracture modeling	85
4.5.2.	Strip undergoing homogeneous uniaxial tensile stress state using a J_2 plasticity model– Mode II fracture modeling.....	87
4.5.3.	Slope stability problem using a J_2 plasticity model	90
4.6.	Summary and conclusions	93
 Chapter 5 Weak\strong discontinuity injection procedures		95
5.1.	Strong discontinuities.....	96
5.1.1.	The Strong discontinuity kinematics	96
5.1.2.	The boundary value problem with strong discontinuities.....	97
5.1.3.	A three field $(\hat{\mathbf{u}}, \hat{\varepsilon}, [\hat{\mathbf{u}}])$ mixed formulation	98
5.1.4.	Three field mixed finite element formulation – Un-symmetric formulation.....	100
5.1.5.	Symmetric formulation.....	104
5.1.6.	The Strong discontinuity injection.....	107
5.2.	Weak discontinuities.....	109
5.2.1.	Weak discontinuity kinematics.....	110
5.2.2.	Three field $(\hat{\mathbf{u}}, \hat{\varepsilon}, [\hat{\mathbf{u}}])$ mixed formulation.....	111
5.2.3.	Three field mixed formulation – Finite element approximation – Un-symmetric formulation.....	112
5.2.4.	The Weak discontinuity injection.....	115

5.3.	The crack path and the discontinuity domain	116
5.3.1.	One-dimension-problem: Motivation (double smoothing)	116
5.3.2.	The crack-propagation problem	118
5.3.3.	Discretization	119
5.3.4.	Matrix equations.....	119
5.3.5.	The crack propagation path	121
5.3.6.	The discontinuity injection domain	123
5.3.7.	Staggered resolution of the coupled problem	124
5.4.	Summarizing the strain injection procedure as a two stage method	125
5.4.1.	The injection domains	126
5.4.2.	Two stage method - equilibrium equations	127
5.4.3.	Implementation aspects	128
5.5.	Representative numerical simulations	132
5.5.1.	Isotropic continuum damage model: double cantilever beam (DCB) with diagonal loads	132
5.5.2.	Strip in homogeneous uniaxial tensile stress state – Mode II fracture modeling.....	135
5.5.3.	Strip undergoing homogeneous uniaxial tensile stress – Mode I fracture modeling.....	138
5.5.4.	Four point bending test.....	141
5.5.5.	Slope stability problem using a J_2 plasticity model.....	147
5.5.6.	Rigid strip footing using a J_2 plasticity model.....	151
	Chapter 6 Conclusions	161
	Appendix A Rankine model IMPL-EX integration	163
A.1.	Implicit evaluation of the consistency parameter.....	164
A.2.	Explicit evaluation of the stress tensor	167
A.3.	Integration scheme.....	172
A.4.	Alternatives for implementation	173
A.4.1	Previous step flow	173
A.4.2	Original flow	174
	Appendix B Stress locking in finite elements with embedded discontinuities	175
B.1.	Motivation.....	176
B.2.	Specification for 2D elements.....	178
B.2.1	Linear triangles, $(\hat{\mathbf{u}}, [\hat{\mathbf{u}}])$ formulation.....	178
B.2.2	Bilinear quadrilateral elements, $(\hat{\mathbf{u}}, [\hat{\mathbf{u}}])$ formulation (fully integrated quads).....	179
B.2.3	Bilinear quadrilateral elements, $(\hat{\mathbf{u}}, \hat{\mathbf{e}}, [\hat{\mathbf{u}}])$ formulation (reduced integration).....	180
B.3.	Numerical example	181

Appendix C Weak/strong discontinuity injection: Element matrices	185
.....	185
C.1. Symmetric strong discontinuity formulation	187
C.2. Un-symmetric strong discontinuity formulation.....	188
C.3. Weak discontinuity formulation.....	189

List of Figures

Figure 2.1 <i>A bar problem with strain softening material: a) homogenous bar, b) stress-strain relations.</i>	7
Figure 2.2 <i>a) Stress-strain relation, b) force-displacement solutions.</i>	8
Figure 2.3 <i>Fracture process zones (adapted from [Oliver and Huespe 2004b]).</i> ...	9
Figure 2.4 <i>Continuum body.</i>	11
Figure 2.5 <i>a) Elastic domain and yielding surface, b) hardening law.</i>	15
Figure 2.6 <i>Rankine yield surface: a) three dimensional view, b) octahedral plane Sections.</i>	17
Figure 2.7 <i>Von Mises yield surface: a) three dimensional perspective, b) deviatoric Section.</i>	18
Figure 2.8 <i>a) Illustration of the elastic domain and damage surface, b) Uniaxial generic curves.</i>	22
Figure 2.9 <i>Continuum body with discontinuity.</i>	25
Figure 2.10 <i>Strip stretching in the horizontal direction.</i>	35
Figure 2.11 <i>Iso-displacement curves at the end of analysis (damage model).</i>	36
Figure 2.12 <i>Iso-displacement curves at the end of analysis (Rankine plasticity model)(standard finite element formulation).</i>	36
Figure 2.13 <i>Load patterns for two different stages of the deformation process (standard finite element formulation).</i>	39
Figure 2.14 <i>Load patterns for two different stages of the deformation process</i> ...	39
Figure 2.15 <i>Force-displacement curves: a) Isotropic damage, b) Rankine plasticity model (standard finite element formulation).</i>	39
Figure 3.1 <i>Finite element with continuous liner displacements $\mathbf{u}^{(e)}$ and element-wise constant discontinuous strains $\epsilon^{(e)}$</i>	47

Figure 3.2 Double cantilever beam with diagonal load: a) geometrical data, b) loading data, c) finite element discretization.....	52
Figure 3.3 Iso-displacement plots for different stabilization parameters τ	53
Figure 3.4 Deformed mesh.....	53
Figure 3.5 Result for $\tau = 0.0001$: a) mesh deformation, b) iso-displacement contours.....	54
Figure 3.6 Force-displacement curves.....	54
Figure 3.7 Strip stretching in the horizontal direction.....	55
Figure 3.8 Iso-displacement plots (isotropic damage model). Results obtained with the irreducible formulation ($\tau = 1$) and with mixed stabilized formulation ($\tau = 0.1$) are shown in the left and in the right hand side of the figure respectively, for three different levels of discretization.....	56
Figure 3.9 Iso-displacement plots (plasticity Rankine model). Results obtained with the irreducible formulation ($\tau = 1$) and with mixed stabilized formulation ($\tau = 0.1$) are shown in the left and in the right hand side of the figure respectively, for three different levels of discretization.....	56
Figure 3.10 Force-displacement curves: a) Isotropic damage, b) Rankine plasticity model.....	57
Figure 3.11 Strip stretched in the horizontal direction (J_2 plasticity model).....	58
Figure 3.12 Iso-displacement plots (J_2 plasticity model). Results obtained with the mixed stabilized formulation for different values of τ , at the final stage of analysis.....	58
Figure 3.13 Force-displacement curve.....	59
Figure 3.14 a) Mixed injection domain, b) Hardening softening law.....	61
Figure 3.15 Double cantilever beam with diagonal load: a) geometrical data, b) loading data, c) finite element discretization.....	66
Figure 3.16 Evolution of the mixed injection domain (shaded zones) along different times of the analysis.....	66
Figure 3.17 Results for the injection strategy: a) deformed mesh, b) Iso-displacement plots.....	67
Figure 3.18 Curves, F_1 vs. Crack Mouth Opening Displacement (CMOD), obtained with different procedures.....	67
Figure 3.19 Strip stretching in the horizontal direction.....	68
Figure 3.20 Force-displacement curves (for mesh c) – see Figure 3.9) obtained with different procedures.....	68
Figure 3.21 Strip stretching in the horizontal direction.....	69

Figure 3.22 Evolution of the mixed injection domain (shaded zones) during different stages of the analysis.	69
Figure 3.23 Force-displacement curves obtained with different procedures. ...	70
Figure 3.24 Iso-displacement plots a) Mixed form ($\tau = 0.0001$), b) CSM Injection.	70
Figure 3.25 Force-displacement curves. Comparison of results using the incremental and total versions of the injection formulation.	71
Figure 4.1 a) Continuum body with strong discontinuity, b) Strong discontinuity kinematics.	76
Figure 4.2 Continuum body a with strong discontinuity.	76
Figure 4.3 a) Continuum body with discontinuity band b) Regularized strong discontinuity kinematics.	77
Figure 4.4 Regularized Dirac's delta function.	77
Figure 4.5 Discretized body with localization band.	80
Figure 4.6 a) Finite element crossed by discontinuity, b) Localization domain.	84
Figure 4.7 Strip stretching in the horizontal direction.	85
Figure 4.8 a) aligned mesh, b) misaligned mesh – irreducible formulation, c) misaligned mesh – Constant strain mode injection.	86
Figure 4.9 a) Force-displacement curves, b) Localization indicator I_2	86
Figure 4.10 Distribution of strain localization mismatch indicator $i^{(e)}$ a) irreducible formulation, b) Constant strain mode injection.	87
Figure 4.11 Strip stretching in the horizontal direction.	87
Figure 4.12 Iso-displacement plots for three different meshes, a) B-bar element, b) Constant strain mode injection.	88
Figure 4.13 a) Force-displacement curves, b) Localization indicator I_2	89
Figure 4.14 Spatial distribution of the local strain localization mismatch indicator $i^{(e)}$ (CSM injection), a) diagonal aligned mesh (mesh ii), b) unstructured mesh (mesh iii).	90
Figure 4.15 Slope stability problem.	91
Figure 4.16 Iso-displacement contours for two different meshes, a) Aligned mesh, b) Misaligned mesh.	91
Figure 4.17 a) Force-displacement curves, b) Global Localization indicator I_2	92

Figure 4.18 <i>Spatial distribution of the local incremental strain localization mismatch indicator $i^{(e)}$ for two loading stages.</i>	92
Figure 5.1 <i>Strong discontinuity kinematics.</i>	97
Figure 5.2 <i>Continuum body with discontinuity.</i>	97
Figure 5.3 a) <i>Discretized body with discontinuity, b) Description of functions \mathcal{M}^h, \mathcal{H}_S and φ^h along line \mathcal{T}</i>	101
Figure 5.4 <i>Elemental functions $\mathcal{H}_S^{(e)}$, $\varphi^{(e)}$ and $\mathcal{M}^{(e)}$.</i>	101
Figure 5.5 <i>Finite element with regularized strong discontinuity.</i>	102
Figure 5.6 <i>Variable bandwidth model, $k(q)$</i>	108
Figure 5.7 <i>Strong discontinuity with regularized kinematics.</i>	109
Figure 5.8 <i>Weak discontinuity kinematics.</i>	110
Figure 5.9 a) <i>Discretized body with discontinuity, b) Elemental functions $\mathcal{H}_{\Omega_S}^{(e)}$, $\varphi^{(e)}$</i>	112
Figure 5.10 a) <i>Finite element with embedded weak discontinuity, b) Weak discontinuity band.</i>	113
Figure 5.11 <i>Hypothetical distribution of a localizing strain-like internal variable and its derivative in a continuum one dimensional problem.</i>	116
Figure 5.12 <i>Discretized one dimensional problem a) Hypothetical distribution of a localizing strain-like internal variable. b) Hypothetical distribution of the derivative of a localizing strain-like internal variable.</i>	117
Figure 5.13 <i>Double smoothing process.</i>	117
Figure 5.14 <i>Interpretation of variable $\hat{\alpha}^{(e)}$</i>	121
Figure 5.15 <i>Elemental crack-propagation field $\mu_i^{(e)}$</i>	122
Figure 5.16 <i>Construction of the elemental vector $\varphi_i^{(e)}$</i>	122
Figure 5.17 <i>Localization and weak/strong discontinuity domains.</i>	124
Figure 5.18 <i>Thresholds in the evolution of the stress/strain-like internal variables.</i>	127
Figure 5.19 <i>Evolution of the mixed and discontinuity domains for three typical stages of loading</i>	128
Figure 5.20 <i>Sampling points involved in the numerical integration.</i>	129

Figure 5.21 <i>Stress-strain relation until the discontinuity injection in a hypothetical one dimensional case.</i>	130
Figure 5.22 <i>Double cantilever beam with diagonal loads: a) geometrical data, b) loading data, c) finite element discretization.</i>	132
Figure 5.23 <i>Evolution of the injection zones along different times of the analysis.</i>	133
Figure 5.24 <i>Crack propagation path $\mathcal{S}^h(\mu^h = 0)$, at two different times of analysis.</i>	134
Figure 5.25 <i>Force-displacement curves.</i>	134
Figure 5.26 <i>Strip stretching in the horizontal direction (J_2 plasticity model).</i> ...	135
Figure 5.27 <i>Finite element meshes: a) unstructured mesh, b) miss aligned mesh.</i>	135
Figure 5.28 <i>Force-displacement curves.</i>	136
Figure 5.29 <i>Iso-displacement contours (J_2 plasticity mode).</i>	136
Figure 5.30 <i>Deformed finite element mesh (J_2 plasticity mode).</i>	137
Figure 5.31 <i>Injection domains for two different times of analysis: a) time immediately after the bifurcation point (signalized with B at Figure 5.28-a), b) Time when the discontinuity injection threshold is attained</i>	137
Figure 5.32 <i>Strip stretching in the horizontal direction</i>	138
Figure 5.33 <i>Force-displacement curves: a) Isotropic damage, b) Rankine plasticity model.</i>	139
Figure 5.34 <i>Rankine plasticity model: a), b) and c) Iso-displacement plots. d) Crack propagation path $\mathcal{S}^h(\mu^h = 0)$.</i>	139
Figure 5.35 <i>Damage model. a), b) and c) Iso-displacement plots. d) crack propagation path \mathcal{S}^h</i>	140
Figure 5.36 <i>Four points bending test.</i>	141
Figure 5.37 <i>Force-displacement curves.</i>	142
Figure 5.38 <i>Displacement jump vector: a) SD inj. ($k = 1E - 2\ell^{(e)}$), b) WD inj..</i> 142	
Figure 5.39 <i>Evolution of the injection domains: a) SD inj. (plot corresponding to point B of Figure 5.38), b) WD inj.(plot corresponding to point A of Figure 5.38).</i>	143
Figure 5.40 <i>Force-displacement curves.</i>	144
Figure 5.41 <i>Iso-displacement plots: a) WD Injection, b) Irreducible formulation.</i>	144

Figure 5.42 Evolution of the injection domains (WD. Injection) different times of the analysis.	145
Figure 5.43 Crack propagation path \mathcal{S}^h , at two different times of analysis	146
Figure 5.44 Iso-displacement contours for three different degrees of mesh refinement (results obtained using the weak discontinuity injection).....	147
Figure 5.45 Force-displacement curves for three different degrees of mesh refinement (results obtained using the weak discontinuity injection).....	147
Figure 5.46 Slope stability problem.	148
Figure 5.47 Finite element meshes: a) aligned mesh, b) miss-aligned mesh.	148
Figure 5.48 Force-displacement curves.	149
Figure 5.49 a) Iso-displacement contours, b) In-loading bifurcated elements at the final stage of the analysis.	149
Figure 5.50 Evolution of the injection zones along different times of the analysis (Weak discontinuity injection).	150
Figure 5.51 Crack propagation path \mathcal{S}^h , at two different times of analysis.	151
Figure 5.52 Rigid strip footing using a J2 plasticity model.	151
Figure 5.53 Force-displacement curves (The points plotted over the curve stand for the times depicted in Figure 5.53 to Figure 5.65).	152
Figure 5.54 Evolution of the inj. domain (WD Injection Step-A of Figure 5.53).	152
Figure 5.55 Evolution of the inj. domain (WD Injection, Step-B of Figure 5.53).	153
Figure 5.56 Crack propagation path $\mathcal{S}^h(\mu^h = 0)$ (WD Inj. Step-B of Figure 5.53).	153
Figure 5.57 Evolution of the injection domain (WD Injection, Step-C of Figure 5.53).	153
Figure 5.58 Evolution of the injection domain (WD Injection, Step-D of Figure 5.53).	154
Figure 5.59 Crack propagation path $\mathcal{S}^h(\mu^h = 0)$ (WD Injection, Step-D of Figure 5.53).	154
Figure 5.60 Evolution of the injection domain (WD Injection, Step – E of Figure 5.53).	155
Figure 5.61 Iso-displacement contours (WD Injection, Step – F of Figure 5.53).	155

Figure 5.62 Deformed meshes (WD Injection, Step – F of Figure 5.53).	156
Figure 5.63 Bifurcated in-loading elements (B-bar, Step-G of Figure 5.53).	156
Figure 5.64 Bifurcated in-loading elements (B-bar, Step-H of Figure 5.53).	156
Figure 5.65 Iso-displacement contours (B-bar, Step-I of Figure 5.53).	157
Figure 5.66 Iso-displacement contours for three different degrees of mesh refinement (results obtained by using the weak discontinuity injection).	157
Figure 5.67 Force-displacement curves for three different degrees of mesh refinement (results obtained by using the weak discontinuity injection).	158
Figure 5.68 Rigid strip footing.	158
Figure 5.69 a) Un-symmetric mesh (mesh already used at Section 5.5.6.3 (see Figure 5.67-b)), b) Symmetric mesh.	159
Figure 5.70 Force-displacement curves.	159
Figure 5.71 Iso-displacement contours.	160
Figure 5.72 Crack propagation path S^h	160
Figure 5.73 Deformed mesh.	160
Figure B.1 Quadrature rules a) $\hat{\mathbf{u}}, \hat{\boldsymbol{\varepsilon}}, [\hat{\mathbf{u}}]$ formulation b) $\hat{\mathbf{u}}, [\hat{\mathbf{u}}]$ formulation.	176
Figure B.2 Quadrilateral element with a discontinuity inducing a rigid body motion in Ω^+ with respect to Ω^-	176
Figure B.3 Linear triangle.	179
Figure B.4 Quadrilateral element associated to a $\hat{\mathbf{u}}, [\hat{\mathbf{u}}]$ formulation.	179
Figure B.5 Quadrilateral element associated to $\hat{\mathbf{u}}, \hat{\boldsymbol{\varepsilon}}, [\hat{\mathbf{u}}]$ formulation.	180
Figure B.6 Bending one element test: a) geometrical data, b) theoretical deformed shape, c) loading data.	181
Figure B.7 Reaction force vs. imposed displacement at the top comparing the analytical solution with solutions computed with the standard $\hat{\mathbf{u}}, [\hat{\mathbf{u}}]$ strong discontinuity formulation that is integrated with 4 gauss points (SDA 4GP) and with the proposed $\hat{\mathbf{u}}, \hat{\boldsymbol{\varepsilon}}, [\hat{\mathbf{u}}]$ formulation integrated with just 1 gauss point (SDA 1GP).	182

List of Boxes

Box 2.1 <i>Strong form of the boundary value problem.</i>	11
Box 2.2 <i>Rankine constitutive model.</i>	18
Box 2.3 <i>J_2 constitutive model.</i>	19
Box 2.4 <i>Damage model.</i>	24
Box 2.5 <i>Weak form of the boundary value problem.</i>	29
Box 2.6 <i>Discrete form of the boundary value problem.</i>	30
Box 3.1 <i>Weak form of the boundary value problem (mixed $\hat{\mathbf{u}}, \hat{\boldsymbol{\epsilon}}$ formulation).</i>	47
Box 3.2 <i>Stabilized mixed formulation. Matrix equations.</i>	51
Box 3.3 <i>Constant strain mode injection. Rate form.</i>	63
Box 3.4 <i>Constant strain injection. “Total” form.</i>	64
Box 3.5 <i>Constant strain injection. Incremental strategy.</i>	64
Box 3.6 <i>Constant strain injection. Matrix equations.</i>	65
Box 5.1 <i>Strong form of the boundary value problem with discontinuity.</i>	98
Box 5.2. <i>Mixed $\hat{\mathbf{u}}, \hat{\boldsymbol{\epsilon}}, [[\hat{\mathbf{u}}]]$. Un-symmetric formulation.</i>	103
Box 5.3 <i>Mixed $\hat{\mathbf{u}}, \hat{\boldsymbol{\epsilon}}, [[\hat{\mathbf{u}}]]$. Symmetric strong discontinuity formulation.</i>	107
Box 5.4 <i>Strong discontinuity injection.</i>	108
Box 5.5 <i>Mixed $\hat{\mathbf{u}} - \hat{\boldsymbol{\epsilon}} - [[\hat{\mathbf{u}}]]$ weak discontinuity formulation.</i>	114
Box 5.6 <i>Weak discontinuity injection.</i>	115
Box 5.7 <i>The crack-propagation problem.</i>	118
Box 5.8 <i>Discretized crack-propagation problem.</i>	119
Box 5.9 <i>Injection procedure. Matrix equations - Implementation</i>	129
Box 5.10 <i>Crack-propagation problem. Matrix equations - Implementation</i>	131

Box A.1 Rankine constitutive model.....	164
Box A.2 Determination of the plastic multiplier	166
Box A.3 Rankine model IMPL-EX integration scheme.	173
Box B.1 Mixed $\hat{\mathbf{u}}, [[\dot{\mathbf{u}}]]$ symmetric formulation considering rotation degrees of freedom (linear displacement along \mathcal{S}).....	178
Box C.1 Symmetric strong discontinuity formulation.....	187
Box C.2 Un-symmetric strong discontinuity formulation.	188
Box C.3 Weak discontinuity formulation.....	189

Chapter 1

Introduction

Failure Mechanics has attracted large interest in the last decades being object of intensive research and important developments. Notwithstanding, nowadays modeling failure processes still remains a challenging problem. Research on this field is justified by an important variety of practical applications. In the ambit of civil engineering, structures are designed to behave in linear elastic regimes, far from the possible collapse mechanism. Nevertheless, structures which failure can potentially cause possible catastrophic scenarios, like dams, bridges, oil/gas pipelines *etc.*, can be object of additional deep studies related to failure scenarios.

In addition, in the ambit of mechanical engineering, failure analysis is an important tool when ships, planes, cars and its respective components and accessories are being designed and developed. Possible additional applications of this research topic can encompass the development of new materials, fracture in the biomedical engineering field, nuclear engineering, *etc.*

1.1. State of the art

In this Section a general insight about failure analysis is given. It is not intended to provide a detailed state of art review. Instead, the aim here is to refer the most important historical and actual lines of research. For a more detailed review, see *e.g.* [Gerstle 1997; Bazant and Planas 1998].

In the beginning of the 20th century, supported by the classic elasticity theory, failure processes began to be studied. The first steps were done by Inglis in 1913 [Inglis 1913], who introduce some new concepts like “the stress concentration factor”. Later on, Griffith [Griffith 1921] propose an energy criterion of failure to study the stability or propagation of pre-existing crack. The contributions of both authors gave rise to a new discipline called: Linear Elastic Fracture Mechanics.

This discipline was then developed by other authors, like Irwin [Irwin 1948] that systematized the different modes of fracture.

The advent of computers in 1940s and the subsequent rapid development of the finite element method in the 1950s have permitted, in the 1960s, a rapid increment of practical contributions related to computational failure mechanics. Linear Elastic Fracture Mechanics was just applicable to very brittle materials such as glass. In this class of materials, discrete cracks or displacement jumps develop almost instantly. In contrast, highly ductile materials exhibit real displacement jumps only for very late stages of failure. The quasi-brittle¹ materials are in an intermediate stage where in a first period strains start localizing in thin diffuse zones (as microcracks or other distinct dissipative phenomena is growing) that collapse afterwards in physical discontinuities.

To extend the application of failure mechanics to quasi-brittle and ductile materials, classical non-linear fracture mechanics theories start being developed considering a yielding zone in the tip of the crack [Gallagher 1971]. Two major descriptions were developed: *equivalent elastic crack* models and *cohesive crack models*. In the former, the treatment is similar to that used in linear fracture mechanics, being the model formulated in terms of stress intensity factors. Nevertheless, some additional rules are added to express how the equivalent crack extends under increasing load [Kraft et al. 1961; Jenq and Shah 1985]. In the later, discrete constitutive equations (tractions *vs.* displacement jumps) are introduced *i.e.* the crack is assumed to open while is still transferring stresses, from one face to the other face of the crack, according the correspondent constitutive equation [Hillerborg et al. 1976] [Dugdale 1960].

Parallely to these methodologies, which are based in fracture mechanics, another large family of methodologies, based on the continuum mechanics, was developed. This new class of methodologies uses standard continuum (stress *vs.* strain) constitutive models equipped with strain softening to approach a phenomenon physically discrete: the fracture. This family of methodologies can be termed in general *as classical strain localization methods* (see Chapter 2) since their main assumption/idea is that the fracture can be studied as a consequence of concentration of strains in narrow bands (strain localization), being therefore, the fracture displacement jumps captured through a finite length in a “smeared” manner [Rashid 1968]. This approach has attracted considerable attention of the scientific community due to its inherent simplicity and easiness of implementation in the finite element context. On the other hand, very soon it was detected that the finite element solution suffers from numerical pathologies. Rots systematized the principal problems: stress locking and directional mesh bias dependence [Rots 1988]. In the nineteen’s, in the ambit of continuum mechanics, two sub-families were developed to face the numerical problems inherent to the classical localization methods.

One of them is based on the regularization of the standard strain-softening continua (by incorporating an internal characteristic length): non-local [Pijaudier

¹ A wide range of engineering materials can be considered as quasi-brittle materials as concrete, masonry, some metals, polymers, *etc.*

Cabot and Bazant 1987], gradient [de Borst and Mühlhaus 1992], micro-polar [Mühlhaus and Vardoulakis 1987] methods fall within this category that proved to be efficient in achieving results independent of the mesh directions. The principal inconvenient of these methods is that, in order to capture that internal length, the resulting localization band has to encompass a certain number of finite elements, which, due the small character of the involved internal length, demands the use of very fine finite element discretizations or auxiliary re-meshing techniques.

The second sub-family is the so-called Strong Discontinuity Approach (SDA). This methodology was inspired in the original work of Ortiz involving embedded discontinuities [Ortiz et al. 1987]. It essentially consists of enriching the (continuous) displacement modes of the standard finite elements, with additional (discontinuous) displacements, devised for capturing the physical discontinuity. The discontinuity is placed inside the elements irrespective of the size and specific orientation of them. For the enriching technique, two possibilities can be distinguished in terms of the support of the enriching functions: elemental-based enrichment (embedded-discontinuities) [Simo et al. 1993] or nodal-based enrichment (X-FEM methods)[Belytschko et al. 2001]. These methodologies, associated to global tracking algorithms (that rule the crack propagation) proved to be efficient in providing results free from either stress-locking or mesh-bias dependence, for impressive coarse meshes. The SDA permits also to establish a direct link between the methods based on continuum mechanics (using stress-strain constitutive models) with those coming from fracture mechanics (typically based on traction-separation models embedded into the localization band) [Oliver et al. 2002]. This theoretical result has high significance since establishes direct connections between methodologies developed from very different starting points. The principal drawback of the methodology is related with the need to resort to global crack tracking algorithms, which increase the sophistication of the methodology (the procedure is not purely local). Moreover, global tracking algorithms seem to impose some limitation in applications to dynamics problems, when more complex phenomena, like branching, is intended to be modeled.

Still in the ambit of continuous methods, a new group of methodologies is recently emerging – the phase field models [Francfort and Marigo 1998; Miehe et al. 2010a; Miehe et al. 2010b]. The phase-field refers to a variable that interpolates between the unbroken and the broken states of the material. The crack propagation is then controlled by suitable equations (*e.g.* dissipation functions obtained by minimization principles) that govern the evolution of the crack phase field. These procedures are generally computationally demanding, since fine meshes are required.

Outside the ambit of the finite element method (FEM), discrete element methods (DEM) have also been used to analyze fracture processes [Bažant et al. 1990] [Potyondy and Cundall 1996]. These models leave aside the idea of continuum media, and concepts like stress strain relations being formulated in terms of rigid discrete elements that interact with each other according to contact laws. For

modeling fracture the discrete elements are generally chosen to be circular or spherical particles and the correspondent inter-particle contacts can either be assumed as brittle or following a given softening curve [Meguro and Hakuno 1989] [Azevedo et al. 2008]. These discrete models use generally the meso-structure of the material being therefore computationally more demanding than the continuum models (that are at the macro-scale level). For this reason, intending to reduce the computational cost, also some hybrid models FEM-DEM have been developed [Azevedo and Lemos 2006], that use the finite element method outside the fracture process area and the discrete particle element method in the areas of interest.

Lattice models have also been used for modeling fracture. In these models, developed to deal with random heterogeneous [Herrmann and Roux 1990], the material is discretized as a lattice composed of Bernoulli beams that transfer normal forces shear forces and bending moments. Usually linear elastic analyses are performed and beam elements that exceed tensile strength are removed [Schlangen and Garboczi 1997; Kozicki and Tejchman 2006].

In addition, some more sophisticated multi-scale approaches have been developed (see [Saether et al. 2009] for a general insight). Usually in the multi-scale approaches, near the crack tip some micro scale approach is used intending to capture the complex phenomena of fracture deriving from the material micro-structure (*e.g.* the atomistic simulations of [Gumbsch 1995]), whereas in regions away from the crack tip a macro approach is used (typically based in elasticity and the finite element method). A different multi-scale approach was used in [Belytschko et al. 2008] in the context of continuum mechanics and strong discontinuities. In this approach, the authors use the concept of unit cell which provide the stress response, the orientation and magnitude of the displacement discontinuity that is afterwards introduced in the coarse-scale model by the X-FEM method.

1.2. Adopted approach

In this work, when we refer to *classical strain localization methods* we mean: finite element solutions of material failure problems based uniquely on strain localization techniques, using standard continuum stress-strain constitutive models equipped with strain softening. The softening modulus is properly regularized in order to give objectivity to the model (*e.g.* using the characteristic element size [Oliver 1989]).

The approach adopted in this work, uses the finite element method in a continuum mechanics framework and the main assumptions are the isothermal quasi-static regime and small deformations. The material is assumed homogeneous and isotropic.

The proposed methodologies explore a combination of classical strain localization methods and strong discontinuity approaches to remove the flaws (stress-locking and mesh bias dependence) of the former, and simultaneously abdicate of global tracking, that are usually used in conjunction with the later. The idea is to use, after bifurcation, *i.e.* after the time that elements are amenable to develop discontinuities, a mixed *continuous displacements - discontinuous constant strains* condensable finite element formulation. This formulation provides improved behavior results, specially, in terms of avoiding mesh bias dependence (this issue has also been reported by other authors using a non-condensable mixed *continuous displacements and strains* formulation [Cervera et al. 2011]). In earlier stages of localization (in a first stage) the concept of strong discontinuity is then leaved aside, being the displacement jump captured through the finite element length (smeared) in a classical strain localization setting. However, in a second stage, and in order to minimize stress locking, the elemental kinematics of those finite elements that are developing deep enough strain localization is enhanced with the injection of a weak/strong discontinuity mode. The necessary data to inject the discontinuity (the discontinuity direction and its position inside the finite element) is not obtained by resorting to global tracking algorithm, but instead, is obtained with a local methodology based in the strain-like internal variable field that is computed with the mixed finite element formulation (the crack-propagation problem).

1.3. Objectives

The main objectives of this research work are:

- Develop a method enjoying the benefits of the strong discontinuities approach (stress locking free and mesh bias independent), at a complexity similar to the classical and simpler localization methods, *i.e.* a pure local method is to be devised abdicating of auxiliary global (tracking) algorithms.
- The computational cost of the method should be kept low, *i.e.* in the order of the standard finite element methods, and coarse meshes should be allowed for use.
- The methodology should be applicable to any constitutive model (damage, elasto-plasticity *etc.*).

A secondary objective is to revisit the classical strain localization methods and inquire about the quality of the solutions provided by these classical methodologies. The main idea is to discern whether the finite element solutions of material failure problems based on strain localization techniques, using standard continuum stress-strain constitutive models equipped with strain softening, have physi-

cal sense as solutions of de-cohesive fracture mechanics problem. Thus, to assess quality of the solutions, several objective indicators to be computed without a-priori knowledge of the exact fracture mechanism of the problem will be proposed.

1.4. Outline

This research work has four main Chapters (2-5), an introduction (Chapter 1), where a very general state of art is included, and conclusions (Chapter 6) where the main conclusions of the work are presented and future lines of work are suggested.

Chapter 2 is a preliminary Chapter where most of the ingredients necessary for developing the subsequent Chapters are included. All the ingredients integrated in this Chapter make part of the state of art *i.e.* no original contributions are given. A general insight of the strain localization phenomena and classical strain localization models is given, with emphasis in its classical flaws (mesh bias dependence (2.4.4) and stress locking (2.4.5)).

The subsequent three Chapters introduce developing issues where original contributions are given. All of them are organized in an analogous form: in the beginning, a specific state-of-art is included and the main ideas that motivate the Chapter are mentioned. Then, in the core part of the Chapter, the principal mathematical ingredients are introduced and developed. Finally, in its last part, representative numerical simulations are shown (illustrating the methodology and validating the proposals of this work) and the main conclusions of the Chapter are summarized².

In Chapter 3, to overcome the classic mesh bias dependence of standard irreducible formulations, a condensable *mixed displacement-strain* finite element formulation is developed. In order to avoid instabilities related with hourglass modes, an injected version is proposed: the constant strain mode injection.

In Chapter 4, several objective indicators to assess quality of classical strain localization methods solutions, which can be computed without a-priori knowledge of the exact fracture mechanism of the problem, are proposed.

In Chapter 5, inspired in the strong discontinuity approach, a full methodology for material failure modeling is proposed, based in the injection, in two stages, of specific strain modes: the constant strain mode and the weak/strong discontinuity mode.

² In chapter 5, are not included conclusions since they are postponed for the chapter 6 where general conclusions are given.

Chapter 2

Strain Localization

In the context of Continuum Solid Mechanics, strain localization is a natural consequence of the introduction of softening in constitutive relations between stresses and strains. To motivate some important aspects of this Work, we present a brief summary of a one-dimensional problem, which is often used in the literature ([Bazant and Planas 1998],[de Borst 1986] and [Oliver 2002]) to illustrate the strain localization phenomena.

Let us consider a homogenous bar loaded uniaxially. The material is linearly elastic until the moment that the uniaxial stresses σ exceed the ultimate tensile strength σ_u . After this point the material softens according to the linear softening diagram presented in Figure 2.1, where E and H are the Young's and softening modulus respectively (in Section 2.2 some nonlinear continuum constitutive models are presented in detail).

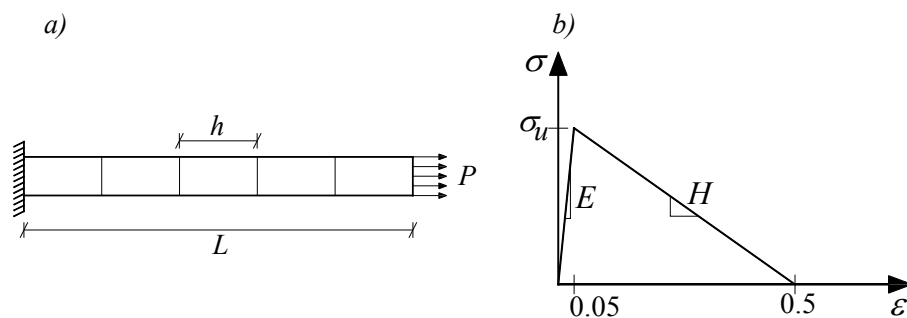


Figure 2.1 A bar problem with strain softening material: a) homogenous bar, b) stress-strain relations.

Since the structure is perfectly homogenous, all points of the bar reach the ultimate stress at the same time. Afterwards, they will enter into softening regime and the consequence is a homogenous solution with constant values of stresses

and strains ε along the bar length. The total elongation is then equal to $\Delta l = \varepsilon L = 0.5L$ (see Figure 2.2-b).

In practice, the bar cannot be perfectly homogenous; and some part/section is slightly weaker (due to some imperfection, *etc.*). In this view, the structural behavior of the bar is completely different relatively to the homogeneous case. In fact, since some point of the bar has the lowest ultimate strength, the stress limit is reached in advance, and after that, the point softens. Due to equilibrium considerations, stresses in the remaining part of the bar have also mandatorily to decrease, nevertheless, since the correspondent ultimate stress was not reached yet, stresses do not soften, but instead, unload elastically, giving a *localized solution*, with nonlinear loading in the localization band and linear unloading in the remaining part of the body.

Let us admit that the central part $h = L/5$ of the bar (Figure 2.1) is slightly weaker. At the end of the loading process, in this central region, strains are deeply localized and stresses fully released. By equilibrium, elastic stresses outside the localization band are zero and, consequently, strains in this region also vanish. The total elongation of the bar is then $\Delta l = \varepsilon h = \varepsilon L/5 = 0.1L$.

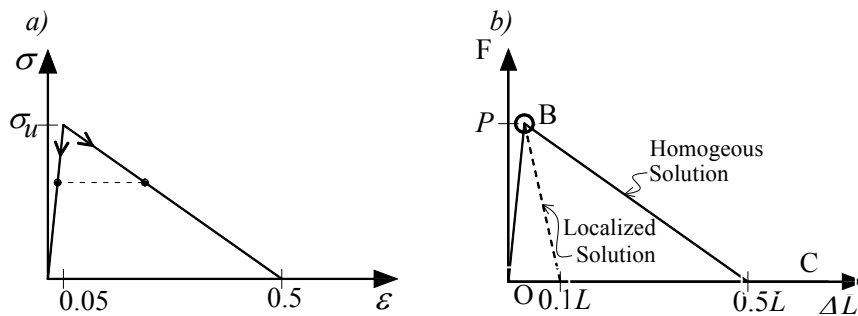


Figure 2.2 a) Stress-strain relation, b) force-displacement solutions.

Two different solutions for the same problem were presented. From the point of view of statics both solutions are possible, since they satisfy the complete governing equations of the boundary value problem (see Section 2.1). The point B in Figure 2.2-b is called a bifurcation point (see Section 2.3), since after this point, depending on the width and the position of the localization band, a multiplicity of solutions are admissible. From a mathematical point of view, it is said that the character of the governing set of differential equations cease to be elliptical ([Marsden and Hughes 1983] [Knops and Payne 1971]), the problem loses uniqueness and this simple problem becomes mathematically ill-posed (in the sense of Hadamard [Hadamard 1902]).

The homogeneous solution is said to be unstable (almost impossible to obtain in practice) since a slight perturbation on the homogeneity of the bar will cause a sudden change in the structural behavior to a “more stable” localized solution [Crisfield 1998]. In this view, one can think that deformations in real problems

are localized on the minimum length, since this solution would tend to be less dissipative and, therefore, would be more stable. However, this question is not straightforward since this conclusion leads to an inconsistency solution. Note that, for the theoretical bar problem of Figure 2.1, for $h \rightarrow 0$, the softening branch B-C approaches the initial elastic loading path O-B, giving a brittle fracture progressing with null energy dissipation, what is unacceptable³ from a physical point of view. This unacceptable behavior gives raise to the classical lack of objectivity of models that study the fracture as a consequence of strain concentration in narrow zones (the strain localization methods).

It is known from experience, that formation of cracks is a gradual process that evolves throughout different stages. This process can be associated to three different spatial zones that define the commonly termed Fracture Process Zone [Bazant 1983; Oliver and Huespe 2004b]:

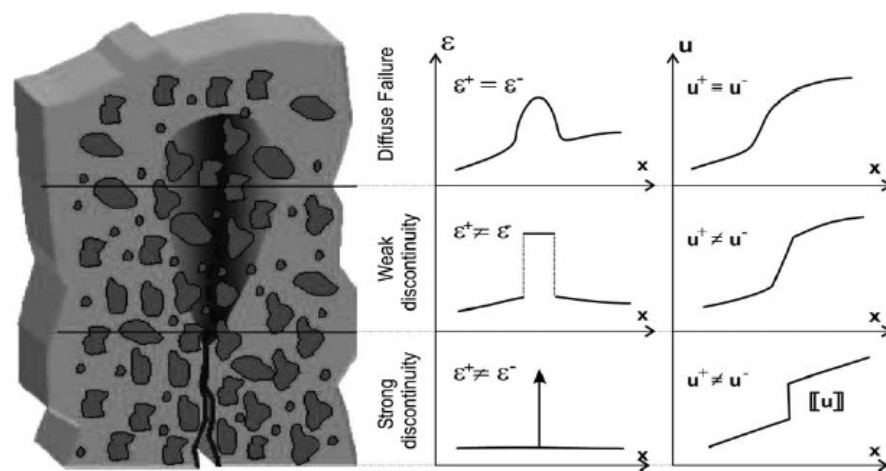


Figure 2.3 Fracture process zones (adapted from [Oliver and Huespe 2004b]).

- Diffuse failure zone. It corresponds to the initiation of the dissipative phenomena. Notwithstanding the increase of strain concentration, the stress and strain fields remain spatially smooth.
- Weak discontinuity zone. The diffuse zone becomes narrower and the strain concentration sharper up to collapse in a discontinuous strain field. Despite of this fact, the displacement field remains continuous, however it exhibits an apparent jump across both sides of the weak discontinuity localization band.
- Strong discontinuity zone. The narrower process of the previous zone evolves up to collapse in a zero thickness discontinuity band. Now,

³ This paradoxical result was understood on the light of the strong discontinuity approach [Oliver 2000], where the softening modulus was reinterpreted in a distributional sense, allowing dissipation to occur in a region of zero measure.

the displacement field become discontinuous, exhibiting a real jump and the correspondent strain field becomes therefore unbounded.

This theoretical phenomenological model intends representing the fracture phenomena for a wide range of materials, where strain localization stems from different physical mechanisms⁴, and where the process eventually evolves up to the collapse into a macroscopical discontinuity.

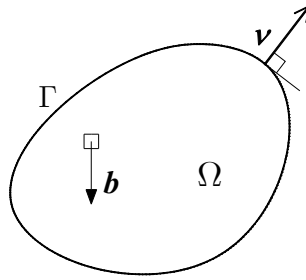
In the light of this evolutive process, the identification of a fixed length for crack formation analysis, as was done in the previously presented bar example of Figure 2.1, may be regarded as an artifice for convenience of the simulation. Additionally, to overcome the lack of objectivity of the strain localization methods, concepts like the regularization of the softening modulus (that link the regularized softening modulus to the fracture energy) were introduced in order to ensure realistic energy dissipation. In ambit of the strong discontinuity approach, by means of a variable bandwidth model [Oliver 2000], a gradual transition from a weak discontinuity that collapses in a strong discontinuity of zero thickness was proposed. At the strong discontinuity regime, since strains are unbounded, the regularization of the softening modulus has a distributional sense (so the stresses remain regular). An interesting consequence of this interpretation is that dissipation can occur in a region of zero measure.

2.1. The initial boundary value problem in non-linear solid mechanics

Let us consider the classical boundary value problem in nonlinear solid mechanics. In this work, infinitesimal deformations are assumed, thus the nonlinearity arises from the constitutive behavior between stresses and strains.

Denoting the continuum body by Ω , and by Γ its boundary that may be subdivided in two parts: Γ_u where displacements $\mathbf{u}(\mathbf{x})^*$ are imposed (called, in the literature, essential boundary conditions) and Γ_σ where tractions $\mathbf{t}(\mathbf{x})^*$ are prescribed (called natural boundary conditions), with $\Gamma_\sigma \cap \Gamma_u = \emptyset$ and $\overline{\Gamma_\sigma} \cup \overline{\Gamma_u} = \overline{\Gamma} = \Gamma$, where the bar means set closure [Hughes 1987]. The vector $\boldsymbol{\nu}$, is the outward unit normal to Γ and \mathbf{b} are the body forces.

⁴ Voids nucleation and coalescence in metals, micro cracking in concrete, shear banding in soils, *etc.*

Figure 2.4 *Continuum body.*

The rate equations (strong form) of the boundary value problem are summarized in Box 2.1.

Given the external actions $\dot{\mathbf{u}}^*(\mathbf{x}) : \Omega \rightarrow \mathbb{R}^N$, $\dot{\mathbf{i}}^*(\mathbf{x}) : \Omega \rightarrow \mathbb{R}^N$ and $\dot{\mathbf{b}}(\mathbf{x}) : \Omega \rightarrow \mathbb{R}^N$, find $\dot{\mathbf{u}}(\mathbf{x}) : \Omega \rightarrow \mathbb{R}^N$ such that:	
$\nabla \cdot \dot{\boldsymbol{\sigma}} + \dot{\mathbf{b}} = 0$, $\forall \mathbf{x} \in \Omega$	(equilibrium equation) (2.1)
$\dot{\boldsymbol{\sigma}} = \dot{\boldsymbol{\Sigma}}(\dot{\boldsymbol{\varepsilon}})$, $\forall \mathbf{x} \in \Omega$	(constitutive equation) (2.2)
$\dot{\boldsymbol{\varepsilon}} = \nabla^s \dot{\mathbf{u}}$, $\forall \mathbf{x} \in \Omega$	(compatibility equation) (2.3)
$\left. \begin{array}{l} \dot{\mathbf{u}} = \dot{\mathbf{u}}^* \\ \dot{\boldsymbol{\sigma}} \cdot \boldsymbol{\nu} = \dot{\mathbf{i}}^* \end{array} \right\} \text{, } \forall \mathbf{x} \in \Gamma_u \text{ and } \forall \mathbf{x} \in \Gamma_\sigma$	(boundary conditions) (2.4)

Box 2.1 *Strong form of the boundary value problem.*

In Box 2.1, N stands for the number of space dimensions, \mathbb{R} stands for the set of real numbers and $\dot{\boldsymbol{\sigma}}$ is the rate Cauchy stress tensor that is related to the infinitesimal rate strain tensor $\dot{\boldsymbol{\varepsilon}}$ through a nonlinear constitutive function $\dot{\boldsymbol{\Sigma}}$ (the constitutive model is detailed in Section 2.2). The infinitesimal strain tensor $\dot{\boldsymbol{\varepsilon}}$ is computed from the compatibility equation (kinematics), whereas the superscript $(\bullet)^S$ means the symmetric part of the tensor (\bullet) .

2.2. Material nonlinearity - continuum constitutive models

2.2.1. Plasticity models

The mathematical theory of the macroscopic phenomenological plasticity theory has its roots on the pioneering work of Saint-Venant, Lévy, Tresca and von Mises at the end of the nineteenth century. These original works have been object of deep investigation over the last century. Nowadays, phenomenological plasticity models have been systematized by several authors, and are widely used in practical and research proposes.

Applications are frequent to that class of materials that suffer ductile failure mechanisms, associated to irreversible (plastic) deformations, such as metals, some kind of soils and plastic materials. Moreover, with an adequate failure criterion, the modern plasticity theory offers a proper mathematical framework for phenomenological modeling of a larger set of materials, where also the quasi-brittle materials⁵ are included.

Mathematical rate-independent plasticity with infinitesimal strain assumption, is here adopted. An internal variables approach with thermodynamic basis is used. A complete description can be consulted in the following references [Simo and Hughes 1998], [Lubliner 1990], [Neto et al. 2008].

The principal ingredients of the model are:

1. Additive decomposition of the strain tensor (main assumption).

$$\boldsymbol{\varepsilon} = \boldsymbol{\varepsilon}^e + \boldsymbol{\varepsilon}^p \rightarrow \boldsymbol{\varepsilon}^e = \boldsymbol{\varepsilon} - \boldsymbol{\varepsilon}^p, \quad (2.5)$$

where $\boldsymbol{\varepsilon}^e$ is the elastic strain tensor and $\boldsymbol{\varepsilon}^p$ is the plastic irreversible strain, whose evolution is provided by the flow rule.

2. Free energy.

It is assumed that the specific free energy (disregarding the dependence on thermal effects) depends on:

$$\varphi = \varphi(\boldsymbol{\varepsilon}^e, \boldsymbol{\alpha}), \quad (2.6)$$

where $\boldsymbol{\alpha}$ is the set of thermodynamically consistent strain-like internal variables that rule the plastic effects. This set may contain scalar, vectorial or tensorial entities, depending on the complexity of the phenomenology that is

⁵ For this kind of materials, the “model internal variables”, like the irreversible plastic deformation $\boldsymbol{\varepsilon}^p$, have a somewhat distinct physical meaning, than the one it has when it is used to describe ductile materials behavior, [Lubliner et al. 1989].

intended to be captured. In this work, the analysis is restricted to isotropic softening materials, thus, just one scalar variable α is required.

Accordingly, regarding the decomposition of the strain tensor, the free energy may be rewritten as:

$$\varphi = \varphi^e(\varepsilon^e) + \varphi^p(\alpha), \quad (2.7)$$

where φ^e is the elastic free energy function (elasticity strain potential) $\varphi^e = \frac{1}{2} \varepsilon^e : \mathbf{C}^{el} : \varepsilon^e$, φ^p is the plastic free energy depending on the internal variable α and \mathbf{C}^{el} stands for the linear elastic fourth order tensor.

3. Constitutive laws.

Exploiting the Clausius-Duhem inequality (second law of thermodynamics) with expression (2.7) (Coleman's method) the constitutive relations follows as (see [Coleman and Noll 1963],[Lubliner 1990]):

$$\boldsymbol{\sigma} = \frac{\partial \varphi^e}{\partial \varepsilon^e}, \quad (2.8)$$

$$\alpha = \frac{\partial \varphi^p}{\partial q}, \quad (2.9)$$

where q is the stress-like internal variable, thermodynamically conjugated with α by the hardening law. Equations (2.8) and (2.5) lead to:

$$\boldsymbol{\sigma} = \mathbf{C}^{el} : (\varepsilon - \varepsilon^p). \quad (2.10)$$

4. Elastic domain.

The elastic domain and yield surface are defined by means of a scalar function in the stress space,

$$f(\boldsymbol{\sigma}, q) \leq 0, \quad (2.11)$$

where q is the stress-like internal variable, that controls the size of the elastic domain. This function defines the admissible stress state and cannot be violated. From the preceding function the elastic domain and the yield surface are defined, respectively, as:

$$\mathbb{E} = \{ \boldsymbol{\sigma}, q | f(\boldsymbol{\sigma}, q) < 0 \} \quad ; \quad \partial \mathbb{E} = \{ \boldsymbol{\sigma}, q | f(\boldsymbol{\sigma}, q) = 0 \}. \quad (2.12)$$

For the family of plasticity models of our interest, the function that defines the yield surface may be written in the particular form of (see Figure 2.5-a)):

$$\begin{aligned} f(\boldsymbol{\sigma}, q) &= \hat{f}(\boldsymbol{\sigma}) - q, \\ q_0 &= \sigma_y, \quad q_\infty = 0, \end{aligned} \quad (2.13)$$

where $\hat{f}(\boldsymbol{\sigma})$ is the “effective stress” or “equivalent uniaxial stress” being a scalar valued function that depends exclusively on the actual stress state. The initial value q_0 defines the initial size of the elastic domain and is therefore equal to the yield stress σ_y (the stress threshold from where material starts flowing). Since our attention is restricted to strain softening models, we consider that at the end of the loading process the material is completely exhausted ($q_\infty = 0$).

5. Flow rule.

The flow rule governs the evolution of plastic flow and can be assumed to have the general form of:

$$\begin{aligned} \dot{\boldsymbol{\epsilon}}^p &= \gamma \mathbf{m}(\boldsymbol{\sigma}, q), \\ \dot{\alpha} &= \gamma s(\boldsymbol{\sigma}, q), \end{aligned} \quad (2.14)$$

where \mathbf{m} is a function defining the direction of the flow, $\gamma \geq 0$ is termed the consistency or plastic multiplier parameter that defines the magnitude of the plastic deformations, and $s \geq 0$ is a proportionality factor between γ and $\dot{\alpha}$.

The flow rule is termed associative if the prescribed function assumes the particular form of:

$$\mathbf{m} = \partial_{\boldsymbol{\sigma}} f ; \quad s = -\partial_q f, \quad (2.15)$$

i.e., for this case the flow rule is associated to a flow potential that coincides with the yield surface,

$$\begin{aligned} \dot{\boldsymbol{\epsilon}}^p &= \gamma \partial_{\boldsymbol{\sigma}} f, \\ \dot{\alpha} &= -\gamma \partial_q f = \gamma. \end{aligned} \quad (2.16)$$

6. Hardening law.

The hardening law defines the type of hardening/softening and the evolution of q (see Figure 2.5-b)). Using equation (2.9),

$$\dot{\alpha} = \underbrace{\frac{\partial \alpha}{\partial q}}_{H^{-1}} \dot{q} = \underbrace{\frac{\partial^2 \varphi^p}{\partial q^2}}_{H^{-1}} \dot{q}, \quad (2.17)$$

and rewriting the previous equation:

$$\dot{q} = H(\alpha) \dot{\alpha}, \quad (2.18)$$

where the function $H(\alpha) \leq 0$ is the isotropic softening modulus that depends on the strain-like internal variable. Distinct definitions of φ^p (or

$H(\alpha)$), lead to distinct forms of softening (linear, exponential, *etc.*). The linear isotropic softening case arises from admitting H constant and independent of α .

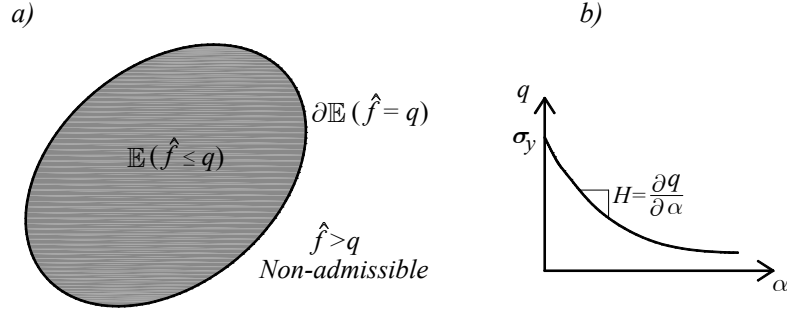


Figure 2.5 a) Elastic domain and yielding surface, b) hardening law.

7. Karush-Kuhn-Tucker Loading/un-loading conditions.

$$\gamma \geq 0 ; f(\boldsymbol{\sigma}, q) \leq 0 ; \gamma f(\boldsymbol{\sigma}, q) = 0 . \quad (2.19)$$

This condition implies that for $f(\boldsymbol{\sigma}, q) < 0$: $\gamma = 0$, *i.e.*, when the stress state is inside the elastic domain no plastic flow takes place. In the other hand, $f(\boldsymbol{\sigma}, q) = 0$ means that the pair $(\boldsymbol{\sigma}, q)$ is on the yield surface and plastic flow can occur.

8. Consistency condition.

$$\gamma \dot{f}(\boldsymbol{\sigma}, q) = 0 . \quad (2.20)$$

The previous expression is derived from (2.19) and requires that for plastic deformation rising ($\gamma > 0$), the pair $(\boldsymbol{\sigma}, q)$ must persist on the yield surface $\dot{f}(\boldsymbol{\sigma}, q) = 0$. Manipulating that equation the consistency parameter may be explicitly solved (see [Simo and Hughes 1998]).

9. Tangent elastoplastic operator.

The tangent elastoplastic operator, is the fourth order tensor that relates the incremental stresses with the incremental strains ($\dot{\boldsymbol{\sigma}} = \mathbf{C}^{ep} : \dot{\boldsymbol{\epsilon}}$). It has the following general form:

$$\mathbf{C}^{ep} = \left\{ \begin{array}{l} \mathbf{C}^{el} \quad \text{if } \gamma = 0 \\ \mathbf{C}^{el} - \frac{\mathbf{C}^{el} : \partial_{\boldsymbol{\sigma}} f \otimes \mathbf{C}^{el} : \partial_{\boldsymbol{\sigma}} f}{\partial_{\boldsymbol{\sigma}} f : \mathbf{C}^{el} : \partial_{\boldsymbol{\sigma}} f + H} \quad \text{if } \gamma > 0 \end{array} \right\} . \quad (2.21)$$

This expression is obtained by substituting the explicit expression of the consistency parameter (obtained by the consistency condition) on the incre-

mental constitutive equation $\dot{\boldsymbol{\sigma}} = \mathbf{C}^{el} : (\dot{\boldsymbol{\epsilon}} - \gamma \partial_{\boldsymbol{\sigma}} f)$, and rearranging terms on the form $\dot{\boldsymbol{\sigma}} = \mathbf{C}^{ep} : \dot{\boldsymbol{\epsilon}}$. The tensor expressed by (2.21) is symmetric since the flow rule is considered associative ($\mathbf{m} = \partial_{\boldsymbol{\sigma}} f$).

2.2.1.1. Rankine plasticity model

The Rankine plasticity model falls into a kind of more general models known on the classical literature as multisurface plasticity models. The elastic domain is then composed, in general, by n smooth yield surfaces (f_i , $i = 1, \dots, n$) that intersect each other nonsmoothly. The mathematical ingredients may be generalized from the single surface plasticity models.

Each boundary of the elastic domain is now defined by the i -th equation:

$$f^i(\boldsymbol{\sigma}, q) = \hat{f}^i(\boldsymbol{\sigma}) - q = 0 \quad (2.22)$$

Therefore, the elastic domain and yield surface are defined, respectively, as:

$$\begin{aligned} \partial \mathbb{E} &= \{ \boldsymbol{\sigma}, q \mid f_i(\boldsymbol{\sigma}, q) = 0, \text{ for some } i \in [1, \dots, n] \} . \\ \mathbb{E} &= \{ \boldsymbol{\sigma}, q \mid f_i(\boldsymbol{\sigma}, q) < 0, \forall i \in [1, \dots, n] \} , \end{aligned} \quad (2.23)$$

The generalizations of the flow rule and hardening law for multisurface plasticity read, respectively,

$$\dot{\boldsymbol{\epsilon}}^p = \sum_{i=1}^n \gamma^i \partial_{\boldsymbol{\sigma}} f^i(\boldsymbol{\sigma}, q), \quad (2.24)$$

$$\dot{q} = H(\alpha) \underbrace{\sum_{i=1}^n \gamma^i}_{\dot{\alpha}} . \quad (2.25)$$

Similarly the Karush-Kuhn-Tucker loading/un-loading conditions read:

$$\gamma^i \geq 0 ; f^i(\boldsymbol{\sigma}, q) \leq 0 ; \gamma^i f^i(\boldsymbol{\sigma}, q) = 0, \quad (2.26)$$

where γ^i is the i -th plastic consistency parameter (no summation on i). The consistency condition reads:

$$\gamma^i \dot{f}^i(\boldsymbol{\sigma}, q) = 0 \quad i = 1, \dots, n . \quad (2.27)$$

The particularization of the general model for the Rankine's model case is done by the specification of the yield surface:

$$\begin{aligned} f^i(\boldsymbol{\sigma}, q) &= \hat{f}^i(\boldsymbol{\sigma}) - q ; \hat{f}^i(\boldsymbol{\sigma}) = \sigma^i , i = I, II, III \\ q_0 &= \sigma_y , q_{\infty} = 0 , \end{aligned} \quad (2.28)$$

where σ^i is the i principal stress.

Rankine proposed this yield criterion in 1876, and its principal feature it is the assumption that yield occurs when the maximum normal stress (the higher prin-

principal stress) reaches the yielding uniaxial stress. Since this model does not consider the influence of shear stresses, it is not suitable for ductile materials modeling, nevertheless it is appropriated for concrete, masonry and other quasi-brittle materials. Here, the Rankine yield criterion is developed in the framework of computational plasticity, aiming to modeling concrete cracking in tension and disregarding crushing in compression.

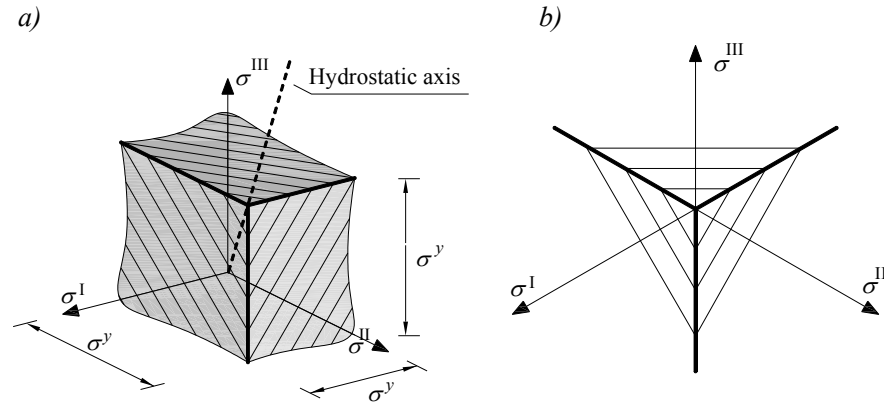


Figure 2.6 Rankine yield surface: a) three dimensional view, b) octahedral plane sections.

Recalling the spectral representation of the stress tensor,

$$\boldsymbol{\sigma} = \sum_{i=1}^{III} \sigma^i \mathbf{p}^i \otimes \mathbf{p}^i, \quad (2.29)$$

where \mathbf{p}^i is the i -th principal direction,

$$\sigma^i = \boldsymbol{\sigma} : \mathbf{p}^i \otimes \mathbf{p}^i. \quad (2.30)$$

From the particularization of equation (2.24), the flow rule reads:

$$\dot{\boldsymbol{\epsilon}}^p = \sum_{i=1}^{III} \gamma^i \mathbf{p}^i \otimes \mathbf{p}^i, \quad (2.31)$$

where $\mathbf{m}^i = \mathbf{p}^i \otimes \mathbf{p}^i$ is the flow tensor correspondent to the i -th yield surface.

In Box 2.2 the main ingredients of the Rankine constitutive model are summarized.

Additive strain decomposition	$\varepsilon = \varepsilon^e + \varepsilon^p$	(2.32)
Constitutive equation	$\sigma = \mathbb{C}^{el} : (\varepsilon - \varepsilon^p)$	(2.33)
Yield surface	$f^i(\sigma, q) = \hat{f}^i(\sigma) - q$ $\hat{f}^i(\sigma) = \sigma^i$, with $i = I, II, III$	(2.34)
Flow rule	$\dot{\varepsilon}^p = \sum_{i=I}^{III} \gamma^i \mathbf{m}^i$; $\mathbf{m}^i(\sigma) = \mathbf{p}^i \otimes \mathbf{p}^i$	(2.35)
Hardening law	$\dot{q} = H \sum_{i=I}^{III} \gamma^i$	(2.36)
Loading-unloading conditions	$\gamma^i \geq 0$; $f^i(\sigma, q) \leq 0$; $\gamma^i f^i(\sigma, q) = 0$	(2.37)

Box 2.2 Rankine constitutive model.

2.2.1.2. J_2 (von Mises) plasticity model

This yield surface was first introduced by von Mises in 1913. Actually, it is one of the most widely used criteria for failure modeling of ductile materials.

In crystalline materials such as metals, crystallographic plane slip is generally the principal mechanism of plastic deformation [Lubliner 1990], therefore in modeling such materials, pressure is generally negligible. Von Mises yield surface is independent of the invariant I_1 , and is stated exclusively in terms of the second deviatoric invariant J_2 , implying that yielding derives from the deviatoric components of the stress tensor, and under hydrostatic loading, the model material behaves elastically.

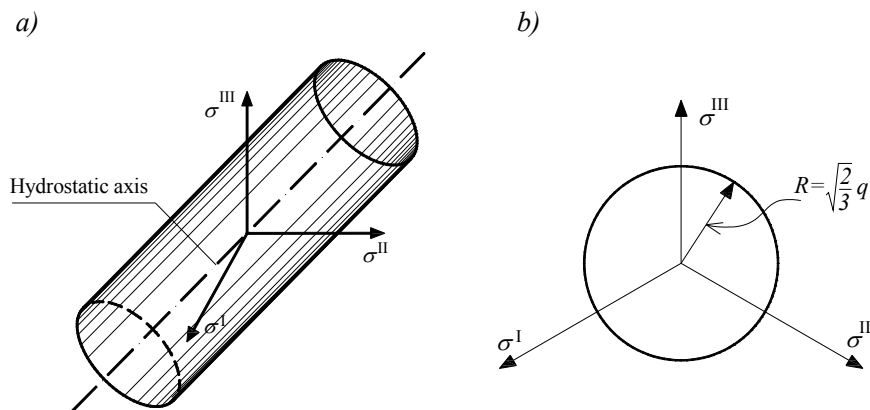


Figure 2.7 Von Mises yield surface: a) three dimensional perspective, b) deviatoric Section.

Particularizing the general model for the Von Mises yield surface,

$$\begin{aligned} f^i(\boldsymbol{\sigma}, q) &= \hat{f}^i(\boldsymbol{\sigma}) - q \quad , \quad \hat{f}^i(\boldsymbol{\sigma}) = \sqrt{\frac{3}{2}} \|\mathbf{s}\|, \\ q_0 &= \sigma_y \quad , \quad q_\infty = 0, \end{aligned} \quad (2.38)$$

where \mathbf{s} is the deviatoric part of the stress tensor $\boldsymbol{\sigma}$ and the norm $\|\mathbf{s}\| = \sqrt{\mathbf{s} : \mathbf{s}}$ represents the minimum distance from the current stress state $\boldsymbol{\sigma}$ to the hydrostatic axis.

From a geometric point of view, this function represents the external surface of an infinite cylinder with hydrostatic axis and initial radius $R_0 = \sqrt{\frac{2}{3}} \sigma_y$ (note that $q_0 = \sigma_y$), (see Figure 2.7).

Particularizing equation (2.24), the flow rule reads:

$$\dot{\boldsymbol{\varepsilon}}^p = \gamma \sqrt{\frac{3}{2}} \frac{\mathbf{s}}{\|\mathbf{s}\|}, \quad (2.39)$$

where $\mathbf{m} = \sqrt{\frac{3}{2}} \frac{\mathbf{s}}{\|\mathbf{s}\|}$ is the flow tensor.

In Box 2.3 the principal ingredients of J_2 constitutive model are summarized:

Additive strain decomposition	$\boldsymbol{\varepsilon} = \boldsymbol{\varepsilon}^e + \boldsymbol{\varepsilon}^p$	(2.40)
Constitutive equation	$\boldsymbol{\sigma} = \mathbf{C}^{\text{el}} : (\boldsymbol{\varepsilon} - \boldsymbol{\varepsilon}^p)$	(2.41)
Yield surface	$f(\boldsymbol{\sigma}, q) = \hat{f}(\boldsymbol{\sigma}) - q$ $\hat{f}(\boldsymbol{\sigma}) = \sqrt{\frac{3}{2}} \ \mathbf{s}\ $	(2.42)
Flow rule	$\dot{\boldsymbol{\varepsilon}}^p = \gamma \mathbf{m}(\boldsymbol{\sigma}) \quad ; \quad \mathbf{m}(\boldsymbol{\sigma}) = \sqrt{\frac{3}{2}} \frac{\mathbf{s}}{\ \mathbf{s}\ }$	(2.43)
Hardening law	$\dot{q} = \gamma H(\alpha)$	(2.44)
Loading-unloading conditions	$\gamma \geq 0 \quad ; \quad f(\boldsymbol{\sigma}, q) \leq 0 \quad ; \quad \gamma f(\boldsymbol{\sigma}, q) = 0$	(2.45)

Box 2.3 J_2 constitutive model.

2.2.2. Damage models

The scalar continuum damage model concept was first introduced by Kachanov [Kachanov 1958] for the study of creep in metals, becoming after that an emerging field of intense research. An extensive list of models were then proposed by different authors to model the constitutive behavior of brittle, quasi-brittle and even ductile materials (see [Ju 1991; Lemaitre 1992] for a literature review). Due to its intrinsic nature, it is particularly appropriated for concrete constitutive modeling. In this context, the internal damage variable is associated to the material degradation *i.e.* to the initiation, growth and coalescence of microcracks or microvoids. Depending on the complexity of the phenomenology that is intended to be captured, the damage variable can be a scalar, vectorial or tensorial entity.

Here, the isotropic damage model proposed in [Oliver et al. 1990], that is based in the model originally presented in [Simó and Ju 1987], is used. In the following, the main ingredients are presented:

1. Damage variable

In this work, the damage variable is chosen as a scalar variable d representing an isotropic damage case (independent of the direction). The value $d = 0$ corresponds to the undamaged state whereas $d = 1$ means a fully damage state. The following definition for d is assumed:

$$d = 1 - \frac{q(r)}{r}, \quad (2.46)$$

where q and r are, respectively, the stress and strain like internal variables.

2. Free energy.

It is assumed that the specific free energy (disregarding the dependence on thermal effects) has the following form:

$$\varphi = \varphi(\varepsilon, r) = (1 - d(r))\varphi^e(\varepsilon), \quad (2.47)$$

where φ^e is the elastic free energy function (elasticity strain potential)

$\varphi^e = \frac{1}{2}\varepsilon : \mathbf{C}^{el} : \varepsilon$, and r stands for the strain like internal variable.

3. Constitutive laws .

Exploiting the Clausius-Duhem inequality (second law of thermodynamics) with expression (2.47) (Coleman's method) the constitutive relations follows as (see [Coleman and Noll 1963]):

$$\sigma = \frac{\partial \varphi^e}{\partial \varepsilon} = (1 - d) \frac{\partial \varphi^e}{\partial \varepsilon}, \quad (2.48)$$

$$\begin{aligned}\boldsymbol{\sigma} &= (1-d)\bar{\boldsymbol{\sigma}}, \\ \boldsymbol{\sigma} &= \frac{q}{r}\bar{\boldsymbol{\sigma}}.\end{aligned}\tag{2.49}$$

In equation (2.48) the term $(1-d)$ can be interpreted as a reduction factor, being $\bar{\boldsymbol{\sigma}}$ the effective elastic stress (see [Lemaitre 1992] for a physical interpretation).

4. Elastic domain.

The elastic domain and damage surface can be defined by means of a scalar function in the strain space,

$$f(\boldsymbol{\varepsilon}, r) \leq 0,\tag{2.50}$$

where r is the strain-like internal variable controlling the size of the elastic domain. This function defines the admissible strain state and cannot be violated. From the preceding function the elastic domain and the damage surface are defined, respectively, as:

$$\mathbb{E} = \{\boldsymbol{\varepsilon}, r | f(\boldsymbol{\varepsilon}, r) < 0\} \quad ; \quad \partial\mathbb{E} = \{\boldsymbol{\varepsilon}, r | f(\boldsymbol{\varepsilon}, r) = 0\}.\tag{2.51}$$

For the family of models of our interest, the function that defines the damage surface may be written in the particular form of:

$$\begin{aligned}f(\boldsymbol{\varepsilon}, r) &= \Psi(\boldsymbol{\varepsilon}) - r, \\ r|_{t=0} &= r_0 = \frac{\sigma_u}{\sqrt{E}},\end{aligned}\tag{2.52}$$

where $\Psi(\boldsymbol{\varepsilon})$ is a scalar norm of the strains. The initial value r_0 defines the initial size of the elastic domain.

The norm $\Psi(\boldsymbol{\varepsilon})$ can admit different definitions depending on the material that is intended to be modeled. In this work we use the following two possibilities (see Figure 2.8):

1. Damage model with equal degradation in tension and compression:

$$\Psi(\boldsymbol{\varepsilon}) = \sqrt{\boldsymbol{\varepsilon} : \mathbf{C}^{el} : \boldsymbol{\varepsilon}} = \sqrt{\bar{\boldsymbol{\sigma}} : \mathbf{C}^{el^{-1}} : \bar{\boldsymbol{\sigma}}}.\tag{2.53}$$

This model exhibits equal compressive/tensile strength ratio being therefore inadequate to model concrete.

2. Damage model with degradation only in tension:

$$\Psi(\boldsymbol{\varepsilon}) = \sqrt{\bar{\boldsymbol{\sigma}}^+ : \mathbf{C}^{el^{-1}} : \bar{\boldsymbol{\sigma}}},\tag{2.54}$$

where $\bar{\boldsymbol{\sigma}}^+$ is the positive part of the effective stresses.

$$\boldsymbol{\sigma}^+ = \sum_{i=1}^3 \langle \sigma^i \rangle \mathbf{p}^i \otimes \mathbf{p}^i, \quad (2.55)$$

where σ^i and \mathbf{p}^i are respectively the i -th principal stress and the i -th principal direction and $\langle \bullet \rangle$ is referred to as the McCauley bracket, that has the following definition:

$$\langle \sigma^i \rangle = \begin{cases} \sigma^i & \text{if } \sigma^i > 0 \\ 0 & \text{if } \sigma^i \leq 0 \end{cases}. \quad (2.56)$$

Expression (2.54) defines an unbounded elastic domain in the compression octants. Therefore this model is useful for those situations where tension is dominant, *i.e.* where tension leads to the structural failure.

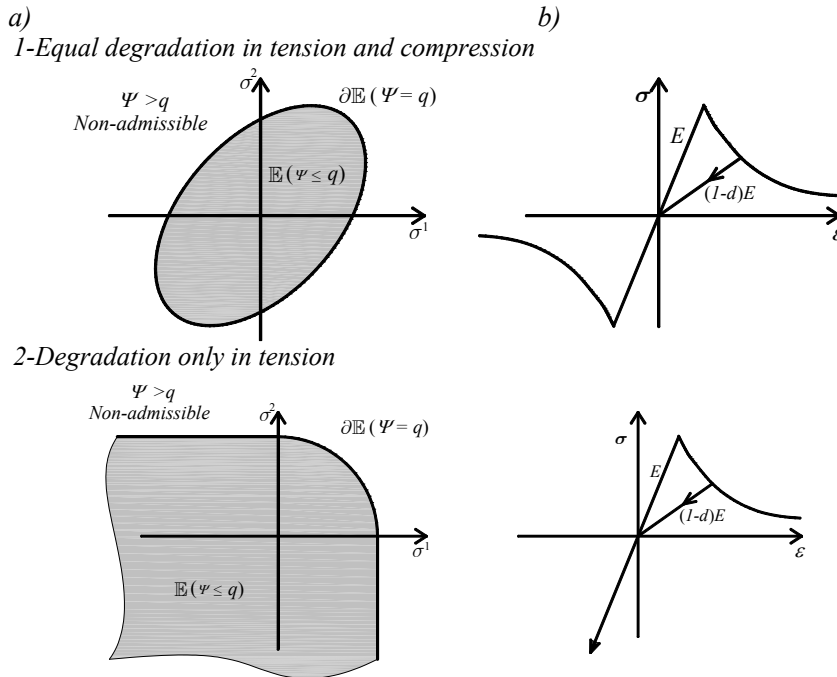


Figure 2.8 a) Illustration of the elastic domain and damage surface, b) Uniaxial generic curves.

5. Evolution laws

For the damage threshold $q(r)$ the following evolution law is defined:

$$\dot{r} = \gamma, \quad r \in [r_0, \infty), \quad (2.57)$$

where $\gamma \geq 0$ is termed the damage consistency parameter used to define the loading/unloading conditions according to the Karush-Kuhn-Tucker relations:

$$\gamma \geq 0 ; \quad f(\varepsilon, r) \leq 0 ; \quad \gamma f(\varepsilon, r) = 0. \quad (2.58)$$

6. Hardening law.

The hardening law defines the type of hardening/softening and the evolution of q .

$$\dot{q} = \frac{\partial q}{\partial r} \dot{r}, \quad (2.59)$$

where the function $H(r) \leq 0$ is the isotropic softening modulus that depends on the strain-like internal variable. Distinct definitions of $H(r)$, lead to distinct forms of softening (linear, exponential, *etc.*). The linear isotropic softening case arises from admitting H constant and independent of r .

7. Consistency condition.

$$\gamma \dot{f}(\varepsilon, r) = 0. \quad (2.60)$$

The previous expression requires that for damage status ($\gamma > 0$), the pair (ε, r) must persist on the damage surface *i.e.* $\dot{f}(\varepsilon, r) = 0$.

8. Integration of the evolution law

For loading cases $\gamma = \dot{r} > 0$ and $f(\varepsilon, r) = 0$

$$f(\varepsilon, r) = \Psi(\varepsilon) - r = 0 \Rightarrow \Psi(\varepsilon) = r. \quad (2.61)$$

By the consistency condition (2.60):

$$\dot{f}(\varepsilon, r) = 0 \Rightarrow \dot{\Psi}(\varepsilon) = \dot{r} = \gamma, \quad (2.62)$$

so that r_t (the value of r at instant t) is given by the expression

$$r_t = \max_{s \in [0, t]} (r_0, \Psi_t(\varepsilon, s)). \quad (2.63)$$

9. Tangent operator.

The tangent operator, is the fourth order tensor that relates the incremental stresses with the incremental strains ($\dot{\sigma} = \mathbf{C} : \dot{\varepsilon}$). Depending on the damage surface, it has the following forms:

1. Damage model with equal degradation in tension and compression

$$\mathbf{C} = \begin{cases} (1-d)\mathbf{C}^{el} = \frac{q}{r}\mathbf{C}^{el} & \text{if } \gamma = 0 \\ \frac{q(r)}{r}\mathbf{C}^{el} - \frac{q(r) - Hr}{r^3}\bar{\sigma} \otimes \bar{\sigma} & \text{if } \gamma > 0 \end{cases}. \quad (2.64)$$

2. Damage model with degradation only in tension

$$\mathbf{C} = \begin{cases} (1-d)\mathbf{C}^{el} = \frac{q}{r}\mathbf{C}^{el} & \text{if } \gamma = 0 \\ \frac{q(r)}{r}\mathbf{C}^{el} - \frac{q(r) - Hr}{r^3}\bar{\sigma}^+ \otimes \bar{\sigma} & \text{if } \gamma > 0 \end{cases}, \quad (2.65)$$

In Box 2.4 the principal ingredients of damage constitutive model are summarized:

Damage variable	$d = 1 - \frac{q(r)}{r}$	(2.66)
Constitutive equation	$\boldsymbol{\sigma} = (1 - d(r)) \underline{\mathbf{C}}^{el} : \underline{\boldsymbol{\varepsilon}}$	(2.67)
Damage surfaces:	$f(\boldsymbol{\varepsilon}, r) = \Psi(\boldsymbol{\varepsilon}) - r,$	
1-Symmetric	$\Psi(\boldsymbol{\varepsilon}) = \sqrt{\bar{\boldsymbol{\sigma}} : \mathbf{C}^{el-1} : \bar{\boldsymbol{\sigma}}}$	(2.68)
2-Only tension	$\Psi(\boldsymbol{\varepsilon}) = \sqrt{\bar{\boldsymbol{\sigma}}^+ : \mathbf{C}^{el-1} : \bar{\boldsymbol{\sigma}}}$	
Evolution law	$\dot{r} = \gamma, \quad r \in [r_0, \infty)$	(2.69)
Hardening law	$\dot{q} = H\dot{r}; \quad q_0 = r_0 = \frac{\sigma_u}{\sqrt{E}}$	(2.70)
Loading-unloading conditions	$\gamma \geq 0; \quad f(\boldsymbol{\varepsilon}, r) \leq 0; \quad \gamma f(\boldsymbol{\varepsilon}, r) = 0$	(2.71)

Box 2.4 *Damage model.*

2.3. Material bifurcation - localization analysis

At the beginning of this Chapter, a brief description of strain localization was given. It was mentioned that strain localization, in continuum numerical models, is a direct consequence of the introduction of softening in the constitutive model. As a consequence, in order to derive a methodology to detect the onset of strain localization, attention must be focused in the constitutive response. This approach has been developed by several authors. The basic theoretical principles were introduced by Hadamard [Hadamard 1903] and Hill [Hill 1962]. Later, Rudnicki and Rice link these pioneering concepts to the onset of strain localization [Rudnicki and Rice 1975] [Rice 1976].

The main idea of the classical localization analysis is to verify under what conditions (related to the local constitutive response), the solution in terms of strains and stresses, is no longer continuous and smoothly varying, and may bifurcate giving rise to a highly concentrated band of localized strains (denoted as Ω_{loc} in Figure 2.9). So let us consider the continuum body of Section 2.1 now subdivided into two parts by the discontinuity band Ω_{loc} , where \mathbf{n} is the unit vector orthogonal to the discontinuity.

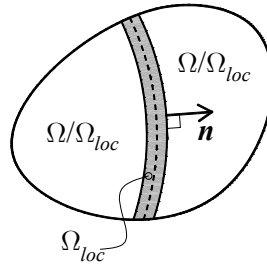


Figure 2.9 Continuum body with discontinuity.

The basic assumption is to admit that the stress and strain rates display a jump across the discontinuity. In spite of that, the jump is not arbitrary, and it is constrained by two restrictions. One of them follows from equilibrium considerations, the traction continuity, and implies that the traction rates must remain continuous across the localization band:

$$\dot{\boldsymbol{\sigma}}_{\Omega_{loc}} \cdot \mathbf{n} = \dot{\boldsymbol{\sigma}}_{\Omega \setminus \Omega_{loc}} \cdot \mathbf{n}. \quad (2.72)$$

The second restriction is a kinematic constraint. The Maxwell's compatibilities relations define the admissible structure of the strain tensors displaying jumps or discontinuities (see *e.g.* [Huespe and Oliver 2011] for further details)

$$\nabla \mathbf{u}_{\Omega_{loc}} = \nabla \mathbf{u}_{\Omega \setminus \Omega_{loc}} + (\boldsymbol{\beta} \otimes \mathbf{n}) \Rightarrow \nabla^S \mathbf{u}_{\Omega_{loc}} = \nabla^S \mathbf{u}_{\Omega \setminus \Omega_{loc}} + (\boldsymbol{\beta} \otimes \mathbf{n})^S, \quad (2.73)$$

where $\boldsymbol{\beta}$ is a vector that defines the jump on the strain field.

A clear physical interpretation may be seen if we write $\boldsymbol{\beta} = \xi \mathbf{g}$, where $\mathbf{g} = \boldsymbol{\beta} / \|\boldsymbol{\beta}\|$ and $\xi = \|\boldsymbol{\beta}\|$. The vector \mathbf{g} represents the deformation mode and ξ its magnitude. The opening (mode I) and the sliding mode (mode II) are obtained for $\mathbf{g} \parallel \mathbf{n}$ and $\mathbf{g} \perp \mathbf{n}$ respectively. For general cases, a mixed mode is obtained (see Table 2.1).

a) Mixed mode	b) Mode I	c) Mode II
$(\mathbf{g} \otimes \mathbf{n})^S = \begin{bmatrix} g_n & \frac{1}{2}g_t \\ \frac{1}{2}g_t & 0 \end{bmatrix}$	$(\mathbf{g} \otimes \mathbf{n})^S = \begin{bmatrix} g_n & 0 \\ 0 & 0 \end{bmatrix}$	$(\mathbf{g} \otimes \mathbf{n})^S = \begin{bmatrix} 0 & \frac{1}{2}g_t \\ \frac{1}{2}g_t & 0 \end{bmatrix}$

Table 2.1 Deformation modes. a) mixed mode, b) opening mode, c) sliding mode.

The tensor $(\mathbf{g} \otimes \mathbf{n})^S$ is expressed in two dimensional coordinate system with axes oriented with the discontinuity surface $\{\hat{\mathbf{n}}, \hat{\mathbf{t}}\}$.

When the incipient discontinuity is formed, two situations are admissible (see [Rice and Rudnicki 1980]):

- a) Plastic loading inside and outside of the discontinuity band (continuous bifurcation).
- b) Plastic loading inside the discontinuity band and elastic unloading outside (discontinuous bifurcation).

From experience, it is known that in practice only discontinuous bifurcation is found, since around the localization zone the material unloads elastically. Nevertheless, it is interesting to examine both scenarios.

The traction rate continuity equation (2.72) can be expressed as:

$$\mathbf{C}_{\Omega_{loc}} : \dot{\boldsymbol{\varepsilon}}_{\Omega_{loc}} \cdot \mathbf{n} = \mathbf{C}_{\Omega \setminus \Omega_{loc}} : \dot{\boldsymbol{\varepsilon}}_{\Omega \setminus \Omega_{loc}} \cdot \mathbf{n}, \quad (2.74)$$

where for case a): $\mathbf{C}_{\Omega_{loc}} = \mathbf{C}_{\Omega \setminus \Omega_{loc}} = \mathbf{C}^{ep}$, and for case b): $\mathbf{C}_{\Omega_{loc}} = \mathbf{C}^{ep}$; $\mathbf{C}_{\Omega \setminus \Omega_{loc}} = \mathbf{C}^{el}$.

By substituting expression (2.73) in (2.74) and reorganizing terms, (2.74) yields respectively the two following conditions:

a) Continuous bifurcation	b) Discontinuous bifurcation
$(\mathbf{n} \cdot \mathbf{C}^{ep} \cdot \mathbf{n}) \cdot \dot{\boldsymbol{\xi}} \mathbf{g} = 0$	$(\mathbf{n} \cdot \mathbf{C}_{\Omega_{loc}} \cdot \mathbf{n}) \cdot \dot{\boldsymbol{\xi}} \mathbf{g} = (\mathbf{C}_{\Omega \setminus \Omega_{loc}} - \mathbf{C}_{\Omega_{loc}}) : \dot{\boldsymbol{\varepsilon}}_{\Omega \setminus \Omega_{loc}} \cdot \mathbf{n} \quad (2.75)$

The bifurcation analysis consists of verifying when the previous equations are fulfilled for the first time (bifurcation time), for at least one critical direction \mathbf{n}^{crit} . H_{cont}^{crit} is the softening modulus superior limit that verify condition (2.75)-a) for a given critical direction and it is called the critical softening parameter. In that sense, one can ensure that for values $H > H_{cont}^{crit}$ the material does not bifurcate. The critical direction is obviously the direction that maximize H_{cont}^{crit} .

Reminding some historical results, Hill showed that elastic/plastic bifurcation (case b), can never precede plastic/plastic bifurcation (case a), [Hill 1962]. Later, it was shown by Rice and Rudnicki that “*continuous bifurcations provide the lower limit to the range of deformations for which discontinuous bifurcations can occur*”. The authors conclude that discontinuous bifurcation is just possible for $H < H_{cont}^{crit}$ [Rice and Rudnicki 1980].

This conclusion (the continuous bifurcation regarded as the lower limit of the discontinuous bifurcation), has an important consequence since the critical condition for discontinuous bifurcation may be found through the analysis of the continuous bifurcation expression, with a considerable gain of simplification.

Defining $\mathbf{Q}^{loc} = \mathbf{n} \cdot \mathbf{C}^{ep} \cdot \mathbf{n}$, condition (2.75)-a) is written as:

$$\mathbf{Q}^{loc} \cdot \dot{\boldsymbol{\xi}} \mathbf{g} = 0, \quad (2.76)$$

where the second order tensor, $\mathbf{Q}^{loc}(\mathbf{n})$, is often called in the literature, *localization tensor*. Equation (2.76) implies, for non-trivial solutions (*i.e.* for $\dot{\boldsymbol{\xi}} \neq 0$), the singularity of the tensor \mathbf{Q}^{loc} (this condition corresponds to the loss of strong ellipticity of the tangent constitutive operator \mathbf{C}^{ep}), and from that implication follows the classical localization condition:

$$\det[\mathbf{Q}^{loc}(H, \mathbf{n})] = 0. \quad (2.77)$$

This condition may be interpreted, as a necessary condition for the appearance of a strain jump in the direction \mathbf{n} . We remark that since the analysis is completely local, this condition is necessary but not sufficient. The onset and evolution of a discontinuity depends additionally on the surrounding material and on the boundary conditions.

In the last 20 years, in the context of the finite element method, several approaches based in the assumed enhanced strain methods have been developed [Simo, Oliver et al. 1993], [Ortiz, Leroy et al. 1987]). These methodologies, among others, enrich the original shape functions with information provided by the bifurcation analysis. As a consequence of this practical application, bifurcation analysis become a very interesting research topic and a lot of effort has been dedicated to find analytical explicit expressions to compute the critical values (\mathbf{n}^{crit} and H^{crit}) that fulfill the condition expressed in (2.77), for a wide range of constitutive models [Runesson et al. 1991; Oliver and Huespe 2004a]).

In this work, the analysis is restricted to associated plasticity and damage models in two dimensions, and the expression proposed by Oliver in [Oliver and Huespe 2004a] are used. For more general and complex cases, analytical expression may not be available. In [Oliver et al. 2010] a robust numerical algorithm to compute solutions to these situations is provided.

2.4. Classical strain localization methods – Standard (irreducible) finite element formulations

Based on the earlier work of [Rashid 1968], standard finite element formulations (Section 2.4.2), start to be fairly applied to the study of material failure. These classical strain localization methods employ a continuum mechanics framework, equipped with local stress-strain softening relations, to approach a

phenomenon physically discrete: the fracture. The main assumption/idea is that the fracture displacement jump is captured through the finite element length in a “smeared” manner. The main advantage, and the principal reason of its popularity among the scientific community, was the inherent simplicity and easiness of implementation in the finite element context. On the other hand, soon it was detected that the finite element solution was dependent on the element size (this problem became known as “lack of mesh objectivity”) (Section 2.5.3). To overtake this problem the softening modulus, H , of the constitutive model was reinterpreted and linked to the fracture energy (enforcing, by means of this, the energy dissipated by the numerical model to have a physical meaning) [Bazant and Oh 1983], [Hillerborg, Modeer et al. 1976].

Additionally, irreducible finite element formulations show also some other numerical pathologies related to the non-uniqueness of the solution. Rots systematized the principal problems: Stress locking and directional mesh bias dependence [Rots 1988]. In Sections 2.4.4 and 2.4.5 these pathologic phenomena are illustrated by several numerical examples. We remark that these numerical pathologies cannot be easily removed. In the last years, considerable research effort has been dedicated to resolve these issues. The Strong Discontinuity Approach with elemental-based enrichment (embedded-discontinuities) [Simo, Oliver et al. 1993] or nodal-based enrichment (X-FEM methods)[Belytschko, Moes et al. 2001], associated to global tracking algorithms proved to be efficient in providing results free from either stress-locking and mesh-bias dependence, for impressive coarse meshes. Besides, also enhanced continuum regularization methods [de Borst 1993] have proved to provide good results at the expenses of higher computational costs.

The development of a numerical methodology, in the ambit of the classical pure local methods, able to provide mesh independent results without adding any kind sophistication (non local regularizations, global tracking techniques) and without increasing the computational cost, is, due to the inherent simplicity of these methods, of evident convenience.

2.4.1. Weak formulation of the boundary value problem

The weak or variational formulation of the boundary value problem. may be derived in a traditional fashion from the strong form of Box 2.1 (see for example [Hughes 1987]). Thus, testing the strong form of the problem defined in the equations (2.1) with the test functions $\boldsymbol{\eta}$, and integrating over the domain, yields:

$$\int_{\Omega} \nabla^s \boldsymbol{\eta} : \dot{\boldsymbol{\Sigma}}(\nabla^s \dot{\boldsymbol{u}}) d\Omega - \left[\int_{\Omega} \boldsymbol{\eta} \cdot \boldsymbol{b} d\Omega + \int_{\Gamma_\sigma} \boldsymbol{\eta} \cdot \boldsymbol{t}^* d\Gamma \right] = 0, \forall \boldsymbol{\eta} \in \mathcal{N} \quad (2.78)$$

The previous expression, is equivalent to the one that is obtained by the principle of the virtual displacement, often used in the literature of solid me-

chanics, where $\nabla^s \boldsymbol{\eta}$ represent the virtual strains and $\boldsymbol{\eta}$ the virtual displacements [Bathe 1982].

The weak form of the boundary value is completely defined after selecting the spaces where the solution functions \boldsymbol{u} and the weighting functions $\boldsymbol{\eta}$ should belong. As usual, are selected the spaces that ensure the minimum necessary regularity, thus:

$$\mathcal{U} := \left\{ \boldsymbol{u} \mid \boldsymbol{u} \in [H^1(\Omega)]^n; \boldsymbol{u}|_{\Gamma_u} = \boldsymbol{u}^* \right\},$$

$$\mathcal{N} := \left\{ \boldsymbol{\eta} \mid \boldsymbol{\eta} \in [H^1(\Omega)]^n; \boldsymbol{\eta}|_{\Gamma_u} = 0 \right\},$$

where $H^1(\Omega)$ is the space of square integrable functions defined in Ω , whose first derivatives are also square integrable [Hughes 1987].

The weak form of the problem may be stated as:

Given $\boldsymbol{u}^* : \Gamma_u \rightarrow \mathbb{R}^N$, $\boldsymbol{t}^* : \Gamma_s \rightarrow \mathbb{R}^N$ and $\dot{\boldsymbol{b}} : \Omega \rightarrow \mathbb{R}^N$ find $\dot{\boldsymbol{u}} \in \mathcal{U}$ such that for all $\boldsymbol{\eta} \in \mathcal{N}$

$$\int_{\Omega} \nabla^s \boldsymbol{\eta} : \dot{\boldsymbol{\Sigma}}(\nabla^s \dot{\boldsymbol{u}}) d\Omega = \int_{\Omega} \boldsymbol{\eta} \cdot \dot{\boldsymbol{b}} d\Omega + \int_{\Gamma_\sigma} \boldsymbol{\eta} \cdot \boldsymbol{t}^* d\Gamma \quad (2.79)$$

Box 2.5 Weak form of the boundary value problem.

2.4.2. Finite element approximation

The first step to introduce the finite element approximation to the continuum problem, defined in Box 2.5, is the definition the finite dimensional spaces \mathcal{U}^h and \mathcal{N}^h that approximate \mathcal{U} and \mathcal{N} :

$$\mathcal{U}^h := \left\{ \dot{\boldsymbol{u}}^h \mid \dot{\boldsymbol{u}}^h(\boldsymbol{x}) = \sum_{i=1}^{n_{nodes}} N_i(\boldsymbol{x}) \dot{\boldsymbol{u}}_i \right\} ; \mathcal{U}^h \subset \mathcal{U}, \quad (2.80)$$

$$\mathcal{N}^h := \left\{ \boldsymbol{\eta}^h \mid \boldsymbol{\eta}^h(\boldsymbol{x}) = \sum_{i=1}^{n_{modes}} N_i(\boldsymbol{x}) \boldsymbol{\eta}_i \right\} ; \mathcal{N}^h \subset \mathcal{N},$$

where the vector $\dot{\boldsymbol{u}}_i$ contains the displacement degrees of freedom associated to the node i and N_i are the standard finite element isoparametric shape functions.

Considering an element point of view, the discrete version of equation (2.79) that outcome from the choice of the finite element shape functions defined in (2.80), may be stated as:

Given the vector \mathbf{F}^{ext} find $\dot{\mathbf{u}}^h$ such that:

$$\begin{aligned} \dot{\mathbf{F}}^{int} = \mathcal{A} \left(\int_{\Omega^{(e)}} \mathbf{B}^{(e)T} \cdot \left\{ \dot{\Sigma}(\{\nabla^s \dot{\mathbf{u}}^h\}^{(e)}) \right\} d\Omega \right) = \dot{\mathbf{F}}^{ext} \\ \{\nabla^s \dot{\mathbf{u}}^h\}^{(e)} = \mathbf{B}^{(e)} \cdot \{\dot{\mathbf{u}}\}^{(e)} \end{aligned} \quad (2.81)$$

Box 2.6 *Discrete form of the boundary value problem.*

In Box 2.6, $\dot{\mathbf{F}}^{int}$ and $\dot{\mathbf{F}}^{ext}$ stands for the internal and external forces respectively, \mathcal{A} is the assembling operator, $\mathbf{B}^{(e)}$ is the standard deformation matrix and $\{\dot{\mathbf{u}}\}^{(e)}$ is the elemental vector of nodal displacements (Voigt notation is used).

2.4.3. Lack of objectivity and regularization

If the finite element method is used to solve the differential equations of the nonlinear boundary value problem of continuum mechanics, equipped with strain softening, strains will tend to concentrate (localize) in narrow bands corresponding to the element size. Having in mind the discussion developed in the beginning of this Chapter, one realizes that the total amount of dissipated energy will depend on the size of the finite element. The natural idea is that, independently of the element size, the dissipation of the continuum model should be enforced to match the material fracture energy⁶ G_f (obtained experimentally).

Note that continuum strain softening models dissipate energy on a per unit volume basis, since the crack opening (displacement jump) is captured in a smeared manner over a certain length ℓ . This length parameter should therefore be introduced to make the dissipated energy per unit area (*i.e.* fracture like). For softening models with $q|_{t=\infty} = 0$, it can be written:

$$G_f = \int_0^\ell g_f ds, \quad (2.82)$$

where g_f is the specific energy (per unit of volume) consumed during the deformation process:

$$g_f = \int_{t=0}^{t=\infty} \boldsymbol{\sigma} : \dot{\boldsymbol{\epsilon}} dt. \quad (2.83)$$

Considering a discrete domain, and admitting a constant strain field in the localization domain, equation (2.82) may be rewritten as,

⁶ The fracture energy is the necessary energy to open a crack of unit area and was a concept originally developed in the ambit^{of} fracture mechanics [Griffith 1921].

$$G_f = \ell^{(e)} g_f, \quad (2.84)$$

where $\ell^{(e)}$ is a finite element characteristic length, that depends on the size, the shape and on the manner that the element is crossed by the crack [Oliver 1989].

2.4.3.1. Softening regularization for elastoplastic models

For the elastoplastic models considered in Section 2.2.1 the specific energy may be computed as:

$$g_f = \int_{t=0}^{t=\infty} \boldsymbol{\sigma} : \dot{\boldsymbol{\epsilon}} dt = \int_{t=0}^{t=\infty} \boldsymbol{\sigma} : \mathbf{C}_{el}^{-1} : \dot{\boldsymbol{\sigma}} dt + \int_{t=0}^{t=\infty} \boldsymbol{\sigma} : \dot{\boldsymbol{\epsilon}}^p dt, \quad (2.85)$$

where the additive decomposition of the strain rate tensor $\dot{\boldsymbol{\epsilon}} = \dot{\boldsymbol{\epsilon}}^e + \dot{\boldsymbol{\epsilon}}^p$ and the constitutive relation $\dot{\boldsymbol{\epsilon}}^e = \mathbf{C}_{el}^{-1} : \dot{\boldsymbol{\sigma}}$ are considered.

Integrating on time the first term, and using the flow rule (2.16) $\dot{\boldsymbol{\epsilon}}^p = \gamma \partial_{\boldsymbol{\sigma}} \hat{f} = \dot{\alpha} \partial_{\boldsymbol{\sigma}} \hat{f}$, we obtain:

$$g_f = \underbrace{\left[\frac{1}{2} \boldsymbol{\sigma} : \mathbf{C}^{-1} : \boldsymbol{\sigma} \right]_{t=0}^{t=\infty}}_{=0} + \int_{t=0}^{t=\infty} \dot{\alpha} \partial_{\boldsymbol{\sigma}} \hat{f} : \boldsymbol{\sigma} dt. \quad (2.86)$$

Considering that the function \hat{f} defined in (2.13) is homogenous of degree one⁷ with respect to the argument sigma, by the Euler's theorem for homogeneous functions:

$$\partial_{\boldsymbol{\sigma}} \hat{f} : \boldsymbol{\sigma} = \hat{f}(\boldsymbol{\sigma}). \quad (2.87)$$

For a loading processes, since $\gamma = \dot{\alpha} > 0$, the loading/unloading conditions defined in (2.19) imply $f(\boldsymbol{\sigma}, q) = 0$, thus:

$$f(\boldsymbol{\sigma}, q) = \hat{f}(\boldsymbol{\sigma}) - q = 0 \Rightarrow \hat{f}(\boldsymbol{\sigma}) = q. \quad (2.88)$$

Finally by considering (2.87) and (2.88), expression (2.86) yields:

$$g_f = \int_{t=0}^{t=\infty} q \dot{\alpha} dt. \quad (2.89)$$

The integral in equation (2.89) represents the area below the $\alpha - q$ curves. In following table, expressions for linear and exponential softening, are presented.

⁷ Note that this requirement is fulfilled by many usual yield functions (Von-Mises, Tresca, Rankine, etc.) [Khan 1995].

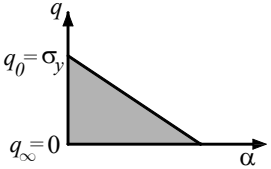
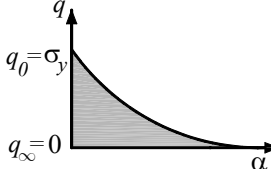
a) Linear softening ($q = \sigma_y + H\alpha$) ($H < 0$)	b) Exponential softening ($q = \sigma_y e^{(A\alpha)}$) ($H(\alpha) < 0$; $A < 0$)
	
$g_f = \int_{t=0}^{t=\infty} q \dot{\alpha} dt = \int_{t=0}^{t=\infty} q \frac{\dot{q}}{H} dt$ $g_f = \int_{q_0}^{q_\infty} \frac{q}{H} dq = \left[\frac{q^2}{2H} \right]_{q_0=\sigma_y}^{q_\infty=0} = -\frac{\sigma_y^2}{2H}$	$g_f = \int_{t=0}^{t=\infty} q \dot{\alpha} dt = \int_{t=0}^{t=\infty} \sigma_y e^{(A\alpha)} \dot{\alpha} dt$ $g_f = \int_{\alpha_0}^{\alpha_\infty} \sigma_y e^{(A\alpha)} d\alpha = \left[\frac{\sigma_y}{A} e^{(A\alpha)} \right]_0^\infty = -\frac{\sigma_y}{A}$

Table 2.2 $q - \alpha$ curves a) linear softening, b) exponential softening.

By substituting the results of Table 2.2 in equation (2.84) and solving for H and A :

$$H = -\frac{\sigma_y^2}{2G_f} \ell^{(e)} = \hat{H} \ell^{(e)} \quad \Bigg| \quad A = -\frac{\sigma_y}{G_f} \ell^{(e)} = \hat{A} \ell^{(e)}. \quad (2.90)$$

The softening parameter H and the A parameter, that ensure objectivity between the constitutive model dissipation and the fracture energy, may be regarded as regularized forms of intrinsic material parameters \hat{H} and \hat{A} .

These results are consistent with those obtained through the strong discontinuity approach, where the strong discontinuity kinematics induce discrete constitutive relations (traction vs. displacement jump). In this approach, the parameter \hat{H} was identified as the discrete softening parameter [Oliver 2000].

2.4.3.2. Softening regularization for damage models

As it was done for the elastoplastic models in Section 2.4.3.1, the specific energy may be computed for damage models as:

$$g_f = \int_{t=0}^{t=\infty} \boldsymbol{\sigma} : \dot{\boldsymbol{\varepsilon}} dt = \int_{t=0}^{t=\infty} \frac{q}{r} \bar{\boldsymbol{\sigma}} : \dot{\boldsymbol{\varepsilon}} dt. \quad (2.91)$$

For loading stages, from (2.62) and (2.63), $r(\boldsymbol{\varepsilon}) = \Psi$. Considering the damage model with equal degradation in tension and compression ($\Psi(\boldsymbol{\varepsilon}) = \sqrt{\boldsymbol{\varepsilon} : \mathbf{C}^{el} : \boldsymbol{\varepsilon}}$), the time derivative of $r(\boldsymbol{\varepsilon})$, reads:

$$\dot{r}(\varepsilon) = \frac{\partial r}{\partial \varepsilon} \dot{\varepsilon} = \frac{1}{r} \varepsilon : \mathbf{C}^{el} : \dot{\varepsilon} = \frac{1}{r} \bar{\sigma} : \dot{\varepsilon}, \quad (2.92)$$

thus:

$$\dot{r} = \frac{1}{r} \bar{\sigma} : \dot{\varepsilon}, \quad (2.93)$$

and by substituting (2.93) in (2.91) we obtain

$$g_f = \int_{t=0}^{t=\infty} q \dot{r} dt. \quad (2.94)$$

Notice that, for the Damage model with degradation only in tension expression (2.94) is also derived. For this case $r = \Psi(\varepsilon) = \sqrt{\bar{\sigma}^+ : \varepsilon}$

$$\dot{r} = \frac{\partial r}{\partial \varepsilon} \dot{\varepsilon} = \frac{1}{2r} \frac{\partial(\bar{\sigma}^+ : \varepsilon)}{\partial \varepsilon} : \dot{\varepsilon} = \frac{1}{2r} \left(\bar{\sigma}^+ + \frac{\partial \bar{\sigma}^+}{\partial \varepsilon} : \varepsilon \right) : \dot{\varepsilon} = \frac{1}{r} \bar{\sigma}^+ : \dot{\varepsilon}, \quad (2.95)$$

and by substituting (2.95) in (2.91) expression (2.94) is obtained.

The integral in equation (2.94) represents the area below the $q - r$ curves. In following table, expression for linear and exponential softening cases, are presented.

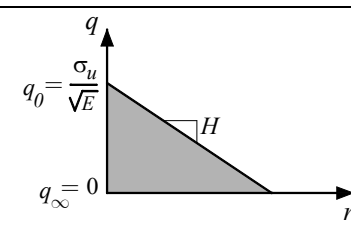
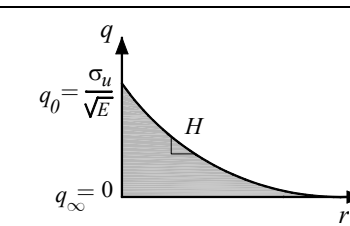
a) Linear softening ($q = r_0 + H(r - r_0)$); ($H < 0$)	b) Exponential soft. $q = r_0 e^{A(\frac{r}{r_0} - 1)}$ ($H(\alpha) < 0$; $A < 0$)
	
$g_f = \int_{t=0}^{t=\infty} q \dot{r} dt = \int_{t=0}^{t=\infty} q \frac{\dot{q}}{H} dt$	$g_f = \int_{t=0}^{t=\infty} q \dot{\alpha} dt = \int_{t=0}^{t=\infty} r_0 e^{A(\frac{r}{r_0} - 1)} \dot{\alpha} dt$
$g_f = \int_{q_0}^{q_\infty} \frac{q}{H} dq = \left[\frac{q^2}{2H} \right]_{q_0 = \frac{\sigma_u}{\sqrt{E}}}^{q_\infty = 0} = -\frac{\sigma_u^2}{2EH}$	$g_f = \left[\frac{r_0^2}{A} e^{A(\frac{r}{r_0} - 1)} \right]_{r_0 = \frac{\sigma_u}{\sqrt{E}}}^{r_\infty = \infty} = -\frac{\sigma_u^2}{EA}$

Table 2.3 $q - \alpha$ curves for damage models a)linear softening, b)exponential softening.

By substituting the results of Table 2.3 in equation (2.84) and solving for H and A :

$$H = -\frac{\sigma_u^2}{2EG_f} \ell^{(e)} = \hat{H} \ell^{(e)} \quad \Bigg| \quad A = -\frac{\sigma_u^2}{EG_f} \ell^{(e)} = \hat{A} \ell^{(e)}, \quad (2.96)$$

where parameters H and A , are the regularized forms of the intrinsic material parameters \hat{H} and \hat{A} .

2.4.4. Mesh bias dependence

One of the principal drawbacks of the localization methods based on local standard constitutive models is the spurious tendency of the crack to follow certain preferred directions related to the mesh alignment, *i.e.* the crack tends to propagate parallelly to the finite element mesh avoiding zigzagging. Several authors [Rots 1988], [de Borst et al. 1993],[Oliver, Cervera et al. 1990]), among others, have reported this undesirable behavior, that is termed in the literature, mesh bias or mesh alignment dependence. This issue is of maximum significance since results can become strongly mesh dependent, *i.e.* for different meshes, remarkable different results are obtained. Additionally, erroneous crack propagation can lead to unrealistic/unphysical failure mechanisms with consequences in the prediction of the ultimate structural load carrying capacity, that may be over or under-estimated.

Several approaches have been developed to face this problem. One of them is based on the regularization of the standard strain-softening continua (by incorporating a internal characteristic length): non-local [Pijaudier Cabot and Bazant 1987], gradient [de Borst and Mühlhaus 1992], micro-polar [Mühlhaus and Vardoulakis 1987] methods fall within this category that proved to be efficient in achieve results independent of the mesh directions. The principal inconvenient of these methods is that, in order to capture that internal length, the resulting localization band has to encompass a certain number of finite elements which, due the small character of the involved internal length, demands the use of very fine finite element discretizations or auxiliary re-meshing techniques.

The use of global crack tracking techniques also demonstrate to be very effective, since the propagation of the localization band is controlled not by the local constitutive model but instead by a global tracking algorithm governed by a different set of differential equations. The use of these kind of algorithms, in the ambit of the strong discontinuity approach [Oliver et al. 2004], provide mesh independent results for impressive coarse meshes. We remark that when strong discontinuities are used, the tracking algorithms are essential for achieving results not depending in mesh alignment. In [Mosler and Meschke 2004] the authors, by using embedded discontinuities without resorting to global tracking algorithms, also conclude this issue. Outside the ambit of the strong discontinuity approach, these algorithms have also been

used with success, for example, for a local continuum damage models [Cervera and Chiumenti 2006]). Recently, the use of mixed strain-displacement finite element formulations have been also advocated as a way to alleviate this flaw, at the expense of adding additional strain degrees of freedom (3 per node for two dimensional analyses) [Cervera et al. 2010].

2.4.4.1. Assessment of the mesh bias dependence through representative numerical solutions

To have a better understanding about mesh bias influence in standard finite element formulations, some numerical simulations of a rectangular strip stretching in the horizontal direction, are here presented.

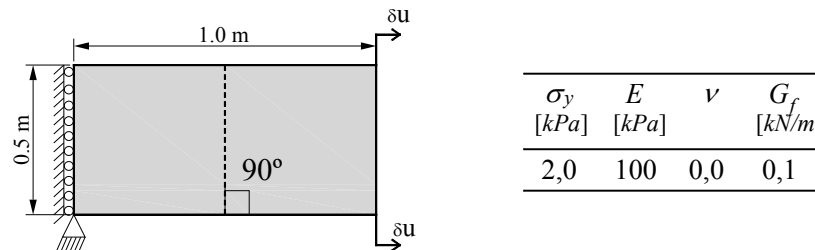


Figure 2.10 Strip stretching in the horizontal direction.

The material is modeled by means of two different constitutive models: an isotropic damage model and a Rankine plasticity model. For both options, the plain strain problem, predicts the same analytical solution, corresponding to a vertical crack, in mode I of fracture.

It is well known, that for a perfectly aligned vertical mesh, the obtained result would match exactly the theoretical solution. Therefore, to evidence mesh bias dependence, a 65° inclined mesh is used. Note that this mesh is chosen such that the row inclination in the zone where strains localize, strongly challenges the theoretical vertical propagation of the localization band.

It is also showed the mesh refinement influence by using three different degrees of mesh refinement (the meshes are obtained from the previous by subdividing the quads in four new elements). For all meshes, the yield stress of a small area (at the lower part of the strip) is perturbed, in order to break the problem homogeneity and trigger the strain localization at that zone. In order to make possible a rigorous comparison, the perturbed area is the same in all cases.

In Figure 2.11 and Figure 2.12, for the different degrees of mesh refinement, plots of the displacement field contours at the end of analysis (when the structural load carrying capacity is totally exhausted), are shown. In these Figures, it must be noted that strain localization zones are represented by a clustering of iso-displacement contours meaning the developing of a crack, slip line, shear band, etc..

- **Isotropic damage model**

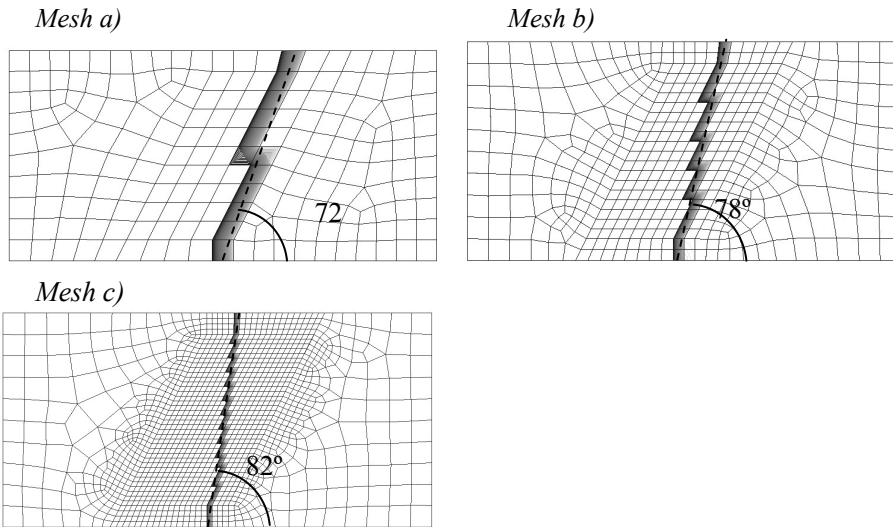


Figure 2.11 *Iso-displacement curves at the end of analysis (damage model) (standard finite element formulation).*

- **Rankine plasticity model**

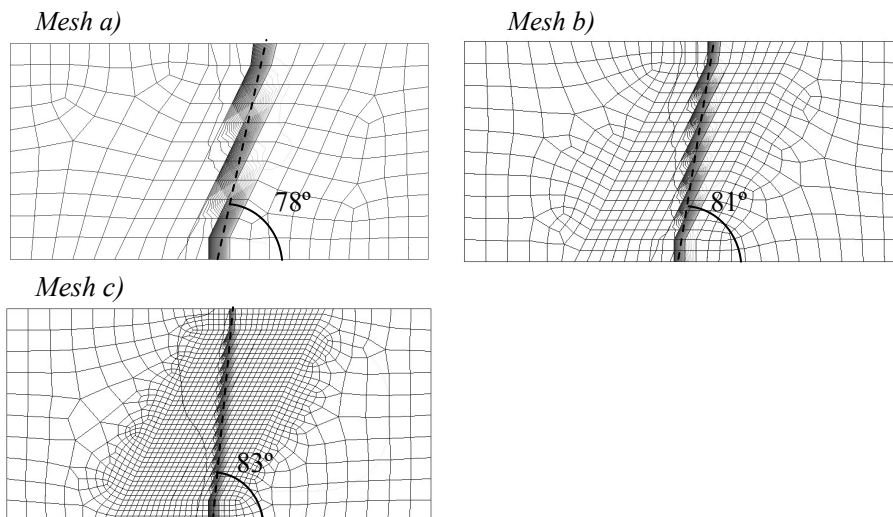


Figure 2.12 *Iso-displacement curves at the end of analysis (Rankine plasticity model)(standard finite element formulation).*

The previous results show two main ideas that corroborate some “believes” about the traditional localization methods:

- Both constitutive models, either plasticity or damage, suffer from mesh bias. Notice that the localization band tends to follow the mesh align-

ment avoiding zigzagging. Then, the obtained numerical strain localization localized solutions do not coincide with the vertical crack predicted by the theoretical solution. Moreover, the isotropic damage model seems to be more susceptible to this issue (mesh bias dependence).

- Mesh refinement reduce mesh sensitivity, however it is not completely removed (or would be needed extremely impracticable fine meshes).

In this topic we recall here some published results. Rots (in [Rots 1988]) refer that “*mesh bias sensitivity seems to vanish for very fine meshes*” (at least for quadrilateral elements). Jirásek in a recent publication [Jirasek and Grassl 2008] refer that “*mesh refinement often reduces sensitivity to the mesh orientation, but is not a universal remedy*”. Moreover, the same authors report that some constitutive models are more susceptible to mesh bias influence than others, for example the isotropic damage model is strongly sensitive while the anisotropic version is much less sensitive.

2.4.5. Stress locking

In the context of strain localization, stress locking refers to the lack of ability of standard finite elements formulations to capture strain localization, in a one-element-width band without spurious stress transfer to the neighboring elements.

The causes of stress locking are mainly related to the poor strain kinematics that derives from displacement compatibility. This kinematic flaw, is compensated by the finite element displacement interpolation, by smearing the discontinuity out, over several elements, inducing consequently stress locking. An additional inconvenient, is that, since the fundamental assumption on the displacement compatibility is always considered, stress locking is not expected to be reduced on mesh refinement [Rots 1988].

Stress locking was primarily reported in the ambit of the smeared crack models [Rots 1988]. Moreover, it has been also reported, that local plasticity models also suffer from this feature. Local damage models, are less affected by this issue, since stresses totally vanish as soon as the damage variable reaches the unity ([Jirásek 1998]). Even though, for earlier stages of the strain localization process, this model still locks as is shown in the example of Section 2.4.5.1 (see Figure 2.15 a)).

The practical undesirable consequence of stress locking is the over-stiffer behavior of the structure that leads to an overestimation of the ultimate structural load carrying capacity load. Additionally, thinking in the force-displacement diagram, one should expect that for sufficiently high displacements, the resisting force should vanish. Nevertheless, if the numerical solution experiences stress locking, the force-displacement curve would tend to a residual value of the load carrying capacity, this reflecting the spurious stresses being transferred by the open crack.

In general, stress locking is noticeable for zigzagging crack patterns and is not observed when the discontinuity propagates parallelly to the elements sides.

A natural and effective solution to remove this flaw, is the one proposed by the Strong Discontinuity Approach (SDA), where the elemental kinematics is enhanced by a discontinuous deformation mode [Simo, Oliver et al. 1993]. The principal inconvenient of this methodology is the decision about which elements have to be enriched and about the position of the discontinuity inside each finite element. In the SDA, this information is generally obtained by resorting to global tracking algorithms. This algorithm also guarantees the geometric continuity of the band across the finite element mesh.

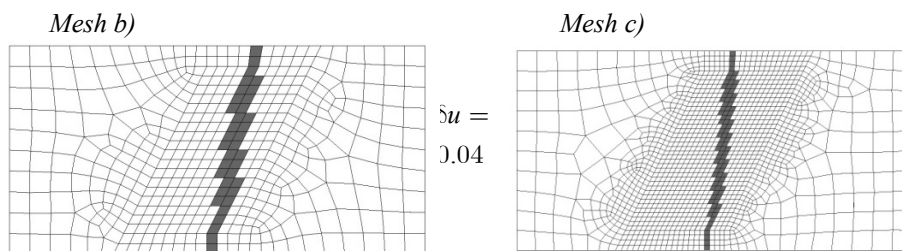
2.4.5.1. Assessment of stress locking through representative numerical solutions

The numerical example considered previously in Section 2.4.4, is re-examined, being now the attention focalized in the stress locking effects (see Figure 2.10).

First, the load patterns (*i.e.* the elements that are in nonlinear loading condition) are presented. The interest of these pictures lays in the fact that, for problems with no locking effects, the localization band should be one-element-wide, and therefore, the neighboring elements (to those displaying strain localization) should unload elastically. For that reason, when the localization band encompasses several elements, this gives a local idea of stress locking. Results for two different representative stages of loading (earlier and deep stages of localization) are shown in Figure 2.13 and Figure 2.14 for damage and rankine plasticity models, respectively.

Secondly, the force-displacement curves are presented, where a global idea of stress locking is given in terms of the extra dissipation (area below the curves) and in terms of the residual loading that is still spuriously transferred through the crack surfaces.

- **Isotropic damage model**



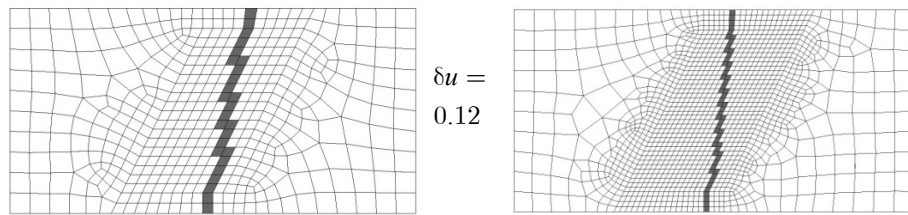
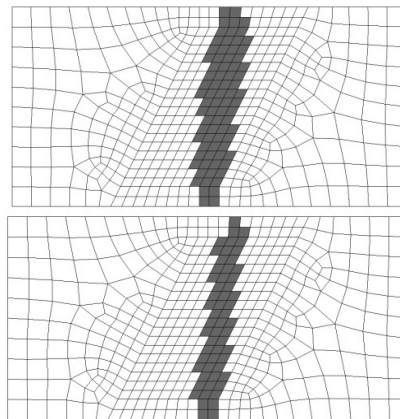


Figure 2.13 Load patterns for two different stages of the deformation process (standard finite element formulation).

• Rankine plasticity model

Mesh b)



Mesh c)

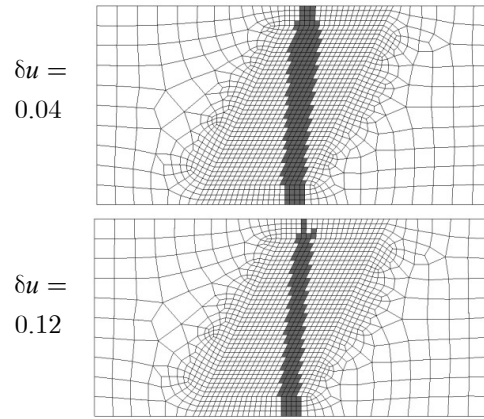


Figure 2.14 Load patterns for two different stages of the deformation process (standard finite element formulation).

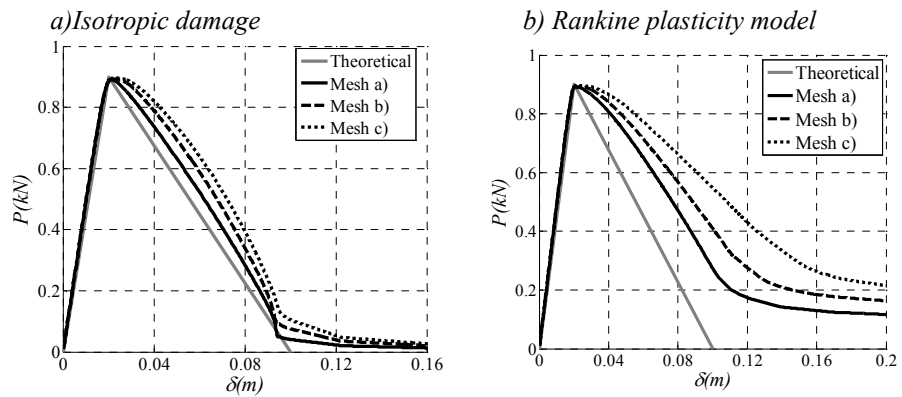


Figure 2.15 Force-displacement curves: a) Isotropic damage, b) Rankine plasticity model (standard finite element formulation).

Analyzing the preceding results in terms of **stress locking**, some important observations should be remarked:

- The damage model is almost stress locking free at the end of analysis. However, from Figure 2.13, it is shown that for earlier stages of localization, the finite element solution still locks. On the other hand, as stresses decreased (*i.e.* $d \rightarrow 1.0$), the neighboring “locked in” elements tend to unload elastically. Finally, the residual load being transferred by the crack surfaces, almost vanish.
- The Rankine plasticity model is significantly affected by stress locking. This may be observed in Figure 2.15-b) by the extra dissipation and residual load. Additionally, in the patterns presented in Figure 2.14, it is clearly shown that the discontinuity is smeared out over several elements along the complete analysis.
- Mesh refinement does not reduce stress locking.
- In this example, the ultimate structural load carrying capacity was correctly predicted. This is mainly related to the specific quasi-homogeneous character of this problem. For more general problems, the ultimate load, is expected to be overestimated for solutions suffering of stress locking.

The observations here remarked and in Section 2.4.4, have also been reported by several authors, are well known by the research fracture community, and illustrate the traditional flaws of the strain localization classical methods in terms of mesh bias and stress locking.

2.5. Integration of the constitutive equation - IMPL-EX scheme

When nonlinear softening constitutive models are used for material failure modeling, the robustness of the numerical procedure is a very important issue. The problems involving lack of robustness are well known in the context of modeling crack formation/propagation with the finite element method and are well described in the literature [Crisfield 1997].

Discretizing in time, $t \in [0, T]$, the nonlinear problem of solid mechanics of Box 2.6, the momentum balance equations at the time step $n+1$ reads (Voigt notation is used):

$$\begin{aligned} \mathbf{F}_{n+1}^{int}(\mathbf{u}_{n+1}) - \mathbf{F}_{n+1}^{ext} &= \mathbf{G}_{n+1} = 0, \\ \mathbf{F}_{n+1}^{int} &= \mathcal{A} \left(\int_{\Omega^{(e)}} \mathbf{B}^{(e)T} \cdot \{ \boldsymbol{\sigma}(\nabla^s \mathbf{u}_{n+1}) \}^{(e)} d\Omega \right), \end{aligned} \quad (2.97)$$

where \mathbf{G}_{n+1} is the out-of-balance force vector which we intend to make null.

Using a traditional iterative Newton-Raphson procedure, the displacement vector \mathbf{u}_{n+1} is updated until the out of balance forces are lower than a given tolerance. In this process the updated tangent stiffness matrix is computed as:

$$\mathbf{K}_{n+1}^{tang} = \frac{\partial \mathbf{F}^{int}(\mathbf{u}_{n+1})}{\partial \mathbf{u}_{n+1}} = \mathcal{A}_e \left(\int_{\Omega^{(e)}} \mathbf{B}^{(e)T} \cdot \{ \mathbf{C}_{n+1}^{alg} \} \cdot \mathbf{B}^{(e)} d\Omega \right), \quad (2.98)$$

$$\mathbf{C}_{n+1}^{alg} = \frac{\partial \boldsymbol{\sigma}_{n+1}}{\partial \boldsymbol{\varepsilon}_{n+1}}.$$

Since in our case the non-linearity arises from the constitutive model, $\boldsymbol{\sigma}_{n+1} = \boldsymbol{\Sigma}(\boldsymbol{\varepsilon}_{n+1})$, the algorithmic tangent constitutive tensor \mathbf{C}_{n+1}^{alg} is updated in the iterative process.

During the loading process in the softening regime, after bifurcation, negative eigenvalues arise in the constitutive tangent algorithm operator \mathbf{C}_{n+1}^{alg} (that loses positive definiteness), which translate afterwards in negative eigenvalues in the element stiffness matrix. As load progress, and more elements localize, the global stiffness matrix becomes worse conditioned, the numerical procedure become further ill posed and convergence may not be achieved [Oliver et al. 2008a]. Theoretically, this is related to the existence of several possible equilibrium paths (loss of uniqueness of the BVP). Crisfield [Crisfield 1982] refers that when several closed equilibrium states are possible, numerical procedures appear to encounter great difficulty in deciding on which equilibrium state to converge, increasing significantly the difficulty of obtaining numerical convergence, even when powerful numerical control techniques, like arc-length methods and line-searches, are used.

In this work, in order to avoid this kind of difficulties the implicit/explicit (IMPL-EX) integration of the constitutive model proposed by Oliver [Oliver, Huespe et al. 2008a] [Oliver et al. 2006] is adopted. This strategy is a combination of implicit and explicit integration schemes aiming to exploit the benefits and minimize the drawbacks of both.

The main idea of IMPL-EX integration scheme is the extrapolation of the strain like internal variable for the time step $\tilde{\alpha}_{n+1}$ ⁸, from its implicit value computed in previous time step α_n .

$$\tilde{\alpha}_{n+1} = \alpha_n + \frac{\Delta t_{n+1}}{\Delta t_n} \Delta \alpha_n. \quad (2.99)$$

where $\Delta t_{n+1} = t_{n+1} - t_n$, $\Delta t_n = t_n - t_{n-1}$ and $\Delta \alpha_n = \alpha_n - \alpha_{n-1}$.

With this extrapolated variable, an explicit evaluation of the stress tensor $\tilde{\boldsymbol{\sigma}}$ is performed and the momentum balance (2.81) is imposed in terms of these IMPL-EX stresses:

⁸ Relatively to the stress like internal variable, the strain like variable, α , has the advantage of being strictly increasing.

$$\begin{aligned} \tilde{\mathbf{F}}^{int}(\mathbf{u}_{n+1}) - \mathbf{F}_{n+1}^{ext} = \mathbf{G}_{n+1} = 0 \\ \tilde{\mathbf{F}}^{int}(\mathbf{u}_{n+1}) = \mathcal{A} \left(\int_{\Omega^{(e)}} \mathbf{B}^{(e)T} \cdot \{\tilde{\boldsymbol{\sigma}}_{n+1}\}^{(e)} d\Omega \right). \end{aligned} \quad (2.100)$$

The most significant properties of the IMPL-EX integration are [Oliver, Huespe et al. 2006]:

1. The algorithmic tangent operators are semi-positive definite. This numerical attribute has particular relevance, since numerical problems related to the ill-condition of the global tangent stiffness matrix should disappear, improving considerably the robustness of the methodology.
2. In general (for damage models, and for linear plastic flow cases), the dependence of the IMPL-EX stresses $\tilde{\boldsymbol{\sigma}}_{n+1}$ (that emerge from the extrapolated values of the strain-like internal variable $\tilde{\alpha}_{n+1}$) on the actual value of the strain $\boldsymbol{\varepsilon}_{n+1}$ becomes linear. From this feature, a step linear algorithm with a constant tangent operator arises naturally, that provide important benefits in terms of computational cost, since the Newton Raphson procedure will converge in just one iteration,

$$\begin{aligned} \tilde{\mathbf{K}}_{n+1}^{tang} = \frac{\partial \tilde{\mathbf{F}}^{int}(\mathbf{u}_{n+1})}{\partial \mathbf{u}_{n+1}} = \mathcal{A} \left(\int_{\Omega^{(e)}} \mathbf{B}^{(e)T} \cdot \{\tilde{\mathbf{C}}_{n+1}^{alg}\} \cdot \mathbf{B}^{(e)} d\Omega \right) (\text{con-} \\ \text{stant}), \quad (2.101) \\ \tilde{\mathbf{C}}_{n+1}^{alg} = \frac{\partial \tilde{\boldsymbol{\sigma}}_{n+1}}{\partial \boldsymbol{\varepsilon}_{n+1}} (\text{constant}). \end{aligned}$$

The principal drawback of the methodology lays on the introduction of a specific error associated to the extrapolation of the internal variable. Note that due the explicit character of $\tilde{\boldsymbol{\sigma}}_{n+1}$, the consistency condition (2.20) is violated. For this reason, shorter time steps are necessary to facilitate results with the desired degree of accuracy. Thinking on the fact that the correspondent implicit scheme also demands short time steps in order to achieve convergence (in the strain localization modeling context), this drawback does not seem to introduce any practical limitation, in terms of additional computational cost. Contrarily, since convergence is attained in the first iteration, the computational cost is generally highly reduced if compared with a fully implicit integration scheme.

Details of the methodology may be consulted in the reference [Oliver, Huespe et al. 2006], where the implementation of the IMPL-EX algorithm, for the isotropic damage and for the J_2 plasticity model are presented. Details relative to the IMPL-EX implementation for the Rankine plasticity model, can be found in Appendix A.

Chapter 3

Mixed Finite Element Formulations and Localized Strain Injection

3.1. Mixed strain-displacement formulation

In solid mechanics, mixed finite formulations have been mainly used in the context of near incompressible media and in the analysis of bending dominated problems. For both cases, the motivation for using mixed interpolations is related to the poor performance of standard displacement formulations due volumetric and shear locking respectively ([Hughes 2000] [Bathe 1982]).

In the seventies, several families of methodologies were introduced to overcome this problem. One of them was based on the selective/reduced integration [Zienkiewicz et al. 1971]. For plate analysis, it was found that reducing the integration order of the shear stress, or of the complete stress tensor, leads to considerably improved behavior. The inconvenient of performing full reduced integration turns out to be the propagation of zero energy (hourglass) modes that become dominant, polluting the solution in terms of the displacement field. For this reason, for the analysis of elastic incompressible media, selective reduced techniques, where just the volumetric part is under-integrated, become preferable [Malkus 1976]. Moreover in [Hughes 1980], the selective integration procedures were generalized to nonlinear problems and the methodology became recognized as B-bar method. Nevertheless, due the lower computational cost of full reduced integration schemes, this method become also very popular, especially in the ambit of explicit dynamic computations and some hourglass control techniques

were proposed to avoid the development of the spurious modes [Flanagan and Belytschko 1981].

Other family of methods was based in a different concept. The idea was not to degenerate, but instead, augment the strain field. The method of incompatible modes was first introduced by Wilson aiming to enhance the performance of low-order (typically 4-node) elements in bending dominated problems [Wilson et al. 1973].

This class of methods (reduced integration, incompatible modes), provide unquestionable improved results, however, in its beginnings, they were just seen as “useful tricks”, due to the lack of mathematical variational foundations. Malkus and Hughes proved the equivalence of a class of mixed models with the reduced/selective integration of the displacement formulation [Malkus and Hughes 1978]. For example, the mixed bilinear displacement constant pressure element (Q1-P0) turns out to be equivalent to the B-bar element. The authors remarked the theoretical significance of this equivalence result, since “*convergence proofs and error estimates developed for the mixed methods [Babuska et al. 1977] immediately apply to the reduced/selective integration displacement elements*”.

A very general variational framework was introduced by Simo based on a nonlinear version of a three-field Hu-Washizu variational principle involving the displacement, stress, and an enhanced strain [Simo and Rifai 1990]. Additionally, if the space of stresses is required to be L_2 -orthogonal to the space of the enhanced strains, stresses can be eliminated from the problem. This class of mixed assumed strain methods proposed by Simo allows the systematic development of low order elements possessing good accuracy properties for coarse meshes. Depending on the chosen interpolating fields, the methodology, encompass a variety of finite element procedures like the previously referred B-bar or incompatible modes methods. Also, some more recent methodologies, like the Strong Discontinuity Approach fall inside this variational framework [Oliver 1996a].

In practical applications, the previous methodologies were used to improve the performance of low order elements, typically the 4-node quadrilateral element, without increasing the computational cost since the additional discontinuous interpolated field is eliminated at the element level by a standard condensation procedure. Applications of some of the previous methodologies to the simplicial element (triangle in 2D and tetrahedral in 3D) are not straightforward. For example, techniques based on under-integration do not apply to this element, since the element is fully integrated with just one quadrature (gauss) point.

To approach the incompressible problem, using simplicial elements, attention was therefore focus in mixed \mathbf{u}, p formulations [Herrmann 1965] with continuous pressure interpolation. The practical interest of this approach is related to the easy tetrahedral mesh generation for 3D complex geometries, and the principal inconveniences are the higher computational cost (since the additional continuous pressure field cannot be eliminated at the elemental level) and the lack of stability that derive from the fact that equal order displacement pressure interpolations do not verify the Babuska-Brezzi inf-sup condition [Brezzi and Fortin 1991]. To circumvent this condition, stabilization procedures inspired in those used for the

stokes problem of fluid dynamics have been proposed [Pastor et al. 1997] [Klaas et al. 1999]. Also the discontinuous pressure element (Q1-P0) does not verify the inf-sup condition. Nevertheless, for this elements some theoretical results have been obtained that explain its good performance without any stabilization technique. In [Johnson and Pitkäranta 1982] the author had obtained optimal convergence rate for the displacement field. For the pressure field the author had not obtained convergence but proved that a simple local averaging process gives convergence for the smoothed pressure. Following a similar analysis, analogous results were obtained for the Simo enhanced element [Reddy and Simo 1995].

In the context of non-linear solid mechanics, and particularly in strain localization analysis, mixed formulations have been applied when isochoric plastic flow constitutive models are used, *i.e.* for materials that do not exhibit plastic change of volume, as is the case of the J_2 constitutive model. The previously referred methods, developed in the ambit of the incompressible elasticity, have been tested for strain localization purposes by several authors. An example of a B-bar element applied to nonlinear analysis is the one proposed in [Nagtegaal et al. 1990]. In [Steinmann and Willam 1991a] the author compares the performance of several condensable elements (B-bar, enhanced elements, *etc.*) for capturing localized failure. Recently, also some stabilized mixed continuous pressure formulations have been used, for example the works presented in [Sánchez et al. 2008] and [Cervera et al. 2004].

We remark here, that the mixed methods used in the ambit of strain localization analysis, have been applied to address the problem of volumetric locking inherent to the isochoric constitutive models. Recently, Cervera had used a stabilized mixed linear displacement linear strain formulation, with the purpose of addressing the mesh bias dependence of the classical localization methods [Cervera, Chiumenti et al. 2011].

3.1.1. Using mixed $(\mathbf{u}, \varepsilon)$ formulations for strain localization problems: motivation

In Section 2.4.4, the mesh bias dependence was explained and exemplified with practical examples. The reasons why cracks tend to spuriously propagate parallelly to the mesh directions are not completely clear. Standard finite element formulations appear to be excessively stiffer⁹, and the crack seems to be locked in the mesh alignment avoiding zigzag. Mixed strain-displacement formulations, deriving from the weakly enforcement of the compatibility equation, may give some flexibility to the finite elements allowing them, to adapt their kinematic to the large distortions required to reproduce strain localization bands reducing the mesh bias dependence. In [Argyris and Willam 1974] the authors, based on ei-

⁹ It is known that the standard finite element formulations underestimate displacements and hence the stiffness is overestimated [Bathe 1982].

genvalues analysis on the stiffness matrices, conclude that mixed strain-displacement models are more flexible than the associated displacement models.

Moreover, one can think that, when the crack is propagating, stresses in the tip of the crack may not be accurately predicted¹⁰. In standard finite element formulation strains (that are used to compute stresses) are usually obtained by differentiation of the displacement solution at the points of interest. This direct operation results in lower order of accuracy, *i.e.* generally stresses and strains have one order less of accuracy than the nodal displacements.

In reference [Cervera, Chiumenti et al. 2011], the authors suggest that this spurious behavior is related to the “*lack of point-wise convergence of the strains and stresses in quasi-singular situations. For the linear case, such a convergence cannot be proved for the standard approach, but it happens in the mixed case*”. Nevertheless, the authors also refer, that for the non-linear case of interest no rigorous analysis of the mixed formulation is available. Apart of this theoretical reason, the authors report a clear improvement of the results when a mixed linear displacement linear strain formulation is used. The drawback of this formulation is that the additional degrees of freedom (3 and 6 per node, for 2D and 3D respectively) are not condensable at the elemental level and therefore the computational cost is higher.

In next Section a condensable mixed constant strain linear displacement formulation is proposed. Improvements in terms of avoiding mesh bias dependence and in terms of stress locking reduction are reported.

3.1.2. Mixed constant strain linear displacement variational formulation

The mixed strain-displacement formulation is introduced considering, in addition to the displacement, the strain field as an independent variable. The necessary additional equation to solve the new unknown is obtained imposing the compatibility equation in a weak form. Thus, testing the strong form of the problem defined in the equations (2.1) and (2.2) with the test functions $\boldsymbol{\eta} \in \mathcal{N}$, $\boldsymbol{\mu} \in \mathcal{V}$ and integrating over the domain, yields:

$$\int_{\Omega} \nabla^s \boldsymbol{\eta} : \dot{\boldsymbol{\Sigma}}(\dot{\boldsymbol{\varepsilon}}) d\Omega - \underbrace{\left[\int_{\Omega} \boldsymbol{\eta} \cdot \dot{\boldsymbol{b}} d\Omega + \int_{\Gamma_{\sigma}} \boldsymbol{\eta} \cdot \dot{\boldsymbol{t}}^* d\Gamma \right]}_{\dot{\boldsymbol{j}}^{ext}} = 0, \quad \forall \boldsymbol{\eta} \in \mathcal{N} \quad (\text{equilibrium}), \quad (3.1)$$

$$\int_{\Omega} \boldsymbol{\mu} : (\dot{\boldsymbol{\varepsilon}} - \nabla^s \dot{\boldsymbol{u}}) d\Omega = 0, \quad \forall \boldsymbol{\mu} \in \mathcal{V} \quad (\text{compatibility}).$$

The integrals in the previous equation are meaningful if the spaces of strains $\dot{\boldsymbol{\varepsilon}}$ and test functions $\boldsymbol{\mu}$ (\mathcal{V} and \mathcal{E} respectively) consist of symmetric second or-

¹⁰ Following the linear elastic fracture theory developed by Inglis the stresses in the crack tip are singular [Inglis 1913].

der tensors with components in $L^2(\Omega)$ (space of square integrable functions defined in Ω):

$$\mathcal{V} := \left\{ \boldsymbol{\mu} \mid \boldsymbol{\mu} \in [L^2(\Omega)]^{n \times n} \right\}, \quad \mathcal{E} := \left\{ \boldsymbol{\varepsilon} \mid \boldsymbol{\varepsilon} \in [L^2(\Omega)]^{n \times n} \right\}.$$

The displacement space \mathcal{U} and \mathcal{N} are defined as:

$$\mathcal{U} := \left\{ \mathbf{u} \mid \mathbf{u} \in [H^1(\Omega)]^n; \mathbf{u}|_{\Gamma_u} = \mathbf{u}^* \right\},$$

$$\mathcal{N} := \left\{ \boldsymbol{\eta} \mid \boldsymbol{\eta} \in [H^1(\Omega)]^n; \boldsymbol{\eta}|_{\Gamma_u} = 0 \right\},$$

where $H^1(\Omega)$ is the space of square integrable functions defined in Ω , whose first derivatives are also square integrable [Hughes 1987].

The weak form of the problem is summarized in Box 3.1.

Given $\dot{\mathbf{u}}^* : \Gamma_u \rightarrow \mathbb{R}^N$, $\dot{\mathbf{t}}^* : \Gamma_\sigma \rightarrow \mathbb{R}^N$ and $\dot{\mathbf{b}} : \Omega \rightarrow \mathbb{R}^N$; find $\dot{\mathbf{u}} \in \mathcal{U}$ and $\dot{\boldsymbol{\varepsilon}} \in \mathcal{E}$ such that for all $\boldsymbol{\eta} \in \mathcal{N}$ and $\boldsymbol{\mu} \in \mathcal{V}$

$$\begin{aligned} \int_{\Omega} \nabla^s \boldsymbol{\eta} : \dot{\boldsymbol{\Sigma}}(\dot{\boldsymbol{\varepsilon}}) d\Omega - \dot{\mathbf{f}}^{ext} &= 0, \\ \int_{\Omega} \boldsymbol{\mu} : (\dot{\boldsymbol{\varepsilon}} - \nabla^s \dot{\mathbf{u}}) d\Omega &= 0 \end{aligned} \quad (3.2)$$

Box 3.1 Weak form of the boundary value problem (mixed $\dot{\mathbf{u}}$, $\dot{\boldsymbol{\varepsilon}}$ formulation).

3.1.3. Finite element approximation

When mixed methods are used, a wide range of possible interpolation pairs are possible. Here, in order to obtain a computationally efficient condensable formulation, a quadrilateral finite element (Q1/ ε^0) equipped with standard bilinear interpolations in the displacement field and element-wise constant discontinuous interpolations for the strains, is used (see Figure 3.1).

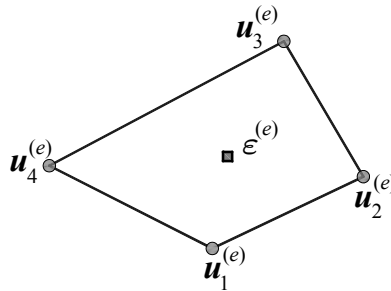


Figure 3.1 Finite element with continuous linear displacements $\mathbf{u}^{(e)}$ and element-wise constant discontinuous strains $\boldsymbol{\varepsilon}^{(e)}$.

Likewise for the irreducible formulation case in Section 2.4.2, the displacement field is approximated by the standard linear shape functions:

$$\dot{\mathbf{u}}^h(\mathbf{x}) = \sum_{i=1}^{nnodes} N_i(\mathbf{x}) \dot{\mathbf{u}}_i \quad ; \quad \boldsymbol{\eta}^h(\mathbf{x}) = \sum_{i=1}^{nnodes} N_i(\mathbf{x}) \boldsymbol{\eta}_i, \quad (3.3)$$

whereas the finite element approximations \mathcal{E}_h and \mathcal{U}_h for the spaces \mathcal{E} and \mathcal{U} :

$$\dot{\boldsymbol{\varepsilon}}^h(\mathbf{x}) = \sum_{e=1}^{nelem} \phi^{(e)}(\mathbf{x}) \dot{\boldsymbol{\varepsilon}}^{(e)} \quad ; \quad \boldsymbol{\mu}^h(\mathbf{x}) = \sum_{e=1}^{nelem} \phi^{(e)}(\mathbf{x}) \boldsymbol{\mu}^{(e)}, \quad (3.4)$$

where $nelem$ and $nnode$ are, respectively, the number of nodes and elements of the finite element mesh, N_i stands for the standard shape function associated to node i , $\dot{\mathbf{u}}_i$ and $\dot{\boldsymbol{\varepsilon}}^{(e)}$ stand, respectively, for the corresponding nodal displacement and elemental strain degrees of freedom. The element-wise-constant function $\phi^{(e)}$ is defined on $\Omega^{(e)}$, as

$$\phi^{(e)}(\mathbf{x}) = \begin{cases} 1 & \text{if } \mathbf{x} \in \Omega^{(e)} \\ 0 & \text{if } \mathbf{x} \notin \Omega^{(e)}, \end{cases}$$

$$\mathcal{U}_h := \left\{ \boldsymbol{\mu}^h \mid \boldsymbol{\mu}^h(\mathbf{x}) = \sum_{e=1}^{nelem} \phi^{(e)}(\mathbf{x}) \boldsymbol{\mu}^{(e)} \right\}; \quad \mathcal{U}_h \subset \mathcal{U},$$

$$\mathcal{E}_h := \left\{ \dot{\boldsymbol{\varepsilon}}^h \mid \dot{\boldsymbol{\varepsilon}}^h(\mathbf{x}) = \sum_{e=1}^{nelem} \phi^{(e)}(\mathbf{x}) \dot{\boldsymbol{\varepsilon}}^{(e)} \right\}; \quad \mathcal{E}_h \subset \mathcal{E}.$$

Considering the previous finite element approximations, equation (3.2) reads:

$$\sum_{e \in \Omega} \int_{\Omega^{(e)}} \nabla^s \boldsymbol{\eta}^h : \dot{\boldsymbol{\Sigma}}(\dot{\boldsymbol{\varepsilon}}^{(e)}) d\Omega = \dot{\mathbf{f}}^{ext}, \quad \forall \boldsymbol{\eta}^h \in \mathcal{N}^h, \quad a)$$

$$\int_{\Omega^{(e)}} \boldsymbol{\mu}^{(e)} (\dot{\boldsymbol{\varepsilon}}^{(e)} - \nabla^s \dot{\mathbf{u}}^h) d\Omega = 0, \quad \forall e \in \Omega, \quad \forall \boldsymbol{\mu}^h \in \mathcal{V}^h. \quad b)$$

Since the weighting function $\boldsymbol{\mu}^{(e)}$ and the interpolated strain $\dot{\boldsymbol{\varepsilon}}^{(e)}$ are element-wise constant, equation (3.5)-b) can be trivially solved at the element level for $\dot{\boldsymbol{\varepsilon}}^{(e)}$:

$$\dot{\boldsymbol{\varepsilon}}^{(e)} = \frac{\int_{\Omega^{(e)}} \nabla^s \dot{\mathbf{u}}^h d\Omega}{meas(\Omega^{(e)})} = \nabla^s \dot{\mathbf{u}}_{mean}^{h(e)}, \quad \forall e \in \Omega. \quad (3.6)$$

By substituting equation (3.6) into (3.5)-(a), it yields:

$$\sum_{e \in \Omega} \int_{\Omega^{(e)}} \nabla^s \boldsymbol{\eta}^h : \dot{\boldsymbol{\Sigma}}(\nabla^s \dot{\mathbf{u}}_{mean}^{h(e)}) d\Omega = \dot{\mathbf{f}}^{ext}, \quad \forall \boldsymbol{\eta}^h \in \mathcal{N}^h. \quad (3.7)$$

Remark 3.1.3.1: In the view of equation (3.6), $\nabla^s \dot{\mathbf{u}}_{mean}^{(e)}$ refers to the mean value of the symmetric gradient of the displacement field. For convenience of the finite element implementation, this will be replaced by the evaluation of this kernel in a sampling point coincident with the finite element centroid $\overline{\nabla^s \dot{\mathbf{u}}^h}^{(e)}$, *i.e.*:

$$\dot{\boldsymbol{\varepsilon}}^{(e)} = \overline{\nabla^s \dot{\mathbf{u}}^h}^{(e)}, \forall e \in \Omega. \quad (3.8)$$

Notice that with mesh refinement $\overline{\nabla^s \dot{\mathbf{u}}^h}^{(e)} \rightarrow \nabla^s \dot{\mathbf{u}}_{mean}^{(e)}$ and thus, also $\dot{\Sigma}(\nabla^s \dot{\mathbf{u}}_{mean}^{(e)}) \rightarrow \dot{\Sigma}(\overline{\nabla^s \dot{\mathbf{u}}^h}^{(e)})$.

$$\int_{\Omega^{(e)}} \nabla^s \boldsymbol{\eta}^h : \dot{\Sigma}(\nabla^s \dot{\mathbf{u}}_{mean}^{(e)}) d\Omega \approx \int_{\Omega^{(e)}} \nabla^s \boldsymbol{\eta}^h : \dot{\Sigma}(\overline{\nabla^s \dot{\mathbf{u}}^h}^{(e)}) d\Omega. \quad (3.9)$$

Remark 3.1.3.2: Notice that $\dot{\Sigma}(\overline{\nabla^s \dot{\mathbf{u}}^h}^{(e)})$ is constant within the element domain, thus:

$$\sum_{e \in \Omega} \dot{\Sigma}(\overline{\nabla^s \dot{\mathbf{u}}^h}^{(e)}) : \int_{\Omega^{(e)}} \nabla^s \boldsymbol{\eta}^h d\Omega = \dot{\mathbf{f}}^{ext}, \quad \forall \boldsymbol{\eta}^h \in \mathcal{N}^h. \quad (3.10)$$

Due to the linear character of $\nabla^s \boldsymbol{\eta}^h$

$$\int_{\Omega^{(e)}} \nabla^s \boldsymbol{\eta}^h d\Omega = meas(\Omega^{(e)}) \overline{\nabla^s \boldsymbol{\eta}^h}^{(e)} = \int_{\Omega^{(e)}} \overline{\nabla^s \boldsymbol{\eta}^h}^{(e)} d\Omega, \quad (3.11)$$

where $\overline{\nabla^s \boldsymbol{\eta}^h}^{(e)}$ is the value of $\nabla^s \boldsymbol{\eta}^h$ evaluated in the central point of the finite element. Expression (3.7) may then alternatively be written in the following form:

$$\sum_{e \in \Omega} \int_{\Omega^{(e)}} \overline{\nabla^s \boldsymbol{\eta}^h}^{(e)} : \dot{\Sigma}(\overline{\nabla^s \dot{\mathbf{u}}^h}^{(e)}) d\Omega = \dot{\mathbf{f}}^{ext}, \quad \forall \boldsymbol{\eta}^h \in \mathcal{N}^h, \quad (3.12)$$

where, the symmetric character of the nonlinear system of equations is evident.

Taking in mind Remark 3.1.3.1, the equivalence of the chosen two field $\mathbf{u}, \boldsymbol{\varepsilon}$ mixed formulation (Q1/ $\varepsilon 0$) with a reduced integration procedure of the displacement based formulation approach¹¹, with an integration point at the element centroid, becomes obvious, *i.e.*:

$$\begin{aligned} & \int_{\Omega^{(e)}} \overline{\nabla^s \boldsymbol{\eta}^h}^{(e)} : \dot{\Sigma}(\overline{\nabla^s \dot{\mathbf{u}}^h}^{(e)}) d\Omega \\ & \Leftrightarrow \\ & \text{Reduced} \\ & \text{Integration of } \left(\int_{\Omega^{(e)}} \nabla^s \boldsymbol{\eta}^h : \dot{\Sigma}(\nabla^s \dot{\mathbf{u}}^h) d\Omega \right), \end{aligned} \quad (3.13)$$

¹¹In [Malkus and Hughes 1978] was proven the equivalence of a class of mixed models with the reduced/selective integration of the displacement formulation.

It is well known that this kind of full reduced integration techniques lead to propagation of zero energy (hourglass) modes, that become dominant polluting the solution in terms of the displacement field. For the point of view of the equivalent mixed problem, the interpolation pairs: bilinear displacement constant strain, do not fulfill the inf-sup condition [Brezzi and Fortin 1991] and therefore no stability on the interpolated fields can be guaranteed.

3.1.4. Stabilization

In the past, some hourglass control techniques with different theoretical foundations have been proposed to overcome the lack of stability of the reduced integration methods [Kosloff and Frazier 1978; Belytschko and Bachrach 1986]. Here we propose the following stabilization term (3.12):

$$\mathbf{j}^{stab(e)} = \tau \int_{\Omega^{(e)}} \nabla^s \boldsymbol{\eta}^h : (\dot{\boldsymbol{\Sigma}}(\dot{\boldsymbol{\varepsilon}}^{(e)}) - \dot{\boldsymbol{\Sigma}}(\nabla^s \dot{\mathbf{u}}^h)) d\Omega, \quad (3.14)$$

that must be added to expression (3.12) as follows:

$$\sum_{e \in \Omega} \int_{\Omega^{(e)}} \overline{\nabla^s \boldsymbol{\eta}^h}^{(e)} : \dot{\boldsymbol{\Sigma}} \left(\overline{\nabla^s \dot{\mathbf{u}}^h}^{(e)} \right) d\Omega + \sum_{e \in \Omega} \mathbf{j}^{stab(e)} = \mathbf{j}^{ext}, \quad (3.15)$$

where τ is the stabilization parameter. Notice that the term proposed in (3.14) does not correspond to the residual of the equilibrium equation (3.5)-a) neither to the residual of the compatibility equation (3.5)-b). However, equation (3.5)-b) implies that, with mesh refinement: $\dot{\boldsymbol{\varepsilon}}^{(e)} \rightarrow \nabla^s \dot{\mathbf{u}}^h$, and since the constitutive equation is point-wisely imposed also: $\dot{\boldsymbol{\Sigma}}(\dot{\boldsymbol{\varepsilon}}^{(e)}) \rightarrow \dot{\boldsymbol{\Sigma}}(\nabla^s \dot{\mathbf{u}}^h)$, meaning this, that the stabilization forces of (3.14) decrease with mesh refinement and vanish for exact solutions (regardless the value of the stabilization parameter τ). By this reason the proposed stabilization term (3.14) can be considered to belong to the family of consistently stabilized methods (see *e.g.* [Bochev and Gunzburger 2004] [Dohrmann and Bochev 2004]).

Considering the result of (3.8): $\dot{\boldsymbol{\varepsilon}}^{(e)} = \overline{\nabla^s \dot{\mathbf{u}}^h}^{(e)}$, and the property remarked at 3.1.3.2., equation (3.15) can be written, after rearranging terms, as:

$$\begin{aligned} & \sum_{e \in \Omega} (1 - \tau) \underbrace{\int_{\Omega^{(e)}} \overline{\nabla^s \boldsymbol{\eta}^h}^{(e)} : \dot{\boldsymbol{\Sigma}} \left(\overline{\nabla^s \dot{\mathbf{u}}^h}^{(e)} \right) d\Omega}_{\text{mixed form.}} + \\ & + \sum_{e \in \Omega} \tau \underbrace{\int_{\Omega^{(e)}} \nabla^s \boldsymbol{\eta}^h : \dot{\boldsymbol{\Sigma}}(\nabla^s \dot{\mathbf{u}}^h) d\Omega}_{\text{displacement form.}} = \mathbf{j}^{ext}. \end{aligned} \quad (3.16)$$

Remark 3.1.4.1: Analyzing expression (3.16), it is noticeable that for $\tau = 1$ the method is equivalent to the standard irreducible formulation, whereas for $\tau = 0$, the stabilization term vanishes and the unstable mixed formulation is recovered.

Remark 3.1.4.2: The stabilized formulation (3.16) may be regarded as a weighted combination of the irreducible displacement based formulation (fully integrated term) with the mixed displacement-strain formulation (reduced integrated term), weighted by τ and $1-\tau$ respectively. The τ term, associated to the displacement formulation, provides stability to the mixed formulation.

Remark 3.1.4.3: Expression (3.16) may be rewritten in a more compact equivalent form:

$$\sum_{e \in \Omega} \int_{\Omega^{(e)}} \nabla^s \boldsymbol{\eta}^h : \dot{\boldsymbol{\sigma}}^{(e)} d\Omega = \dot{\mathbf{f}}^{ext}, \quad (3.17)$$

$$\dot{\boldsymbol{\sigma}}^{(e)} = (1-\tau) \dot{\boldsymbol{\Sigma}}(\overline{\nabla^s \dot{\mathbf{u}}^h}^{(e)}) + \tau^{(e)} \dot{\boldsymbol{\Sigma}}(\nabla^s \dot{\mathbf{u}}^h),$$

where $\dot{\boldsymbol{\sigma}}^{(e)}$ is interpreted as a stabilized stress. Notice that this version preserves the typical structure of the internal force vector of a standard non-linear finite element code, where the tensor $\boldsymbol{\sigma}^{(e)}$ is substituted by $\dot{\boldsymbol{\sigma}}^{(e)}$. Hence, the previous expression can be integrated by a standard quadrature rule, for example using 2×2 Gauss integration points. The nuance is that, previously to the integration of expression (3.17), the tensor $\dot{\boldsymbol{\Sigma}}(\overline{\nabla^s \dot{\mathbf{u}}^h}^{(e)})$ should be evaluated and stored at the additional central sampling point¹² and then kept constant in the integration procedure.

3.1.5. Matrix equations

In this Section the problem matrix equations are summarized (Voigt notation is used):

<p>Given the external force vector \mathbf{F}^{ext}, find \mathbf{u}^h such that</p> $\dot{\mathbf{F}}^{int} = \mathcal{A} \left(\int_{\Omega^{(e)}} \mathbf{B}^{(e)} \cdot \{\dot{\boldsymbol{\sigma}}\}^{(e)} d\Omega \right) = \dot{\mathbf{F}}^{ext}$ $\{\dot{\boldsymbol{\sigma}}\}^{(e)} = (1-\tau)\{\dot{\boldsymbol{\sigma}}\}^{(e)} + \tau\{\dot{\boldsymbol{\sigma}}\}^{(e)}$ $\{\dot{\boldsymbol{\sigma}}\}^{(e)} = \dot{\boldsymbol{\Sigma}}(\overline{\nabla^s \dot{\mathbf{u}}^h}^{(e)}) ; \{\dot{\boldsymbol{\sigma}}\}^{(e)} = \dot{\boldsymbol{\Sigma}}(\nabla^s \dot{\mathbf{u}}^h)^{(e)}$ $\{\overline{\nabla^s \dot{\mathbf{u}}}\}^{(e)} = \overline{\mathbf{B}}^{(e)} \cdot \{\dot{\mathbf{u}}\}^{(e)} ; \{\nabla^s \dot{\mathbf{u}}\}^{(e)} = \mathbf{B}^{(e)} \cdot \{\dot{\mathbf{u}}\}^{(e)}$ $\mathbf{K}^{tang} = \mathcal{A} \left((1-\tau) \int_{\Omega^{(e)}} \overline{\mathbf{B}}^{(e)T} \cdot \{\overline{\mathbf{C}}^{ep}\} \cdot \overline{\mathbf{B}}^{(e)} d\Omega + \tau \int_{\Omega^{(e)}} \mathbf{B}^{(e)T} \cdot \{\mathbf{C}^{ep}\} \cdot \mathbf{B}^{(e)} d\Omega \right) \quad (3.19)$
--

Box 3.2 Stabilized mixed formulation. Matrix equations.

¹² This additional sampling point can be therefore regarded as a zero weight integration point, just used for stress evaluation.

In Box 3.2, $0 < \tau < 1$ stands for stabilization parameter (that should be specified by the user), $\mathbf{B}^{(e)}$ is the standard deformation matrix, $\bar{\mathbf{B}}^{(e)}$ is the (constant) \mathbf{B} -matrix evaluated at the center of the finite element and \mathbf{K}^{tang} is the tangent stiffness matrix that stems from (3.18).

3.1.6. A first set of representative numerical examples

To assess the performance of the proposed stabilized mixed \mathbf{u}, ε formulation, several numerical simulations, considering different constitutive models, are presented in the next Sections.

3.1.6.1. Isotropic continuum damage model: double cantilever beam (DCB) with diagonal loads

Figure 3.1a) shows the geometric description and the spatial and temporal loading conditions of the problem [Kobayashi et al. 1985]. It is considered a plane strain model. The diagonal compression forces, F_2 , are initially introduced together with the wedge loads, F_1 , increasing along the time, until reaching 3.78 kN. Then, the diagonal loads remain constant while the wedge loads increase.

It is used a damage model with degradation only in tension and the material parameters are: Young's modulus: $E = 30500$ MPa, Poisson's ratio: $\nu = 0.2$, fracture energy: $G_f = 100$ N/m, ultimate tensile strength: $\sigma_y = 3$ MPa and specimen thickness: 50.8 mm.

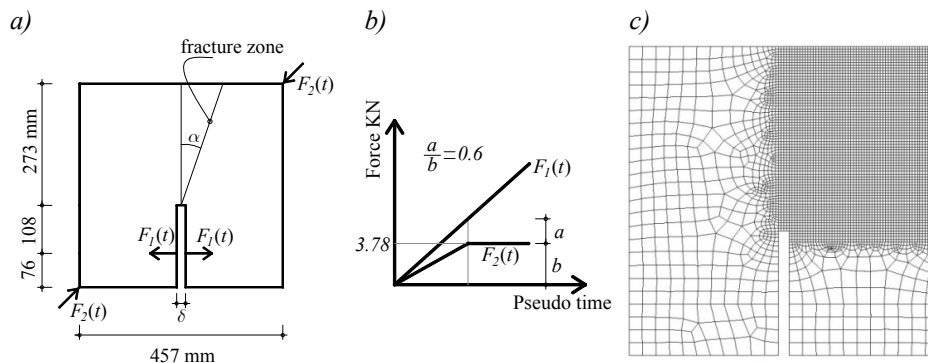


Figure 3.2 Double cantilever beam with diagonal load: a) geometrical data, b) loading data, c) finite element discretization.

The reported experimental crack path follows a straight line (inclined $\alpha = 19^\circ$ with the vertical axis) as shown in Figure 3.2-a). Therefore, vertical meshes lines (Figure 3.1c) will strongly challenge the standard finite element formulations since the experimentally observed discontinuity path intersects the elements in directions not coincident with the mesh alignment.

Regarding the proposed stabilized method, it was referred on Remark 3.1.4.1, that for values of τ approaching the unity (*i.e.* for $\tau \rightarrow 1$) the method is equivalent to the irreducible standard finite element approximation and therefore, the benefits inherent to the mixed formulations are expected to vanish. Figure 3.3 shows the localization pattern for different values of the stabilization parameter τ .

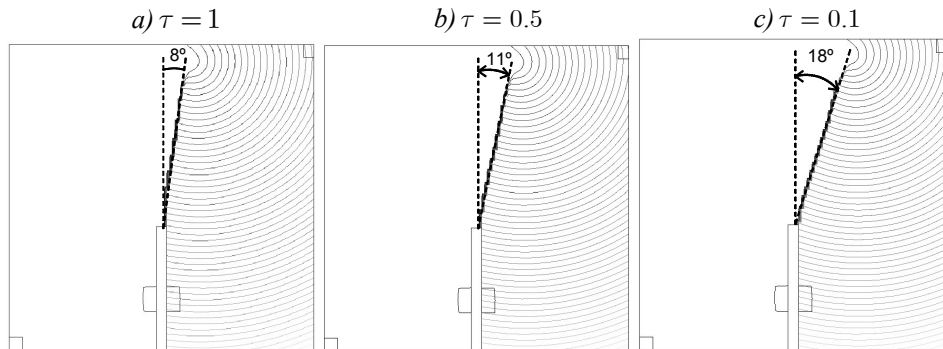


Figure 3.3 Iso-displacement plots for different stabilization parameters τ .

It is notorious the improvement on the element performance in terms of mesh bias independence for decreasing values of τ . For $\tau = 0.1$, it is shown the good agreement between the simulated strain localization pattern with that reported by experimental observation, while for $\tau = 1$ the crack is clearly affected by the vertical mesh alignment only zigzagging to the next row after having propagated vertically a large number of elements.

Figure 3.4 displays the deformed mesh for solutions corresponding to $\tau = 1$ and $\tau = 0.1$.

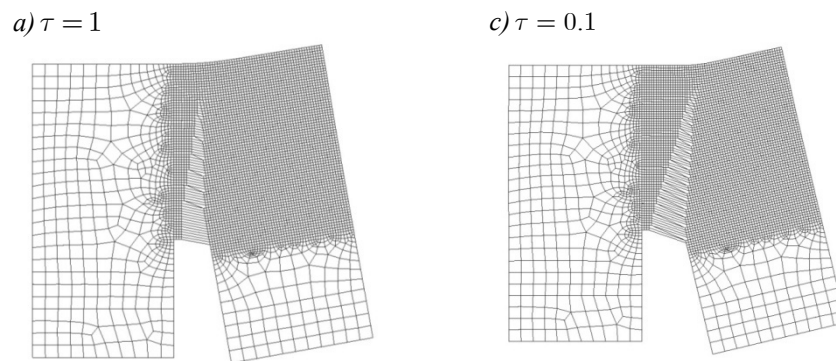


Figure 3.4 Deformed mesh.

For $\tau = 0$ the unstable mixed formulation is recovered. On this view, for decreasing values of τ (*i.e.* for $\tau \rightarrow 0$), it is expected that instabilities may come out. Figure 3.5 and Figure 3.6 present the numerical solutions obtained with $\tau = 0.0001$.

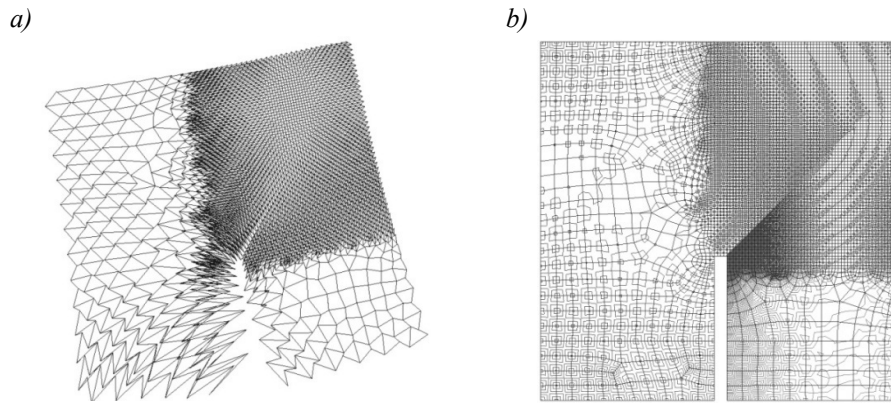


Figure 3.5 Result for $\tau = 0.0001$: a) mesh deformation, b) iso-displacement contours.

In Figure 3.5, it is noticeable the appearance of hourglass modes dominating the solution in terms of the displacement field. These spurious modes propagate across the mesh leading to a miss predicted collapse mechanism.

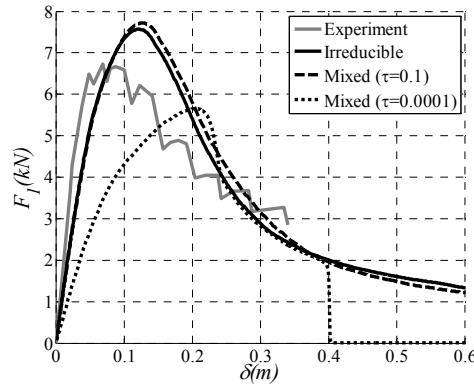


Figure 3.6 Force-displacement curves.

Figure 3.6 plots the force vs. displacements curves for solutions with different parameters τ . As it can be observed in the Figure the, stabilized mixed formulation ($\tau = 0.1$) is slightly more dissipative than the irreducible formulation. Note that, this extra dissipation is not attributed to an increment of stress locking for the mixed formulation¹³, but, instead, it is caused by the differences in the collapse mechanisms. For the mixed formulation, the localization pattern is more inclined (Figure 3.3) giving a larger crack length that justifies the extra-dissipation. The lower residual load obtained for the mixed formulation supports this argument.

¹³ on the contrary, stress locking is expected to decrease when the mixed formulation is used, as it will be shown on the next examples.

Relatively to the unstable solution ($\tau = 0.0001$), the miss predicted collapse mechanism leads to an unrealistic force-displacement curve.

3.1.6.2. Strip undergoing an homogeneous uniaxial tensile stress state

Next, the example shown in Section 2.4.4. is re-examined. Results previously presented in that Section, are now complemented with solutions obtained using the stabilized mixed approach and taking $\tau = 0.1$. We recall that the theoretical solution consists of a vertical crack passing through the perturbed elements. The three meshes used to obtain the numerical solutions are coincident with those adopted in Section 2.4.4.

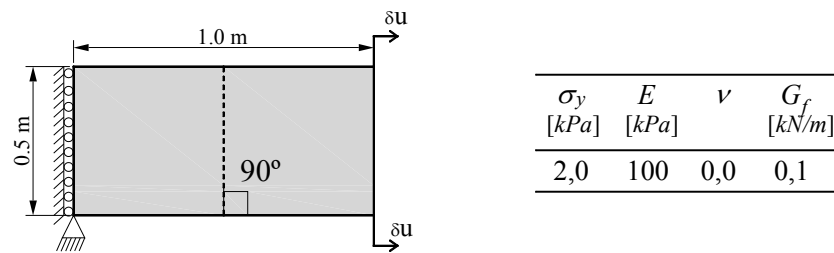
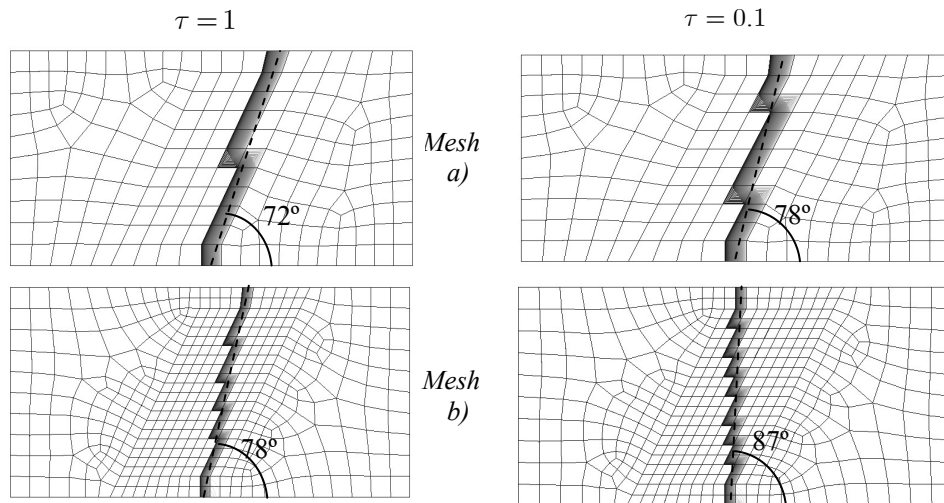


Figure 3.7 Strip stretching in the horizontal direction.

Figure 3.8 and Figure 3.9 show the displacement contour lines of the solutions obtained by using $\tau = 1.0$ and $\tau = 0.1$, and adopting the damage and Rankine plastic models.

- **Isotropic damage model**



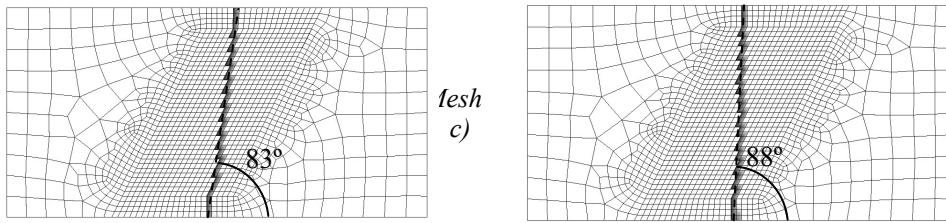


Figure 3.8 Iso-displacement plots (isotropic damage model). Results obtained with the irreducible formulation ($\tau = 1$) and with mixed stabilized formulation ($\tau = 0.1$) are shown in the left and in the right hand side of the figure respectively, for three different levels of discretization.

- Rankine plasticity model

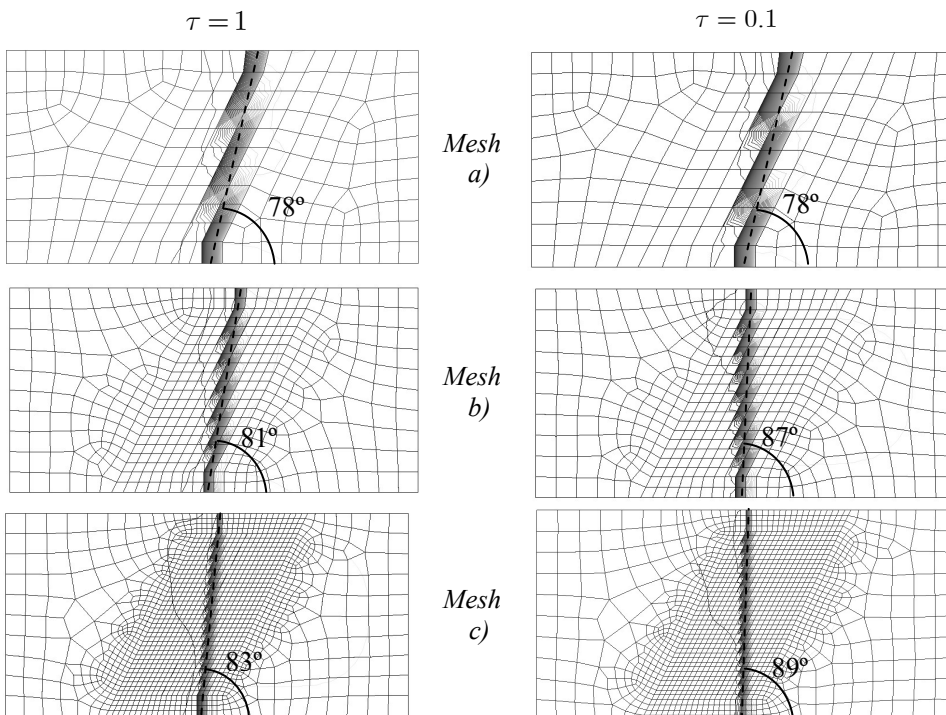


Figure 3.9 Iso-displacement plots (plasticity Rankine model). Results obtained with the irreducible formulation ($\tau = 1$) and with mixed stabilized formulation ($\tau = 0.1$) are shown in the left and in the right hand side of the figure respectively, for three different levels of discretization.

The solutions with $\tau = 1.0$ coincides with that shown in Section 2.4.4. (Figure 2.11 and Figure 2.12.) since the same finite element formulation is used. For $\tau = 0.1$, a clear improvement in terms of mesh bias independence is noticed. Note that for both constitutive models and for meshes b) and c) the stabilized mixed formulation ($\tau = 0.1$), approaches well the vertical theoretical solution.

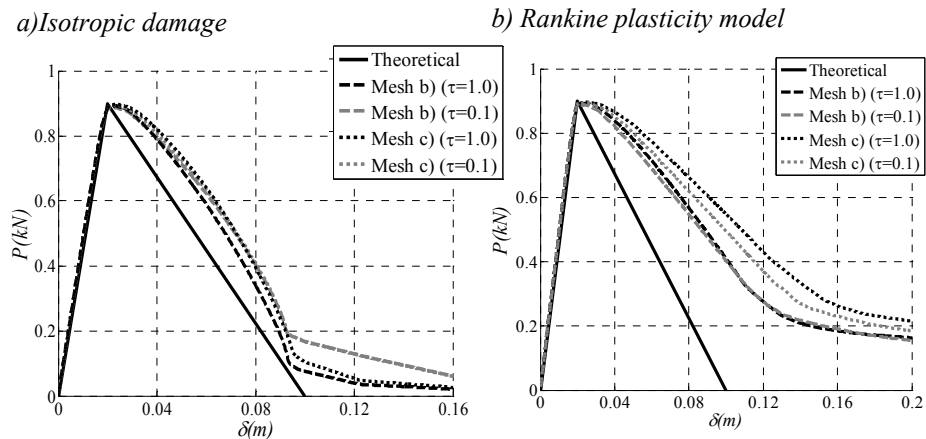


Figure 3.10 Force-displacement curves: a) Isotropic damage, b) Rankine plasticity model.

In Figure 3.10, the force-displacement curves are presented. A small decrease in terms of stress locking is generally obtained with the stabilized mixed method, which can be better observed in the curves correspondent to the Rankine constitutive model for Mesh c) (less dissipation and lower residual load). Nevertheless, the change is not significant, and the result clearly overestimates the dissipative energy, due to stress locking. This fact evidences that the element equipped with $\mathbf{u} - \boldsymbol{\varepsilon}$ kinematics still exhibits a limited capability to resolve a discontinuity in a one-element band, and like in the irreducible formulation, the discontinuity is smeared out over several elements. In Chapter 4 this issue is addressed.

- **J_2 plasticity model**

Next the potential applicability of the stabilized mixed element to isochoric plastic flow constitutive models is examined, *i.e.* for materials that do not exhibit plastic change of volume, as is the case of the J_2 constitutive model. It is known that due to the incompressibility of the plastic flow, the irreducible formulation fully locks and no strain localization is obtained. Thinking on the similar aspects between the stabilized mixed method and the selective integration [Malkus 1976], here, not only the hydrostatic part, but all the stress tensor is under-integrated. Thus, if no relevant instabilities occur, and if the stabilization forces are not significant, the benefits of the selective integration should be recovered by the presented mixed formulation.

For this constitutive model the considered material properties are the following: Young's modulus: $E = 120$ kPa, Poisson's ratio: $\nu = 0.49$, fracture energy: $G_f = 22.72$ N/m, and yield stress: $\sigma_y = 1$ kPa. The theoretical solution of the problem consists of a straight shear band inclined $\pm 45^\circ$.

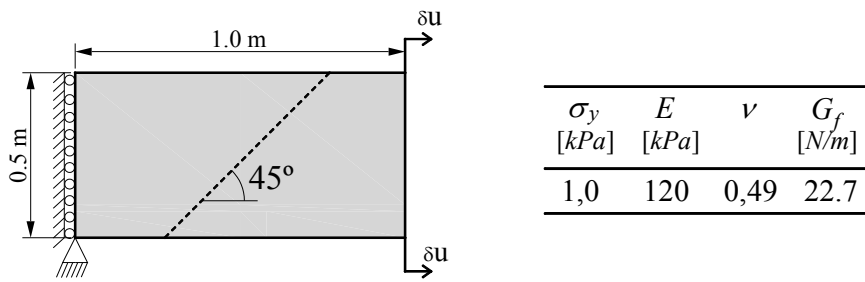


Figure 3.11 Strip stretched in the horizontal direction (J_2 plasticity model).

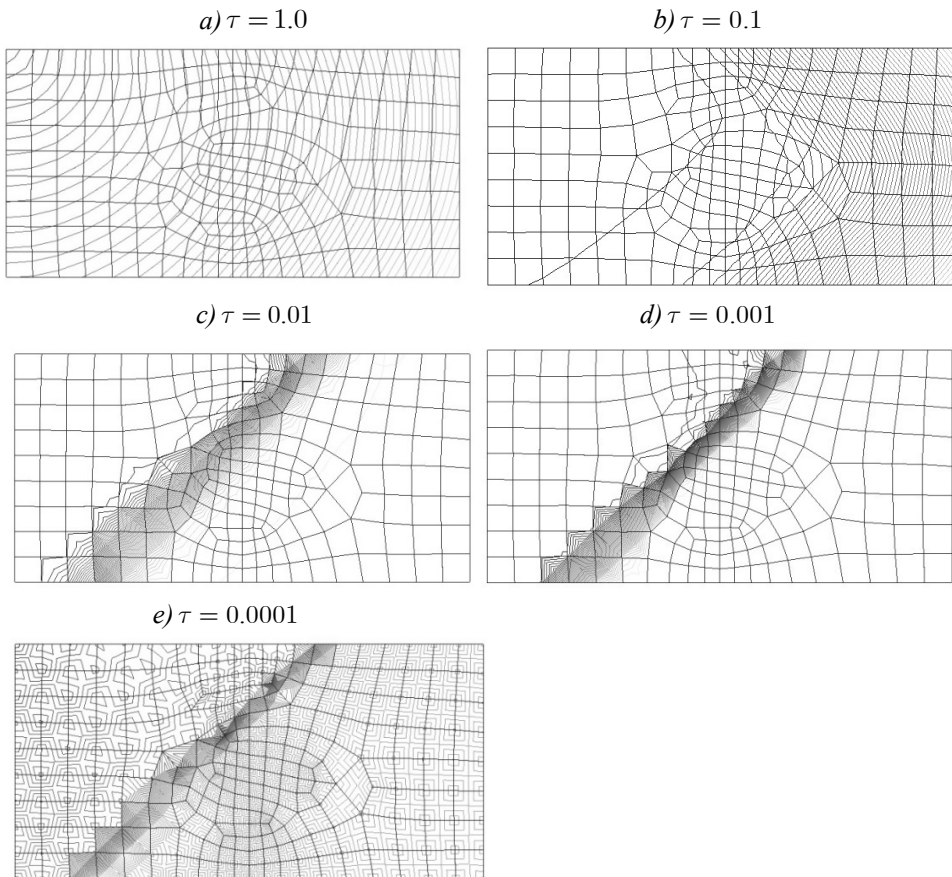


Figure 3.12 Iso-displacement plots. (J_2 plasticity model). Results obtained with the mixed stabilized formulation for different values of τ , at the final stage of analysis.

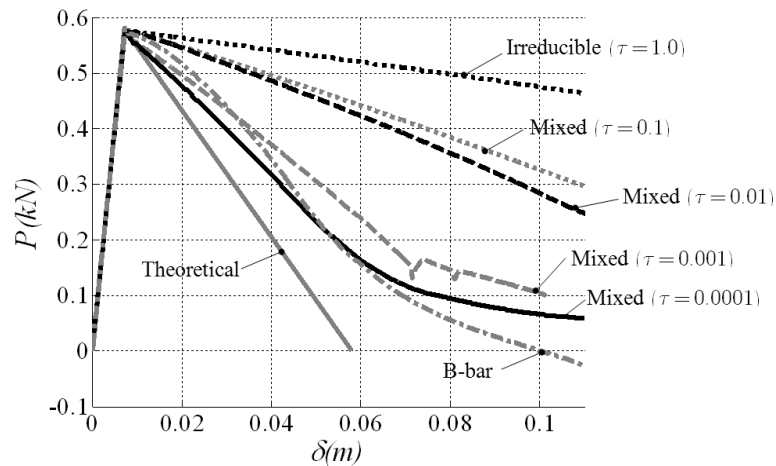


Figure 3.13 Force-displacement curve.

In Figure 3.12 and Figure 3.13 it is observed that the irreducible formulation ($\tau = 1.0$) fully locks and no strain localization is obtained. For decreasing values of τ , the solution improves in terms of the sharpness of the localization band and in terms of the correspondent force-displacement curves that show lower energy dissipation. However, Figure 3.12-e) shows that for $\tau = 0.0001$ hourglass instabilities are present polluting the solution in terms of the displacement field. It is interesting to note, that despite the instabilities on the displacement field, the solution in terms of the force-displacement curve is quite good (either in terms of the ultimate load and post bifurcation behavior, see Figure 3.13). This fact would have been expected since zero energy modes do not generate forces and the numerical example was carried out under displacement control. Nevertheless this behavior cannot be expected in general, as it was seen in the example presented in Section 3.1.6.1. In that case, the appearance of instabilities leads to underestimate the ultimate structural load carrying capacity. For additional comparison, the results obtained for this problem using the B-bar formulation have also been included in Figure 3.13.

3.2. Constant strain mode injection. Domain restricted mixed $(\mathbf{u}, \boldsymbol{\varepsilon})$ formulation

From the previous results it was observed that the proposed τ -stabilized mixed formulation incorporate considerable benefits without significantly increasing the numerical costs, and with a trivial finite element implementation. The benefits are related to the mesh bias dependence, which is strongly alleviated.

Additionally, stress locking is also reduced. This reduction is not substantial for the Rankine plasticity model, but is very significant for the J_2 plasticity model, what gives generality to the formulation, since incompressible problems may also be handled.

In the other hand, the principal drawback of the τ – stabilized method is the requirement of a specification of the stabilization parameter τ . This specification usually requires experience from the user about the range of possible “good” values for τ . Additionally, the optimal value of τ is generally problem dependent (since may depend on geometry, on the elastic properties and on the finite element discretization), being often difficult to find an optimum value, since for small values of τ ($\tau \rightarrow 0$) instabilities may destroy the solution, and for higher values ($\tau \rightarrow 1$) the benefits of the mixed stabilized formulation may cancel. Due to these drawbacks, dispending of this “user” parameter and at the same time potentiate the benefits of the mixed formulation is the main motivation for using a domain restricted mixed \mathbf{u}, ε formulation.

The basic idea is to restrict the mixed formulation to the part of the domain where the fracture is being processed. Numerical experiences show that by restricting the reduced integration procedure to a small part of the domain, instabilities due to zero energy modes are avoided (even for $\tau = 0$), while the benefits related to the mixed formulation are maintained, since the part of the domain where strains localize is still “specifically treated” by a mixed formulation. Note that this strategy also allows potentiates the benefits of a pure mixed displacement strain formulation, since the stabilizing forces are no-longer necessary, and these forces may have a “perverse” effect on the element performance, as it was observed in the previous numerical examples.

3.2.1. The mixed injection domain

Regarding the idea of using the one-point integration procedure in a reduced part of the domain, one may *reinterpret* the restricted mixed constant strain linear displacement formulation, as a Constant Strain¹⁴ Mode (CSM) being injected on those elements that belong to the domain part of interest. This part of the domain is then called the *mixed injection domain* Ω_{mixed} (see Figure 3.14), that we propose to be identified by means of bifurcation analysis (Section 2.3), *i.e.* as the geometrical locus of *in-loading bifurcated* points:

$$\Omega_{mixed}(t) := \{ \mathbf{x} \in \Omega \mid t \geq t_B(\mathbf{x}) ; \dot{\alpha}(\mathbf{x}, t) > 0 \}. \quad (3.20)$$

The motivation for the definition (3.20) is rather intuitive. The bifurcated points are the points amenable to develop a localization of a strain field. Addi-

¹⁴ The constant strain interpretation of reduced integration was referred also by other authors without relay in the equivalent mixed *constant strain* finite element formulation [Steinmann and Willam 1991b], [Argyris and Willam 1974]. The main innovation here is the injection concept.

tionally strain localization cannot develop in unloading processes $\dot{\alpha}(\mathbf{x}, t) = 0$. Notice that when an element unloads, it leaves the mixed injection domain, and by means of this, this domain remains as smaller as possible.

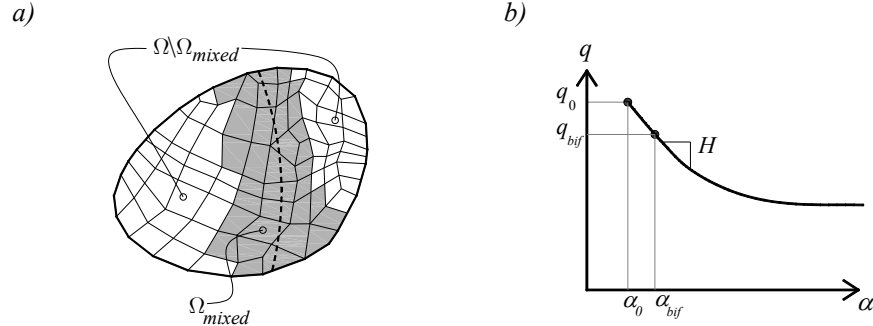


Figure 3.14 a) Mixed injection domain, b) Hardening softening law.

Remark 3.2.1.1: In the finite element context, we propose to verify the in-loading bifurcated condition at the Gauss point of the reduced integration scheme (centroid of the element). Note that this point is coincident with the commonly called optimal stress points. These points, are optimal in the sense that stresses and strains are there better accurately predicted than at any other point of the finite element [Barlow 1976]. Moreover, Barlow had also related its accuracy properties with the improved behavior of the reduced integrations schemes [Barlow 1989]. These points, also identified in the literature as superconvergent points¹⁵, had attracted large attention due its practical interest [Zienkiewicz and Zhu 1992], nevertheless for general non-linear problems and distorted meshes, there is neither theoretical nor computer-based proofs on the existence of the superconvergent points [Babuška et al. 1996].

3.2.2. Variational formulation

The variational equations corresponding to the restricted mixed \mathbf{u}, ε formulation, in rate form, read as follows:

$$\int_{\Omega \setminus \Omega_{mixed}} \nabla^s \boldsymbol{\eta}^h : \dot{\boldsymbol{\Sigma}}(\nabla^s \dot{\mathbf{u}}^h) d\Omega + \sum_{e \in \Omega_{mixed}} \int_{\Omega^{(e)}} \nabla^s \boldsymbol{\eta}^h : \dot{\boldsymbol{\Sigma}}(\dot{\varepsilon}_{inj}^{(e)}) d\Omega = \dot{\mathbf{f}}^{ext}, \quad a) \quad (3.21)$$

$$\int_{\Omega^{(e)}} \boldsymbol{\mu}^{(e)} : \{ \nabla^s \dot{\mathbf{u}}^h - \dot{\varepsilon}_{inj}^{(e)} \} d\Omega = 0 \quad \forall e \in \Omega_{mixed}, \quad b)$$

¹⁵ In those points one order more of convergence is obtained for the derivatives of the displacement field, *i.e.* the strains computed at the superconvergent point have the same order of convergence that the nodal displacements.

where $\dot{\epsilon}_{inj}^{(e)}$ is the element-wise-constant injected strain rate field and $\mu^{(e)}$ the corresponding (element-wise-constant) weighting function. Comparing equation (3.21) with (3.5), the difference lies on the kinematic equation that now is weakly imposed only for those elements belonging to the mixed injection domain.

Solution of (3.21)-b) is trivially found, and it is given by:

$$\dot{\epsilon}_{inj}^{(e)} = \overline{\nabla^s \dot{\mathbf{u}}^h}^{(e)}, \forall e \in \Omega_{mixed}, \quad (3.22)$$

and substitution of equation (3.22) in (3.21)-a) yields:

$$\int_{\Omega \setminus \Omega_{mixed}} \nabla^s \boldsymbol{\eta}^h : \dot{\boldsymbol{\Sigma}}(\nabla^s \dot{\mathbf{u}}^h) d\Omega + \sum_{e \in \Omega_{mixed}} \int_{\Omega^{(e)}} \overline{\nabla^s \boldsymbol{\eta}}^{(e)} : \dot{\boldsymbol{\Sigma}}(\overline{\nabla^s \dot{\mathbf{u}}^h}^{(e)}) d\Omega = \dot{\mathbf{f}}^{ext}. \quad (3.23)$$

As explained previously, the term ‘‘injection’’ for this procedure is justified since equation (3.23) corresponds to the virtual work principle where the constant strain field, $\overline{\nabla^s \dot{\mathbf{u}}^h}^{(e)}$, is injected into the constitutive equation only in those elements belonging to the injection zone, defined here as the mixed injection domain (see Figure 3.14). Moreover this interpretation is also convenient since additional strain modes, may be proposed to be injected, to further enhance the localization performance of the finite elements as it will be done in Chapter 5.

3.2.3. Isochoric constitutive model – special treatment

The idea behind the injection concept is to enrich that part of the domain where strains localize, enhancing the performance of the finite elements in terms of propagation and localization. Intuitively, it seems reasonable to define the domain of injection as the set of elements where discontinuous material bifurcation is detected. Nevertheless, when J_2 plasticity is used, an additional difficulty emerges due the isochoric character of this constitutive model. In fact, for this model, in earlier stages of the nonlinear loading, the irreducible formulation fully locks (unlike for other constitutive models). So for this specific case, we propose a slightly different strategy. The idea is to use as underlying element, not the irreducible, but instead the mixed formulation with a stabilization parameter ($\tau = 0.1$)¹⁶. The injection of the CSM is then performed as explained before. Thus, by considering (3.17) and (3.23):

$$\sum_{e \in \Omega \setminus \Omega_{mixed}} \int_{\Omega^{(e)}} \nabla^s \boldsymbol{\eta}^h : \dot{\boldsymbol{\sigma}}^{(e)} d\Omega^{(e)} + \sum_{e \in \Omega_{mixed}} \int_{\Omega^{(e)}} \overline{\nabla^s \boldsymbol{\eta}}^{(e)} : \dot{\boldsymbol{\sigma}}^{(e)} d\Omega = \dot{\mathbf{f}}^{ext}, \quad (3.24)$$

$$\dot{\boldsymbol{\sigma}}^{(e)} = (1 - \tau) \dot{\boldsymbol{\sigma}}^{(e)} + \tau \dot{\boldsymbol{\sigma}}^{(e)} \quad ; \quad \tau = 0.1.$$

From now on, for simplification of the writing, we abbreviate the notation as follows: $\dot{\boldsymbol{\sigma}}^{(e)} = \dot{\boldsymbol{\Sigma}}\left(\overline{\nabla^s \dot{\mathbf{u}}^h}^{(e)}\right)$ and $\dot{\boldsymbol{\sigma}}^{(e)} = \dot{\boldsymbol{\Sigma}}(\nabla^s \dot{\mathbf{u}}^h)$.

¹⁶ In practice, no instabilities have been noticed with $\tau = 0.1$

3.2.4. Implementation aspects

For implementation purposes, it is advantageous writing equation (3.24) in the following equivalent form:

$$\sum_{e \in \Omega} \left(\int_{\Omega^{(e)}} \nabla^s \boldsymbol{\eta}^h : \dot{\boldsymbol{\sigma}}^{(e)} d\Omega \right) = \dot{\boldsymbol{f}}^{ext} \quad a) \quad (3.25)$$

$$\dot{\boldsymbol{\sigma}}^{(e)} = (1 - \tau^{(e)}) \dot{\boldsymbol{\sigma}}^{(e)} + \tau^{(e)} \dot{\boldsymbol{\sigma}}^{(e)} \quad b)$$

where:

$$\tau^{(e)} = 0.0 \quad \forall e \in \Omega_{mixed}$$

$$\tau^{(e)} = 0.1 \quad \forall e \in \Omega \setminus \Omega_{mixed} \quad \text{for isochoric constitutive models}$$

$$\tau^{(e)} = 1.0 \quad \forall e \in \Omega \setminus \Omega_{mixed} \quad \text{for general constitutive models (except isochoric)}$$

Box 3.3 Constant strain mode injection. Rate form.

Notice that the stabilization parameter, $\tau^{(e)}$, can now take specific values for every element (e).

The implementation of the injection procedure (3.25), in a non-linear finite element code equipped with linear quadrilateral elements is remarkably simple¹⁷. The first step, in the numerical implementation of the procedure, consists of introducing an additional quadrature point (in addition to the standard (2×2) gauss points), positioned in the center of the finite element, where $\dot{\boldsymbol{\sigma}}^{(e)}$ is evaluated. The second step consists of defining the domains $\Omega \setminus \Omega_{mixed}$ and Ω_{mixed} . Initially, all the elements are considered to belong to $\Omega \setminus \Omega_{mixed}$, and so, according to (3.25) $\tau^{(e)}$ is set to 1.0 or 0.1 (depending on the constitutive model). Then, in all elements and for all the time steps, equation (3.20) should be verified with the converged values of $\dot{\boldsymbol{\sigma}}^{(e)}$. If conditions of equation (3.20) are fulfilled, the element is flagged as belonging to the mixed domain, and for this element the parameter $\tau^{(e)}$ is automatically set to zero, giving $\dot{\boldsymbol{\sigma}}^{(e)} = \dot{\boldsymbol{\sigma}}^{(e)}$.

3.2.5. Total vs. incremental time formulations

In this work, the governing equations have been presented in a “rate” form. In fact it is convenient that the finite element implementation pays attention to this issue. Alternatively, if a “total” implementation of the formulation is used, the evolution of the mixed domain can potentially cause sudden changes in the total

¹⁷ Notice that equation (3.25)-a), has the structure of the standard finite element formulation internal force vector, where $\dot{\boldsymbol{\sigma}}$ is substituted by $\dot{\boldsymbol{\sigma}}$.

stiffness of the domain¹⁸, which translates afterwards into spurious oscillations, as may be observed in Figure 3.25. Equations in Box 3.4 correspond to a “total” time-discretized version of the equilibrium equations obtained with the injection strategy, which can be derived in a similar manner, as it was done for the rate version.

$$\begin{aligned}
 \sum_{e \in \Omega} \left(\int_{\Omega^{(e)}} \nabla^s \boldsymbol{\eta}^h : \tilde{\boldsymbol{\sigma}}_{n+1}^{(e)} d\Omega \right) &= \mathbf{f}_{n+1}^{ext} \\
 \tilde{\boldsymbol{\sigma}}_{n+1}^{(e)} &= (1 - \tau^{(e)}) \bar{\boldsymbol{\sigma}}_{n+1}^{(e)} + \boldsymbol{\sigma}_{n+1}^{(e)} \\
 \text{where :} & \\
 \tau^{(e)} &= 0.0 \quad \forall e \in \Omega_{mixed} \\
 \tau^{(e)} &= 1.0 \quad \forall e \in \Omega \setminus \Omega_{mixed} \quad \text{for general constitutive models} \\
 \tau^{(e)} &= 0.1 \quad \forall e \in \Omega \setminus \Omega_{mixed} \quad \text{for isochoric constitutive models}
 \end{aligned} \tag{3.26}$$

Box 3.4 Constant strain injection. “Total” form

Numerous finite element programs are developed in a “total” implementation framework, and, in order to maintain the generality of the code, performing modifications at this level is usually not convenient. For that case, the strategy summarized at Box 3.5 may be applied:

$$\begin{aligned}
 \sum_{e \in \Omega} \left(\int_{\Omega^{(e)}} \nabla^s \boldsymbol{\eta}^h : \tilde{\boldsymbol{\sigma}}_{n+1}^{(e)} d\Omega \right) &= \mathbf{f}_{n+1}^{ext} & a) \\
 \Delta \tilde{\boldsymbol{\sigma}}_{n+1}^{(e)} &= (1 - \tau^{(e)}) \underbrace{(\bar{\boldsymbol{\sigma}}_{n+1}^{(e)} - \bar{\boldsymbol{\sigma}}_n^{(e)})}_{\Delta \bar{\boldsymbol{\sigma}}_{n+1}^{(e)}} + \tau^{(e)} \underbrace{(\boldsymbol{\sigma}_{n+1}^{(e)} - \boldsymbol{\sigma}_n^{(e)})}_{\Delta \boldsymbol{\sigma}_{n+1}^{(e)}} & b) \\
 \tilde{\boldsymbol{\sigma}}_{n+1}^{(e)} &= \tilde{\boldsymbol{\sigma}}_n^{(e)} + \Delta \tilde{\boldsymbol{\sigma}}_{n+1}^{(e)} & c)
 \end{aligned} \tag{3.27}$$

where :

$$\begin{aligned}
 \tau^{(e)} &= 0.0 \quad \forall e \in \Omega_{mixed} \\
 \tau^{(e)} &= 1.0 \quad \forall e \in \Omega \setminus \Omega_{mixed} \quad \text{for general constitutive models} \\
 \tau^{(e)} &= 0.1 \quad \forall e \in \Omega \setminus \Omega_{mixed} \quad \text{for isochoric constitutive models}
 \end{aligned}$$

Box 3.5 Constant strain injection. Incremental strategy.

Even though equation (3.27)-a) is defined with the “total” stress tensor, it is important to remark, that this version of the formulation is equivalent to an incremental procedure. Notice that any modification on the $\tau^{(e)}$ value of the finite

¹⁸ When reduced integration is used, the computed element stiffness is generally softer than that obtained with full integration. The evolution of the mixed domain, causes continuous modifications on the number of elements to be fully or under-integrated which, therefore, produces sudden changes on total stiffness of the domain.

element, would only affect the increment $\Delta\tilde{\sigma}_{n+1}^{(e)}$, and not the total stress tensor, $\tilde{\sigma}_{n+1}^{(e)}$. The previous time step values, $\bar{\sigma}_n^{(e)}$, $\sigma_n^{(e)}$ and $\tilde{\sigma}_n^{(e)}$, should be stored in memory.

3.2.6. Matrix equations

In this Section the matrix equations of the problem are summarized (Voigt notation is used):

<p>Given the external force vector \mathbf{F}^{ext}, find \mathbf{u}^h such that</p> $\dot{\mathbf{F}}^{\text{int}} = \mathcal{A} \left(\int_{\Omega^{(e)}} \mathbf{B}^{(e)} \cdot \{\dot{\boldsymbol{\sigma}}\}^{(e)} d\Omega \right) = \dot{\mathbf{F}}^{\text{ext}}$ $\{\dot{\boldsymbol{\sigma}}\}^{(e)} = (1 - \tau^{(e)}) \{\dot{\bar{\boldsymbol{\sigma}}}\}^{(e)} + \tau^{(e)} \{\dot{\boldsymbol{\sigma}}\}^{(e)}$ $\{\dot{\bar{\boldsymbol{\sigma}}}\}^{(e)} = \dot{\boldsymbol{\Sigma}}(\{\overline{\nabla^S \dot{\mathbf{u}}}\}^{(e)}) ; \{\dot{\boldsymbol{\sigma}}\}^{(e)} = \dot{\boldsymbol{\Sigma}}(\{\nabla^S \dot{\mathbf{u}}\}^{(e)}) \quad (3.28)$ $\{\overline{\nabla^S \dot{\mathbf{u}}}\}^{(e)} = \bar{\mathbf{B}}^{(e)} \cdot \{\dot{\mathbf{u}}\}^{(e)} ; \{\nabla^S \dot{\mathbf{u}}\}^{(e)} = \mathbf{B}^{(e)} \cdot \{\dot{\mathbf{u}}\}^{(e)}$ $\mathbf{K}^{\text{tang}} = \mathcal{A} \left((1 - \tau) \int_{\Omega^{(e)}} \bar{\mathbf{B}}^{(e)T} \cdot \{\bar{\mathbf{C}}^{\text{ep}}\} \cdot \bar{\mathbf{B}}^{(e)} d\Omega + \tau \int_{\Omega^{(e)}} \mathbf{B}^{(e)T} \cdot \{\mathbf{C}^{\text{ep}}\} \cdot \mathbf{B}^{(e)} d\Omega \right) \quad (3.29)$ <p>where:</p> $\tau^{(e)} = 0.0 \quad \forall e \in \Omega_{\text{mixed}}$ $\tau^{(e)} = 1.0 \quad \forall e \in \Omega \setminus \Omega_{\text{mixed}} \quad \text{for general constitutive models}$ $\tau^{(e)} = 0.1 \quad \forall e \in \Omega \setminus \Omega_{\text{mixed}} \quad \text{for isochoric constitutive models}$
--

Box 3.6 Constant strain injection. Matrix equations.

where $\mathbf{B}^{(e)}$ is the standard deformation matrix, $\bar{\mathbf{B}}^{(e)}$ is the (constant) \mathbf{B} -matrix evaluated at the center of the finite element and \mathbf{K}^{tang} is the tangent stiffness matrix that stems from (3.28).

3.2.7. A second set of representative numerical examples - Numerical assessment of the injection procedure

To illustrate the differences and similitudes between the stabilized mixed formulation and the domain restricted mixed formulation (CSM injection), several numerical simulations are presented in the following.

3.2.7.1. Isotropic continuum damage model: double cantilever beam (DCB) with diagonal loads

Here, the example of Section 3.1.6.1 is re-examined. Now results obtained with the injection of the CSM (Box 3.6) are compared with those obtained with the stabilized mixed formulation (Box 3.2).

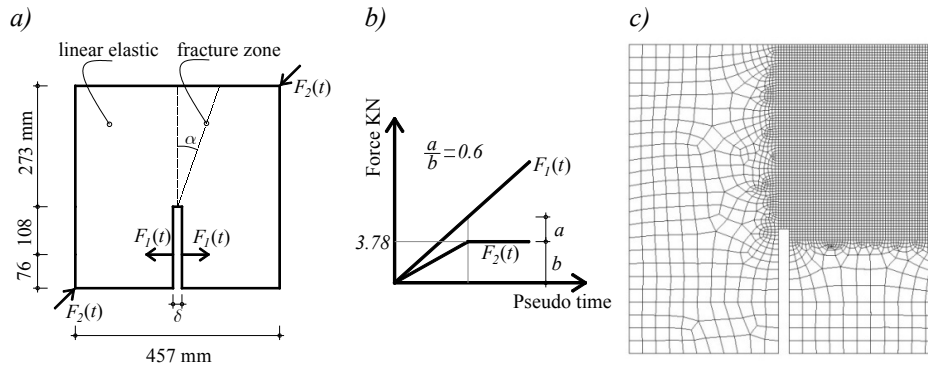


Figure 3.15 Double cantilever beam with diagonal load: a) geometrical data, b) loading data, c) finite element discretization.

For this non-homogeneous problem, where the strain localization band evolves along time, it is interesting to see the evolution of the mixed injection domain. In Figure 3.16 the mixed domain evolution is depicted in four representative sequential time steps.

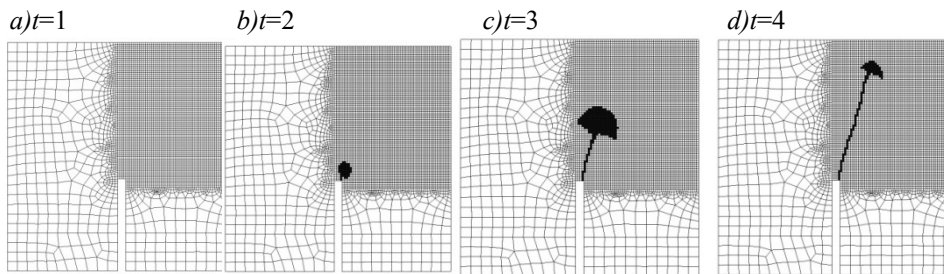


Figure 3.16 Evolution of the mixed injection domain (shaded zones) along different times of the analysis.

Notice that for initial stages of loading (Figure 3.16-a)) the body behaves elastically (thus no injection domain is observed) and the irreducible standard formulation is applied all over the body. For increasing loading, (Figure 3.16-b)), some elements enter in a nonlinear regime and material bifurcation is detected. Those elements are then considered to belong to the mixed domain Ω_{mixed} , and therefore the CSM is injected. For this example, the mixed domain is bulb-shaped, propagating at the tip of the advancing localization band. Soon later (Figure 3.16-c) and d)), most of the bifurcated elements behind the bulb unload (*i.e.* $\dot{\alpha} = 0$) returning

to an elastic condition so they leave the Ω_{mixed} domain, according to equation (3.20), except for an inclined band, behind the bulb, which remains in inelastic loading and corresponds to the strain localization band.

Figure 3.17-a) depicts the deformed mesh obtained with the CSM injection procedure, and Figure 3.17-b) the final crack simulated with it. In terms of propagation, the crack pattern is almost identical to the one obtained previously with the stabilized mixed formulation ($\tau = 0.1$) (see Figure 3.17-b) and Figure 3.3-c)). The principal difference is found on the force-displacement curves (see Figure 3.18). The CSM injection provides a somewhat more flexible response, that seems to be a consequence of a diminution of the stress locking in earlier stages of the non-linear damage process.

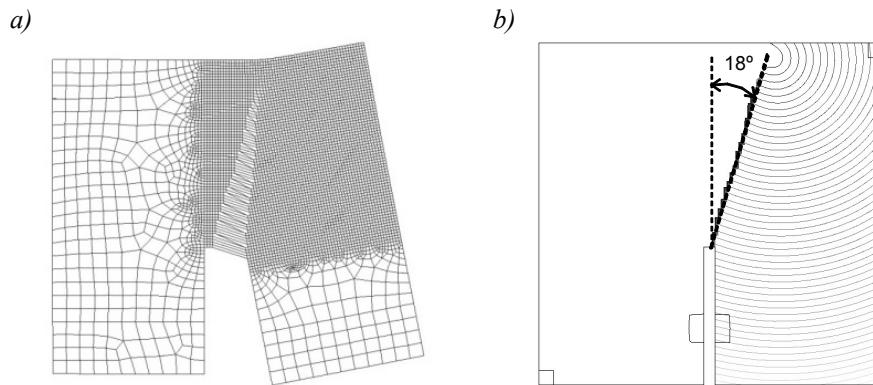


Figure 3.17 Results for the injection strategy: a) deformed mesh, b) Iso-displacement plots.

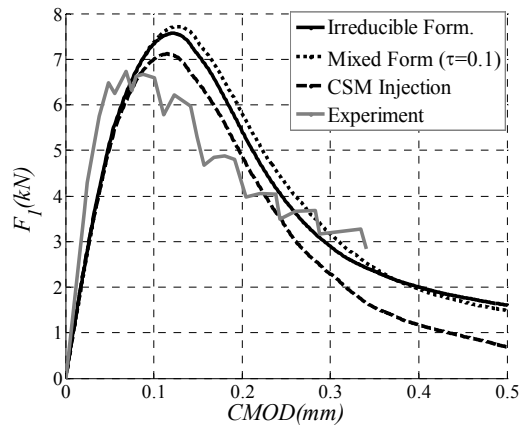


Figure 3.18 Curves, F_1 vs. Crack Mouth Opening Displacement (CMOD), obtained with different procedures.

3.2.7.2. Strip subjected to homogeneous uniaxial tensile stress state

Next, the examples introduced in Sections 2.4.4 and 3.1.6.2. are re-examined with the CSM injection methodology.

- **Rankine plasticity model**

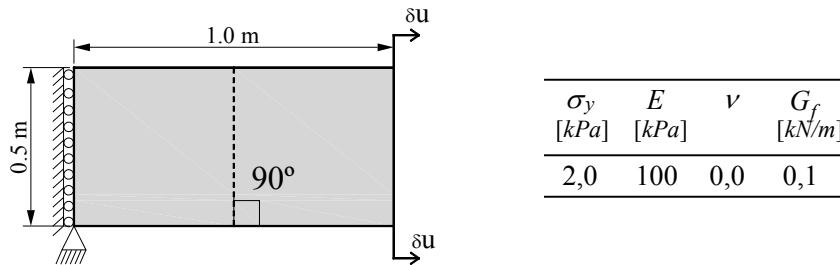


Figure 3.19 Strip stretching in the horizontal direction.

For this example, was also found that the localization pattern obtained with CSM injection coincides with the result obtained with the mixed method (see Figure 3.9). For that reason we do not reproduce here the iso-displacement contours. Moreover, from force-displacement curves (see Figure 3.20), it can be concluded that stress locking slightly decrease when the strain injection procedure is used.

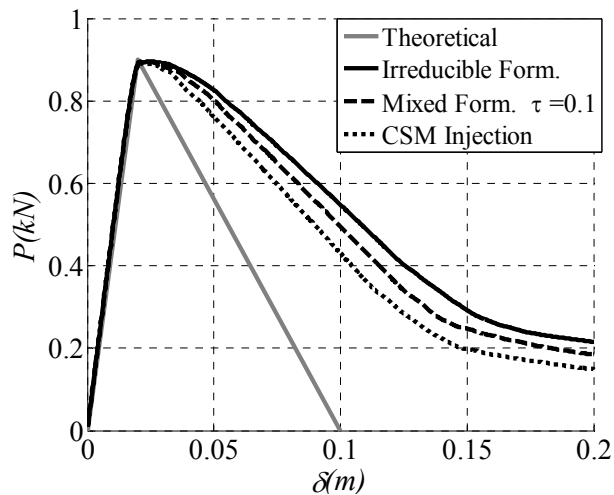


Figure 3.20 Force-displacement curves (for mesh c) – see Figure 3.9) obtained with different procedures.

- **J₂ plasticity model**

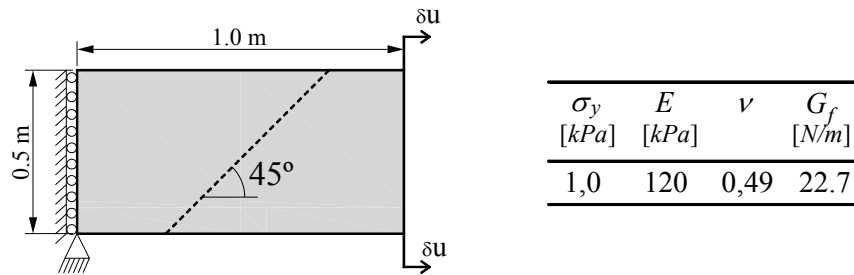


Figure 3.21 Strip stretching in the horizontal direction.

In Figure 3.22, the mixed domains for two different time steps are displayed. The first picture a), corresponds to earlier stages of loading when the body behaves elastically, thus no mixed domain is observed. The second picture, b), corresponds to the bifurcation point (identified in Figure 3.23 by point B). In this plot two different branches related to the theoretical solutions of the problem ($\pm 45^\circ$) are observed. As the loading process progresses, due to the shape of the numerical perturbation, strain localization collapses in one of the branches, as it is shown in picture c).

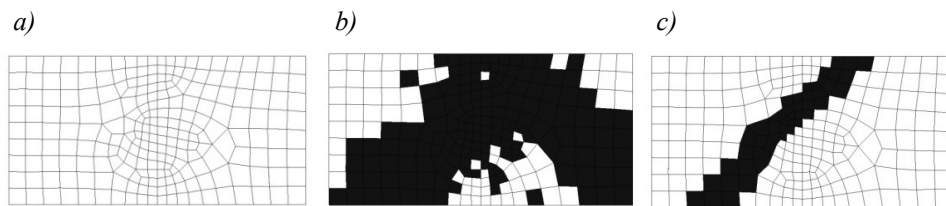


Figure 3.22 Evolution of the mixed injection domain (shaded zones) during different stages of the analysis.

In Section 3.1.6.2 (for the J_2 plasticity model), it was mentioned that, when using the stabilized mixed formulation ($\tau = 0.0001$), “*despite, the instabilities on the displacement field, the solution in terms of the force-displacement curve is quite good*”. It is shown in the load vs. displacement plots of Figure 3.23, that using the injection strategy, the numerical solution in terms of force-displacement curve is similar to the mixed procedure with $\tau = 0.0001$; however, the solution in terms of the displacement field is now fully stable, *i.e.* no hourglass modes develop (see Figure 3.24).

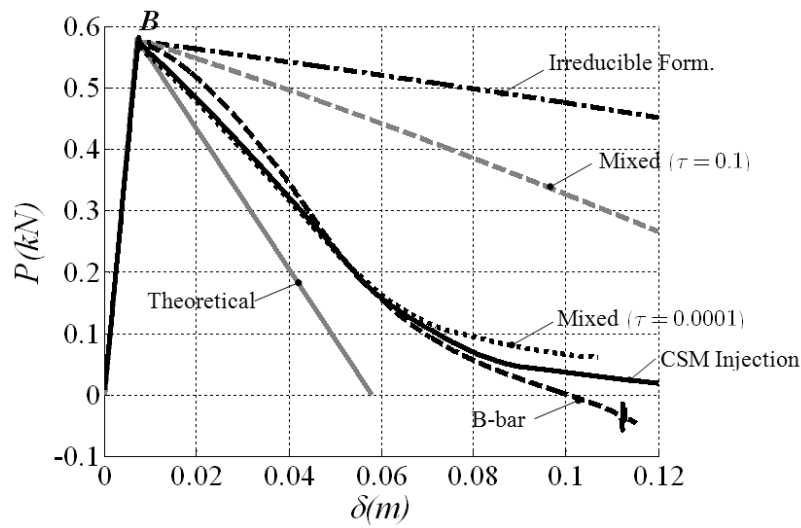


Figure 3.23 Force-displacement curves obtained with different procedures.

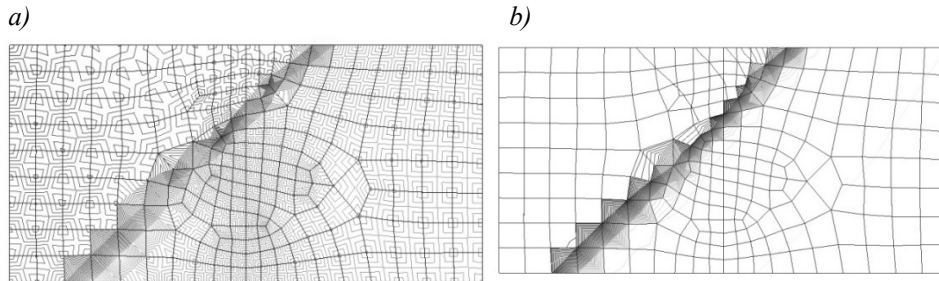


Figure 3.24 Iso-displacement plots a) Mixed form ($\tau = 0.0001$), b) CSM Injection.

It is important to notice that all the previous results were obtained with an “incremental” implementation version of the injection procedure. Here, in this practical example, it is remarked the importance of this issue. In Figure 3.25 results obtained with the “incremental” formulation Box 3.5 are compared with those obtained with the “total” formulation Box 3.4.

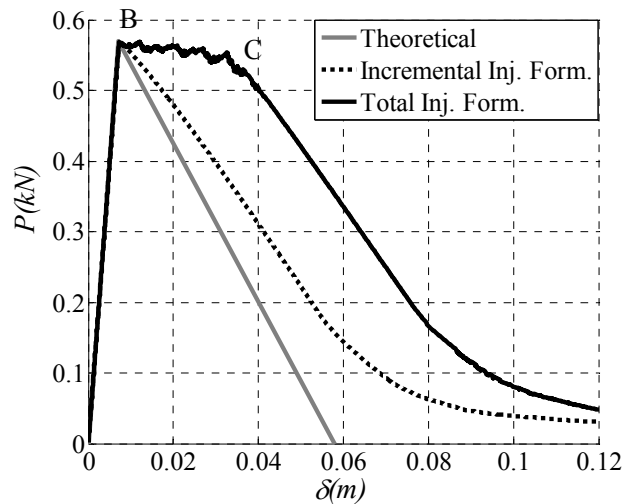


Figure 3.25 Force-displacement curves. Comparison of results using the incremental and total versions of the injection formulation.

When a “total” formulation is used, oscillations are observable after crossing the bifurcation point B, since it is at this point that the mixed domain changes quickly (see Figure 3.22). Moreover, after crossing the point C, the localization band is already formed, thus the mixed domain does not change anymore and the smooth response of the plot is recovered. This comment is valid for more general examples and constitutive models.

3.3. Summary and conclusions

In this Chapter it was shown that, restricting the mixed formulation to a part of the domain (*i.e.* using the strain injection procedure), the obtained results are similar or better than those provided by the stabilized mixed formulation, with the advantage that the injected method does not depend on a stabilization parameter defined by the user, and the danger of instabilities is avoided.

The improved behavior of the reduced integration methods, to face strain localization problem, has been also previously reported by other authors. In [Steinmann and Willam 1991a] the authors state that “*The reduced one point integration strategy is equally capable in reproducing weak localization, however at the cost of the rank-two deficiency of the eigenspectrum. Stabilization would eliminate not only the hour-glass modes, but also destroy its excellent localization properties*”. The authors also state that controlling the instabilities on the structural, rather than on the element level (by stabilization), would make the reduced

integration element readily for application to localization problems. The injection strategy falls inside this definition, since the use of the standard formulation in the larger part of the domain (outside the localization band) prevents the hourglass modes to propagate at the structural level. Additionally, the reduced integration points have also advantages in terms of accuracy, since stresses are there better accurately predicted than at any other point of the finite element (optimal stress points, see Remark 3.2.1.1).

In other cases, authors are reluctant to use reduced integration techniques for non-linear problems. For example, in [Crisfield 1986] the author advert against “*the dangers of under-integration*”, nevertheless in those earlier works, no stabilization or any method to prevent hourglass instabilities were used.

Moreover, was shown at Section 3.2.3 that, the combination of the constant strain injection with the mixed stabilized element (used as underlying element), gives generality to the formulation, since problems involving volumetric locking can also be handled. Therefore, the methodology can be also regarded as an interesting alternative to the B-bar methods, when nonlinear isochoric constitutive models (*e.g.* J_2 plasticity) are used for strain localization analysis.

However, despite the improvements, reported in the preceding Sections in terms of propagation (mesh bias independence) and in terms of stress locking, it is observed that results are still not entirely satisfactory. The obtained solutions still suffer from stress locking, as it is shown in Figure 3.20 and Figure 3.23 by the extra dissipation and residual loads. Additionally, it is seen in Figure 3.22 that the localization band encompasses more than one element. This indicates that constant strain kinematics is not sufficiently rich to describe the strain localization in an one-element band, in other words, the finite element kinematics is not able to describe a weak discontinuity.

In next Chapter, inspired by the Strong Discontinuity Approach [Oliver 1996a], this problem is analyzed in detail.

Chapter 4

Strain localization, strong discontinuities and material fracture

In Chapter 3, a methodology aiming at improving the capabilities of the classical strain localization methods for material fracture modeling was proposed. This Chapter focuses on the quality of solutions obtained by means of those methods. That is, the idea here is to discern whether the finite element solutions of material failure problems based on strain localization techniques, using standard continuum stress-strain constitutive models equipped with strain softening, have physical sense as solutions of de-cohesive fracture mechanics problems [Hillerborg 1985].

The methodology to be proposed, takes into consideration the well-established links between the continuum strong discontinuity approach and cohesive fracture [Oliver, Huespe et al. 2002], *i.e.* the strong discontinuity approach represents here an intermediate link between strain localization and fractures mechanics. Thus, since the link between the strong discontinuity approach and fracture mechanics is already well-established, attention will be focused on the connections between strain localization methods and the strong discontinuity approach, such that, the ability of the standard finite element solutions to represent discrete fractures will be then analyzed in the sense that the solution in terms of the displacement field might be interpreted as a regularized strong discontinuity embedded into the localization band. To assess this equivalence, several objective indicators will be proposed.

4.1. The continuum strong discontinuity approach

The continuum strong discontinuity approach was introduced in the nineties [Simo, Oliver et al. 1993; Oliver 1996a]. Its main ingredient was the reformulation of the kinematics (Section 4.1.1), admitting discontinuous displacement fields¹⁹ within a continuum framework. Soon it was recognized that strong discontinuities can only be successfully induced, if the stress states fulfill certain restrictions – the so called strong discontinuity conditions [Oliver et al. 1999]. A variable bandwidth model was introduced in order to induce such stress state prior to the introduction of a strong discontinuity inside the localization band. Subsequently, in the beginnings of 2000's, the methodology was further explored [Oliver 2000; Oliver, Huespe et al. 2002; Oliver and Huespe 2004b]. In those contributions, a clear link between the methods based on continuum mechanics (using stress-strain $\sigma - \varepsilon$ constitutive models) with those based on cohesive fracture techniques [Dvorkin et al. 1990; Lofti and Shing 1995] typically based on traction-separation $\mathcal{T}-[\mathbf{u}]$ models embedded into the localization band, was established. From this link, some significant theoretical points were clarified:

- It was shown the consistence between continuum stress-strain constitutive models and traction separation ones, since the introduction of the strong discontinuity kinematics in the former, automatically induces the later at the discontinuity path. That is, the traction-separation $\mathcal{T}-[\mathbf{u}]$ model is a projection of the original continuum $\sigma - \varepsilon$ model (which lives in a 3D domain Ω) onto the 2D domain of the discontinuity interface \mathcal{S} .
- The re-interpretation of the softening law in a distributional sense (ensuring bounded stresses for even unbounded strains) provides a clear physical interpretation of the softening modulus, since the discrete softening modulus is straightforwardly related to the fracture energy, establishing a direct connection between the material parameters of both models.
- Moreover, the re-interpretation of the softening law in a distributional sense also makes possible dissipation to occur in a region of zero measure, what helped to clarify the classic paradoxical unacceptable result of the strain localization methods, where, localization bands of zero thickness imply brittle fracture progressing with null energy dissipation (see Chapter 2).
- The concept of characteristic length²⁰, *i.e.* the constant width of the strain localization band, that do not meet an equivalent parameter on the cohesive

¹⁹ At the discontinuity surface, the displacement field is discontinuous (a jump appear) and strains are therefore unbounded.

²⁰ The strain localization width in the ambit of the smearing crack models, has been claimed to be a material property [Bazant 1983], representing *e.g.* the width of “bands of

models, loses physical sense at the strong discontinuity regime, since this length play no role further than the Dirac's regularization, that is limited by the machine precision (see Section 4.1.2). Nevertheless, prior to the introduction of the strong discontinuity, the bandwidth evolution law²¹, rather than a useful numerical technical to induce strong discontinuities, can be understood as a physical length [Oliver and Huespe 2004b] that characterizes the fracture process zone [Bazant and Planas 1998] (see Chapter 2) for different kind of materials (this issue is not explored in this work).

Taking in mind the previously mentioned links between the continuum strong discontinuity approach and cohesive fracture, in the evaluation set proposed here, the ability of strain localization solutions to represent real, physical meaningful, fracture mechanics solutions, it is considered as good as its ability to be interpreted as a strong discontinuity embedded into the localization band. Remark, that once a general localized strain field matches a strong discontinuity all the theoretical links between the strong discontinuity approach and the cohesive fracture mechanics apply to that solution.

On the other hand, it is known that standard finite element solutions suffer from numerical flaws (stress locking and mesh bias dependence – see Sections 2.4.4 and 2.4.5) and hence, in general, these solutions would fail to represent strong discontinuities, or they are representative just for a very specific set of cases, (*e.g.* when the finite element mesh is properly aligned with the fracture to be modeled). Nevertheless, by relating the results of the strain localization models with the ones obtained by the strong discontinuity approach, indicators to access the quality of the former models may be derived. This subject will be developed in the following Sections.

4.1.1. Strong discontinuity kinematics

Let us consider the continuum body Ω (see Figure 4.1), divided in two parts Ω^+ and Ω^- by a strong discontinuity \mathcal{S} . Across the discontinuity, the displacement field $\mathbf{u}(\mathbf{x})$ experiences a jump $\llbracket \mathbf{u} \rrbracket = \mathbf{u}|_{\mathbf{x} \in \Omega^+ \cap \mathcal{S}} - \mathbf{u}|_{\mathbf{x} \in \Omega^- \cap \mathcal{S}}$.

micro-cracks" in brittle materials. On the other hand, in the ambit of the strong discontinuity approach, this parameter loses physical sense.

²¹ The bandwidth evolution law or variable bandwidth model, governs the transition between the weak and strong discontinuity regime.

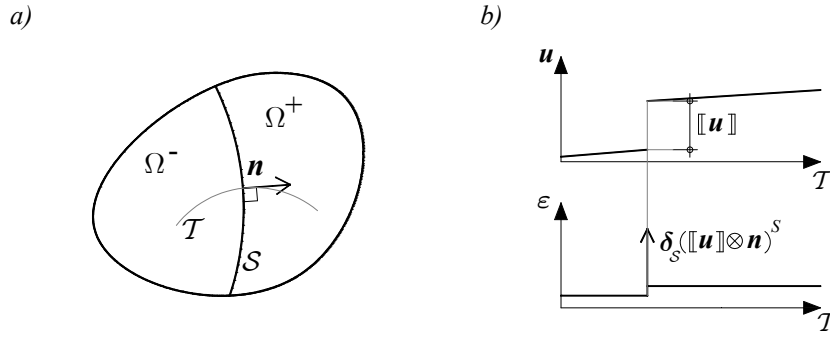


Figure 4.1 a) Continuum body with strong discontinuity, b) Strong discontinuity kinematics.

where \mathbf{n} is the unit vector orthogonal to \mathcal{S} . The rate of the displacement field may be mathematically described as [Oliver and Huespe 2004b]:

$$\dot{\mathbf{u}} = \dot{\hat{\mathbf{u}}} + \mathcal{H}_{\mathcal{S}} [[\dot{\mathbf{u}}]], \quad (4.1)$$

where $\dot{\hat{\mathbf{u}}}$ stands for the smooth part of the displacement field and $\mathcal{H}_{\mathcal{S}}$ stands for the Heaviside (step) function ($\mathcal{H}_{\mathcal{S}}(\mathbf{x}) = 0 \forall \mathbf{x} \in \Omega^-$ and $\mathcal{H}_{\mathcal{S}}(\mathbf{x}) = 1 \forall \mathbf{x} \in \Omega^+$). The corresponding compatible strain field (strong discontinuity kinematics) reads:

$$\dot{\epsilon} = \nabla^S \dot{\mathbf{u}} = \underbrace{\nabla^S \dot{\hat{\mathbf{u}}} + \mathcal{H}_{\mathcal{S}} (\nabla^S [[\dot{\mathbf{u}}]])}_{\bar{\epsilon} \text{ (regular)}} + \underbrace{\delta_S ([[\dot{\mathbf{u}}] \otimes \mathbf{n})^S}_{\text{(singular)}}, \quad (4.2)$$

where δ_S is the Dirac's distribution, shifted to \mathcal{S} fulfilling [Stakgold 1998]:

$$\int_{\Omega^*} \varphi(\mathbf{x}) \delta_S(\mathbf{x}) d\Omega = \int_{\mathcal{S}^*} \varphi(\mathbf{x}) d\mathcal{S}, \quad (4.3)$$

for any test function $\varphi(\mathbf{x})$ sufficiently regular and for any portion Ω^* of Ω ($\Omega^* \subset \Omega$) containing a portion \mathcal{S}^* of \mathcal{S} ($\mathcal{S}^* \subset \mathcal{S}$ and $\mathcal{S}^* \equiv \Omega^* \cap \mathcal{S}$, see Figure 4.2).

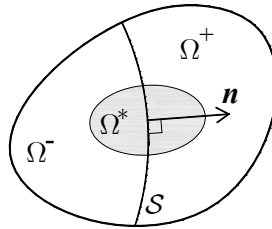


Figure 4.2 Continuum body a with strong discontinuity.

Assuming the required regularity for the term $([[\dot{\mathbf{u}}] \otimes \mathbf{n})^S$, the specific application of equation (4.3) to the singular term of equation (4.2) reads:

$$\int_{\Omega^*} \delta_S ([[\dot{\mathbf{u}}] \otimes \mathbf{n})^S d\Omega = \int_{\mathcal{S}^*} ([[\dot{\mathbf{u}}] \otimes \mathbf{n})^S d\mathcal{S}. \quad (4.4)$$

4.1.2. Regularized strong discontinuities kinematics

Let us now consider the discontinuity band Ω_{loc} , of very small bandwidth k (the regularization parameter) containing \mathcal{S} , as shown in Figure 4.3.

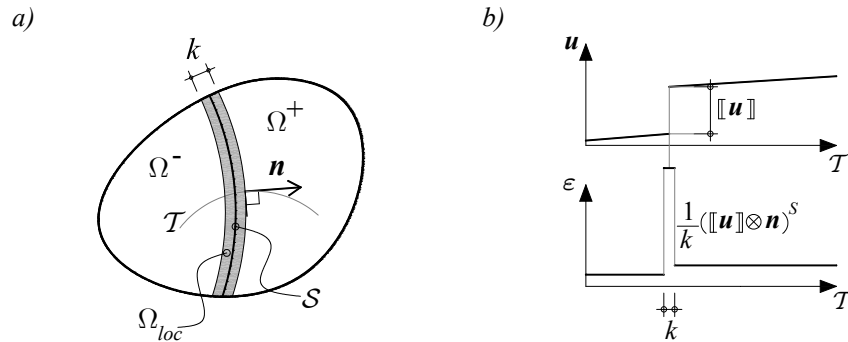


Figure 4.3 a) Continuum body with discontinuity band b) Regularized strong discontinuity kinematics.

The Dirac's function can be regularized over Ω_{loc} as: $\delta_{\mathcal{S}} \rightarrow \mu_{\Omega_{loc}}/k$, where $\mu_{\Omega_{loc}}$ is a collocation function on Ω_{loc} such that:

$$\mu_{\Omega_{loc}}(\mathbf{x}) = \begin{cases} 1 & \forall \mathbf{x} \in \Omega_{loc} \\ 0 & \forall \mathbf{x} \in \Omega \setminus \Omega_{loc} \end{cases}. \quad (4.5)$$

Thus the regularized version of equation (4.2) reads:

$$\dot{\epsilon} = \nabla^S \dot{\mathbf{u}} = \dot{\epsilon} + \frac{\mu_{\Omega_{loc}}}{k} ([\dot{\mathbf{u}}] \otimes \mathbf{n})^S, \quad (4.6)$$

where the term $1/k$ in equation (4.6) may be interpreted as an intensification factor of the strains in Ω_{loc} , see Figure 4.4.

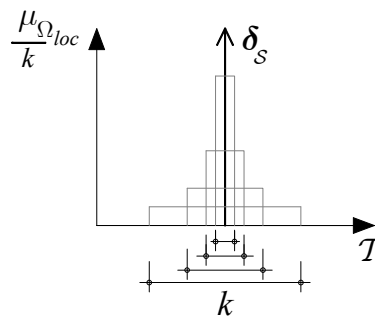


Figure 4.4 Regularized Dirac's delta function.

As $k \rightarrow 0$ then $\Omega_{loc} \rightarrow \mathcal{S}$ and $\mu_{\Omega_{loc}}/k \rightarrow \delta_{\mathcal{S}}$, in the sense of distributions; *i.e.*:

$$\lim_{k \rightarrow 0} \int_{\Omega^*} \varphi(\mathbf{x}) \frac{\mu_{\Omega_{loc}}(\mathbf{x})}{k} d\Omega = \int_{\Omega^*} \varphi(\mathbf{x}) \delta_{\mathcal{S}}(\mathbf{x}) d\Omega = \int_{\mathcal{S}^*} \varphi(\mathbf{x}) d\mathcal{S}. \quad (4.7)$$

4.2. Strain localization and strong discontinuities

So far, in Chapters 2 and 3, for material fracture modeling, classical strain localization methods were used and no strong discontinuity enrichment was introduced. Here, we intend to relate the obtained results with the strong discontinuity approach in order to assess the quality of those results.

Let us now consider a general strain field $\dot{\epsilon}_{loc}$ exhibiting strain localization in the band Ω_{loc} . For this general case, the strain field structure is assumed as follows:

$$\dot{\epsilon}_{loc} = \nabla^S \dot{\mathbf{u}} = \dot{\bar{\epsilon}} + \underbrace{\frac{\mu_{\Omega_{loc}}}{k} \dot{\mathbf{L}}}_{\text{localized component}}, \quad (4.8)$$

where $\dot{\epsilon}_{loc}$ is subdivided in a nonlocalized term, $\dot{\bar{\epsilon}}$, plus a localized component which intensity is proportional to the inverse of the bandwidth k .

The fundamental point is if a general strain field, as the one expressed by (4.8), may be representative of a strong discontinuity and what are the conditions that $\dot{\mathbf{L}}$ must fulfill in order to accomplish this equivalence.

Comparing expressions (4.8) and (4.6), and having in mind (4.7), for they to be equivalent the following equality has to be fulfilled:

$$\lim_{k \rightarrow 0} \int_{\Omega^*} \frac{\mu_{\Omega_{loc}}}{k} \dot{\mathbf{L}} d\Omega = \lim_{k \rightarrow 0} \int_{\Omega^*} \frac{\mu_{\Omega_{loc}}}{k} ([\dot{\mathbf{u}}] \otimes \mathbf{n})^S d\Omega. \quad (4.9)$$

Taking a sufficiently small domain $\Delta\Omega^* \equiv \Omega^*$ such that the corresponding portion of the discontinuity path $\Delta\mathcal{S} \equiv \Delta\Omega^* \cap \mathcal{S}$ is sufficiently small for \mathbf{n} to be considered constant, equation (4.9) can be rewritten as:

$$\lim_{k \rightarrow 0} \int_{\Delta\Omega^*} \frac{\mu_{\Omega_{loc}}}{k} \dot{\mathbf{L}} d\Omega = \lim_{k \rightarrow 0} \left(\int_{\Delta\Omega^*} \frac{\mu_{\Omega_{loc}}}{k} [\dot{\mathbf{u}}] d\Omega \otimes \mathbf{n} \right)^S. \quad (4.10)$$

Considering for all points of \mathcal{S} , the local orthonormal basis $\{\hat{\mathbf{e}}_1 = \mathbf{n}, \hat{\mathbf{e}}_2, \hat{\mathbf{e}}_3\}$, the components of the tensorial entities $[\dot{\mathbf{u}}]$, $([\dot{\mathbf{u}}] \otimes \mathbf{n})^S$ and $\dot{\mathbf{L}}$ are:

$$[\dot{\mathbf{u}}] = \begin{bmatrix} [\dot{\mathbf{u}}]_1 \\ [\dot{\mathbf{u}}]_2 \\ [\dot{\mathbf{u}}]_3 \end{bmatrix}; ([\dot{\mathbf{u}}] \otimes \mathbf{n})^S = \begin{bmatrix} [\dot{\mathbf{u}}]_1 & \frac{1}{2}[\dot{\mathbf{u}}]_2 & \frac{1}{2}[\dot{\mathbf{u}}]_3 \\ \frac{1}{2}[\dot{\mathbf{u}}]_2 & 0 & 0 \\ \frac{1}{2}[\dot{\mathbf{u}}]_3 & 0 & 0 \end{bmatrix}; \dot{\mathbf{L}} = \begin{bmatrix} \dot{L}_{11} & \dot{L}_{12} & \dot{L}_{13} \\ \dot{L}_{12} & \dot{L}_{22} & \dot{L}_{23} \\ \dot{L}_{13} & \dot{L}_{23} & \dot{L}_{33} \end{bmatrix}. \quad (4.11)$$

Thus, for the equivalence expressed by (4.10), the following requirements on $\dot{\mathbf{L}}$ appear:

$$\begin{aligned} \lim_{k \rightarrow 0} \int_{\Delta\Omega^*} \frac{\mu_{\Omega_{loc}}}{k} \dot{L}_{22} d\Omega &= \lim_{k \rightarrow 0} \left[\int_{\Delta\Omega^*} \frac{\mu_{\Omega_{loc}}}{k} [\dot{\mathbf{u}}] d\Omega \otimes \mathbf{n} \right]_{22}^S = 0, \\ \lim_{k \rightarrow 0} \int_{\Delta\Omega^*} \frac{\mu_{\Omega_{loc}}}{k} \dot{L}_{33} d\Omega &= \lim_{k \rightarrow 0} \left[\int_{\Delta\Omega^*} \frac{\mu_{\Omega_{loc}}}{k} [\dot{\mathbf{u}}] d\Omega \otimes \mathbf{n} \right]_{33}^S = 0, \\ \lim_{k \rightarrow 0} \int_{\Delta\Omega^*} \frac{\mu_{\Omega_{loc}}}{k} \dot{L}_{23} d\Omega &= \lim_{k \rightarrow 0} \left[\int_{\Delta\Omega^*} \frac{\mu_{\Omega_{loc}}}{k} [\dot{\mathbf{u}}] d\Omega \otimes \mathbf{n} \right]_{23}^S = 0, \end{aligned} \quad (4.12)$$

which can be formalized to:

$$\lim_{k \rightarrow 0} \int_{\Delta\Omega^*} \frac{\mu_{\Omega_{loc}}}{k} \dot{\mathbf{L}}_M d\Omega = 0 \quad \forall \Delta\Omega^* \subset \Omega, \quad (4.13)$$

with:

$$\begin{aligned} \dot{\mathbf{L}}_M &= \mathbb{P}_M : \dot{\mathbf{L}} = \dot{L}_{22} \hat{\mathbf{e}}_2 \otimes \hat{\mathbf{e}}_2 + \dot{L}_{33} \hat{\mathbf{e}}_3 \otimes \hat{\mathbf{e}}_3 + \dot{L}_{23} \hat{\mathbf{e}}_2 \otimes \hat{\mathbf{e}}_3 + \dot{L}_{32} \hat{\mathbf{e}}_3 \otimes \hat{\mathbf{e}}_2, \\ \mathbb{P}_M &= \hat{\mathbf{e}}_2 \otimes \hat{\mathbf{e}}_2 \otimes \hat{\mathbf{e}}_2 \otimes \hat{\mathbf{e}}_2 + \hat{\mathbf{e}}_3 \otimes \hat{\mathbf{e}}_3 \otimes \hat{\mathbf{e}}_3 \otimes \hat{\mathbf{e}}_3 + \\ &\quad + \hat{\mathbf{e}}_2 \otimes \hat{\mathbf{e}}_3 \otimes \hat{\mathbf{e}}_2 \otimes \hat{\mathbf{e}}_3 + \hat{\mathbf{e}}_3 \otimes \hat{\mathbf{e}}_2 \otimes \hat{\mathbf{e}}_3 \otimes \hat{\mathbf{e}}_2, \end{aligned} \quad (4.14)$$

where $\dot{\mathbf{L}}_M$ will be termed the *strain localization mismatch*, i.e. the part of $\dot{\mathbf{L}}$ not matching the strong discontinuity format $([\dot{\mathbf{u}}] \otimes \mathbf{n})^S$; and \mathbb{P}_M stands for the fourth order *strain localization mismatch operator*.

Let us assume, as it is usually done in computational material failure, that after the localized part of the strain $(\mu_{\Omega_{loc}}/k)\dot{\mathbf{L}}$ corresponds to the inelastic strain, $\dot{\boldsymbol{\varepsilon}}^{inel}$, whereas the remaining part of the strain is its elastic counterpart $\dot{\boldsymbol{\varepsilon}}^{el}$:

$$\begin{aligned} \dot{\boldsymbol{\varepsilon}}^{el} &= \dot{\boldsymbol{\varepsilon}} = (\mathbb{C}^{unl})^{-1} : \dot{\boldsymbol{\sigma}} \quad ; \quad \dot{\boldsymbol{\varepsilon}}^{inel} = \frac{\mu_{\Omega_{loc}}}{k} \dot{\mathbf{L}}, \\ \dot{\boldsymbol{\varepsilon}}_{loc} &= \dot{\boldsymbol{\varepsilon}} + \frac{\mu_{\Omega_{loc}}}{k} \dot{\mathbf{L}} = \dot{\boldsymbol{\varepsilon}}^{el} + \dot{\boldsymbol{\varepsilon}}^{inel}, \end{aligned} \quad (4.15)$$

where \mathbb{C}^{unl} is the unloading constitutive operator. Under the previous assumptions, restrictions (4.13) read:

$$\lim_{k \rightarrow 0} \int_{\Delta\Omega^*} \dot{\boldsymbol{\varepsilon}}_M^{inel} d\Omega = 0 \quad \forall \Delta\Omega^* \subset \Omega, \quad (4.16)$$

where:

$$\dot{\epsilon}_M^{inel} = \frac{\mu_{\Omega_{loc}}}{k} \dot{\mathbf{L}}_M = \frac{\mu_{\Omega_{loc}}}{k} \mathbb{P}_M : \dot{\mathbf{L}} = \mathbb{P}_M : \dot{\epsilon}^{inel}. \quad (4.17)$$

Expression (4.16) establishes a restriction on the inelastic strain $\dot{\epsilon}^{inel}(\boldsymbol{\sigma}, \dot{\boldsymbol{\sigma}})$ to be representative of a strong discontinuity. Here we emphasize the dependence of the inelastic strain $\dot{\epsilon}^{inel}(\boldsymbol{\sigma}, \dot{\boldsymbol{\sigma}})$ on the stress state $\boldsymbol{\sigma}$ and on the stress evolution $\dot{\boldsymbol{\sigma}}$. Note that conditions of equation (4.16) have already been identified in the context of the strong discontinuity approach, constituting the so-called strong discontinuity conditions [Oliver, Cervera et al. 1999].

4.3. Strain localization mismatch indicators

When the localized component $\dot{\epsilon}^{inel}$, of a general strain field $\dot{\epsilon}_{loc}$, obtained via classical strain localization methods, verifies conditions (4.16), it is said that $\dot{\epsilon}_{loc}$ matches a strong discontinuity deformation mode. However, in general, these restrictions are not fulfilled, or they do so for very specific cases, *e.g.* when the finite element mesh is properly aligned with the fracture propagation direction. This fact is related to the traditional flaws observed with classical strain localization methods (stress locking and mesh bias dependence exposed in Sections 2.4.4 and 2.4.5). Moreover, expression (4.16) suggests the development of indicators that could be used to evaluate the quality of the strain localization patterns obtained in the finite element computations.

For this purpose, let us consider a body discretized through a finite element mesh, where a set of elements defining the localization band or localization domain Ω_{loc} (see Section 4.4) is identified (Figure 4.5).

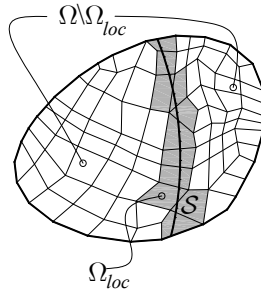


Figure 4.5 Discretized body with localization band.

The discrete version of (4.16) is obtained by considering $\Delta\Omega^* \equiv \Omega^{(e)} \subset \Omega_{loc}$, and $\ell_e = k$, being ℓ_e the typical element size:

$$\lim_{\ell_e \rightarrow 0} \int_{\Omega^{(e)}} (\dot{\epsilon}_M^{inel})^h d\Omega = 0 \quad \forall \Omega^{(e)} \in \Omega_{loc}, \quad (4.18)$$

where h stands for the finite element approximation. Assuming a small enough element size $\ell_e \ll L$ (L standing for the typical dimension of Ω) equation (4.18) may be established as:

$$\int_{\Omega^{(e)}} (\dot{\epsilon}_M^{inel})^h d\Omega \simeq 0 \quad \forall \Omega^{(e)} \in \Omega_{loc}, \quad (4.19)$$

Finally, equation (4.19) can be integrated along time, from the bifurcation time t_B (onset of localization), to the current time, t , as:

$$\int_{\Omega^{(e)}} \left(\int_{t_B}^t (\dot{\epsilon}_M^{inel})^h dt \right) d\Omega \simeq 0 \quad \forall \Omega^{(e)} \in \Omega_{loc}. \quad (4.20)$$

4.3.1. Local mismatch indicator

Motivated by equation (4.19), a first indicator: the *ratio of the inelastic strain mismatch and the inelastic strain tensor* is proposed (in elemental averages and measured in L^2 norms):

$$i^{(e)}(t) = \frac{\frac{1}{\text{meas}(\Omega^{(e)})} \left\| \int_{\Omega^{(e)}} (\dot{\epsilon}_M^{inel})^h d\Omega \right\|}{\frac{1}{\text{meas}(\Omega^{(e)})} \left\| \int_{\Omega^{(e)}} (\dot{\epsilon}^{inel})^h d\Omega \right\|}. \quad (4.21)$$

Simplifying equation (4.21), and setting the indicator $i^{(e)}$ to zero for those elements outside the localization domain, the indicator of the strain localization mismatch, at a given time t , and for the specific element $\Omega^{(e)}$, reads:

$$i^{(e)}(t) = \begin{cases} \frac{\left\| \int_{\Omega^{(e)}} (\dot{\epsilon}_M^{inel})^h d\Omega \right\|}{\left\| \int_{\Omega^{(e)}} (\dot{\epsilon}^{inel})^h d\Omega \right\|} & \text{for } \Omega^{(e)} \in \Omega_{loc} \\ 0 & \text{for } \Omega^{(e)} \in \Omega / \Omega_{loc} \end{cases}. \quad (4.22)$$

Inspection of the previous equation reveals that the proposed indicator has the following properties:

- For perfectly localized elements (fully representing a strong discontinuity), $i^{(e)}$ is null. In fact, for those elements, the inelastic strain $\dot{\epsilon}^{inel}$ fulfills condition (4.19), which substituted in equation (4.22) returns a null value of the indicator
- For imperfectly localized elements in Ω_{loc} , the indicator returns a value $0 < i^{(e)} \leq 1$. The larger is the value of $i^{(e)}$ the larger is the localization mismatch of the element. Therefore the elemental map $i^{(e)}$ (in the interval

$[0,1]$) across the finite element discretization provides a spatial description of the quality of the incremental strain localization (understood as its match with a regularized strong discontinuity). The examples presented in Section 4.5 illustrate this point.

- For elements outside the localization domain, the index is null by definition.
- If the indicator is computed for the case of embedded strong discontinuities [Oliver and Huespe 2004b], it will return a null value since, again, the inelastic strain fulfills, by construction, equation (4.19).

4.3.2. Global Mismatch indicators

The local indicator in equation (4.22) provides a spatial map of the distribution, at every time of the analysis, of the localized strain mismatch over the finite element mesh. As an alternative to the indicator $i^{(e)}$, the following global incremental strain localization mismatch indicator is proposed:

$$I_1(t) = \begin{cases} \frac{\sum_{\Omega^{(e)} \in \Omega_{loc}} \left\| \int_{\Omega^{(e)}} (\dot{\epsilon}_M^{inel})^h d\Omega \right\|}{\sum_{\Omega^{(e)} \in \Omega_{loc}} \left\| \int_{\Omega^{(e)}} (\dot{\epsilon}^{inel})^h d\Omega \right\|} & \text{for } \Omega^{(e)} \in \Omega_{loc} \\ 0 & \text{for } \Omega^{(e)} \in \Omega / \Omega_{loc} \end{cases} \quad (4.23)$$

Notice that $I_1(t) \in [0,1]$ is an extension of the local indicator $i^{(e)}(t)$, from the local domain, $\Omega^{(e)}$, to the global domain Ω_{loc} . It exhibits the following properties:

- The indicator is objective with the size of the bandwidth in the sense that, for a given domain Ω and discontinuity path \mathcal{S} , the result at the asymptotic stage is independent of the localization bandwidth k . In fact, assuming a general (not necessarily perfect) localized strain field $\dot{\epsilon}_{loc}$ we can write the entities in equation (4.23) as:

$$\begin{aligned} \lim_{k \rightarrow 0} \int_{\Omega^{(e)}} (\dot{\epsilon}_M^{inel})^h d\Omega &= \lim_{k \rightarrow 0} \int_{\Omega^{(e)}} \frac{\mu_{\Omega_{loc}}}{k} \dot{\mathbf{I}}_M^h d\Omega = \int_{\mathcal{S}^{(e)}} \dot{\mathbf{I}}_M^h d\mathcal{S}, \\ \lim_{k \rightarrow 0} \int_{\Omega^{(e)}} (\dot{\epsilon}^{inel})^h d\Omega &= \lim_{k \rightarrow 0} \int_{\Omega^{(e)}} \frac{\mu_{\Omega_{loc}}}{k} \dot{\mathbf{I}}^h d\Omega = \int_{\mathcal{S}^{(e)}} \dot{\mathbf{I}}^h d\mathcal{S}, \end{aligned} \quad (4.24)$$

where, the result of (4.7), the assumptions of (4.15) have been used, and $\mathcal{S}^{(e)} = \Omega^{(e)} \cap \mathcal{S}$ stands for the portion of the discontinuity path in element (e) . Substitution of equations (4.24) into (4.23) yields:

$$\lim_{k \rightarrow 0} I_1(t) = \frac{\sum_{\Omega^{(e)} \in \Omega_{loc}} \left\| \int_{S^{(e)}} \dot{\mathbf{l}}_M^h dS \right\|}{\sum_{\Omega^{(e)} \in \Omega_{loc}} \left\| \int_{S^{(e)}} \dot{\mathbf{l}}^h dS \right\|}, \quad (4.25)$$

not depending on the localization bandwidth k .

- For time steps with no localizing elements, the index is null $I_1 = 0$. This stems directly from the fact that $\Omega_{loc} = \emptyset$, and thus, by definition, $I_1 = 0$.
- For time steps with perfect localization in all elements (fully representing a strong discontinuity that evolves across the mesh) the global indicator is null, since in this case $\dot{\epsilon}_M^{inel} = 0$ in all elements.
- The indicator is also null, by construction, when embedded strong discontinuities are utilized.
- For imperfect localization, the indicator returns a not null value in the interval $[0,1]$. This index gives a mean value idea about of the quality of the numerical solution for capturing a strain rate localization pattern. The nearer that the value I_1 is to zero, the higher the quality of the localized strain field.

The localization mismatch index I_1 has an incremental character and informs about the quality of the localization of the rate (incremental) strains. In view of equations (4.19) and (4.20) the extension to the total strain case follows immediately giving raise to the following global *accumulated* strain localization mismatch indicator:

$$I_2(t) = \begin{cases} \frac{\sum_{\Omega^{(e)} \in \Omega_{loc}} \left\| \int_{\Omega^{(e)}} \left(\int_{t_B}^t (\dot{\epsilon}_M^{inel})^h dt \right) d\Omega \right\|}{\sum_{\Omega^{(e)} \in \Omega_{loc}} \left\| \int_{\Omega^{(e)}} \left(\int_{t_B}^t (\dot{\epsilon}^{inel})^h dt \right) d\Omega \right\|} & \text{for } \Omega^{(e)} \in \Omega_{loc} \\ 0 & \text{for } \Omega^{(e)} \in \Omega / \Omega_{loc} \end{cases}, \quad (4.26)$$

with properties similar to those of index I_1 . The indicator I_2 is expected to be smoother than I_1 , since sudden changes on the incremental structural behavior will be directly reflected in the incremental index I_1 , whereas they will be smoothed in the accumulated one I_2 (since this index takes into account the previous history).

All the proposed indicators can be computed without an a-priori knowledge of the fracture mechanics “exact” solution of the problem, since the vector \mathbf{n} , normal to the discontinuity path, may be computed by bifurcation analysis (see Section 4.4).

4.4. The localization domain

The indicators in equations (4.22), (4.23) and (4.26) are based on the knowledge of the inelastic strain mismatch ε_M^{inel} , which, in turn, requires the knowledge of the normal vector \mathbf{n} to the discontinuity path. For this purpose, we resort to the material bifurcation analysis already discussed in Section 2.3. For the family of constitutive models of our interest (associated plasticity and damage models), explicit expressions for \mathbf{n} are available in the literature [Oliver and Huespe 2004a]. Those expressions may be used to compute the normal vector \mathbf{n} at the finite element centroid²². This normal is representative of a straight discontinuity surface (\mathbf{n} is considered constant inside the finite element) that approximate the part of the discontinuity crossing the finite element $\mathcal{S}^{(e)} = \Omega^{(e)} \cap \mathcal{S}$ (see Figure 4.6).

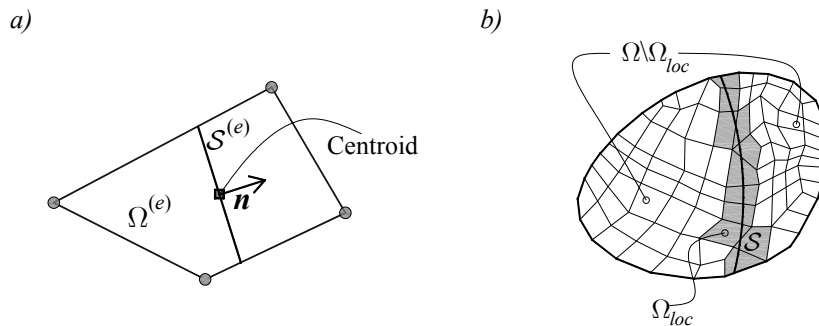


Figure 4.6 a) Finite element crossed by discontinuity, b) Localization domain.

Additionally, for the computation of the proposed indicators, definition of the localization domain is also necessary. Intuitively, defining the localization domain as the set of in-loading elements where bifurcation has been detected, as it was done for the mixed domain in Section 3.2.1 (see equation (3.20)), seems reasonable, since bifurcation is a *necessary* condition for the appearance of strain localization in the direction \mathbf{n} . Nevertheless, since bifurcation analysis is a local procedure, this condition is necessary but not sufficient. The onset and evolution of a discontinuity depends additionally on the surrounding material and on the boundary conditions.

In fact, in practical computations, large quantity of elements (*e.g.* on the vicinity or at the tip of a propagating discontinuity) where the bifurcation condition is fulfilled (at a given time step) are observed but no discontinuity develops and the elements generally unload in subsequent time steps. To avoid noise in the proposed indicators (produced by these elements that exhibit very reduced amount of strain localization), we also require in the definition of the localization domain

²² Note that for the case of standard quadrilateral elements, the central point (centroid) has usually special properties in terms of accuracy (see *Remark 3.2.1.1*)

Ω_{loc} , that the material point had experienced a *sufficient degree* of softening. This condition is evaluated in terms of the stress-like internal variable $q(\mathbf{x}, t)$ (decreasing along the deformation process for softening models).

Hence, the localization threshold, q_{loc} , is defined at each point as:

$$q_{loc}(\mathbf{x}) = \gamma q_{bif}(\mathbf{x}) ; \gamma \in [0, 1], \quad (4.27)$$

being q_{bif} the value of q evaluated at the bifurcation time $q_{bif}(\mathbf{x}) = q(\mathbf{x}, t_B)$, and γ a parameter controlling the softening “degree” (typically $\gamma = 0.95$).

The localization domain may be then formalized as:

$$\Omega_{loc}(t) := \{ \mathbf{x} \in \Omega \mid t \geq t_B(\mathbf{x}) ; \dot{\alpha}(\mathbf{x}, t) > 0 ; q(\mathbf{x}, t) \leq q_{loc}(\mathbf{x}) \}. \quad (4.28)$$

4.5. Numerical simulations

In this Section, the proposed strain localization indicators are assessed through their application to a set of numerical examples. Some of the examples used in previous Sections are here re-examined.

4.5.1. Strip in homogeneous uniaxial tensile stress state – Mode I fracture modeling

This numerical example, already presented in Sections 2.4.4 and 3.1.6.2, admits an analytical solution corresponding to a straight vertical crack (for a isotropic damage model).

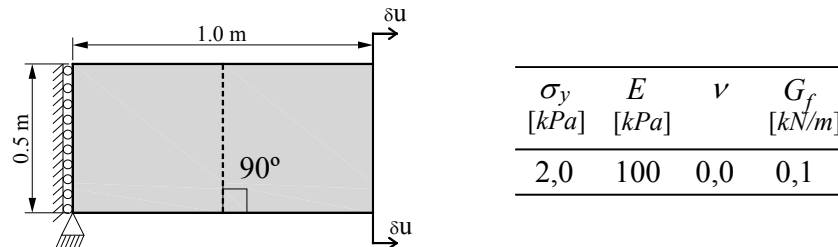


Figure 4.7 Strip stretching in the horizontal direction.

For this case a well-aligned mesh (with the crack) can be constructed and results, in terms of the strain localization indicators, can be compared with the ones obtained by using misaligned meshes.

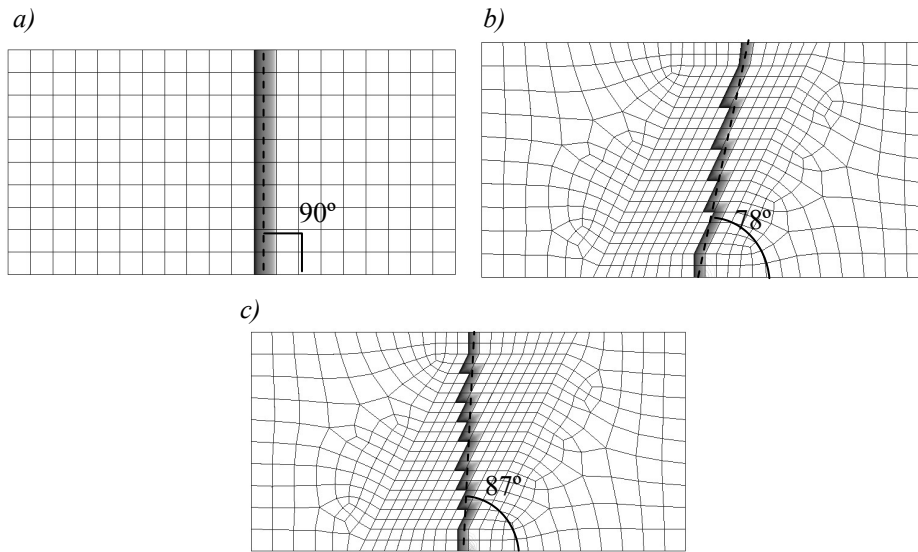


Figure 4.8 a) aligned mesh, b) misaligned mesh – irreducible formulation, c) misaligned mesh – Constant strain mode injection.

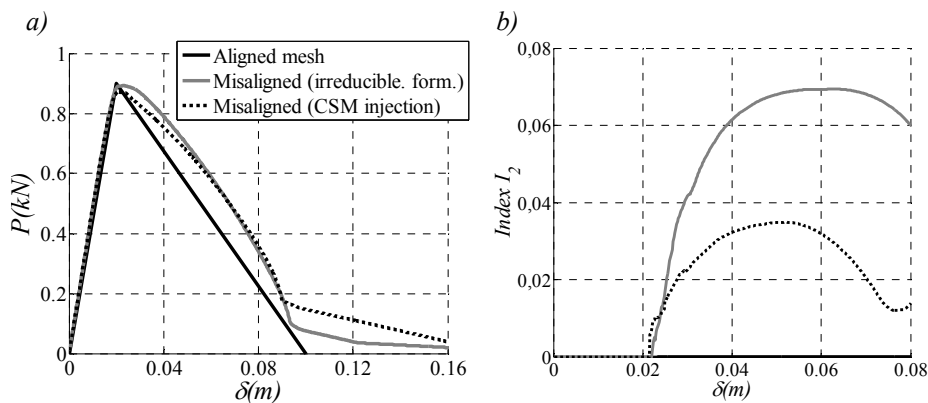


Figure 4.9 a) Force-displacement curves, b) Localization indicator I_2 .

In Figure 4.8, iso-displacement contours for different cases are presented. When a well oriented mesh is used, a perfect vertical solution is obtained (regardless of the employed formulation). Identical conclusion can also be extended to the force-displacement curves. Solutions match exactly the theoretical behavior, and thus, the indicator I_2 is null (Figure 4.9-b)). In the other hand, for the misaligned meshes, the indicator I_2 provides non-zero values, grading the results in terms of the mismatch with a regularized strong discontinuity.

It is observed that, for the irreducible formulation, the mismatch predicted by the index I_2 is higher, this indicating that results obtained by this formulation are strongly affected by mesh bias, as may be observed in Figure 4.8-b). With the constant strain mode (CSM) injection, mesh bias is alleviated and index I_2 gives

lower values. Despite the improvement of the results, (already observed in previous Chapters), is noticeable that index I_2 still gives non negligible values, indicating that the solution cannot be interpreted as a regularized strong discontinuity.

For the misaligned mesh, Figure 4.10 displays the spatial distribution map of the local mismatch indicator $i^{(e)}$ at two different stages of the analysis characterized by the displacement δ . For both cases, all elements of the localization band show a non negligible strain localization mismatch, whereas, the higher local values are generally obtained for the irreducible formulation. Alternatively, for the aligned structured mesh (that is not shown in the figure), the indicator remains zero.

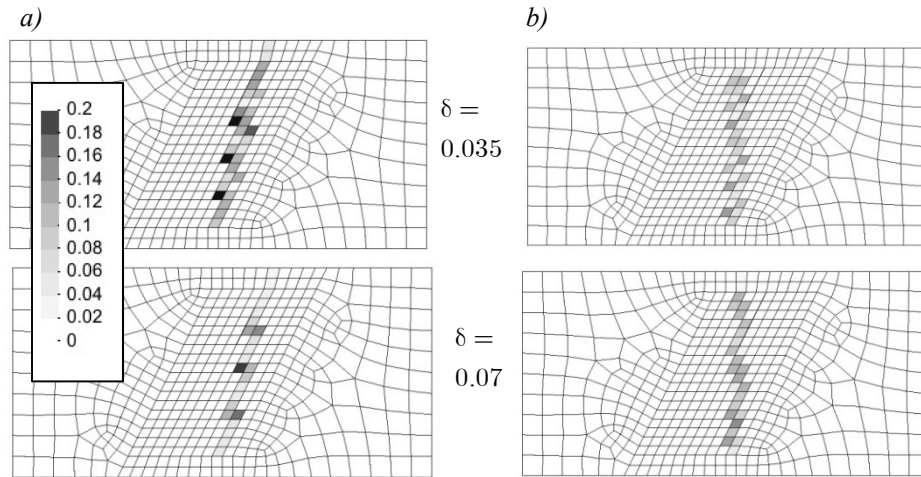


Figure 4.10 Distribution of strain localization mismatch indicator $i^{(e)}$ a) irreducible formulation, b) Constant strain mode injection.

4.5.2. Strip undergoing homogeneous uniaxial tensile stress state using a J_2 plasticity model– Mode II fracture modeling

In this case, previously presented in Sections 3.1.6.2 and 3.2.7.2, the analytical solution displays a mode II fracture characterized by a straight shear band crossing the strip at 45° (see Figure 4.11)

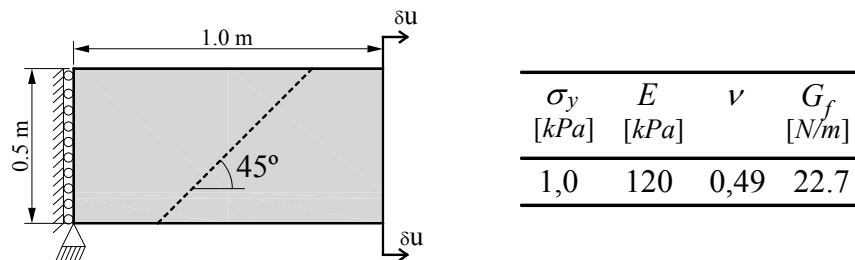


Figure 4.11 Strip stretching in the horizontal direction.

Likewise was done in the previous example, an well aligned mesh (with the theoretical solution) can be constructed. For this example the following meshes are considered: i) a mesh in which the central row of elements is exactly aligned with the theoretical inclination of the slip line intended to be captured, ii) a mesh of squared elements structured in such a way that the diagonals of the elements are aligned with the 45° inclination of the slip line and, finally, iii) an unstructured mesh with irregular mesh size. Here, the irreducible formulation is not considered since for this case no strain localization is obtained²³. Results obtained with the mixed bilinear-displacements/constant pressure (B-bar element) [Hughes 1980] and by the proposed injection procedure are compared.

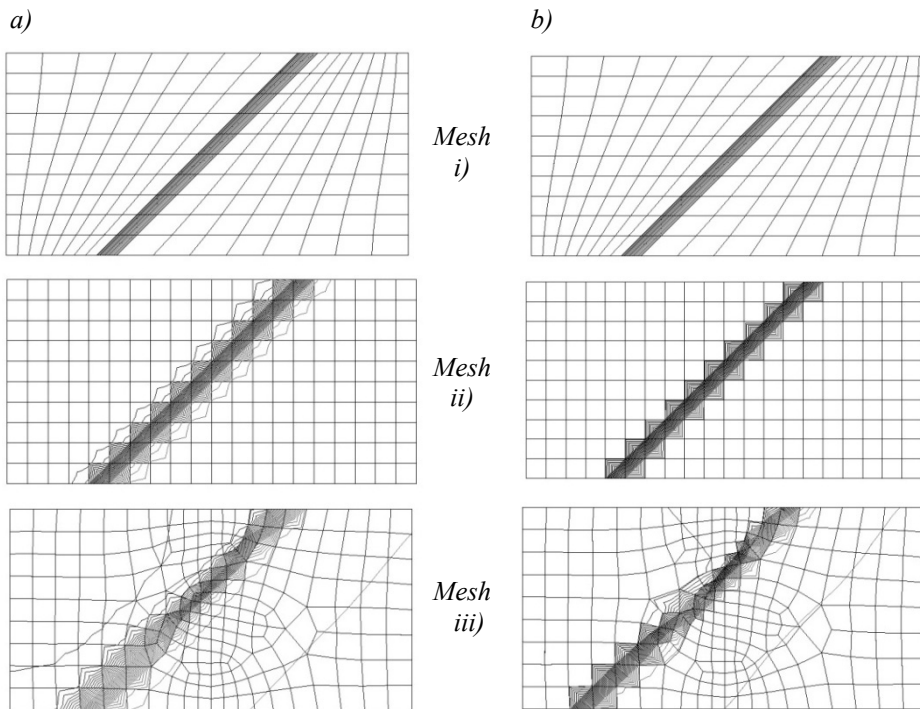


Figure 4.12 Iso-displacement plots for three different meshes, a) B-bar element, b) Constant strain mode injection.

In Figure 4.12, it is noticeable that for the aligned mesh i), and for both finite element formulations, perfect (one element bandwidth) slip lines are obtained, as is corroborated by the corresponding structural responses $P - \delta$ (Figure 4.13-a)), matching exactly the expected triangular analytical solution and by the incremental global mismatch indicator I_I that remains null throughout the analysis (Figure 4.13-b)).

²³ For the irreducible formulation, no localization is obtained due locking effects related with the incompressible character of the J_2 plasticity model (as was shown in Section 3.1.6.2).

When mesh ii) is used, it is also observed a one element localization band. Nevertheless, for the B-bar element some residual deformation are noticeable outside the localization band caused by stress locking²⁴ during earlier stages of the loading process, as it can be observed in the corresponding force-displacement curve, that exhibits a kind of bilinear softening behavior, and in the incremental indicator I_I , that is higher in initial stages. The good results obtained with meshes i) and ii) display the well-known ability of the B-bar (Q1-P0) element to capture slip lines aligned with the element sides or diagonals. Here it was also shown (as was discussed in Sections 3.1.6.2 and 3.2.7.2) that the injection procedure based on the mixed $\mathbf{u} - \varepsilon$ formulation, even so that was not initially developed to face incompressible constitutive models²⁵, is able to reproduce, or even enhance, the results obtained with the B-bar element.

For unstructured meshes, the quality of the results deteriorates. It is now observed that the localization bandwidth, due to stress locking, encompasses more than one element in some places. This fact is reflected in the structural curves by extra dissipation and nonzero residual loading obtained in the end of the analysis. Notwithstanding, the more important differences are found on the mismatch indicator, that assumes now much higher values, reflecting that, for mesh c), the obtained localization band is much far from represent a strong discontinuity, than when meshes a) or b) are used.

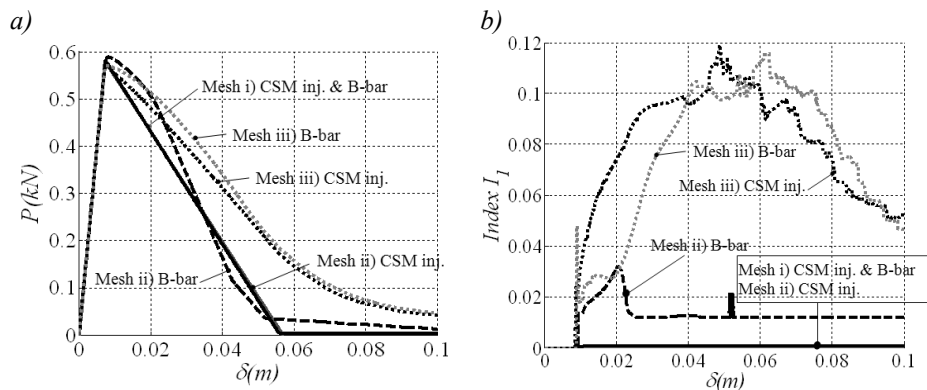


Figure 4.13 a) Force-displacement curves, b) Localization indicator I_I .

The local mismatch indicator $i^{(e)}$ provides additional information about the localization process. In Figure 4.14 maps of this indicator for meshes b) and c) computed with the CSM injection are presented, for two loading stages. To highlight the results, different scales are adopted for each mesh in Figure 4.14 a) and b).

²⁴ The initial bandwidth of the localization band is wider than one element in earlier stages of loading, but it gradually reduces to one element.

²⁵ The injection strategy was developed to face the mesh bias dependence, which is not an issue in this example, since all meshes, included the un-structured one, exhibit a 45° localization band.

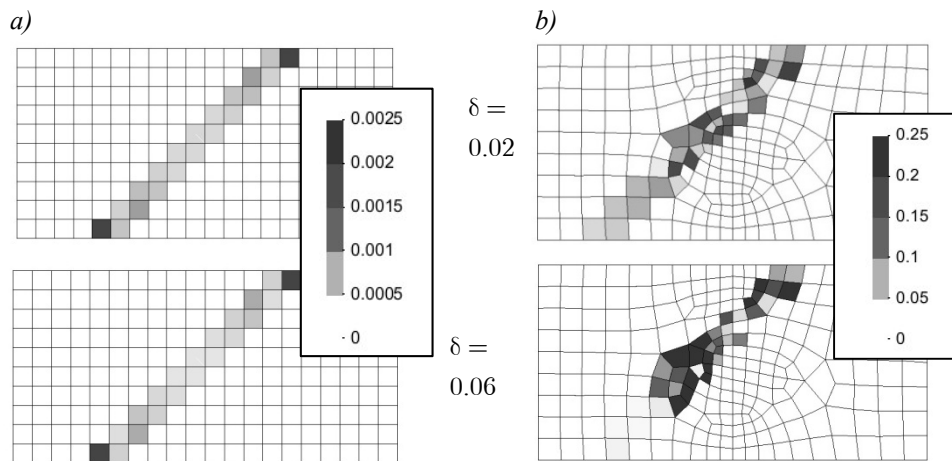


Figure 4.14 *Spatial distribution of the local strain localization mismatch indicator $i^{(e)}$ (CSM injection), a) diagonal aligned mesh (mesh ii), b) unstructured mesh (mesh iii).*

In accordance with previous results, it is observed in Figure 4.14 that for the unstructured mesh, high values of $i^{(e)}$ are attained (around 25%). In the other hand, for the diagonal aligned case, the values are almost negligible.

4.5.3. Slope stability problem using a J_2 plasticity model

In the previous examples near-homogenous problems, where the propagation of the localization band is almost instantaneous, have been considered. Due to the particular homogeneous stress state, in those cases special meshes, fully aligned with the crack, can be easily constructed. For this type of meshes, the finite element solution is fully representative of a de-cohesive fracture type, as it was shown in the previous examples, matching exactly the available analytical solution.

However, in most cases of engineering interest, analytical solutions are not available, and material failure takes place under heterogeneous stress states where structural properties (related to the material, geometry and boundary conditions) provoke high stress intensification in a certain point determining the onset of the failure and giving rise to a propagating localization band. For this type of problems, the construction of meshes fully aligned with the localization band is a extremely difficult task.

Figure 4.15 describes a typical embankment stability loss problem. The soil is simulated through a J_2 plasticity model, under plain strain conditions. Since an analytical elasto-plastic solution is not available, the numerical solution using the continuum strong discontinuity approach is considered as the “reference” solution. This solution consists of a slip line, which can be nearly approximated by a

portion of a circle, as it is shown in Figure 4.15. Then, a first mesh of quadrilateral finite elements is constructed approximately aligned with the slip line solution provided by the reference procedure, as it is shown Figure 4.16-a) and a second misaligned mesh is considered as shown in Figure 4.16-b). For both meshes the computations are performed with the constant strain injection procedure proposed in Box 3.5. The following material properties are adopted: elastic modulus $E = 10000.0 \text{ MPa}$, Poisson's ratio $\nu = 0.45$, yield stress $\sigma_y = 100.0 \text{ MPa}$ and fracture energy $G_f = 8.0 \text{ MN/m}$.

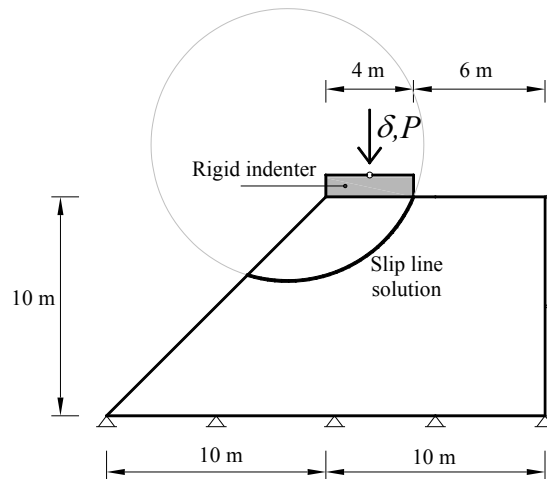


Figure 4.15 Slope stability problem.

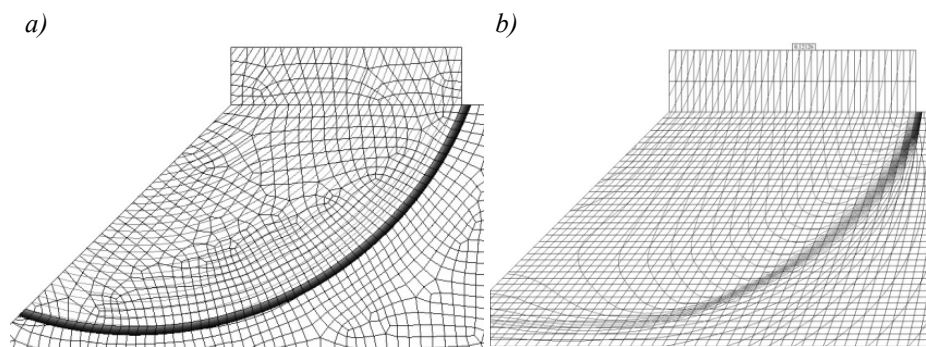


Figure 4.16 Iso-displacement contours for two different meshes, a) Aligned mesh, b) Misaligned mesh.

Figure 4.16 displays the iso-displacement contours, where the numerically obtained localization bands can be observed. For the aligned mesh, the shear band is well captured by the aligned band of elements containing the slip line: the iso-displacement contours are sharply concentrated inside a one-element-width localization band capturing the propagating discontinuity at the considered time of the simulation. Instead, for the misaligned mesh of Figure 4.16-b), though the propa-

gation of the discontinuity path seems to be correct, the bandwidth of the localization band is wider than one element in a large portion of it, and that is translated into additional dissipation of the corresponding failure mechanism, as it can be observed in the structural force-displacement curves in Figure 4.17-a).

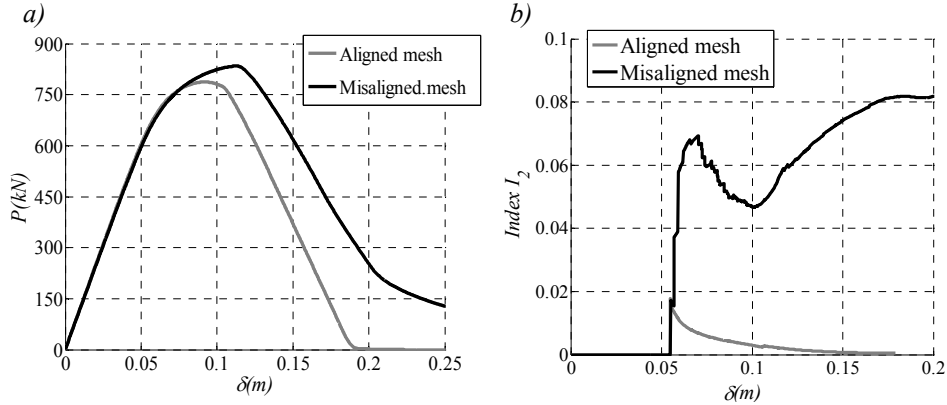


Figure 4.17 a) Force-displacement curves, b) Global Localization indicator I_2 . (results obtained with the constant strain injection)

In Figure 4.17-b) ,the global accumulated mismatch indicator I_2 confirms that results obtained with the non-aligned mesh fails in representing a strong discontinuity. Note that Figure 4.17-b) shows a huge difference on the results provided by both meshes (for the aligned mesh, the value of the indicator is much smaller than for the unaligned mesh). Also notice that, in this case, no exact analytical $P - \delta$ solution is available; however the small values of the strain localization mismatch indicator suggest that, for the aligned mesh, the obtained solution is very close to the fracture mechanics one.

Figure 4.18 displays the distribution of the local incremental strain localization mismatch indicator, $i^{(e)}$, for the misaligned mesh, at two different stages of the loading process. The resulting spatial distribution of the indicator clearly shows the mismatch extending to a band encompassing several elements, this indicating an imperfect representation of a discrete fracture.

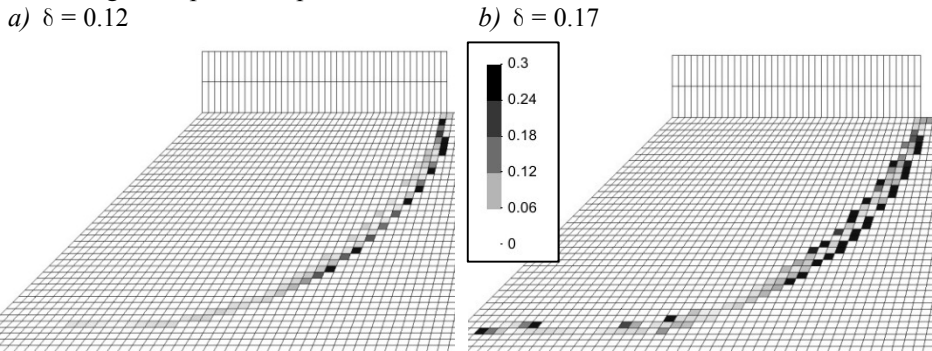


Figure 4.18 Spatial distribution of the local incremental strain localization mismatch indicator $i^{(e)}$ for two loading stages.

4.6. Summary and conclusions

Along this Chapter, the issue of identification of strain localization solutions and the discrete fracture mechanics ones has been tackled, and some mismatch indicators to characterize the quality of the former, in terms of their ability to represent the later, have been derived. The application of such indicators to the strain localization solution of some well established benchmarks allows arriving to the following conclusions:

- In general, strain localization solutions using standard continuum constitutive models, do not match fracture mechanics solutions, excepting for very specific cases, typically finite element meshes specifically aligned with the fracture path (for these specific cases the indicators return null mismatch). This behavior has been also reported by other authors and is here further supported by the results provided by the proposed indicators.
- The mismatch obtained for general unaligned meshes is caused by the limited ability of finite element interpolation field to reproduce strong discontinuity embedded into them. This kinematic flaw is here identified as the ultimate reason of stress locking.
- The injection procedure, based in a mixed \mathbf{u}, ε formulation, substantially reduces the mismatch. However, this improvement is not sufficient for the localized solution to be considered representative of a strong discontinuity, suggesting that, additional strain modes should be subsequently injected in order to further enhance the finite element kinematic performance. This issue will be tackled in the next Chapter.
- The proposed indicators, or similar ones to be derived, can be computed without an a-priori knowledge of the exact fracture mechanics solution of the problem, and used as an objective tool for the quantitative evaluation of the performance of strain localization based methods applied to general heterogeneous problems.

Chapter 5

Weak\strong discontinuity injection procedures

In Chapter 3, inspired in a u, ε mixed finite element formulation, a constant strain mode was proposed to be injected in those elements that are amenable to develop strain localization. Despite the improvement on the obtained results, when compared with those provided by standard formulations, it was noticed that due to stress locking, and after complete failure, residual loads still remain, this meaning that no true separation between both surfaces of the crack is attained.

In Chapter 4, this issue was studied in terms that the displacement field solution might be (or not) interpreted as a regularized strong discontinuity embedded into the localization band. Based on the mismatch indicators proposed in Chapter 4, it was concluded, that this is generally not true, excepting for very specific set of cases where the discretization is fully aligned with the crack.

This mismatch is related to a kinematic deficiency. In fact, the constant strain mode injection seems to provide extra flexibility in order to enhance propagation capabilities of the finite elements, but on the other hand, the constant kinematics still exhibits a limited capability to describe a discontinuity in a one-element finite element band. The natural subsequent idea, in the ambit of the proposed injection procedure, is to further improve the finite element kinematics by the injection of an additional enhanced strain mode, on those elements that develop the discontinuity. This additional injection is inspired by the weak/strong discontinuity kinematics and will be therefore termed as *weak/strong discontinuity mode injection*.

5.1. Strong discontinuities

As it was mentioned at Chapter 4, the continuum strong discontinuity approach was proposed in the nineties [Simo, Oliver et al. 1993; Oliver 1996a] and subsequently, it was further developed and used in a variety of applications by several authors (*e.g.* [Armero and Garikipati 1996; Alfaiate et al. 2002; Alfaiate 2003; Alfaiate et al. 2003; Mosler and Meschke 2003; Blanco et al. 2006; Linero et al. 2006; Linder and Armero 2007; Armero and Kim 2012]).

In this Section, the strong discontinuity kinematics is recalled, and a three field mixed formulation $\hat{\mathbf{u}}, \hat{\boldsymbol{\varepsilon}}, [\hat{\mathbf{u}}]$ is developed, considering a constant regular strain $\hat{\boldsymbol{\varepsilon}}$. Finally, by restricting the mixed formulation to a part of the domain (the injection domain) the strong discontinuity injection is introduced.

5.1.1. The Strong discontinuity kinematics

In Section 4.1.1 the strong discontinuity kinematics was introduced. Here we recall the basic ingredients of the regularized strong discontinuity kinematics:

$$\dot{\mathbf{u}} = \dot{\bar{\mathbf{u}}} + \mathcal{H}_S [[\dot{\mathbf{u}}]], \quad (5.1)$$

where $\dot{\bar{\mathbf{u}}}$ stands for the smooth part of the displacement field, \mathcal{H}_S stands for the Heaviside (step) function ($\mathcal{H}_S(\mathbf{x}) = 0 \forall \mathbf{x} \in \Omega^-$ and $\mathcal{H}_S(\mathbf{x}) = 1 \forall \mathbf{x} \in \Omega^+$) and $[[\dot{\mathbf{u}}]]$ is the displacement jump between both sides of the discontinuity.

Due to computational reasons, related to the imposition of the essential boundary conditions, that we intend to impose just in terms of $\dot{\mathbf{u}}$, expression (5.1) may be reformulated through an equivalent expression (see [Oliver 1996b] for further details):

$$\dot{\mathbf{u}} = \hat{\mathbf{u}} - \varphi [[\dot{\mathbf{u}}]] + \mathcal{H}_S [[\dot{\mathbf{u}}]] = \hat{\mathbf{u}} + \underbrace{(\mathcal{H}_S - \varphi)}_{\mathcal{M}} [[\dot{\mathbf{u}}]], \quad (5.2)$$

where φ is a continuous arbitrary function that fulfills the following two conditions:

$$\varphi(\mathbf{x}) = \begin{cases} 0 & \forall \mathbf{x} \in (\Omega \setminus \Omega_{\mathcal{M}})^- \\ 1 & \forall \mathbf{x} \in (\Omega \setminus \Omega_{\mathcal{M}})^+ \end{cases}, \quad (5.3)$$

being the domain, $\Omega_{\mathcal{M}}$, the support of the “unit jump” function \mathcal{M} (see Figure 5.1).

The regularized strain field corresponding to equation (5.2) reads²⁶:

$$\varepsilon = \nabla^S \dot{\mathbf{u}} = \underbrace{\nabla^S \dot{\mathbf{u}} - (\nabla \varphi \otimes [\dot{\mathbf{u}}])^S}_{\hat{\varepsilon}} + \frac{\mu_S}{k} (\mathbf{n} \otimes [\dot{\mathbf{u}}])^S, \quad (5.4)$$

where \mathbf{n} is the unit vector orthogonal to \mathcal{S} and μ_S is a collocation function on \mathcal{S} :

$$\mu_S(\mathbf{x}) = \begin{cases} 1 & \forall \mathbf{x} \in \mathcal{S} \\ 0 & \forall \mathbf{x} \in \Omega \setminus \mathcal{S} \end{cases}. \quad (5.5)$$

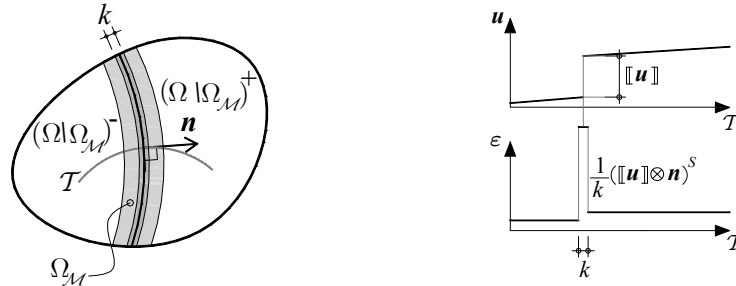


Figure 5.1 *Strong discontinuity kinematics.*

The kinematics represented in equations (5.4) is borrowed from the strong discontinuity approach and it is the basic ingredient of the strong discontinuity injection.

5.1.2. The boundary value problem with strong discontinuities

In this Section, the strong form of the boundary value problem presented at Section 2.1 is reformulated, admitting now, a strong discontinuity crossing the continuum body.

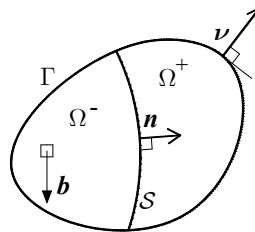


Figure 5.2 *Continuum body with discontinuity.*

²⁶ The compatible strain field corresponding of (5.2) is

$$\varepsilon = \nabla^S \dot{\mathbf{u}} = \nabla^S \dot{\mathbf{u}} + \mathcal{M} \otimes \nabla^S [\dot{\mathbf{u}}] + \nabla^S \mathcal{M} \otimes [\dot{\mathbf{u}}]$$

where the term $\mathcal{M} \otimes \nabla^S [\dot{\mathbf{u}}]$ is bounded with support in Ω_M . For $\Omega_M \rightarrow \mathcal{S}$ ($\Omega_M \ll \Omega$) this term is negligible in front of the remaining terms and can be generally disregarded.

In Figure 5.2 the continuum body, Ω , of boundary Γ , is subdivided in two parts, Ω^+ and Ω^- , by the strong discontinuity path \mathcal{S} . The vector $\boldsymbol{\nu}$, is the outward unit normal to Γ , \mathbf{n} is the unit vector normal to the discontinuity and \mathbf{b} are the body forces.

The strong form of the boundary value problem, admitting a strong discontinuities, is summarized in Box 5.1.

Given the external actions $\dot{\mathbf{u}}^*(\mathbf{x}) : \Omega \rightarrow \mathbb{R}^N$, $\dot{\mathbf{t}}^*(\mathbf{x}) : \Omega \rightarrow \mathbb{R}^N$ and $\dot{\mathbf{b}}(\mathbf{x}) : \Omega \rightarrow \mathbb{R}^N$, find $\dot{\mathbf{u}}(\mathbf{x}) : \Omega \rightarrow \mathbb{R}^N$ such that:

$$\nabla \cdot \dot{\boldsymbol{\sigma}} + \dot{\mathbf{b}} = 0, \quad \forall \mathbf{x} \in \Omega \setminus \mathcal{S} \quad (\text{equilibrium equation}) \quad (5.6)$$

$$\dot{\boldsymbol{\sigma}} = \boldsymbol{\Sigma}(\dot{\boldsymbol{\varepsilon}}), \quad \forall \mathbf{x} \in \Omega \quad (\text{constitutive equation}) \quad (5.7)$$

$$\dot{\mathbf{u}} = \dot{\hat{\mathbf{u}}} - \varphi \llbracket \dot{\mathbf{u}} \rrbracket + \frac{\mu_{\mathcal{S}}}{k} (\mathbf{n} \otimes \llbracket \dot{\mathbf{u}} \rrbracket)^S, \quad \forall \mathbf{x} \in \Omega \quad (\text{strong disc. kinematics}) \quad (5.8)$$

$$\dot{\hat{\boldsymbol{\varepsilon}}} = \nabla^S \dot{\hat{\mathbf{u}}} - (\nabla \varphi \otimes \llbracket \dot{\mathbf{u}} \rrbracket)^S, \quad \forall \mathbf{x} \in \Omega \setminus \mathcal{S} \quad (\text{compatibility equation}) \quad (5.9)$$

$$\dot{\boldsymbol{\varepsilon}} = \nabla^S \dot{\mathbf{u}} = \dot{\hat{\boldsymbol{\varepsilon}}} + \frac{1}{k} (\mathbf{n} \otimes \llbracket \dot{\mathbf{u}} \rrbracket)^S, \quad \forall \mathbf{x} \in \mathcal{S} \quad (\text{compatibility equation}) \quad (5.10)$$

$$\dot{\boldsymbol{\sigma}}^- \cdot \mathbf{n} = \dot{\boldsymbol{\sigma}}^+ \cdot \mathbf{n}, \quad \forall \mathbf{x} \in \mathcal{S} \quad (\text{outer traction continuity}) \quad (5.11)$$

$$\dot{\boldsymbol{\sigma}}^+ \cdot \mathbf{n} = \dot{\boldsymbol{\sigma}}_{\mathcal{S}} \cdot \mathbf{n}, \quad \forall \mathbf{x} \in \mathcal{S} \quad (\text{inner traction continuity}) \quad (5.12)$$

$$\begin{aligned} \dot{\mathbf{u}} &= \dot{\mathbf{u}}^* & , \forall \mathbf{x} \in \Gamma_u \\ \dot{\boldsymbol{\sigma}} \cdot \boldsymbol{\nu} &= \dot{\mathbf{t}}^* & , \forall \mathbf{x} \in \Gamma_{\sigma} \end{aligned} \quad (\text{boundary conditions}) \quad (5.13)$$

Box 5.1 Strong form of the boundary value problem with discontinuity.

In Box 5.1, $\dot{\boldsymbol{\sigma}}^-$ and $\dot{\boldsymbol{\sigma}}^+$ stand for the stress rate fields in both sides of the discontinuity, whereas $\dot{\boldsymbol{\sigma}}_{\mathcal{S}}$ stands for the stresses rate in \mathcal{S} .

Notice, that outside $\Omega_{\mathcal{M}} : \nabla \varphi = 0$, therefore, equation (5.9) gives the standard compatibility equation $\dot{\hat{\boldsymbol{\varepsilon}}} = \nabla^S \dot{\hat{\mathbf{u}}}$.

5.1.3. A three field $(\dot{\hat{\mathbf{u}}}, \dot{\hat{\boldsymbol{\varepsilon}}}, \llbracket \dot{\mathbf{u}} \rrbracket)$ mixed formulation

In Section 3.1.2 based on the strong form of the boundary value problem presented at Section 2.1, a mixed $\dot{\mathbf{u}}, \dot{\boldsymbol{\varepsilon}}$ formulation, where strains were also considered an independent variable, was introduced. Here, motivated by the strong discontinuity kinematics, a three field formulation $\dot{\hat{\mathbf{u}}}, \dot{\hat{\boldsymbol{\varepsilon}}}, \llbracket \dot{\mathbf{u}} \rrbracket$ is proposed. In the strong discontinuity approach, generally a $\dot{\hat{\mathbf{u}}}, \llbracket \dot{\mathbf{u}} \rrbracket$ formulation is used, *i.e.* the reg-

ular part of the displacement field, $\hat{\mathbf{u}}$, and the displacement jump, $[[\mathbf{u}]]$, are interpolated independently according the split stated in (5.2). Here, the regular part of the strain field $\hat{\dot{\boldsymbol{\varepsilon}}}$, is also selected as an independent primal variable. The selection of $\hat{\dot{\boldsymbol{\varepsilon}}}$, and not $\dot{\boldsymbol{\varepsilon}}$, as the additional strain variable to interpolate is related to the strong discontinuity concept. When using strong discontinuities, due to the bounded nature of the stress field and the zero thickness of the discontinuity surface, the stresses at the discontinuity surface do not contribute to the generation of internal forces, *i.e.*:

$$\int_{\Omega} \nabla^s \hat{\boldsymbol{\eta}} : \dot{\boldsymbol{\Sigma}}(\dot{\boldsymbol{\varepsilon}}) d\Omega = \int_{\Omega \setminus \mathcal{S}} \nabla^s \hat{\boldsymbol{\eta}} : \dot{\boldsymbol{\Sigma}}(\hat{\dot{\boldsymbol{\varepsilon}}}) d\Omega = \int_{\Omega} \nabla^s \hat{\boldsymbol{\eta}} : \dot{\boldsymbol{\Sigma}}(\hat{\dot{\boldsymbol{\varepsilon}}}) d\Omega. \quad (5.14)$$

Likewise, in Section 3.1.2, we intend to interpolate element-wise-constant strain fields, thus a reasonable option is to choose $\hat{\dot{\boldsymbol{\varepsilon}}}$ as the independent variable, instead of the total strain, since the equilibrium equation can be stated just in terms of this regular strain field, as it is shown in equation (5.14).

To introduce the mixed formulation, equations (5.6) and (5.9) are tested with the test functions $\hat{\boldsymbol{\eta}}$ and $\boldsymbol{\mu}$. Integrating over the domain, and using the result of (5.14), yields:

$$\begin{aligned} \int_{\Omega} \nabla^s \hat{\boldsymbol{\eta}} : \dot{\boldsymbol{\Sigma}}(\hat{\dot{\boldsymbol{\varepsilon}}}) d\Omega &= \mathbf{j}^{ext} \quad , \quad \forall \hat{\boldsymbol{\eta}} \in \hat{\mathcal{N}}, \quad a) \\ \int_{\Omega} \boldsymbol{\mu} : [\hat{\dot{\boldsymbol{\varepsilon}}} - (\nabla^s \hat{\mathbf{u}} - (\nabla \varphi \otimes [[\mathbf{u}]])^S)] d\Omega &= \mathbf{0} \quad , \quad \forall \boldsymbol{\mu} \in \mathcal{V}, \quad b) \end{aligned} \quad (5.15)$$

The functions appearing in equations (5.15)-b) are chosen to belong to the following functional spaces:

$$\mathcal{E} := \left\{ \hat{\dot{\boldsymbol{\varepsilon}}} \mid \hat{\dot{\boldsymbol{\varepsilon}}} \in [L^2(\Omega)]^{n \times n} \right\} \quad , \quad \mathcal{V} := \left\{ \boldsymbol{\mu} = \boldsymbol{\mu} \mid \boldsymbol{\mu} \in [L^2(\Omega)]^{n \times n} \right\}, \quad (5.16)$$

whereas, for equation (5.15)-a), according the decomposition of the displacement field expressed in (5.2):

$$\mathcal{U} = \hat{\mathcal{U}} \oplus \tilde{\mathcal{U}} = \{ \mathbf{u} \mid \mathbf{u} = \hat{\mathbf{u}} + (\mathcal{H}_{\mathcal{S}} - \varphi)[[\mathbf{u}]] \} \quad , \quad (5.17)$$

where:

$$\hat{\mathcal{U}} := \left\{ \hat{\mathbf{u}} \mid \hat{\mathbf{u}} \in [H^1(\Omega)]^n ; \hat{\mathbf{u}}|_{\Gamma_u} = \mathbf{u}^* \right\} \quad , \quad \tilde{\mathcal{U}} := \left\{ [[\mathbf{u}]] \mid [[\mathbf{u}]] \in [L_2(\Omega)]^n \right\} \quad ,$$

and:

$$\hat{\mathcal{N}} := \left\{ \hat{\boldsymbol{\eta}} \mid \hat{\boldsymbol{\eta}} \in [H^1(\Omega)]^n ; \hat{\boldsymbol{\eta}}|_{\Gamma_u} = \mathbf{0} \right\} \quad . \quad (5.18)$$

It can be proved, by standard arguments(see [Oliver 1996b]), that equation (5.15)-a) is equivalent to

$$\begin{aligned} \nabla \cdot \dot{\boldsymbol{\sigma}} + \dot{\mathbf{b}} &= \mathbf{0} & , \forall \mathbf{x} \in \Omega \setminus \mathcal{S}, \\ \dot{\boldsymbol{\sigma}} \cdot \boldsymbol{\nu} &= \dot{\mathbf{i}}^* & , \forall \mathbf{x} \in \Gamma_{\sigma}, \\ \dot{\boldsymbol{\sigma}}^- \cdot \mathbf{n} &= \dot{\boldsymbol{\sigma}}^+ \cdot \mathbf{n} & , \forall \mathbf{x} \in \mathcal{S}, \end{aligned} \quad (5.19)$$

whereas equation (5.15)-b) is equivalent to:

$$\hat{\dot{\boldsymbol{\varepsilon}}} = \nabla^S \hat{\dot{\boldsymbol{u}}} - (\nabla \varphi \otimes \llbracket \dot{\boldsymbol{u}} \rrbracket)^S, \quad \forall \mathbf{x} \in \Omega \setminus \mathcal{S}, \quad (5.20)$$

this implying, that equations (5.6), (5.9), (5.11) and (5.13) are weakly satisfied. Additionally, the inner traction continuity equation (5.12), can be directly imposed, in a strong form, at the discontinuity surface, *i.e.*:

$$\dot{\boldsymbol{\sigma}}_S \cdot \mathbf{n} = \dot{\boldsymbol{\sigma}}^+ \cdot \mathbf{n}, \quad \forall \mathbf{x} \in \mathcal{S}. \quad (5.21)$$

Notice that imposing directly equation (5.21) in a strong form leads to an un-symmetric formulation (Petrov-Galerkin based), since the functional space of the solution functions \mathcal{U} is different from the functional space of the weighting functions $\hat{\mathcal{N}}$ ([Hughes 1987]).

5.1.4. Three field mixed finite element formulation – Un-symmetric formulation

Regarding the finite element approximations, we follow the arguments used in Section 3.1.3, *i.e.* element-wise-constant discontinuous finite element interpolations for the strains $\hat{\dot{\boldsymbol{\varepsilon}}}$ and displacement jump $\llbracket \dot{\boldsymbol{u}} \rrbracket$ are selected. For the smooth part of the displacement field $\hat{\dot{\boldsymbol{u}}}$, standard continuous bilinear interpolations are used:

$$\mathcal{U}^h = \hat{\mathcal{U}}^h \oplus \tilde{\mathcal{U}}^h = \left\{ \mathbf{u}^h \mid \dot{\boldsymbol{u}}^h = \sum_{i=1}^{nnodes} N_i(\mathbf{x}) \dot{\boldsymbol{u}}_i + \sum_{e=1}^{nelem} \mathcal{M}^h(\mathbf{x}) \llbracket \mathbf{u} \rrbracket^{(e)} \right\}; \mathcal{U}^h \subset \mathcal{U}$$

where: $\mathcal{M}^h(\mathbf{x}) = \mathcal{H}_S - \varphi^h(\mathbf{x})$

$$\hat{\mathcal{N}}^h := \left\{ \hat{\boldsymbol{\eta}}^h \mid \hat{\boldsymbol{\eta}}^h(\mathbf{x}) = \sum_{i=1}^{nnodes} N_i(\mathbf{x}) \hat{\boldsymbol{\eta}}_i \right\}; \hat{\mathcal{N}}^h \subset \hat{\mathcal{N}} \quad (5.22)$$

$$\mathcal{V}^h := \left\{ \boldsymbol{\mu}^h = \boldsymbol{\mu}^h \mid \boldsymbol{\mu}^h(\mathbf{x}) = \sum_{e=1}^{nelem} \phi^{(e)}(\mathbf{x}) \boldsymbol{\mu}^{(e)} \right\}; \mathcal{V}^h \subset \mathcal{V}$$

$$\mathcal{E}^h := \left\{ \dot{\boldsymbol{\varepsilon}}^h \mid \dot{\boldsymbol{\varepsilon}}^h(\mathbf{x}) = \sum_{e=1}^{nelem} \phi^{(e)}(\mathbf{x}) \dot{\boldsymbol{\varepsilon}}^{(e)} \right\}; \mathcal{E}^h \subset \mathcal{E},$$

where $nelem$ and $nnode$ are, respectively, the number of nodes and elements of the finite element mesh, $\dot{\boldsymbol{u}}_i$ is the displacement vector associated to the node i , N_i are the standard finite element isoparametric shape functions, $\llbracket \mathbf{u} \rrbracket^{(e)}$ and $\dot{\boldsymbol{\varepsilon}}^{(e)}$ are, respectively, the displacement jump and regular strains associated to the element (e) , and $\phi^{(e)}$ is a collocation function with elemental support:

$$\phi^{(e)}(\mathbf{x}) = \begin{cases} 1 & \text{if } \mathbf{x} \in \Omega^{(e)} \\ 0 & \text{if } \mathbf{x} \notin \Omega^{(e)} \end{cases}$$

Moreover, the function φ^h , appearing in equation (5.22) is chosen as follows:

$$\varphi^h(\mathbf{x}) = \sum_{i=1}^{nnodes} N_i(\mathbf{x})\varphi_i = \sum_{i=1}^{nnodes^+} N_{i^+}(\mathbf{x}), \tag{5.23}$$

where φ_i is a nodal value²⁷, assuming unit and null values for nodes belonging to Ω^+ and Ω^- , respectively. The subscript + refer to nodes belonging to Ω^+ ($\varphi_{i^+} = 1$) (see Figure 5.3-b) and Figure 5.4).

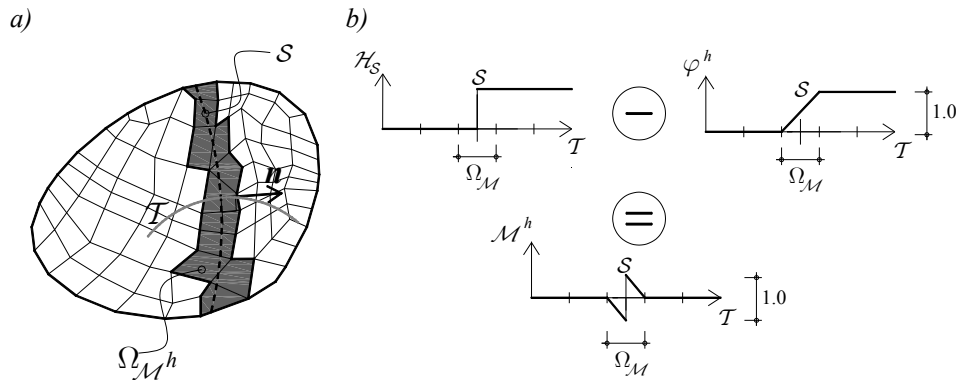


Figure 5.3 a) Discretized body with discontinuity, b) Description of functions \mathcal{M}^h , \mathcal{H}_S and φ^h along line \mathcal{T} .

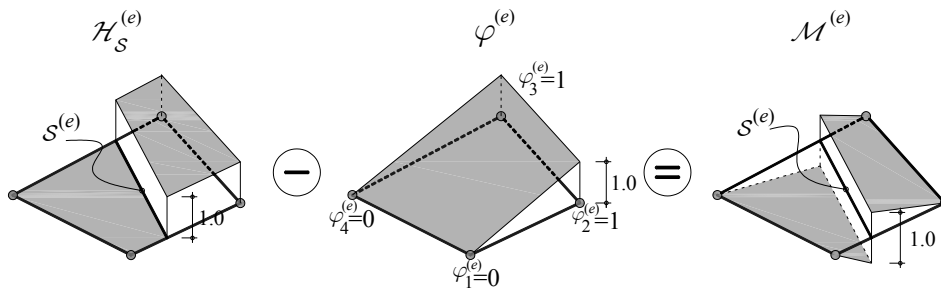


Figure 5.4 Elemental functions $\mathcal{H}_S^{(e)}$, $\varphi^{(e)}$ and $\mathcal{M}^{(e)}$.

²⁷ In order to construct the elemental vectors $\varphi^{(e)}$, distinction between nodes belonging to $\Omega_{(e)}^+$ and $\Omega_{(e)}^-$ is necessary, being therefore required information about the position of the discontinuity inside the finite element. This issue will be tackled at Section 5.3.5.

At the element level, the unit vector $\mathbf{n}^{(e)}$, normal to the discontinuity is admitted constant and orthonormal to that part of the discontinuity $\mathcal{S}^{(e)}$ crossing the finite element (approximated as a straight segment $\mathcal{S}^{(e)} = \Omega^{(e)} \cap \mathcal{S}$).

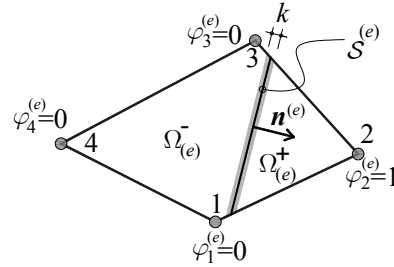


Figure 5.5 Finite element with regularized strong discontinuity.

Regarding the finite element approximations, a discrete version of (5.15) reads:

$$\sum_{e \in \Omega} \int_{\Omega^{(e)}} \nabla^s \hat{\boldsymbol{\eta}}^h : \dot{\boldsymbol{\Sigma}}(\hat{\boldsymbol{\varepsilon}}^{(e)}) d\Omega = \dot{\mathbf{j}}^{ext}, \quad \forall \hat{\boldsymbol{\eta}}^h \in \hat{\mathcal{N}}^h, \quad (5.24)$$

$$\int_{\Omega^{(e)}} \boldsymbol{\mu}^{(e)} : \left(\dot{\boldsymbol{\varepsilon}}^{(e)} - \nabla^s \dot{\boldsymbol{u}}^h + \left(\nabla \varphi^h \otimes \llbracket \dot{\boldsymbol{u}} \rrbracket^{(e)} \right)^S \right) d\Omega = 0, \quad \forall \boldsymbol{\mu}^{(e)} \in \mathcal{V}^h, \quad \forall e \in \Omega, \quad (5.25)$$

$$\dot{\boldsymbol{\Sigma}}(\hat{\boldsymbol{\varepsilon}}^{(e)}) \cdot \mathbf{n}^{(e)} = \dot{\boldsymbol{\Sigma}}(\hat{\boldsymbol{\varepsilon}}_S^{(e)}) \cdot \mathbf{n}^{(e)}, \quad \forall e \in \Omega_{\mathcal{M}}. \quad (5.26)$$

In equation (5.25), the strain field $\hat{\boldsymbol{\varepsilon}}^{(e)}$, the displacement jump $\llbracket \dot{\boldsymbol{u}} \rrbracket^{(e)}$ and the weighting function $\boldsymbol{\mu}^{(e)}$ are chosen to be element-wise-constant and discontinuous across elements. Therefore, equation (5.25) can be solved at the elemental level, being $\hat{\boldsymbol{\varepsilon}}^{(e)}$ the projection of $\nabla^s \dot{\boldsymbol{u}}^h - \left(\nabla \varphi^h \otimes \llbracket \dot{\boldsymbol{u}} \rrbracket^{(e)} \right)^S$ on the elemental constant space:

$$\hat{\boldsymbol{\varepsilon}}^{(e)} = \frac{\int_{\Omega^{(e)}} \nabla^s \dot{\boldsymbol{u}}^h d\Omega}{\Omega^{(e)}} - \frac{\int_{\Omega^{(e)}} \nabla \varphi^h d\Omega}{\Omega^{(e)}} \otimes \llbracket \dot{\boldsymbol{u}} \rrbracket^{(e)S}, \quad (5.27)$$

$$\frac{\int_{\Omega^{(e)}} \nabla^s \dot{\boldsymbol{u}}^h d\Omega}{\Omega^{(e)}} = (\nabla^s \dot{\boldsymbol{u}}^h)_{mean}^{(e)}, \quad \frac{\int_{\Omega^{(e)}} \nabla \varphi^h d\Omega}{\Omega^{(e)}} = (\nabla \varphi^h)_{mean}^{(e)}$$

where the mean values of the entities $(\bullet)_{mean}$ identified in equation (5.27), are replaced by the values at the central point of the finite element²⁸ $\overline{(\bullet)}$, according to Remark 3.1.3.1.

$$\hat{\boldsymbol{\varepsilon}}^{(e)} = (\nabla^s \dot{\boldsymbol{u}}^h)_{mean}^{(e)} - \left((\nabla \varphi^h)_{mean}^{(e)} \otimes \llbracket \dot{\boldsymbol{u}} \rrbracket^{(e)} \right)^S \approx \overline{\nabla^s \dot{\boldsymbol{u}}^h}^{(e)} - \left(\overline{\nabla \varphi^h}^{(e)} \otimes \llbracket \dot{\boldsymbol{u}} \rrbracket^{(e)} \right)^S. \quad (5.28)$$

²⁸ In terms of the finite element implementation, this is achieved by adding an additional sampling point, at the center of the element. This procedure is analogous to the one presented in section 3.1.3 for the $\dot{\boldsymbol{u}}, \dot{\boldsymbol{\varepsilon}}$ formulation.

As for the traction continuity equation (5.26), $\dot{\Sigma}(\hat{\epsilon}^{(e)})$ stands for the stress in the element (unloading) area outside the discontinuity, whereas, $\dot{\Sigma}(\dot{\epsilon}_S^{(e)})$ stands for the stress field at the element discontinuity surface. The localized strain field $\dot{\epsilon}_S^{(e)}$ can be evaluated in an additional sampling point representing the discontinuity., hence:

$$\dot{\epsilon}_S^{(e)} = \overline{\nabla^S \dot{\mathbf{u}}^h}^{(e)} - \left(\overline{\nabla \varphi^h}^{(e)} \otimes \llbracket \dot{\mathbf{u}} \rrbracket^{(e)} \right)^S + \frac{1}{k} \left(\mathbf{n}^{(e)} \otimes \llbracket \dot{\mathbf{u}} \rrbracket^{(e)} \right)^S, \quad (5.29)$$

Remark 5.1.4.1 For the sake of simplicity, avoiding the determination of the exact position of the discontinuity in the element, the additional sampling point used to evaluate $\dot{\Sigma}(\dot{\epsilon}_S^{(e)})$ is placed, also, at the center of the finite element. With mesh refinement, equation (5.26) yields equation (5.21), i.e. for $h \rightarrow 0$, $\dot{\Sigma}(\dot{\epsilon}_S^{(e)}) \rightarrow \sigma_S$ and $\dot{\Sigma}(\hat{\epsilon}^{(e)}) \rightarrow \sigma^+$.

Remark 5.1.4.2: The equilibrium equation (5.24) has dimensions of force whereas equation (5.26) has dimensions of traction. In order to supply dimensions of force to equation (5.26), it can be multiplied by the discontinuity length:

$$\text{meas}(\mathcal{S}^{(e)}) \dot{\Sigma}(\dot{\epsilon}_S^{(e)}) \cdot \mathbf{n} = \text{meas}(\mathcal{S}^{(e)}) \dot{\Sigma}(\hat{\epsilon}^{(e)}) \cdot \mathbf{n}^{(e)}, \quad (5.30)$$

that is equivalent to:

$$\int_{\mathcal{S}^{(e)}} \mathbf{n}^{(e)} \cdot \dot{\Sigma}(\dot{\epsilon}_S^{(e)}) d\mathcal{S} = \frac{\text{meas}(\mathcal{S}^{(e)})}{\underbrace{\text{meas}(\Omega^{(e)})}_{\ell^{(e)-1}}} \int_{\Omega^{(e)}} \mathbf{n}^{(e)} \cdot \dot{\Sigma}(\hat{\epsilon}^{(e)}) d\Omega. \quad (5.31)$$

where $\ell^{(e)}$ can be, by simplification, computed directly according to [Oliver 1989], where the crack is admitted to pass through the finite element centroid.

The un-symmetric finite element formulation is summarized in Box 5.2:

Given $\dot{\mathbf{u}}^* : \Gamma_u \rightarrow \mathbb{R}^N$, $\dot{\mathbf{t}}^* : \Gamma_\sigma \rightarrow \mathbb{R}^N$ and $\dot{\mathbf{b}} : \Omega \rightarrow \mathbb{R}^N$ find $\dot{\mathbf{u}}^h \in \hat{\mathcal{U}}^h$ and $\llbracket \dot{\mathbf{u}} \rrbracket \in \tilde{\mathcal{U}}^h$ such that for all $\hat{\boldsymbol{\eta}}^h \in \hat{\mathcal{N}}^h$:

$$\sum_{e \in \Omega} \int_{\Omega^{(e)}} \nabla^s \hat{\boldsymbol{\eta}}^h : \dot{\Sigma}(\hat{\epsilon}^{(e)}) d\Omega = \dot{\mathbf{F}}^{ext} \quad (5.32)$$

$$\int_{\mathcal{S}^{(e)}} \mathbf{n}^{(e)} \cdot \dot{\Sigma}(\dot{\epsilon}_S^{(e)}) d\mathcal{S} = \ell^{(e)-1} \int_{\Omega^{(e)}} \mathbf{n}^{(e)} \cdot \dot{\Sigma}(\hat{\epsilon}^{(e)}) d\Omega, \quad \forall e \in \Omega_{\mathcal{M}}$$

where :

$$\begin{aligned} \dot{\epsilon}_S^{(e)} &= \overline{\nabla^S \dot{\mathbf{u}}^h}^{(e)} - \left(\overline{\nabla \varphi^h}^{(e)} \otimes \llbracket \dot{\mathbf{u}} \rrbracket^{(e)} \right)^S + \frac{1}{k} \left(\mathbf{n}^{(e)} \otimes \llbracket \dot{\mathbf{u}} \rrbracket^{(e)} \right)^S & a) \\ \dot{\epsilon}^{(e)} &= \overline{\nabla^S \dot{\mathbf{u}}^h}^{(e)} - \left(\overline{\nabla \varphi^h}^{(e)} \otimes \llbracket \dot{\mathbf{u}} \rrbracket^{(e)} \right)^S & b) \end{aligned} \quad (5.33)$$

Box 5.2. Mixed $\dot{\mathbf{u}}, \dot{\epsilon}, \llbracket \dot{\mathbf{u}} \rrbracket$. Un-symmetric formulation.

For those elements not belonging to $\Omega_{\mathcal{M}}$ (*i.e.* not crossed by the strong discontinuity) $\overline{\nabla \varphi^h} = 0$, and according equation (5.33) $\dot{\varepsilon}^{(e)} = \overline{\nabla^S \dot{\mathbf{u}}^h}$.

Remark 5.1.4.2.: The chosen interpolation pairs for the mixed $\dot{\mathbf{u}}, \dot{\varepsilon}, [\![\dot{\mathbf{u}}]\!]$ formulation lead to an element-wise-constant approximation of the strain field in all the domain. Thus, according to the stated at Section 3.1.4, the stability of the interpolated fields cannot be guaranteed. Therefore, to avoid hourglass instabilities, an injected strain formulation will be proposed at Section 5.1.6.

Remark 5.1.4.3.: Analyzing expressions of Box 5.2 a significant difference relatively to the standard strong discontinuity approach can be found. In fact, the mixed $\dot{\mathbf{u}}, \dot{\varepsilon}, [\![\dot{\mathbf{u}}]\!]$ leads to the element-wise-constant regular strain field expressed by (5.33)-b), that can be integrated with one single gauss point, whereas in standard discontinuity approach the regular strain field is not constant and therefore, four gauss points are necessary. The interesting property of this issue is that, by using the $\dot{\mathbf{u}}, \dot{\varepsilon}, [\![\dot{\mathbf{u}}]\!]$ formulation, the stress locking problems associated to quadrilateral elements equipped with, piece-wise constant jump embedded discontinuities²⁹, are avoided (see Appendix B for an explanation of this improved behavior).

5.1.5. Symmetric formulation

In previous Sections, a un-symmetric formulation was presented. Alternatively, in this Section a Galerkin method is followed which derives in a symmetric formulation of the three field mixed finite element. Thus, defining \mathcal{N} and recalling \mathcal{U} from equation (5.17):

$$\mathcal{U} = \hat{\mathcal{U}} \oplus \tilde{\mathcal{U}} = \{ \mathbf{u} | \mathbf{u} = \hat{\mathbf{u}} + \tilde{\mathbf{u}} \}, \quad \mathcal{N} = \hat{\mathcal{N}} \oplus \tilde{\mathcal{N}} = \{ \boldsymbol{\eta} | \boldsymbol{\eta} = \hat{\boldsymbol{\eta}} + \tilde{\boldsymbol{\eta}} \}, \quad (5.34)$$

where:

$$\hat{\mathcal{U}} := \{ \hat{\mathbf{u}} | \hat{\mathbf{u}} \in [H^1(\Omega)]^n; \hat{\mathbf{u}}|_{\Gamma_u} = \mathbf{u}^* \}, \quad \tilde{\mathcal{U}} := \{ \tilde{\mathbf{u}} | \tilde{\mathbf{u}} = \mathcal{M}[\![\mathbf{u}]\!]^{(e)}; [\![\mathbf{u}]\!]^{(e)} \in [L_2(\Omega)]^n \},$$

and:

$$\hat{\mathcal{N}} := \{ \hat{\boldsymbol{\eta}} \in [H^1(\Omega)]^n; \hat{\boldsymbol{\eta}}|_{\Gamma_u} = 0 \}; \quad \tilde{\mathcal{N}} := \{ \tilde{\boldsymbol{\eta}} | \tilde{\boldsymbol{\eta}} = \mathcal{M}\boldsymbol{\beta}^{(e)}; \boldsymbol{\beta}^{(e)} \in [L_2(\Omega)]^n \},$$

²⁹ In [Linder and Armero 2007] and [Manzoli and Shing 2006] was reported that, bilinear quads equipped with piece-wise constant jump embedded discontinuities suffer from stress locking, in the sense that spurious stresses are transmitted through the discontinuity, even for the fully soften state. This type of stress locking, that it is not noticed when the equivalent triangular element (with piece-wise constant jump embedded discontinuities) is used, should not be confused with the classical stress locking of the traditional localization models (that was explained at Section 2.4.5).

and the finite element approximation of those functional spaces:

$$\mathcal{U}^h = \hat{\mathcal{U}}^h \oplus \tilde{\mathcal{U}}^h = \left\{ \mathbf{u}^h \mid \dot{\mathbf{u}}^h = \sum_{i=1}^{nnodes} N_i(\mathbf{x}) \dot{\mathbf{u}}_i^{(e)} + \sum_{e=1}^{nelem} \mathcal{M}^h(\mathbf{x}) [\mathbf{u}]^{(e)} \right\}; \mathcal{U}^h \subset \mathcal{U},$$

$$\mathcal{N}^h = \hat{\mathcal{N}}^h \oplus \tilde{\mathcal{N}}^h = \left\{ \boldsymbol{\eta}^h \mid \boldsymbol{\eta}^h = \sum_{i=1}^{nnodes} N_i(\mathbf{x}) \hat{\boldsymbol{\eta}}_i^{(e)} + \sum_{e=1}^{nelem} \mathcal{M}^h(\mathbf{x}) \boldsymbol{\beta}^{(e)} \right\}; \mathcal{N}^h \subset \mathcal{N}.$$

Additionally, for the functions $\dot{\boldsymbol{\varepsilon}}$ and $\boldsymbol{\mu}$, we select the spaces already defined in (5.16) *i.e.* \mathcal{E} and \mathcal{V} respectively.

Remark 5.1.5.1.: Comparing the functional spaces of the solution functions \mathcal{U} and \mathcal{E} , with the spaces of the weighting functions \mathcal{N} and \mathcal{V} , it is noticeable that, up to the homogeneous boundary, the spaces are equivalent, giving this a symmetric Galerkin formulation.

Testing equations (5.6) and (5.9) with the functions $\boldsymbol{\eta}^h$ and $\boldsymbol{\mu}^{(e)}$, and integrating over the domain, the following weak formulation is obtained:

$$\sum_{e \in \Omega} \int_{\Omega^{(e)}} \nabla^s \hat{\boldsymbol{\eta}}^h : \dot{\boldsymbol{\Sigma}}(\dot{\boldsymbol{\varepsilon}}^{(e)}) d\Omega = \dot{\mathbf{j}}^{ext}, \quad \forall \hat{\boldsymbol{\eta}}^h \in \hat{\mathcal{N}}^h, \quad (5.35)$$

$$\sum_{e \in \Omega} \int_{\Omega^{(e)}} \nabla^s \tilde{\boldsymbol{\eta}}^h : \dot{\boldsymbol{\Sigma}}(\dot{\boldsymbol{\varepsilon}}^{(e)}) d\Omega = 0, \quad \forall \tilde{\boldsymbol{\eta}}^h \in \tilde{\mathcal{N}}^h, \quad (5.36)$$

$$\int_{\Omega^{(e)}} \boldsymbol{\mu}^{(e)} : \left(\dot{\boldsymbol{\varepsilon}}^{(e)} - \nabla^s \dot{\mathbf{u}}^h + \left(\nabla \varphi^h \otimes [\dot{\mathbf{u}}]^{(e)} \right)^S \right) d\Omega = 0, \quad \forall \boldsymbol{\mu}^{(e)} \in \mathcal{V}^h, \quad \forall e \in \Omega. \quad (5.37)$$

Likewise it was done in Section 5.1.4, equation (5.37) can be solved at the element level for $\dot{\boldsymbol{\varepsilon}}^{(e)}$, giving:

$$\dot{\boldsymbol{\varepsilon}}^{(e)} = \overline{\nabla^s \dot{\mathbf{u}}^h}^{(e)} - \left(\overline{\nabla \varphi^h}^{(e)} \otimes [\dot{\mathbf{u}}]^{(e)} \right)^S. \quad (5.38)$$

Since $\nabla^s \tilde{\boldsymbol{\eta}}^h \neq 0$, only for elements belonging to $\Omega_{\mathcal{M}}$, it yields:

$$\int_{\Omega^{(e)}} \nabla^s \tilde{\boldsymbol{\eta}}^h : \dot{\boldsymbol{\Sigma}}(\dot{\boldsymbol{\varepsilon}}^{(e)}) d\Omega = 0, \quad \forall e \in \Omega_{\mathcal{M}}, \quad (5.39)$$

and from (5.34):

$$\nabla^s \tilde{\boldsymbol{\eta}}^h = - \left(\nabla \varphi^h \otimes \boldsymbol{\beta}^{(e)} \right)^S + \delta_S \left(\mathbf{n}^{(e)} \otimes \boldsymbol{\beta}^{(e)} \right)^S, \quad (5.40)$$

by substituting (5.40) in (5.39) and rearranging the terms:

$$\boldsymbol{\beta}^{(e)} \cdot \int_{\Omega^{(e)}} \nabla \varphi^h \cdot \dot{\boldsymbol{\Sigma}}(\dot{\boldsymbol{\varepsilon}}^{(e)}) d\Omega = \boldsymbol{\beta}^{(e)} \cdot \int_{\Omega^{(e)}} \delta_S \mathbf{n}^{(e)} \cdot \dot{\boldsymbol{\Sigma}}(\dot{\boldsymbol{\varepsilon}}^{(e)}) d\Omega, \quad \forall \boldsymbol{\beta}^{(e)}, \quad \forall e \in \Omega_{\mathcal{M}}, \quad (5.41)$$

For the terms on the right and left hand sides the following properties are used, respectively (see equation (4.4) and (5.14)):

$$\int_{\Omega^{(e)}} \delta_S \mathbf{n}^{(e)} \cdot \dot{\Sigma}(\dot{\varepsilon}^{(e)}) d\Omega = \int_{\mathcal{S}^{(e)}} \mathbf{n}^{(e)} \cdot \dot{\Sigma}(\dot{\varepsilon}^{(e)}) d\Omega, \quad (5.42)$$

$$\int_{\Omega^{(e)}} \nabla \varphi^h \cdot \dot{\Sigma}(\dot{\varepsilon}^{(e)}) d\Omega = \int_{\Omega^{(e)}} \nabla \varphi^h \cdot \dot{\Sigma}(\dot{\varepsilon}^{(e)}) d\Omega, \quad (5.43)$$

yielding:

$$\int_{\Omega^{(e)}} \nabla \varphi^h \cdot \dot{\Sigma}(\dot{\varepsilon}^{(e)}) d\Omega = \int_{\mathcal{S}^{(e)}} \mathbf{n}^{(e)} \cdot \dot{\Sigma}(\dot{\varepsilon}^{(e)}) d\Omega. \quad (5.44)$$

Moreover, since $\dot{\varepsilon}^{(e)}$ is constant inside the finite element (see Remark 3.1.3.2) the previous expression is equivalent to:

$$\int_{\Omega^{(e)}} \overline{\nabla \varphi^h}^{(e)} \cdot \dot{\Sigma}(\dot{\varepsilon}^{(e)}) d\Omega = \int_{\mathcal{S}^{(e)}} \mathbf{n}^{(e)} \cdot \dot{\Sigma}(\dot{\varepsilon}^{(e)}) d\mathcal{S}, \quad \forall e \in \Omega_{\mathcal{M}}. \quad (5.45)$$

Integrating the previous expression yields

$$\text{meas}(\Omega^{(e)}) \overline{\nabla \varphi^h}^{(e)} \cdot \dot{\Sigma}(\dot{\varepsilon}_{\Omega, \mathcal{S}}^{(e)}) = \text{meas}(\mathcal{S}^{(e)}) \mathbf{n}^{(e)} \cdot \dot{\Sigma}(\dot{\varepsilon}_{\mathcal{S}}^{(e)}), \quad \forall e \in \Omega_{\mathcal{M}}, \quad (5.46)$$

and simplifying,

$$\mathbf{r}^{(e)} \cdot \dot{\Sigma}(\dot{\varepsilon}_{\Omega, \mathcal{S}}^{(e)}) = \mathbf{n}^{(e)} \cdot \dot{\Sigma}(\dot{\varepsilon}_{\mathcal{S}}^{(e)}), \quad \forall e \in \Omega_{\mathcal{M}}, \quad (5.47)$$

being $\mathbf{r}^{(e)}$ a vector parallel to $\overline{\nabla \varphi}$

$$\mathbf{r}^{(e)} = \frac{\text{meas}(\Omega^{(e)})}{\text{meas}(\mathcal{S}^{(e)})} \overline{\nabla \varphi^h}^{(e)} = \ell^{(e)} \overline{\nabla \varphi^h}^{(e)}. \quad (5.48)$$

Remark 5.1.5.2: Notice that, unlike for the un-symmetric formulation, where traction continuity was directly imposed, expression (5.36) or (5.44) does not impose the traction continuity in a point-wise manner (excepting for the special case $\mathbf{r}^{(e)} = \mathbf{n}^{(e)}$). Nevertheless, it can be proven that this symmetric formulation imposes traction continuity in a variational manner ([Samaniego 2003]). Therefore, it is expected that, with mesh refinement, the results obtained with the symmetric formulation converge to those obtained with the un-symmetrical formulation.

Remark 5.1.5.3: In [Oliver, Huespe et al. 2006] the authors identified the lack of symmetry of the finite element formulation as a possible cause of loss of robustness of the numerical method. Therefore, although the symmetric formulation is more demanding in terms of computational costs, since finer meshes are required (see Remark 5.1.5.2), it is especially suitable for those problems where the robustness issues are critical.

The symmetric strong discontinuity finite element formulation is summarized in Box 5.3.

Given $\dot{\mathbf{u}}^* : \Gamma_u \rightarrow \mathbb{R}^N$, $\dot{\mathbf{t}}^* : \Gamma_\sigma \rightarrow \mathbb{R}^N$ and $\dot{\mathbf{b}} : \Omega \rightarrow \mathbb{R}^N$ find $\dot{\mathbf{u}}^h \in \mathcal{U}^h$ such that for

all $\boldsymbol{\eta}^h \in \mathcal{N}^h$

$$\sum_{e \in \Omega} \int_{\Omega^{(e)}} \nabla^s \boldsymbol{\eta}^h : \dot{\boldsymbol{\Sigma}}(\dot{\hat{\boldsymbol{\varepsilon}}}^{(e)}) d\Omega = \dot{\mathbf{F}}^{ext}$$

$$\int_{\mathcal{S}^{(e)}} \mathbf{n}^{(e)} \cdot \dot{\boldsymbol{\Sigma}}(\dot{\hat{\boldsymbol{\varepsilon}}}^{(e)}) d\mathcal{S} = \int_{\Omega^{(e)}} \overline{\nabla \varphi^h}^{(e)} \cdot \dot{\boldsymbol{\Sigma}}(\dot{\hat{\boldsymbol{\varepsilon}}}^{(e)}) d\Omega, \quad \forall e \in \Omega_{\mathcal{M}}$$

where:

$$\begin{aligned} \dot{\hat{\boldsymbol{\varepsilon}}}^{(e)} &= \overline{\nabla^s \dot{\mathbf{u}}^h}^{(e)} - \left(\overline{\nabla \varphi^h}^{(e)} \otimes [\dot{\mathbf{u}}]^{(e)} \right)^S + \frac{1}{k} \left(\mathbf{n}^{(e)} \otimes [\dot{\mathbf{u}}]^{(e)} \right)^S \\ \dot{\hat{\boldsymbol{\varepsilon}}}^{(e)} &= \overline{\nabla^s \dot{\mathbf{u}}^h}^{(e)} - \left(\overline{\nabla \varphi^h}^{(e)} \otimes [\dot{\mathbf{u}}]^{(e)} \right)^S \end{aligned}$$

Box 5.3 Mixed $\dot{\mathbf{u}}, \dot{\hat{\boldsymbol{\varepsilon}}}, [\dot{\mathbf{u}}]$. Symmetric strong discontinuity formulation.

5.1.6. The Strong discontinuity injection

Restricting the three field mixed formulation to a domain of interest, the strong discontinuity injection can be introduced. The domain of interest is termed here, generically, as the injection domain Ω_{inj} (a domain where are performed injections)³⁰. The injected formulation is developed following a similar procedure to that used in Section 3.2.2, *i.e.*, the functional spaces $\tilde{\mathcal{U}}$, $\tilde{\mathcal{N}}$, \mathcal{E} and \mathcal{V} are just defined in the injection domain, Ω_{inj} , whereas $\hat{\mathcal{U}}$ and $\hat{\mathcal{N}}$ are defined in the entire domain Ω . The following rate equations are derived:

$$\int_{\Omega \setminus \Omega_{inj}} \nabla^s \hat{\boldsymbol{\eta}}^h : \dot{\boldsymbol{\Sigma}}(\nabla^s \dot{\mathbf{u}}^h) d\Omega + \sum_{e \in \Omega_{inj}} \int_{\Omega^{(e)}} \nabla^s \hat{\boldsymbol{\eta}}^h : \dot{\boldsymbol{\Sigma}}(\dot{\hat{\boldsymbol{\varepsilon}}}^{(e)}) d\Omega = \dot{\mathbf{f}}^{ext}, \quad a) \quad (5.49)$$

$$\int_{\Omega^{(e)}} \boldsymbol{\mu}^{(e)} : \left\{ \dot{\hat{\boldsymbol{\varepsilon}}}^{(e)} - \nabla^s \dot{\mathbf{u}}^h + \left(\nabla \varphi^h \otimes [\dot{\mathbf{u}}]^{(e)} \right)^S \right\} d\Omega = 0, \quad \forall e \in \Omega_{inj}. \quad b)$$

Where the injected strain field is solved at the elemental level:

$$\dot{\hat{\boldsymbol{\varepsilon}}}^{(e)} = \overline{\nabla^s \dot{\mathbf{u}}^h}^{(e)} - \left(\overline{\nabla \varphi^h}^{(e)} \otimes [\dot{\mathbf{u}}]^{(e)} \right)^S, \quad \forall e \in \Omega_{inj} \quad (5.50)$$

The element-wise constant kinematics in equation (5.50), is now interpreted as a strong discontinuity mode to be injected into the constitutive equation of those elements belonging to the injection domain Ω_{inj} .

³⁰ At Section 5.3.6 the injection domain where discontinuities are injected, is defined in detail.

As previously shown, depending on the selection of the functional spaces, a symmetric or a un-symmetric formulation can be derived. In Box 5.4 both options are summarized.

Given $\dot{\mathbf{u}}^* : \Gamma_u \rightarrow \mathbb{R}^N$, $\dot{\mathbf{t}}^* : \Gamma_\sigma \rightarrow \mathbb{R}^N$ and $\dot{\mathbf{b}} : \Omega \rightarrow \mathbb{R}^N$ find $\hat{\mathbf{u}}^h \in \hat{\mathcal{U}}^h$ and $[\![\dot{\mathbf{u}}]\!] \in \tilde{\mathcal{U}}^h$ such that for all $\boldsymbol{\eta}^h \in \mathcal{N}^h$:

$$\int_{\Omega \setminus \Omega_{inj}} \nabla^s \hat{\boldsymbol{\eta}}^h : \dot{\boldsymbol{\Sigma}}(\nabla^s \hat{\mathbf{u}}^h) d\Omega + \sum_{e \in \Omega_{inj}} \int_{\Omega^{(e)}} \nabla^s \hat{\boldsymbol{\eta}}^h : \dot{\boldsymbol{\Sigma}}(\dot{\hat{\boldsymbol{\epsilon}}}^{(e)}) d\Omega = \dot{\mathbf{f}}^{ext} \quad (5.51)$$

a) Un-symmetric formulation:

$$\int_{\mathcal{S}^{(e)}} \mathbf{n}^{(e)} \cdot \dot{\boldsymbol{\Sigma}}(\dot{\hat{\boldsymbol{\epsilon}}}_S^{(e)}) d\mathcal{S} = \ell^{(e)-1} \int_{\Omega^{(e)}} \mathbf{n}^{(e)} \cdot \dot{\boldsymbol{\Sigma}}(\dot{\hat{\boldsymbol{\epsilon}}}^{(e)}) d\Omega, \quad \forall e \in \Omega_{inj} \quad (5.52)$$

b) Symmetric formulation

$$\int_{\mathcal{S}^{(e)}} \mathbf{n}^{(e)} \cdot \dot{\boldsymbol{\Sigma}}(\dot{\hat{\boldsymbol{\epsilon}}}_S^{(e)}) d\mathcal{S} = \int_{\Omega^{(e)}} \overline{\nabla \varphi^h}^{(e)} \cdot \dot{\boldsymbol{\Sigma}}(\dot{\hat{\boldsymbol{\epsilon}}}^{(e)}) d\Omega, \quad \forall e \in \Omega_{inj} \quad (5.53)$$

where:

$$\begin{aligned} \dot{\hat{\boldsymbol{\epsilon}}}_S^{(e)} &= \overline{\nabla^s \hat{\mathbf{u}}^h}^{(e)} - \left(\overline{\nabla \varphi^h}^{(e)} \otimes [\![\dot{\mathbf{u}}]\!]^{(e)} \right)^S + \frac{1}{k} \left(\mathbf{n}^{(e)} \otimes [\![\dot{\mathbf{u}}]\!]^{(e)} \right)^S \\ \dot{\hat{\boldsymbol{\epsilon}}}^{(e)} &= \overline{\nabla^s \hat{\mathbf{u}}^h}^{(e)} - \left(\overline{\nabla \varphi^h}^{(e)} \otimes [\![\dot{\mathbf{u}}]\!]^{(e)} \right)^S \end{aligned}$$

Box 5.4 Strong discontinuity injection.

Remark 5.1.6.1: It is well known, that the strong discontinuity kinematics can be only successfully induced, for specific stress states, fulfilling certain restrictions - the so called strong discontinuity conditions ([Oliver, Cervera et al. 1999]). To reach that conditions, a variable bandwidth model, $k(q)$, function of the stress like internal variable q , needs to be introduced. At this point different options are possible. In this work a bandwidth changing according with an exponential function is considered. Figure 5.6 sketches this concept.

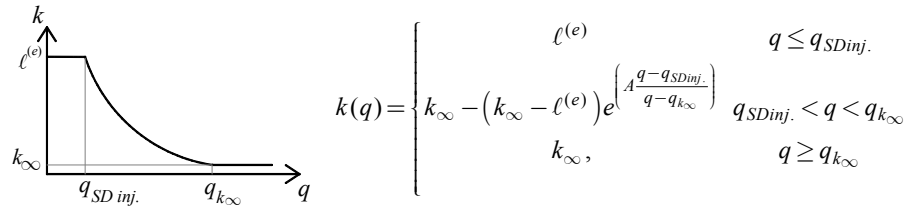


Figure 5.6 Variable bandwidth model, $k(q)$.

In Figure 5.6 $q_{SDinj.}$ stands for the value of the stress like internal variable at the moment when the strong discontinuity is injected, q_{k_∞} establishes the end of

the transition depicted in Figure 5.6, $\ell^{(e)}$ is the finite element characteristic length, k_∞ is a small regularizing parameter (a fraction of the element size) that can be chosen as small as permitted by the machine precision and A stands for a parameter characterizing the exponential curve.

Notice that, at initial stages, immediately after the strong discontinuity injection, the regularizing parameter attains relatively large values with respect to the typical element size. Although, this case should not be confused with a weak discontinuity case³¹ (that will be introduced in next Section), since k represents here just a regularizing parameter being the equilibrium equation (5.51) still fulfilled in terms of the elastic strains (according to the strong discontinuity concept).

Remark 5.1.6.2: In the case described in Remark 5.1.6.1 (for values of k not tending to zero), the strain field is not compatible with the displacement field (see Figure 5.7).

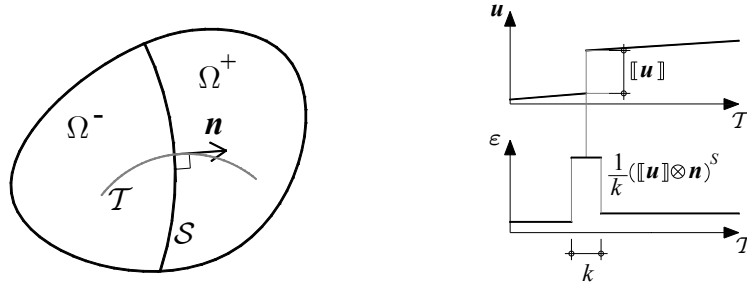


Figure 5.7 Strong discontinuity with regularized kinematics.

5.2. Weak discontinuities

An embedded weak discontinuity model was first proposed in the pioneering work of Ortiz [Ortiz, Leroy et al. 1987]. Recently, in [Huespe et al. 2009] an application to ductile fracture analysis was performed. The conceptual difference between strong and weak discontinuities, concerns the displacement jump, that is captured, not in a zero thickness surface (as it happens in the strong discontinuity case), but instead, it is smeared over a finite length. The main consequences are that the displacement field, \mathbf{u} , remains continuous and the strains, $\dot{\boldsymbol{\epsilon}}$, are bounded.

³¹ In the literature, this case is often referred as a weak discontinuity what is a small abuse of the nomenclature.

5.2.1. Weak discontinuity kinematics

In Section 5.1.1 the regularized strong discontinuity kinematics was introduced. Here, a weak discontinuity kinematics is written as follows, see Figure 5.8:

$$\dot{\mathbf{u}} = \dot{\hat{\mathbf{u}}} + \mathcal{H}_{\Omega_S} [[\dot{\mathbf{u}}]] = \dot{\hat{\mathbf{u}}} + \frac{(\mathcal{H}_{\Omega_S} - \varphi)[[\dot{\mathbf{u}}]]}{\mathcal{M}}, \quad (5.54)$$

where $\dot{\hat{\mathbf{u}}}$ stands for the smooth part of the displacement field, \mathcal{H}_{Ω_S} stands for the ramp function in the direction \mathbf{n} , $\dot{\hat{\mathbf{u}}}$ is a continuous part of the displacement, $[[\dot{\mathbf{u}}]]$ is the apparent displacement jump smeared in the domain Ω_S and φ is a continuous arbitrary function that fulfills the following two conditions:

$$\varphi(\mathbf{x}) = \begin{cases} 0 & \forall \mathbf{x} \in (\Omega \setminus \Omega_{\mathcal{M}})^- \\ 1 & \forall \mathbf{x} \in (\Omega \setminus \Omega_{\mathcal{M}})^+ \end{cases}, \quad (5.55)$$

being the domain, $\Omega_{\mathcal{M}}$, the support of function \mathcal{M} (see Figure 5.8). Notice that $\Omega_{\mathcal{M}} \subset \Omega_S$, *i.e.* Ω_S does not necessarily coincides with $\Omega_{\mathcal{M}}$.

The strain field compatible with (5.54) reads:

$$\dot{\boldsymbol{\varepsilon}} = \nabla^S \dot{\hat{\mathbf{u}}} - (\nabla \varphi \otimes [[\dot{\mathbf{u}}]])^S + \frac{\mu_{\Omega_S}}{h} (\mathbf{n} \otimes [[\dot{\mathbf{u}}]])^S, \quad (5.56)$$

where \mathbf{n} is the unit vector orthogonal to \mathcal{S} , μ_{Ω_S} is a collocation function on Ω_S and $h(\mathbf{x})$ is the finite thickness of the weak discontinuity.

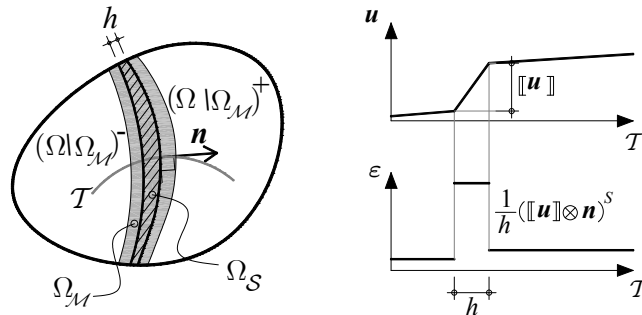


Figure 5.8 *Weak discontinuity kinematics.*

Comparing the regularized strong (5.4) and the weak (5.56) discontinuity kinematics, the difference is that, in the former, k is a regularization parameter tending to zero (a mathematical artifact to deal with displacement discontinuities in an computational mechanics setting), while in the later, h , is a finite length representing the bandwidth of a weak discontinuity. The value of h , might correspond to a physically meaning length (like in non local or gradient methods), or it can be selected for the convenience of the numerical simulation

Regardless the similar aspects between strong and weak discontinuities, that are evident, the conceptual kinematic difference between strong and weak discontinuities implies also some important consequences in terms of practical numerical modeling (this differences will further remarked in the next Sections).

Remark 5.2.1.1: Notice that if the bandwidth h is reduced to very small value ($h \rightarrow 0$) the weak discontinuity represented in (5.56) would collapse into a strong discontinuity since when $h \rightarrow 0$ $\frac{\mu_{\Omega_S}}{h} \rightarrow \delta_S$ and the ramp function \mathcal{H}_{Ω_S} would tend to the step function \mathcal{H}_S . In this work, this property is not exploited, since both finite element formulations are developed from different starting points. However, this issue can be the starting point for developing some more general methodologies, where the transition from a weak to a strong discontinuity is also modeled, according the fracture process presented at the beginning of Chapter 2 (see Figure 2.3).

5.2.2. Three field $(\hat{\mathbf{u}}, \dot{\hat{\boldsymbol{\varepsilon}}}, \llbracket \dot{\hat{\mathbf{u}}} \rrbracket)$ mixed formulation

In Section 5.1.3, based on the strong discontinuity kinematics, a mixed formulation $\hat{\mathbf{u}}, \dot{\hat{\boldsymbol{\varepsilon}}}, \llbracket \dot{\hat{\mathbf{u}}} \rrbracket$ was proposed. Here we derive a mixed formulation for the case of the weak discontinuity kinematics. Unlike in the strong discontinuity kinematics case, here the discontinuity bandwidth has a finite length, this meaning, that the stresses at the discontinuity are no longer negligible in terms of their contribution to the equilibrium equation (5.14). Therefore, for the present case, the natural idea is to consider the full strain $\dot{\hat{\boldsymbol{\varepsilon}}}$ as the independent variable, instead of the regular part of the strain tensor $\dot{\hat{\boldsymbol{\varepsilon}}}$ that was taken in Section 5.1.3. Thus, testing equations (5.6) and (5.9) with the test function $\hat{\boldsymbol{\eta}}$ and $\boldsymbol{\mu}$, and integrating over the domain, the following weak formulation is obtained:

$$\int_{\Omega} \nabla^s \hat{\boldsymbol{\eta}} : \dot{\hat{\boldsymbol{\Sigma}}}(\dot{\hat{\boldsymbol{\varepsilon}}}) d\Omega = \dot{\mathbf{f}}^{ext},$$

$$\int_{\Omega} \boldsymbol{\mu} : \left(\dot{\hat{\boldsymbol{\varepsilon}}} - \left(\nabla^s \hat{\mathbf{u}} - (\nabla \varphi \otimes \llbracket \dot{\hat{\mathbf{u}}} \rrbracket)^S + \frac{\mu_{\Omega_S}}{h} (\mathbf{n} \otimes \llbracket \dot{\hat{\mathbf{u}}} \rrbracket)^S \right) \right) d\Omega = 0, \quad (5.57)$$

being the inner traction continuity imposed in a strong form:

$$\boldsymbol{\sigma}_S \cdot \mathbf{n} = \boldsymbol{\sigma}^+ \cdot \mathbf{n}. \quad (5.58)$$

Relatively to the functional spaces for the functions appearing in equations (5.57) the spaces already defined at Section 5.1.3 are selected.

5.2.3. Three field mixed formulation – Finite element approximation – Un-symmetric formulation

Regarding to the finite element interpolations, the approximations specified at Section 5.1.3 are used, *i.e.* standard continuous bilinear interpolations for the smooth part of the displacement field $\hat{\mathbf{u}}$, and element-wise-constant discontinuous finite element interpolations for the strains $\hat{\boldsymbol{\epsilon}}$ and displacement jump $[[\hat{\mathbf{u}}]]$ (see equations (5.22)).

In the context of the finite element method, the weak discontinuity bandwidth, $h^{(e)}$, introduced in equation (5.56) can be linked to the finite element size, *i.e.* as a fraction of the element characteristic length $\ell^{(e)}$: $h^{(e)} = \kappa \ell^{(e)}$, $\kappa \in (0,1]$.

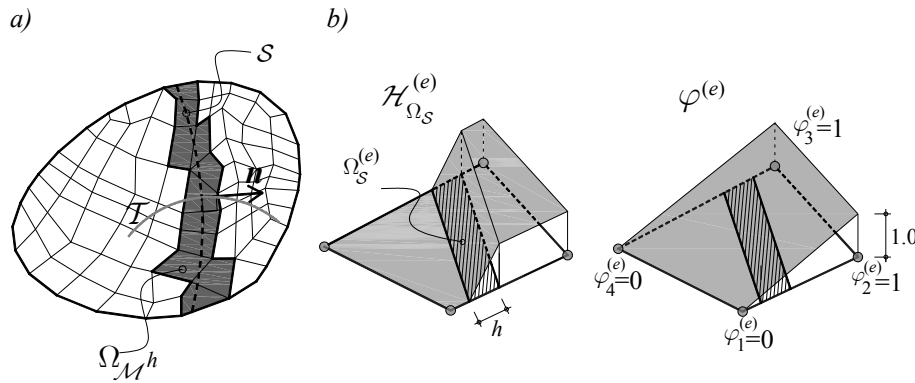


Figure 5.9 a) Discretized body with discontinuity, b) Elemental functions $\mathcal{H}_{\Omega_S}^{(e)}$, $\varphi^{(e)}$.

The function φ^h , is constructed as in Section 5.1.4 (see equation (5.23)), being also $\mathcal{M}^h = \mathcal{H}_{\Omega_S} - \varphi^h$ a function with elemental support.

In this work, we consider the *weak discontinuity bandwidth equal to the element characteristic length* [Oliver 1989], *i.e.* $h^{(e)} = \ell^{(e)}$ and thus $\Omega_S \equiv \Omega_{\mathcal{M}}$ (see Figure 5.10). This case is of special interest, since the weak discontinuity is smeared over all the finite element length, likewise in the classical strain localization methods (where the softening modulus is regularized with the element characteristic length). The advantage, relatively to the classical methods, is that, the enhanced kinematics will permit strain localization to occur, without spurious stress transfer to the neighboring elements. Additionally this option also allows obtaining an element-wise-constant strain field since, at the element level $\Omega_S^{(e)} \equiv \Omega^{(e)}$ and thus $\Omega^{(e)} \setminus \Omega_S^{(e)} = \emptyset$.

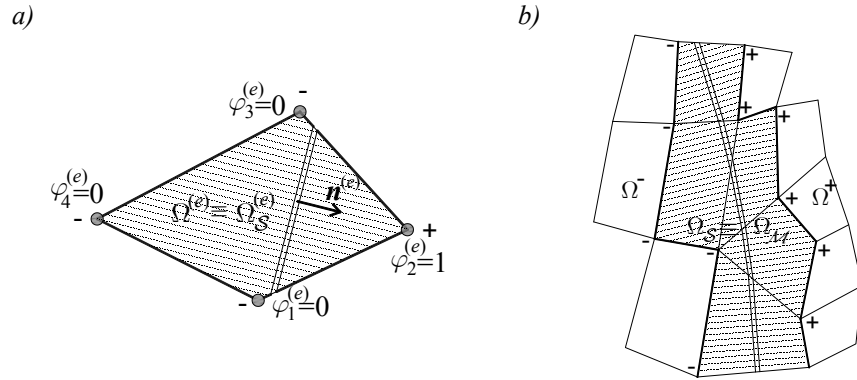


Figure 5.10 a) Finite element with embedded weak discontinuity, b) Weak discontinuity band.

Regarding the finite element approximations, a discrete version of (5.57) reads:

$$\sum_{e \in \Omega} \int_{\Omega^{(e)}} \nabla^s \hat{\boldsymbol{\eta}}^h : \dot{\boldsymbol{\Sigma}}(\dot{\boldsymbol{\varepsilon}}^{(e)}) d\Omega = \mathbf{j}^{ext}, \quad (5.59)$$

$$\int_{\Omega^{(e)}} \boldsymbol{\mu}^{(e)} : \left(\dot{\boldsymbol{\varepsilon}}^{(e)} - \nabla^S \dot{\boldsymbol{u}}^h + \left(\nabla \varphi^h \otimes [\dot{\boldsymbol{u}}]^{(e)} \right)^S + \frac{\mu_{\Omega_S}}{\ell^{(e)}} \left(\mathbf{n}^{(e)} \otimes [\dot{\boldsymbol{u}}]^{(e)} \right)^S \right) d\Omega = 0, \forall e \in \Omega \quad (5.60)$$

$$\dot{\boldsymbol{\Sigma}}(\hat{\boldsymbol{\varepsilon}}_{\Omega \setminus \Omega_S}^{(e)}) \cdot \mathbf{n}^{(e)} = \dot{\boldsymbol{\Sigma}}(\dot{\boldsymbol{\varepsilon}}_{\Omega_S}^{(e)}) \cdot \mathbf{n}^{(e)}, \forall e \in \Omega_{\mathcal{M}^h}. \quad (5.61)$$

where the strain field $\dot{\boldsymbol{\varepsilon}}^{(e)}$, the displacement jump $[\dot{\boldsymbol{u}}]^{(e)}$ and the weighting function $\boldsymbol{\mu}^{(e)}$ are chosen to be element-wise-constant and discontinuous between elements. Then, equation (5.60) can be solved at the element level, being $\dot{\boldsymbol{\varepsilon}}^{(e)}$ the constant projection of $\nabla^S \dot{\boldsymbol{u}}^h + \left(\nabla \varphi^h \otimes [\dot{\boldsymbol{u}}]^{(e)} \right)^S + \frac{1}{\ell^{(e)}} \left(\mathbf{n}^{(e)} \otimes [\dot{\boldsymbol{u}}]^{(e)} \right)^S$:

$$\dot{\boldsymbol{\varepsilon}}^{(e)} = \overline{\nabla^S \dot{\boldsymbol{u}}^h}^{(e)} + \left(\overline{\nabla \varphi^h}^{(e)} \otimes [\dot{\boldsymbol{u}}]^{(e)} \right)^S + \frac{\mu_{\Omega_S}}{\ell^{(e)}} \left(\mathbf{n}^{(e)} \otimes [\dot{\boldsymbol{u}}]^{(e)} \right)^S, \quad \forall e \in \Omega. \quad (5.62)$$

Notice that outside $\Omega_{\mathcal{M}}$: $\dot{\boldsymbol{\varepsilon}}^{(e)} = \overline{\nabla^S \dot{\boldsymbol{u}}^h}^{(e)}$, since $\overline{\nabla \varphi^h}^{(e)} = 0$ and $\mu_{\Omega_S} = 0$.

As for the traction continuity equation (5.61), $\dot{\boldsymbol{\Sigma}}(\dot{\boldsymbol{\varepsilon}}_{\Omega_S}^{(e)})$ is the element-wise-constant stress field representative of the weak discontinuity, being evaluated in a sampling point located in the centroid of the finite element. On the other hand, $\dot{\boldsymbol{\Sigma}}(\hat{\boldsymbol{\varepsilon}}_{\Omega \setminus \Omega_S}^{(e)})$ stands for the stress under the ‘‘elastic strains’’ $\hat{\boldsymbol{\varepsilon}}_{\Omega \setminus \Omega_S}^{(e)}$. For simplicity reasons, the stress state, $\dot{\boldsymbol{\Sigma}}(\hat{\boldsymbol{\varepsilon}}_{\Omega \setminus \Omega_S}^{(e)})$ will be also evaluated in an additional gauss

point at the center of the finite element. In this point an elastic behavior is forced in order to guaranty an unloading process.

$$\begin{aligned}\dot{\hat{\epsilon}}_{\Omega_S}^{(e)} &= \overline{\nabla^S \dot{\hat{\mathbf{u}}^h}^{(e)}} + \left(\overline{\nabla \varphi^h}^{(e)} \otimes [\dot{\hat{\mathbf{u}}}]^{(e)} \right)^S + \frac{1}{\ell^{(e)}} \left(\mathbf{n}^{(e)} \otimes [\dot{\hat{\mathbf{u}}}]^{(e)} \right)^S, \\ \dot{\hat{\epsilon}}_{\Omega \setminus \Omega_S}^{(e)} &= \overline{\nabla^S \dot{\hat{\mathbf{u}}^h}^{(e)}} + \left(\overline{\nabla \varphi^h}^{(e)} \otimes [\dot{\hat{\mathbf{u}}}]^{(e)} \right)^S.\end{aligned}\quad (5.63)$$

Moreover, in those elements belonging to $\Omega_{\mathcal{M}}$, the integral in Equation (5.59) can be subdivided in two parts corresponding to $\Omega_S^{(e)}$ and $\Omega^{(e)} \setminus \Omega_S^{(e)}$:

$$\begin{aligned}\sum_{e \in \Omega \setminus \Omega_{\mathcal{M}}} \int_{\Omega^{(e)}} \nabla^s \hat{\boldsymbol{\eta}}^h : \dot{\hat{\Sigma}} \left(\overline{\nabla^S \dot{\hat{\mathbf{u}}^h}^{(e)}} \right) d\Omega + \sum_{e \in \Omega_{\mathcal{M}}} \underbrace{\int_{\Omega^{(e)} \setminus \Omega_S} \nabla^s \hat{\boldsymbol{\eta}}^h : \dot{\hat{\Sigma}} \left(\dot{\hat{\epsilon}}_{\Omega \setminus \Omega_S}^{(e)} \right) d\Omega}_{=0} + \\ + \sum_{e \in \Omega_{\mathcal{M}}} \int_{\Omega_S^{(e)}} \nabla^s \hat{\boldsymbol{\eta}}^h : \dot{\hat{\Sigma}} \left(\dot{\hat{\epsilon}}_{\Omega_S}^{(e)} \right) d\Omega = \dot{\mathbf{f}}^{ext},\end{aligned}\quad (5.64)$$

since $h^{(e)}$ was chosen to be equal to the element size ($h^{(e)} = \ell^{(e)}$), the weak discontinuity will be smeared over all the element length, *i.e.* $\Omega^{(e)} \equiv \Omega_S^{(e)}$ and $meas(\Omega^{(e)} \setminus \Omega_S^{(e)}) = 0$ this meaning that the second integral in (5.64) vanishes.

Remark 5.2.3.1: Unlike in the strong discontinuity case, here, in those elements containing the discontinuity, the equilibrium equation involves the inelastic stresses, (see (5.64)).

The finite element form of the problem may be then stated as:

Given $\dot{\mathbf{u}}^* : \Gamma_u \rightarrow \mathbb{R}^N$, $\dot{\mathbf{t}}^* : \Gamma_\sigma \rightarrow \mathbb{R}^N$ and $\dot{\mathbf{b}} : \Omega \rightarrow \mathbb{R}^N$ find $\dot{\hat{\mathbf{u}}^h} \in \mathcal{U}^h$ such that for all $\hat{\boldsymbol{\eta}}^h \in \hat{\mathcal{N}}^h$:

$$\begin{aligned}\sum_{e \in \Omega} \int_{\Omega^{(e)}} \nabla^s \hat{\boldsymbol{\eta}}^h : \dot{\hat{\Sigma}}(\dot{\hat{\epsilon}}^{(e)}) d\Omega = \dot{\mathbf{F}}^{ext} \\ \dot{\hat{\Sigma}}(\dot{\hat{\epsilon}}_{\Omega \setminus \Omega_S}^{(e)}) \cdot \mathbf{n}^{(e)} = \dot{\hat{\Sigma}}(\dot{\hat{\epsilon}}_{\Omega_S}^{(e)}) \cdot \mathbf{n}^{(e)}, \forall e \in \Omega_{\mathcal{M}}\end{aligned}\quad (5.65)$$

where:

$$\dot{\hat{\epsilon}}^{(e)} = \overline{\nabla^S \dot{\hat{\mathbf{u}}^h}^{(e)}} + \left(\overline{\nabla \varphi^h}^{(e)} \otimes [\dot{\hat{\mathbf{u}}}]^{(e)} \right)^S + \frac{\mu_{\Omega_S}}{\ell^{(e)}} \left(\mathbf{n}^{(e)} \otimes [\dot{\hat{\mathbf{u}}}]^{(e)} \right)^S$$

Box 5.5 Mixed $\dot{\hat{\mathbf{u}}} - \dot{\hat{\epsilon}} - [\dot{\hat{\mathbf{u}}}]$ weak discontinuity formulation.

5.2.4. The Weak discontinuity injection

The weak discontinuity injection is introduced in the same manner than in Section 5.1.6, that is, by restricting the three field mixed formulation $\dot{\mathbf{u}}, \dot{\boldsymbol{\varepsilon}}, [\dot{\mathbf{u}}]$ to the injection domain.

$$\int_{\Omega \setminus \Omega_{inj}} \nabla^s \hat{\boldsymbol{\eta}}^h : \dot{\boldsymbol{\Sigma}}(\nabla^S \hat{\mathbf{u}}^h) d\Omega + \sum_{e \in \Omega_{inj}} \int_{\Omega^{(e)}} \nabla^s \hat{\boldsymbol{\eta}}^h : \dot{\boldsymbol{\Sigma}}(\dot{\boldsymbol{\varepsilon}}^{(e)}) d\Omega = \mathbf{j}^{ext}, \quad (5.66)$$

$$\int_{\Omega^{(e)}} \boldsymbol{\mu}^{(e)} : \left(\dot{\boldsymbol{\varepsilon}}^{(e)} - \nabla^S \hat{\mathbf{u}}^h + \left(\nabla \varphi^h \otimes [\dot{\mathbf{u}}]^{(e)} \right)^S + \frac{\mu_{\Omega_S}}{\ell^{(e)}} \left(\mathbf{n}^{(e)} \otimes [\dot{\mathbf{u}}]^{(e)} \right)^S \right) d\Omega = 0, \forall e \in \Omega_{inj}$$

where the injected strain field is solved at the element level:

$$\dot{\boldsymbol{\varepsilon}}^{(e)} = \overline{\nabla^S \hat{\mathbf{u}}^h}^{(e)} + \left(\overline{\nabla \varphi^h}^{(e)} \otimes [\dot{\mathbf{u}}]^{(e)} \right)^S + \frac{\mu_{\Omega_S}}{\ell^{(e)}} \left(\mathbf{n}^{(e)} \otimes [\dot{\mathbf{u}}]^{(e)} \right)^S, \forall e \in \Omega_{inj}. \quad (5.67)$$

The constant kinematics represented in equation (5.67), is now interpreted as a weak discontinuity mode to be injected in the constitutive equation of those elements belonging to the injection domain Ω_{inj} .

Remark 5.2.4.1: The weak discontinuity injection has interest since it can be regarded as a *direct enhanced extension of the previous constant strain injection* presented at Section 3.2. That is, the discontinuity is still smeared over all the finite element length, the equilibrium is fulfilled with the inelastic stresses $\dot{\boldsymbol{\Sigma}}(\dot{\boldsymbol{\varepsilon}}_{\Omega_S}^{(e)})$ (representative of the discontinuity) and the softening regularization. is performed with the element characteristic length $\ell^{(e)}$.

Given $\dot{\mathbf{u}}^* : \Gamma_u \rightarrow \mathbb{R}^N$, $\dot{\mathbf{t}}^* : \Gamma_\sigma \rightarrow \mathbb{R}^N$ and $\dot{\mathbf{b}} : \Omega \rightarrow \mathbb{R}^N$ find $\dot{\mathbf{u}} \in \hat{\mathcal{U}}^h$ and $[\dot{\mathbf{u}}]^{(e)} \in \tilde{\mathcal{U}}^h$ such that for all $\hat{\boldsymbol{\eta}}^h \in \hat{\mathcal{N}}^h$

$$\int_{\Omega \setminus \Omega_{inj}} \nabla^s \hat{\boldsymbol{\eta}}^h : \dot{\boldsymbol{\Sigma}}(\nabla^S \hat{\mathbf{u}}^h) d\Omega + \sum_{e \in \Omega_{inj}} \int_{\Omega^{(e)}} \nabla^s \hat{\boldsymbol{\eta}}^h : \dot{\boldsymbol{\Sigma}}(\dot{\boldsymbol{\varepsilon}}_{\Omega_S}^{(e)}) d\Omega = \mathbf{j}^{ext}$$

$$\dot{\boldsymbol{\Sigma}}(\dot{\boldsymbol{\varepsilon}}_{\Omega_S}^{(e)}) \cdot \mathbf{n}^{(e)} = \dot{\boldsymbol{\Sigma}}(\dot{\boldsymbol{\varepsilon}}_{\Omega_S}^{(e)}) \cdot \mathbf{n}^{(e)}, \forall e \in \Omega_{inj}$$

where:

$$\dot{\boldsymbol{\varepsilon}}_{\Omega_S}^{(e)} = \overline{\nabla^S \hat{\mathbf{u}}^h}^{(e)} - \left(\overline{\nabla \varphi^h}^{(e)} \otimes [\dot{\mathbf{u}}]^{(e)} \right)^S + \frac{1}{\ell^{(e)}} \left(\mathbf{n}^{(e)} \otimes [\dot{\mathbf{u}}]^{(e)} \right)^S \quad (5.68)$$

$$\dot{\boldsymbol{\varepsilon}}_{\Omega \setminus \Omega_S}^{(e)} = \overline{\nabla^S \hat{\mathbf{u}}^h}^{(e)} - \left(\overline{\nabla \varphi^h}^{(e)} \otimes [\dot{\mathbf{u}}]^{(e)} \right)^S$$

Box 5.6 Weak discontinuity injection.

We remark that here it is admitted that $\Omega_{inj} \equiv \Omega_{\mathcal{M}}$.

5.3. The crack path and the discontinuity domain

It is well known that standard localization methods are able to provide localized solutions. However, due to kinematics flaws, their performance for capturing real material fracture is considered insufficient (as shown in previous Chapters). It was shown at Section 4.4 that, despite the improvements obtained with the CSM injection, namely in terms of mesh bias independence, results are still not satisfactory. The natural consequent idea is to enhance the element kinematic performance by injecting strong/weak discontinuity modes, as defined at Sections 5.1.6 and 5.2.4

In order to perform the discontinuous mode injection two typical questions arise: Which elements have to be injected? How does the discontinuity cross the finite element? In the ambit of the strong discontinuity approach, this information is generally obtained by resorting to global tracking algorithms that we aim to avoid.

Here we propose an alternative procedure based on a local smoothing technique of the strain-like internal variable: The discontinuity injection is slightly delayed, relatively to the bifurcation time (computed for each element), in order to obtain a diffuse localizing strain field. Then, the idea is to determine where the strong/weak discontinuity “corresponding” to the imperfect localized strain field should be placed. In Section 5.3.2 this idea is formalized as the crack-propagation problem. The set of elements to be injected with a discontinuous mode will constitute the discontinuity injection domain Ω_{Dis} .

5.3.1. One-dimension-problem: Motivation (double smoothing)

First, to illustrate the motivation of the methodology, let us analyze a hypothetical one dimensional spatial distribution of a localizing strain-like internal variable in a continuum problem.

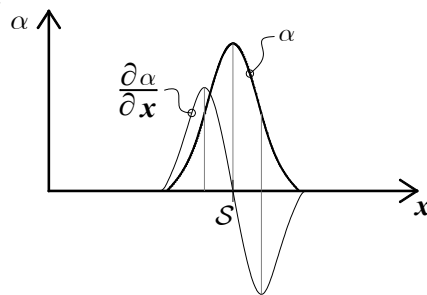


Figure 5.11 *Hypothetical distribution of a localizing strain-like internal variable and its derivative in a continuum one dimensional problem.*

The basis of the proposed methodology is to introduce the strong discontinuity at the maximum value of the continuum function α , that coincides with a zero of the derivative $\frac{\partial \alpha}{\partial \mathbf{x}}$. For the one dimensional case presented in Figure 5.11, \mathcal{S} corresponds to the point, where the strong discontinuity should be inserted, *i.e.* to the crack propagation path.

Let us now consider a hypothetic discrete case. In the finite element method the internal variables are usually computed at the gauss points being discontinuous between elements. Thus, a smooth continuous approximation ψ^h to α^h is also considered (see Figure 5.12-a)). Moreover, in Figure 5.12-b), the derivative $\frac{\partial \psi^h}{\partial \mathbf{x}}$, and, again, its continuous approximation μ^h (a second smoothed variable), are shown.

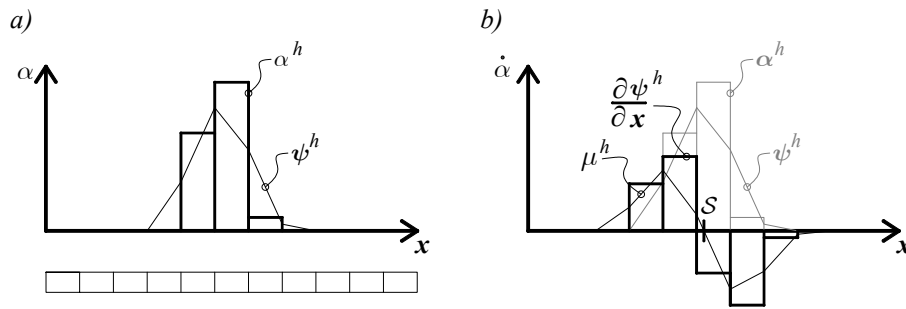


Figure 5.12 Discretized one dimensional problem a) Hypothetical distribution of a localizing strain-like internal variable. b) Hypothetical distribution of the derivative of a localizing strain-like internal variable.

The continuous approximation μ^h , obtained by a *double smoothing procedure* (Figure 5.13), will be termed the *crack propagation field* and its zero contour level ($\mu^h = 0$) defines the *crack propagation path* \mathcal{S} .

$$\begin{array}{ccccc} 1^\circ \text{ Smoothing} & & 2^\circ \text{ Smoothing} & & \\ \downarrow & & \downarrow & & \\ \alpha^h & \longrightarrow & \psi^h & \longrightarrow & \frac{\partial \psi^h}{\partial \mathbf{x}} & \longrightarrow & \mu^h \end{array}$$

Figure 5.13 Double smoothing process.

Remark 5.3.1.1: Notice that outside the localization zone (Figure 5.12-b)), μ^h takes also null values not corresponding to a maximum of α^h and corresponding instead, to the trivial case:

$$\alpha^h = 0 \Rightarrow \psi^h = 0 \Rightarrow \frac{\partial \psi^h}{\partial \mathbf{x}} = 0 \Rightarrow \mu^h = 0. \quad (5.69)$$

In practice, these not interesting zones with $\mu^h = 0$ (not corresponding to \mathcal{S}) do not introduce any additional trouble since they are located in elements outside the non-linear zone where strains localize, whereas we are looking for condition $\mu^h = 0$ in those elements belonging to the localization domain (where $\alpha^h \neq 0$).

5.3.2. The crack-propagation problem

The idea exposed in the previous Section can be formalized through the following crack-propagation problem:

Given $\hat{\alpha} \in \mathcal{A}$ find $\psi \in \mathcal{Y}$ and $\mu \in \mathcal{Y}$ such that for all $v \in \mathcal{Y}$:

$$\int_{\Omega} v(\psi - \alpha) d\Omega = 0, \quad \forall v \in \mathcal{Y} \quad (5.70)$$

$$\int_{\Omega} v \left(\mu - \left(\frac{d\psi}{dn} \right) \right) d\Omega = 0, \quad \forall v \in \mathcal{Y} \quad (5.71)$$

Box 5.7 *The crack-propagation problem.*

where v stands for the weighing functions belonging to \mathcal{Y} :

$$\mathcal{Y} := \left\{ v \mid v \in [H^1(\Omega)]^n; v|_{\Gamma} = 0 \right\}, \quad (5.72)$$

$\frac{d\psi}{dn}$ stands for the derivative of ψ in the direction of the unit vector orthogonal to the discontinuity \mathbf{n} , i.e.:

$$\frac{d\psi}{dn} = \nabla\psi \cdot \mathbf{n}, \quad (5.73)$$

and $\psi \in \mathcal{Y}$ and $\mu \in \mathcal{Y}$ stand for the projections of $\hat{\alpha} \in \mathcal{A}$ and $\frac{d\psi}{dn} \in \mathcal{A}$ onto the space \mathcal{Y} , being the functional space \mathcal{A} defined as:

$$\mathcal{A} := \left\{ \alpha \mid \alpha \in [L^2(\Omega)]^n; \alpha|_{\Gamma} = 0 \right\}. \quad (5.74)$$

Notice that the functional space \mathcal{Y} is selected to be more regular than \mathcal{A} ³², thus ψ and μ are smooth approximations of the internal variable α and of the normal directional derivative of the internal variable $\frac{d\psi}{dn}$, respectively.

³² Notice that for the space \mathcal{Y} both, the function and its derivative, must be square integrable, whereas for the space, \mathcal{A} , just the function is required to be square integrable.

5.3.3. Discretization

Introducing now the finite dimensional spaces \mathcal{Y}^h and \mathcal{A}^h approximating \mathcal{Y} and \mathcal{A} , the problem defined in Box 5.7 reads as:

Given $\alpha^h \in \mathcal{A}^h$ find $\psi^h \in \mathcal{Y}^h$ and $\mu^h \in \mathcal{Y}^h$ such that for all $v^h \in \mathcal{Y}^h$:

$$\int_{\Omega^h} v^h (\psi^h - \alpha^h) d\Omega = 0 \quad , \forall v^h \in \mathcal{Y}^h \quad (5.75)$$

$$\int_{\Omega^h} v^h \left(\mu^h - \left(\frac{d\psi^h}{dn} \right) \right) d\Omega = 0 \quad , \forall v^h \in \mathcal{Y}^h \quad (5.76)$$

Box 5.8 *Discretized crack-propagation problem.*

In Box 5.8, α^h is considered data of the problem, and ψ^h , μ^h , v^h are approximated by standard linear shape functions:

$$\mu^h(\mathbf{x}) = \sum_{i=1}^{nnode} N_i(\mathbf{x}) \mu_i \quad ; \quad \psi^h(\mathbf{x}) = \sum_{i=1}^{nnode} N_i(\mathbf{x}) \psi_i \quad ; \quad v^h(\mathbf{x}) = \sum_{i=1}^{nnode} N_i(\mathbf{x}) v_i, \quad (5.77)$$

where *nnode* stands for the number of nodes of the finite element mesh, μ_i , ψ_i and v_i are degrees of freedom associated to the node i , and N_i , stands for the standard finite element isoparametric shape functions

Remark 5.3.3.1: The crack-propagation field $\mu^h(\mathbf{x}, t)$ is the fundamental unknown of the crack propagation problem (stated in Box 5.8), and its zero contour level ($\mu^h = 0$) determine the crack propagation path \mathcal{S} .

5.3.4. Matrix equations

Equations (5.75) and (5.76) consist of two smoothing processes. Introducing Voigt notation, equation (5.75) reads:

$$\underbrace{\mathcal{A}_e \left(\int_{\Omega^{(e)}} \mathbf{N}^{(e)T} \cdot \mathbf{N}^{(e)} d\Omega \right)}_{\mathbf{M}^{(e)}} \cdot \{\boldsymbol{\psi}\} = \mathcal{A}_e \left(\int_{\Omega^{(e)}} \mathbf{N}^{(e)T} \cdot \alpha^{(e)} d\Omega \right), \quad (5.78)$$

where $\mathbf{N}^{(e)}$ stands for the element vector composed by the $N_i^{(e)}$ shape functions associated to node i ($\mathbf{N}^{(e)} = \{N_1^{(e)} \quad N_2^{(e)} \quad N_3^{(e)} \quad N_4^{(e)}\}$), $\mathbf{M}^{(e)}$ stands for the element mass matrix, $\alpha^{(e)}$ stands for the value of α associated to the element (e) and $\{\boldsymbol{\psi}\}$ stands for the global vector composed by the ψ_i degrees of free-

dom $\{\boldsymbol{\psi}\} = \{\psi_1, \psi_2, \dots, \psi_{nnodes}\}^T$ being $nnodes$ the total number of nodes of the finite element mesh.

$$\mathbf{M} \cdot \{\boldsymbol{\psi}\} = \mathcal{A}_e \left(\int_{\Omega^{(e)}} \mathbf{N}^{(e)T} \cdot \alpha^{(e)} d\Omega \right), \quad (5.79)$$

where \mathbf{M} stand for the global mass matrix $\mathbf{M} = \mathcal{A}_e(\mathbf{M}^{(e)})$. Substituting \mathbf{M} by a lumped mass matrix version \mathbf{M}_L , equation (5.79) can be easily solved for $\{\boldsymbol{\psi}\}$

$$\{\boldsymbol{\psi}\} = (\mathbf{M}_L)^{-1} \cdot \mathcal{A}_e \left(\int_{\Omega^{(e)}} \mathbf{N}^{(e)T} \cdot \alpha^{(e)} d\Omega \right). \quad (5.80)$$

Alternatively to equation (5.80), it can be used an improved version proposed by Weyler³³, consisting of the introduction of a correction in the extrapolation of the gauss point variable $\alpha^{(e)}$ to the nodes. Then, as for equation (5.80), the extrapolated corrected nodal values are weighted by the corresponding nodal masses (lumped global mass matrix):

$$\{\boldsymbol{\psi}\} = \mathbf{M}_L^{-1} \cdot \mathcal{A}_e \left(\underbrace{\mathbf{M}^{(e)-1} \cdot \mathbf{M}_L^{(e)}}_{\text{correction}} \cdot \int_{\Omega^{(e)}} \mathbf{N}^{(e)T} \cdot \alpha^{(e)} d\Omega \right). \quad (5.81)$$

Using the same procedure for equation (5.76):

$$\{\boldsymbol{\mu}\} = \mathbf{M}_L^{-1} \cdot \mathcal{A}_e \left(\int_{\Omega^{(e)}} \mathbf{N}^{(e)T} \cdot \left(\frac{d\psi}{dn} \right)^{(e)} d\Omega \right), \quad (5.82)$$

being $\{\boldsymbol{\mu}\}$ the global vector $\{\boldsymbol{\mu}\} = \{\mu_1, \mu_2, \dots, \mu_{nnodes}\}^T$. The improved version, reads::

$$\{\boldsymbol{\mu}\} = \mathbf{M}_L^{-1} \cdot \mathcal{A}_e \left(\mathbf{M}^{(e)-1} \cdot \mathbf{M}_L^{(e)} \cdot \int_{\Omega^{(e)}} \mathbf{N}^{(e)T} \cdot \left(\frac{d\psi}{dn} \right)^{(e)} d\Omega \right), \quad (5.83)$$

where $\left(\frac{d\psi}{dn} \right)^{(e)}$ can be computed, in an elemental basis, once equation (5.79) is solved for $\{\boldsymbol{\psi}\}$:

$$\left(\frac{d\psi}{dn} \right)^{(e)} = ([\nabla \mathbf{N}]^{(e)} \cdot \{\boldsymbol{\psi}\}^{(e)}) \cdot \mathbf{n}^{(e)}, \quad (5.84)$$

where $\{\boldsymbol{\psi}\}^{(e)}$ is the elemental vector $\{\boldsymbol{\psi}\}^{(e)} = \{\psi_1, \psi_2, \psi_3, \psi_4\}^T$ and $[\nabla \mathbf{N}]^{(e)}$ stands for the elemental matrix:

$$[\nabla \mathbf{N}]^{(e)} = \begin{bmatrix} \frac{\partial N_1}{\partial x} & \frac{\partial N_2}{\partial x} & \frac{\partial N_3}{\partial x} & \frac{\partial N_4}{\partial x} \\ \frac{\partial N_1}{\partial y} & \frac{\partial N_2}{\partial y} & \frac{\partial N_3}{\partial y} & \frac{\partial N_4}{\partial y} \end{bmatrix}. \quad (5.85)$$

³³ R. Weyler, personal communication, 2012.

Remark 5.3.4.1: For the strong discontinuity case, the rate version of the element integral $\int_{\Omega^{(e)}} \mathbf{N}^{(e)T} \cdot \dot{\alpha}^{(e)} d\Omega$ reads as:

$$\int_{\Omega^{(e)}} \mathbf{N}^{(e)T} \cdot \dot{\alpha}^{(e)} d\Omega = \int_{\mathcal{S}^{(e)}} \mathbf{N}^{(e)T} \cdot k \dot{\alpha}^{(e)} d\mathcal{S}. \quad (5.86)$$

For implementation proposes it is interesting (see Box 5.10 in Section 5.4.3) to make the following change of variable: $\dot{\hat{\alpha}}^{(e)}$, such that:

$$\begin{aligned} \dot{\hat{\alpha}}^{(e)} &= \frac{k \dot{\alpha}^{(e)}}{\ell^{(e)}} \Rightarrow \\ \Rightarrow \int_{\mathcal{S}^{(e)}} \mathbf{N}^{(e)T} \cdot k \dot{\alpha}^{(e)} d\mathcal{S} &= \int_{\mathcal{S}^{(e)}} \mathbf{N}^{(e)T} \cdot \dot{\hat{\alpha}}^{(e)} \ell^{(e)} d\mathcal{S} = \overline{\mathbf{N}^{(e)T}} \cdot \dot{\hat{\alpha}}^{(e)} \ell^{(e)} \text{meas}(\mathcal{S}^{(e)}) = \\ &= \int_{\Omega^{(e)}} \overline{\mathbf{N}^{(e)T}} \cdot \dot{\hat{\alpha}}^{(e)} d\Omega = \int_{\Omega^{(e)}} \mathbf{N}^{(e)T} \cdot \dot{\hat{\alpha}}^{(e)} d\Omega. \end{aligned} \quad (5.87)$$

where $\overline{\mathbf{N}^{(e)T}}$ stands for the value of $\mathbf{N}^{(e)T}$ evaluated at the centroid of the finite element and $\ell^{(e)}$ is a finite element characteristic length (according [Oliver 1989]). The operations in (5.87) take in consideration the continuous character of the shape functions and the fact that the integration point in \mathcal{S} was placed at the finite element centroid (see Remark 5.1.4.1). In equation (5.87), $\dot{\hat{\alpha}}^{(e)}$ can be interpreted as a distributed version, of the strong localized variable $\dot{\alpha}^{(e)}$, over the element bandwidth $\ell^{(e)}$ (see Figure 5.14).

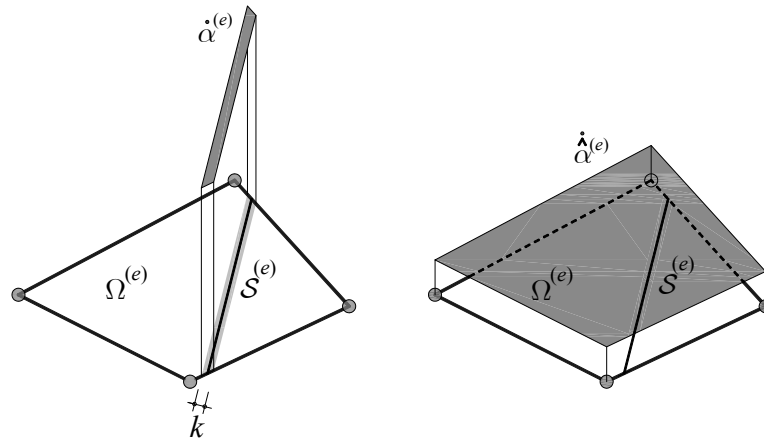


Figure 5.14 Interpretation of variable $\dot{\hat{\alpha}}^{(e)}$.

5.3.5. The crack propagation path

As soon as the element crack-propagation field μ^{l^h} is solved for a given time step, its zero contour level (the crack propagation path) can be, in a ele-

mental basis, easily determined (see Figure 5.15). Notice that since μ^h is continuous across elements, the crack propagation path \mathcal{S}^h (where $\mu^h(\mathbf{x})=0$), will be also continuous throughout the finite element mesh.

$$\mathcal{S}^h := \{ \mathbf{x} \in \Omega ; \mu^h(\mathbf{x}, t) = 0 \} ; \mathcal{S}^{(e)} = \mathcal{S}^h \cap \Omega^{(e)}. \tag{5.88}$$

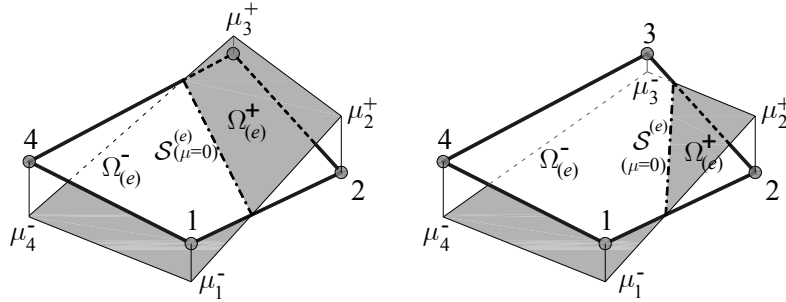


Figure 5.15 Elemental crack-propagation field $\mu_i^{(e)}$.

Remark 5.3.5.1: Determination of \mathcal{S}^h is based on a local smoothing technique of the internal variable $\alpha^{(e)}$. No additional constraints are introduced, and therefore, several paths \mathcal{S}^h (where $\mu^h = 0$) can live together depending on the distribution of the internal variable $\alpha^{(e)}$.

Remark 5.3.5.2: Notice that, to construct the function φ^h (see equation (5.23)), it is not necessary to know the exact position of \mathcal{S}^h , but just to detect the sides being crossed by the discontinuity, *i.e.* the sides where function μ^h changes its sign.

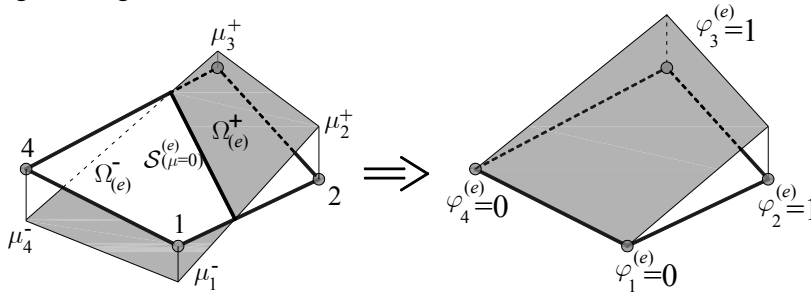


Figure 5.16 Construction of the elemental vector $\varphi_i^{(e)}$.

5.3.6. The discontinuity injection domain

The discontinuity injection domain is that part of the discretized domain composed by the set of finite elements where a discontinuous strain mode is injected. Two conditions are to be fulfilled for elements to be considered as belonging to the injection domain, Ω_{Dis} :

- a) The finite element should be crossed by the crack path \mathcal{S}^h ($\mu^h = 0$)
- b) The centroid of the finite element should be an in-loading ($\dot{\alpha}^{(e)} \neq 0$) bifurcated point experiencing a “sufficient degree” of softening.
($q \leq \gamma q_{bif}$)

Condition a) should be complemented with condition b) for two reasons. The first is related to the zero values of the propagation-crack field \mathcal{S}^h ($\mu^h = 0$), outside the localization zone ($\alpha^{(e)} = 0 \Rightarrow \mu^h = 0$), not corresponding to a crack path (see Remark 5.3.1.1). The second reason concerns the methodology developed to obtain the crack path \mathcal{S}^h - the crack-propagation problem. This methodology is based on a diffuse localizing strain field. Therefore, in order to obtain this diffuse field the discontinuity injection should be slightly delayed, being this delay controlled by requiring a “sufficient degree” of softening.

In Chapter 4, at Section 4.4, in a different context, the localization domain was defined as:

$$\Omega_{loc}(t) := \{ \mathbf{x} \in \Omega \mid t \geq t_B(\mathbf{x}) ; \dot{\alpha}(\mathbf{x}, t) > 0 ; q(\mathbf{x}, t) \leq q_{loc}(\mathbf{x}) = \gamma q_{bif}(\mathbf{x}) \}, \quad (5.89)$$

being $\gamma \in [0, 1]$ a parameter controlling the softening “degree” (see Section 4.4 and equation (4.28)). Notice that the definition of the localization domain (5.89) coincides with the requirements of condition b).

Taking into account conditions a) and b) the discontinuity domain can be formally defined as a subset of the localization domain $\Omega_{Dis} \subset \Omega_{loc}$ such that:

$$\Omega_{Dis}(t) = \{ \mathbf{x} \in \Omega_{loc} \mid \Omega^{(e)} \cap \mathcal{S}^h \neq \emptyset \}, \quad (5.90)$$

i.e. the discontinuity injection domain is composed by those elements of the localization domain Ω_{loc} crossed by the crack path \mathcal{S}^h (see Figure 5.17). In this Chapter, the localization domain Ω_{loc} is merely auxiliary in the definition of the discontinuity domain Ω_{Dis} .

Remark 5.3.6.1: The parameter γ establishing the threshold from where the discontinuity is injected must be introduced by the user. In the homogeneous bar problem of Section 3.2.7.2 the propagation of the localization band is almost instantaneous and, in this cases, the discontinuity injection can be per-

formed almost immediately after the bifurcation (typically $\gamma = 0.99$). On the other hand, in problems exhibiting propagating localization bands, numerical experience advises to delay a little more the discontinuity injection (typically $\gamma = 0.95$). This delay allows tracing properly the crack path \mathcal{S}^h avoiding lack of robustness problems. The drawback is that some stress locking in earlier stages of localization may occur. Notwithstanding these effects are almost negligible, as it will be shown in the set of representative examples of Section 4.5.

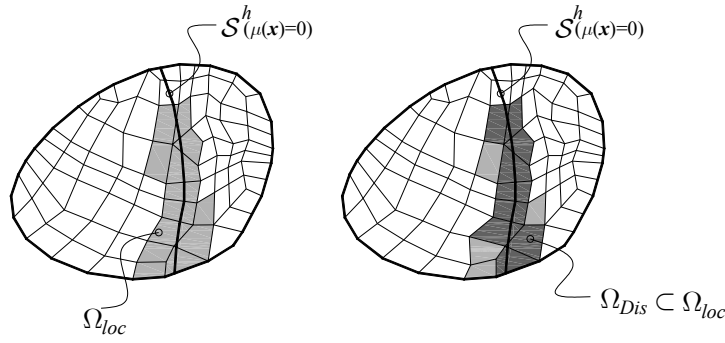


Figure 5.17 Localization and weak/strong discontinuity domains.

5.3.7. Staggered resolution of the coupled problem

The crack-propagation problem defined in Box 5.8, is stated in terms of $\alpha^{(e)}$, which depends directly in the solution of the non-linear mechanical problem of Box 5.1. On the other hand the mechanical problem also depends on the crack path (obtained from the crack-propagation field μ^h). Thus, both problems are coupled, and two sets of discretized, in time, equations can be written in terms of the corresponding residuals:

$$\begin{aligned} \dot{\mathbf{R}}_{mech}(\mathbf{u}_{n+1}^h, \mu_{n+1}^h) &= \mathbf{0}, & a) \\ \dot{\mathbf{R}}_{crack}(\mathbf{u}_{n+1}^h, \mu_{n+1}^h) &= \mathbf{0}, & b) \end{aligned} \quad (5.91)$$

being $\dot{\mathbf{R}}_{mech} = \mathcal{A} \left(\dot{\hat{\mathbf{R}}}^{(e)} \right)$, the residual of the non-linear mechanical problem.

Expressions for computing $\dot{\hat{\mathbf{R}}}^{(e)}$ are provided in Appendix C. $\dot{\mathbf{R}}_{crack}$ stands for the residual of crack-propagation problem in Box 5.8.

Thinking now of the injection procedure, it is noticed that in the initial stages of the non-linear loading, when $q > q_{loc}$, (see definition (5.89) and (5.90)) the discontinuity domain is an empty set of elements, $\Omega_{Dis} = \emptyset$, no strong or weak discontinuity is injected and therefore the problem (5.91) is

uncoupled. Thus equation (5.91)-a) can directly solved for \mathbf{u}_{n+1}^h and then, equation (5.91)-b) can be solved for μ_{n+1}^h :

$$\begin{aligned} \dot{\mathbf{R}}_{mech.}(\mathbf{u}_{n+1}^h) &= \mathbf{0} \rightarrow \mathbf{u}_{n+1}^h, & a) \\ \dot{\mathbf{R}}_{crack}(\mathbf{u}_{n+1}^h, \mu_{n+1}^h) &= \dot{\mathbf{R}}_{crack}^*(\mu_{n+1}^h) = \mathbf{0} \rightarrow \mu_{n+1}^h. & b) \end{aligned} \quad (5.92)$$

As soon as at least one element is considered to belong to Ω_{Dis} , the problem becomes coupled according to (5.91). In spite of this, the coupled problem can be solved in a similar form. In fact the dependence of the mechanical problem in variable $\mu^h(\mathbf{x})$ is only trough the instantaneous position of the discontinuity, so that the coupling between \mathbf{u}_{n+1}^h and μ_{n+1}^h in the term $\dot{\mathbf{R}}_{mech.}(\mathbf{u}_{n+1}^h, \mu_{n+1}^h)$ can be considered weak. This suggests the use of a staggered simplified procedure, replacing μ_{n+1}^h by μ_n^h in equation (5.91)-a), leading to the uncoupled equations:

$$\begin{aligned} \dot{\mathbf{R}}_{mech.}(\mathbf{u}_{n+1}^h, \mu_n^h) &= \dot{\mathbf{R}}_{mech.}^*(\mathbf{u}_{n+1}^h) = \mathbf{0} \rightarrow \mathbf{u}_{n+1}^h, & a) \\ \dot{\mathbf{R}}_{crack}(\mathbf{u}_{n+1}^h, \mu_{n+1}^h) &= \dot{\mathbf{R}}_{crack}^*(\mu_{n+1}^h) = \mathbf{0} \rightarrow \mu_{n+1}^h, & b) \end{aligned} \quad (5.93)$$

that can be solved likewise in (5.92) (when $\Omega_{Dis} = \emptyset$).

Remark 5.3.7.1: The staggered resolution of the coupled problem that lead to the uncoupled equations (5.93), allow us to outlook the crack-propagation problem as a post process procedure of the strain-like internal variable $\alpha^{(e)}$. The crack-propagation problem can be interpreted as a local (elemental based) tracking algorithm that can be locally and straightforwardly implemented in a finite element code in a non invasive manner.

5.4. Summarizing the strain injection procedure as a two stage method

In previous Sections, different strain modes were proposed to be injected: a constant strain mode (see Box 3.5) and a strong or weak discontinuity strain mode (See Box 5.4 and Box 5.6 respectively). At this Section, a unification of the proposed methodology is provided and the main reasons that motivate the method are summarized.

The method seeks to improve the performance of the classical strain localization methods (in terms of reducing stress locking and mesh bias dependence), by injecting specific strain localization modes. The strain localization modes, are proposed to be injected in two different stages of the deformation process.

In a first stage (the tracer stage³⁴), it is injected an elemental constant strain mode (CSM). This injection was already defined at Section 3.2 and its motivation relay on the better kinematic flexibly deriving from the weakly enforcement of the compatibility equation, that proves to exhibit remarkable properties for the correct propagation of the strain localization in initial stages (see examples of Section 3.2.7). This injection is performed on those elements that belong to the mixed injection domain as defined at Section 3.2.1.

Nevertheless, for localization proposes, the element equipped with the constant kinematics still exhibits a limited capability to replicate a strong discontinuity (as concluded in Chapter 4), and some degree of stress-locking appear. Therefore, **in a second stage**, as soon as the element is considered to belong to the discontinuity injection domain (Section 5.3.6), the element kinematics will be enhanced by the injection of an elemental discontinuity mode.

Remark 5.4.1: In the strong discontinuity approach, the propagation of the discontinuity is ruled by a global tracking algorithm based in a different set of differential equations. On the other hand, here, propagation will be controlled at a pure local elemental level by the mixed element equipped with a constant strain kinematics (CSM injection), that exhibits remarkable properties in terms of mesh bias indifference and proper capabilities of propagation.

Remark 5.4.2: Notice that any other “strain localization procedure” providing good information about the strain localization and propagation could have been used in the first stage as “a tracer formulation” as an alternative to the constant strain injection, *e.g.* other mixed formulations, strain localization methods with limiter (gradient methods, non-local methods, *etc.*).

5.4.1. The injection domains

The injection domains Ω_{inj} are those parts of the domain where injections are performed. In this work, two different types of injection domains were defined: the mixed injection domain Ω_{mixed} (see Section 3.2.1) and the discontinuity injection domain Ω_{Dis} (see Section 5.3.6) $\Omega_{inj} \equiv \cup \{ \Omega_{mixed}, \Omega_{Dis} \}$. Typically, in an element crossed by the discontinuity path, the element will firstly fall inside the mixed domain and, in a subsequent stage, in the discontinuity domain, according to the value of the internal variable. (see Figure 5.18, and equations (5.94), (5.95) and (5.96)).

³⁴ The name of this stage comes from the fact that the “strain localization procedure” used in the stage, associated to the crack propagation problem described at Section 5.3, allows tracing the position of the discontinuity (the crack propagation path). This information is essential to inject, subsequently, weak or strong discontinuity modes.

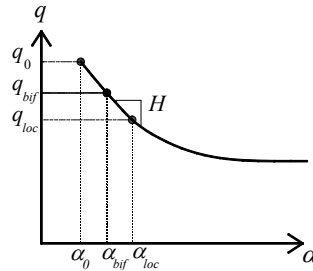


Figure 5.18 *Thresholds in the evolution of the stress/strain-like internal variables.*

$$\Omega_{loc}(t) := \{ \mathbf{x} \in \Omega \mid t \geq t_B(\mathbf{x}) ; \dot{\alpha}(\mathbf{x}, t) > 0 ; q(\mathbf{x}, t) \leq q_{loc}(\mathbf{x}) = \gamma q_{bif}(\mathbf{x}) \}, \quad (5.94)$$

$$\Omega_{Dis}(t) = \{ \mathbf{x} \in \Omega_{loc} \mid \Omega^{(e)} \cap \mathcal{S}^h \neq \emptyset \}, \quad (5.95)$$

$$\Omega_{mixed}(t) := \{ \mathbf{x} \in \Omega \mid t \geq t_B(\mathbf{x}) ; \dot{\alpha}(\mathbf{x}, t) > 0 ; \Omega^{(e)} \notin \Omega_{Dis} \}. \quad (5.96)$$

5.4.2. Two stage method - equilibrium equations

Considering a discretized body subdivided into three sub-domains where the different strain fields are selected to be injected, the equilibrium equation, corresponding to the full injection procedure, reads³⁵:

$$\begin{aligned} \int_{\Omega \setminus \Omega_{inj}} \nabla^s \boldsymbol{\eta}^h : \dot{\boldsymbol{\Sigma}}(\nabla^s \dot{\mathbf{u}}^h) d\Omega + \sum_{e \in \Omega_{mixed}} \int_{\Omega^{(e)}} \nabla^s \boldsymbol{\eta}^h : \dot{\boldsymbol{\Sigma}}(\overline{\nabla^s \dot{\mathbf{u}}^h}^{(e)})_{CSM \text{ Injection}} d\Omega + \\ \sum_{e \in \Omega_{Dis}} \int_{\Omega^{(e)}} \nabla^s \boldsymbol{\eta}^h : \dot{\boldsymbol{\Sigma}}(\underbrace{\dot{\boldsymbol{\epsilon}}_{Dis}^{(e)}}_{Dis. \text{ Injection}}) d\Omega = \dot{\mathbf{F}}^{ext}. \end{aligned} \quad (5.97)$$

where $\overline{\nabla^s \dot{\mathbf{u}}^h}^{(e)}$ stands for the constant strain mode (defined at Section 3.2.1), $\dot{\boldsymbol{\epsilon}}_{Dis}^{(e)}$ represents the injected discontinuous strain field (defined at Section 5.1.6 and 5.2.4 for the case of strong and weak discontinuity, respectively), Ω_{mixed} stands the mixed domain (Section 3.2.1), Ω_{Dis} is the discontinuity injection domain (Section 5.3.6) and $\Omega \setminus \Omega_{inj}$ stand for the remaining part of the domain where no injections are performed.

To give a better illustration of the methodology, a typical loading process is described in the following. For initial stages of loading, the body behaves elastically (thus without any injection domain, since condition (5.94) is not fulfilled for any element) and therefore the standard formulation is used all over the body. For increasing loading, some elements enter into the non-linear regime and bifurcation is detected. According with definition (5.94) these elements are considered to

³⁵ Additionally, in those elements belonging to Ω_{Dis} , the traction continuity equation should also be imposed, according to the weak/strong discontinuity mode to be injected.

belong to the mixed domain and therefore a CSM is injected (see Figure 5.19-a). Later on, some of those elements unload, leaving the injection domain and recovering the irreducible formulation. However, in some other elements, strains remain localizing and condition (5.96) can be subsequently fulfilled. At that moment those elements are considered to belong to the discontinuity domain and a Weak/Strong discontinuity (W/SD) strain mode is injected (see Figure 5.19-b) and c)).

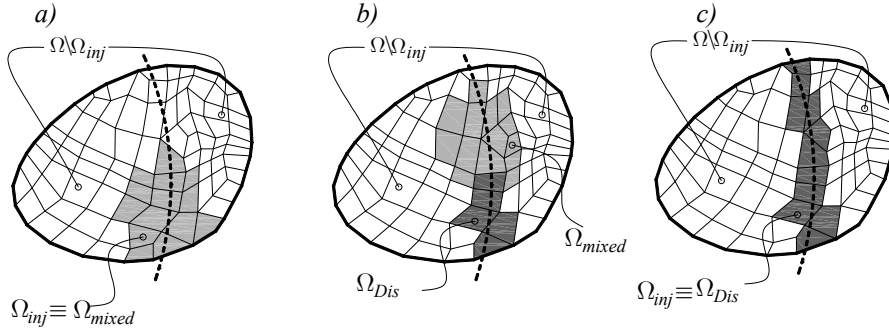


Figure 5.19 Evolution of the mixed and discontinuity domains for three typical stages of loading.

5.4.3. Implementation aspects

In previous Sections, the strain injection procedure was introduced and several strain modes were proposed to be injected: the constant strain mode and the strong or weak discontinuity strain mode. In this Section implementation aspects about those injections are presented.

For the constant strain mode injection, it was mentioned in Section 3.2.4, that one additional sampling point, located at the centroid of the finite element, was needed. For strong/weak discontinuity, in order to impose the traction continuity equation, two additional gauss points are necessary. We arrive therefore to a quadrilateral element with 6 sampling points (see Figure 5.20):

- The 4 standard quadrilateral gauss points, where the standard stresses $\sigma^{(e)}$ are evaluated (see equation (5.100))
- A reduced integration gauss point, located at the centroid of the finite element, where $\hat{\Sigma}(\hat{\epsilon}_{\Omega_S}^{(e)})$ is evaluated, representing the inelastic zone, Ω_S , where strains localize.
- An additional elastic gauss point, also located at the centroid of the element, where an elastic behavior is explicitly forced at the moment that the strong/weak discontinuity is injected, representing the unloading zone $\Omega^{(e)} \setminus \Omega_S$ adjacent to the discontinuity, where $\bar{\sigma}^{(e)} = \hat{\Sigma}(\hat{\epsilon}_{\Omega_S}^{(e)})$ is evaluated

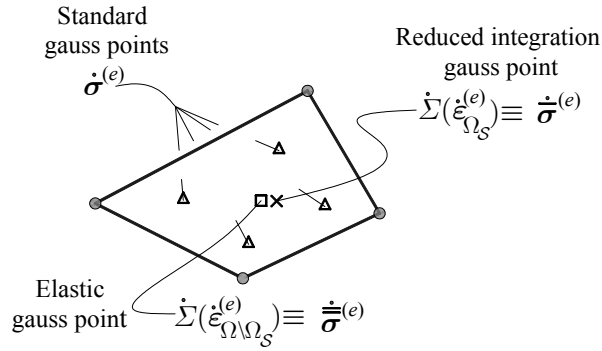


Figure 5.20 Sampling points involved in the numerical integration.

Following a similar strategy to that used in Section 3.2.4, the equilibrium equation can be written in the, suitable for implementation, general form:

$$\mathcal{A}_{e \in \Omega} \left(\int_{\Omega^{(e)}} \mathbf{B}^{(e)} : \{ \tilde{\boldsymbol{\sigma}}_{n+1}^{(e)} \} d\Omega \right) = \mathbf{F}_{n+1}^{ext} \quad (5.98)$$

$$\begin{aligned} \{ \tilde{\boldsymbol{\sigma}}_{n+1}^{(e)} \} &= \{ \tilde{\boldsymbol{\sigma}}_n^{(e)} \} + \{ \Delta \tilde{\boldsymbol{\sigma}}_{n+1}^{(e)} \} \\ \Delta \tilde{\boldsymbol{\sigma}}_{n+1}^{(e)} &= (1 - \xi^{(e)}) \left[\tau^{(e)} \underbrace{(\boldsymbol{\sigma}_{n+1}^{(e)} - \boldsymbol{\sigma}_n^{(e)})}_{\Delta \boldsymbol{\sigma}_{n+1}^{(e)}} + (1 - \tau^{(e)}) \underbrace{(\bar{\boldsymbol{\sigma}}_{n+1}^{(e)} - \bar{\boldsymbol{\sigma}}_n^{(e)})}_{\Delta \bar{\boldsymbol{\sigma}}_{n+1}^{(e)}} \right] + \\ &\quad + \xi^{(e)} \left[(1 - \gamma_{W \setminus SD}^{(e)}) \underbrace{(\bar{\boldsymbol{\sigma}}_{n+1}^{(e)} - \bar{\boldsymbol{\sigma}}_n^{(e)})}_{\Delta \bar{\boldsymbol{\sigma}}_{n+1}^{(e)}} + \gamma_{W \setminus SD}^{(e)} \underbrace{(\bar{\bar{\boldsymbol{\sigma}}}_{n+1}^{(e)} - \bar{\bar{\boldsymbol{\sigma}}}_n^{(e)})}_{\Delta \bar{\bar{\boldsymbol{\sigma}}}_{n+1}^{(e)}} \right] \end{aligned} \quad (5.99)$$

being:

$$\begin{aligned} \{ \dot{\boldsymbol{\sigma}}^{(e)} \} &= \left\{ \dot{\Sigma} \left(\mathbf{B}^{(e)} \cdot \{ \dot{\mathbf{u}} \}^{(e)} \right) \right\} \\ \{ \dot{\bar{\boldsymbol{\sigma}} }^{(e)} \} &= \left\{ \dot{\Sigma} \left(\bar{\mathbf{B}}^{(e)} \cdot \{ \dot{\mathbf{u}} \}^{(e)} + \xi^{(e)} \left[- \left[\overline{\nabla \varphi^h}^{(e)} \right] \cdot [\dot{\mathbf{u}}]^{(e)} + \frac{1}{h^{(e)}} [\mathbf{n}^{(e)}] \cdot [\dot{\mathbf{u}}]^{(e)} \right] \right) \right\} \\ \{ \dot{\bar{\bar{\boldsymbol{\sigma}}}}^{(e)} \} &= \left\{ \dot{\Sigma} \left(\bar{\bar{\mathbf{B}}}^{(e)} \cdot \{ \dot{\mathbf{u}} \}^{(e)} - \xi^{(e)} \left[\overline{\nabla \varphi^h}^{(e)} \right] \cdot [\dot{\mathbf{u}}]^{(e)} \right) \right\} \end{aligned} \quad (5.100)$$

where:

$$\begin{aligned} \tau^{(e)} &= 0.0 \quad \forall e \in \Omega_{inj}; \Omega_{inj} \subset \{ \Omega_{mixed}, \Omega_{Dis} \} \\ \tau^{(e)} &= 1.0 \quad \forall e \in \Omega \setminus \Omega_{inj} \quad (\text{for general constitutive models}) \\ \tau^{(e)} &= 0.1 \quad \forall e \in \Omega \setminus \Omega_{inj} \quad (\text{for isochoric constitutive models}) \\ \xi^{(e)} &= 0.0 \quad \forall e \in \Omega \setminus \Omega_{Dis} \\ \xi^{(e)} &= 1.0 \quad \forall e \in \Omega_{Dis}; \begin{cases} \gamma_{W \setminus SD}^{(e)} = 0.0 & \text{for WD inj. } (h^{(e)} = \ell^{(e)}) \\ \gamma_{W \setminus SD}^{(e)} = 1.0 & \text{for SD inj. } (h^{(e)} = k \rightarrow 0) \end{cases} \end{aligned}$$

Box 5.9 Injection procedure. Matrix equations - Implementation

Additionally, for those elements that belong to the discontinuity domain, one of the following equations is imposed, in terms of the incremental stresses. The additional degrees of freedom, $[[\dot{\mathbf{u}}]]^{(e)}$, are solved at the elemental level as described in Appendix C.

- Un-symmetric formulation (weak or strong discontinuity)

$$[\mathbf{n}^{(e)}] \cdot \{\Delta \bar{\boldsymbol{\sigma}}_{n+1}^{(e)}\} = [\mathbf{n}^{(e)}] \{\Delta \bar{\bar{\boldsymbol{\sigma}}}_{n+1}^{(e)}\}, \forall e \in \Omega_{Dis}. \quad (5.101)$$

- Symmetric formulation (strong discontinuity)

$$\int_S [\mathbf{n}^{(e)}] \cdot \{\Delta \bar{\boldsymbol{\sigma}}_{n+1}^{(e)}\} dS = \int_{\Omega^{(e)}} [\nabla \varphi] \cdot \{\Delta \bar{\bar{\boldsymbol{\sigma}}}_{n+1}^{(e)}\} d\Omega, \forall e \in \Omega_{Dis}. \quad (5.102)$$

Notice that for $\xi = 0.0$ the procedure of Box 5.9 is equivalent to that of Box 3.6 *i.e.* just the CSM is injected. The parameter $\gamma_{W\setminus SD}$, allows the user to select among the strong or the weak discontinuity injection, since, depending on this parameter, the incremental stresses, $\Delta \bar{\boldsymbol{\sigma}}_{n+1}^{(e)}$, are equal to the elastic $\Delta \bar{\bar{\boldsymbol{\sigma}}}_{n+1}^{(e)}$ or inelastic stresses $\dot{\bar{\boldsymbol{\sigma}}}^{(e)}$ (for $\gamma_{W\setminus SD} = 1.0$ and $\gamma_{W\setminus SD} = 0.0$, respectively).

Regarding equation (5.100), it is noticed that the stresses in the central gauss points coincides until the moment that a given element falls inside the discontinuity domain (see Figure 5.21). Then, in order to inject weak/strong discontinuity an elastic behavior is forced in the gauss point where $\bar{\boldsymbol{\sigma}}^{(e)}$ is evaluated.

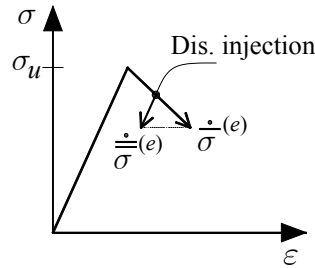


Figure 5.21 *Stress-strain relation until the discontinuity injection in a hypothetical one dimensional case.*

We remark here that equation (5.98) has the structure of standard finite element formulation internal force vector, where $\{\boldsymbol{\sigma}_{n+1}^{(e)}\}$ is substituted by $\{\bar{\boldsymbol{\sigma}}_{n+1}^{(e)}\}$. This translates into a straightforward implementation of the injection procedure in a standard finite element code.

Nevertheless, some extra implementation tasks are needed:

- 1- Previously to the four standard gauss points loop where the elemental force vector is numerically integrated, the constant values of $\{\Delta \bar{\boldsymbol{\sigma}}_{n+1}^{(e)}\}$ and $\{\Delta \bar{\bar{\boldsymbol{\sigma}}}_{n+1}^{(e)}\}$ should have been already evaluated in order to compute $\{\bar{\boldsymbol{\sigma}}_{n+1}^{(e)}\}$ inside the loop.

- 2- At the end of the time step, and for all elements, conditions (5.94) and (5.95) should be verified with the converged values of $\bar{\sigma}^{(e)}$. If any of these conditions is fulfilled the element should be flagged as belonging to the respective domain of injection, Ω_{mixed} or Ω_{Dis} .
- 3- For those elements belonging to the discontinuity domain the displacement jump degrees of freedom should be solved by using a standard condensation procedure (see Appendix C).
- 4- At the end of time step, the crack-path \mathcal{S}^h should be found by solving the crack-propagation problem³⁶. Following, in Box 5.10 are summarized the discretized in time matrix equations of the crack propagation problem.

Given the element values $\Delta\bar{\alpha}_{n+1}^{(e)}$, find $\{\boldsymbol{\mu}_{n+1}\}$ such that:

$$\{\boldsymbol{\psi}\}_{n+1} = \mathbf{M}_L^{-1} \cdot \mathcal{A}_e \left(\underbrace{\mathbf{M}^{(e)-1} \cdot \mathbf{M}_L^{(e)}}_{\text{correction}} \cdot \int_{\Omega^{(e)}} \mathbf{N}^{(e)T} \cdot \hat{\alpha}_{n+1}^{(e)} d\Omega \right) \quad (5.103)$$

$$\{\boldsymbol{\mu}\}_{n+1} = \mathbf{M}_L^{-1} \cdot \mathcal{A}_e \left(\mathbf{M}^{(e)-1} \cdot \mathbf{M}_L^{(e)} \cdot \int_{\Omega^{(e)}} \mathbf{N}^{(e)T} \cdot \left(\frac{d\boldsymbol{\psi}}{dn} \right)_{n+1}^{(e)} d\Omega \right) \quad (5.104)$$

where:

$$\hat{\alpha}_{n+1}^{(e)} = \hat{\alpha}_n^{(e)} + \Delta\hat{\alpha}_{n+1}^{(e)} \quad ; \quad \hat{\alpha}_0^{(e)} = 0$$

being:

$$\Delta\hat{\alpha}_{n+1}^{(e)} = \Delta\bar{\alpha}_{n+1}^{(e)} \quad \text{without SD injection}$$

$$\Delta\hat{\alpha}_{n+1}^{(e)} = \frac{k\Delta\bar{\alpha}_{n+1}^{(e)}}{\ell^{(e)}} \quad \text{with SD injection}$$

and:

$$\left(\frac{d\boldsymbol{\psi}}{dn} \right)_{n+1}^{(e)} = ([\nabla\mathbf{N}]^{(e)} \cdot \{\boldsymbol{\psi}\}_{n+1}^{(e)}) \cdot \mathbf{n}^{(e)}$$

Box 5.10 *Crack-propagation problem. Matrix equations – Implementation.*

In Box 5.10, remark 5.3.4.1 was taken in consideration. The value of $\Delta\bar{\alpha}$ states for the value of $\Delta\alpha$ evaluated in the reduced integration sampling point, according to Figure 5.20.

³⁶ This task can be omitted while the discontinuity domain is empty, *i.e.* if no discontinuous modes are injected.

5.5. Representative numerical simulations

In this Section, several examples illustrate the behavior of the preceding methodologies in material failure modeling. The performance of the methodology is assessed through comparison with analytical, experimental or well-established numerical results.

5.5.1. Isotropic continuum damage model: double cantilever beam (DCB) with diagonal loads

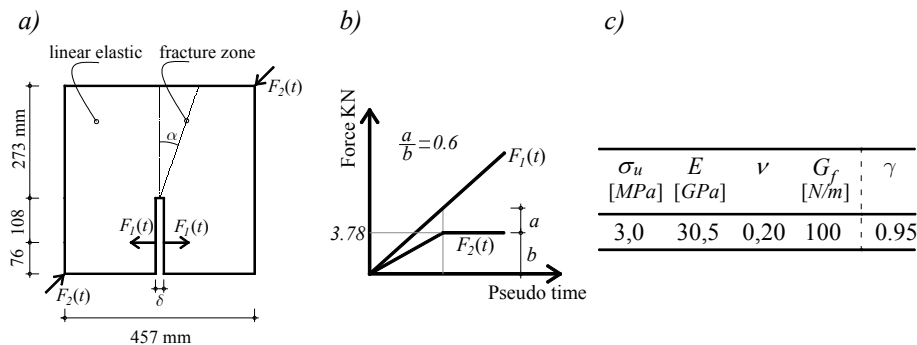


Figure 5.22 Double cantilever beam with diagonal loads: a) geometrical data, b) loading data, c) finite element discretization.

The test used at Sections 3.1.6.1 and 3.2.7.1 is now repeated using the Weak\Strong discontinuity injection. According to Section 5.4, where the injection procedure is described, the methodology consists of the injection of two strain modes: in a first stage, it is injected a constant strain mode (CSM) and in the second stage a strong/weak discontinuity mode. Here just the injection deriving from the un-symmetric strong discontinuity formulation is used. This example is particularly interesting since it gives a clear illustration about the evolution of the domains of interest: where the constant strain (CSM inj.) and the strong discontinuity (SD inj.) are injected. The parameter γ establishing the threshold from where the discontinuity is injected is set to $\gamma = 0.95$ (see Remark 5.3.6.1).

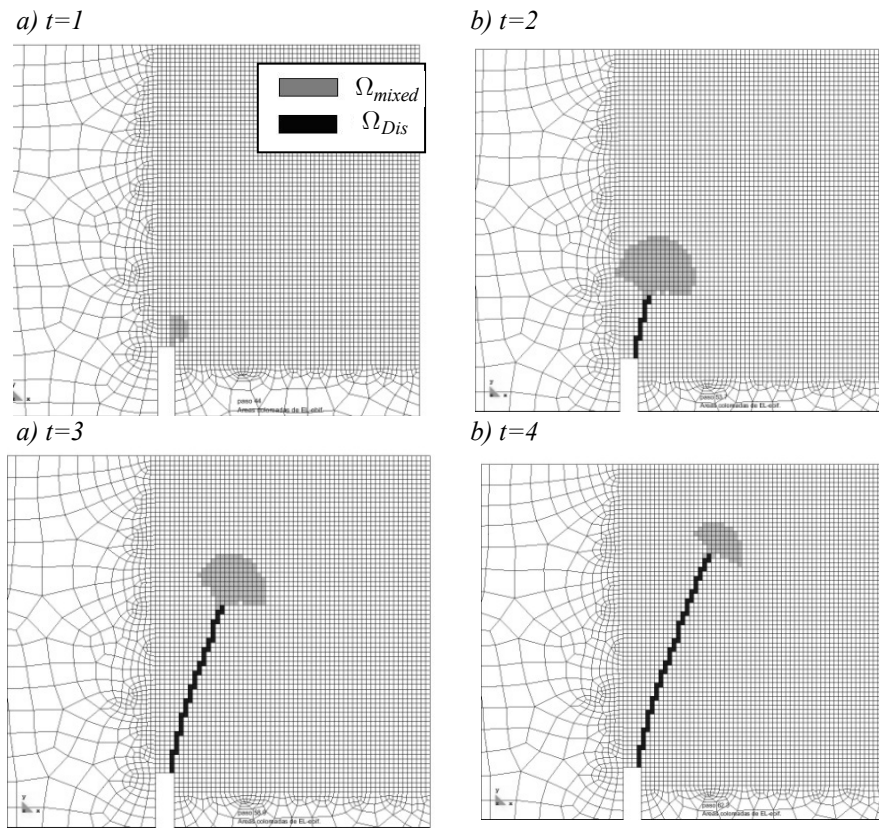


Figure 5.23 Evolution of the injection zones along different times of the analysis.

In Figure 5.23 the evolution of domains of injection is depicted. Its evolution follows the scheme outlined at the end of Section 5.4. It can be observed a bulb-shaped domain, at the tip of the advancing localization band where the material initially bifurcates (fulfilling condition (5.94)) and remains in in-loading state, so that the element-wise-constant deformation mode is injected (this domain corresponds to Ω_{mixed}). Soon later, most of the bifurcated elements behind the bulb unload (*i.e.* $\dot{\alpha} = 0$) so they leave the Ω_{mixed} domain, according to equation (5.94) excepting for an inclined band, crossed by the crack propagation path \mathcal{S}^h (shown in Figure 5.24), behind the bulb and encompassing one element size, which remains in inelastic loading (see Figure 5.23-b).

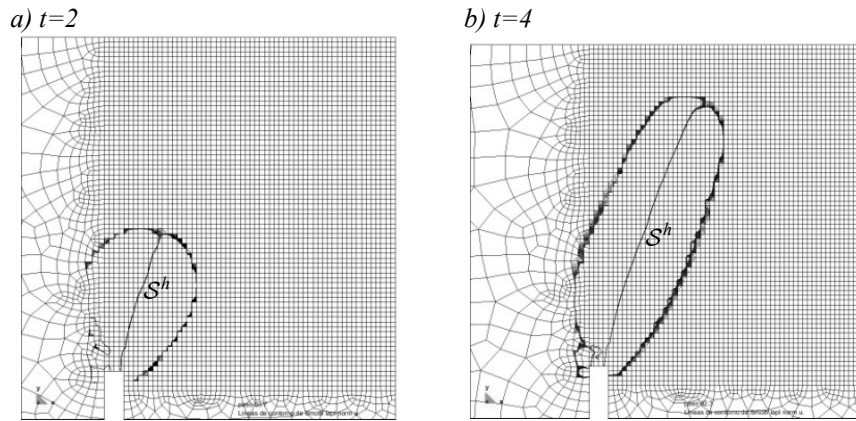


Figure 5.24 Crack propagation path $\mathcal{S}^h(\mu^h = 0)$, at two different times of analysis.

The crack path \mathcal{S}^h , according to the stated at Section 5.3, indicates the position of the strong/weak discontinuity path corresponding to the diffuse localization pattern provided by the constant strain mode injection. As soon as any element crossed by the line \mathcal{S}^h , verifies condition (5.94) ($q \leq q_{loc}$), the element (according to (5.95)) is considered to belong to Ω_{Dis} , as it happens in the darker shaded zone behind the propagating bulb (see Figure 5.23).

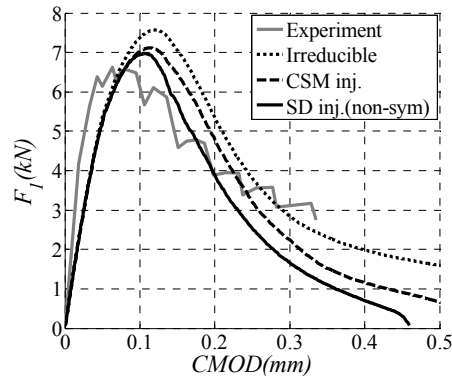


Figure 5.25 Force-displacement curves.

In Figure 5.25, the force-displacement curve obtained with the strong discontinuity injection is compared with results already presented at Section 3.2.7.1. The *CSM inj.* case shown in Figure 5.25 stands for the case introduced at Section 3.2.1, where just the constant strain mode is injected and, then, no further enhanced injection is performed. A significant reduction in terms of stress locking is noticed. In terms of crack propagation no significant differences are found relatively to the results computed at Section 3.2.7.1. with the *CSM inj.* (see Figure 3.17), and by this reason this result is not reproduced here.

5.5.2. Strip in homogeneous uniaxial tensile stress state – Mode II fracture modeling

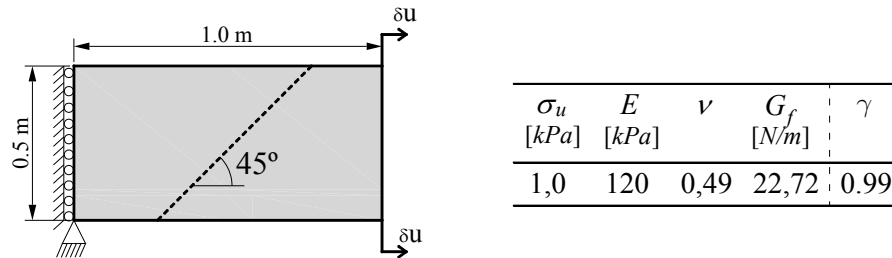


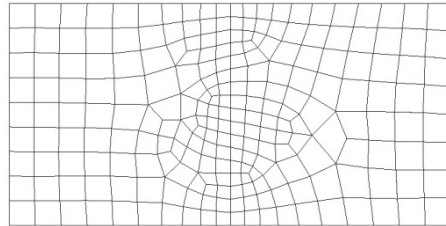
Figure 5.26 Strip stretching in the horizontal direction (J_2 plasticity model).

Figure 5.26 shows a homogeneous strip loaded in a uniaxial direction. The theoretical solution of this numerical example, using a J_2 plasticity model, consisting of a 45° degree slip line, was already introduced at Sections 3.1.6.2, 3.2.7.2 and 4.5.2. Here, we aim to assess the performance of the injection procedure. Using the proposed two-stage methodology, in a first stage, it is injected a constant strain mode and in the second stage, the three following possibilities are compared:

1. The strong discontinuity injection (un-symmetric formulation)
2. The strong discontinuity injection (symmetric formulation)
3. The weak discontinuity injection

Two different challenging meshes are selected. One of them, unstructured, with irregular mesh size and a second one, miss-aligned, *i.e.* the mesh lines and the slip line make different angles with the horizontal axis: 45° and 65° respectively (see Figure 5.26 and -b)). For parameter γ , establishing the threshold from where the discontinuity is injected, it is taken $\gamma = 0.99$ (see Remark 5.3.6.1)

a) Mesh i)



b) Mesh ii

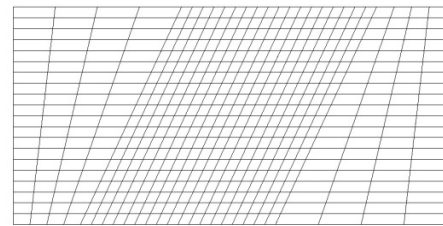


Figure 5.27 Finite element meshes: a) unstructured mesh, b) miss aligned mesh.

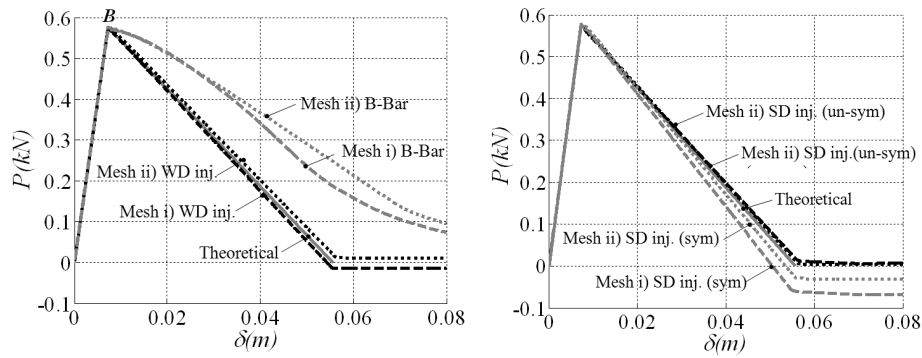
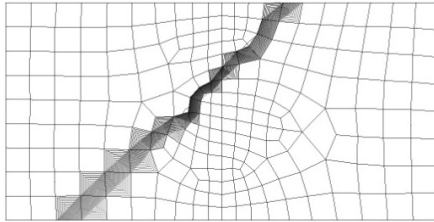


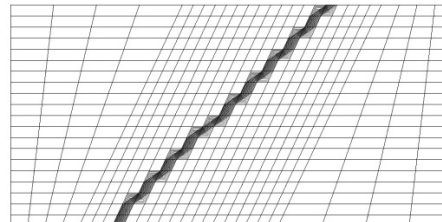
Figure 5.28 Force-displacement curves.

In Figure 5.28 the obtained results with the different strategies are compared in terms of force-displacement curves. It is shown that results provided by the un-symmetric strong discontinuity and by the weak discontinuity injection almost match the theoretical solution. For the symmetric strong discontinuity injection, a small but no depreciable negative residual load is obtained. Notice that for this formulation, the traction continuity equation is not directly imposed and thus fine meshes are required³⁷.

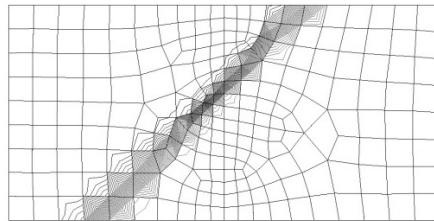
a) Mesh i)- W/SD Injection



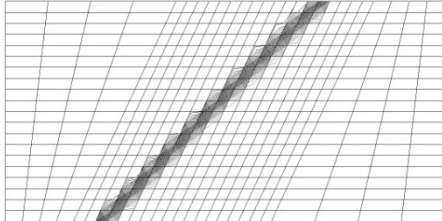
b) Mesh ii)- W/SD Injection



c) Mesh i)- B-bar



d) Mesh ii)- B-bar

Figure 5.29 Iso-displacement contours (J_2 plasticity mode).

In terms of iso-displacement contours, the differences between results obtained with the three enhanced formulations (weak, symmetric and un-symmetric strong discontinuity injections) are minimal and cannot be noticed. By this rea-

³⁷ The main motivation for proposing this formulation is mainly related to the robustness aspects of the numerical method (and not to the accuracy properties) (see Remark 5.1.5.2).

son, the some plot, shown at Figure 5.24 a) and labeled as W/SD injection is considered as being representative of the three enhanced cases.

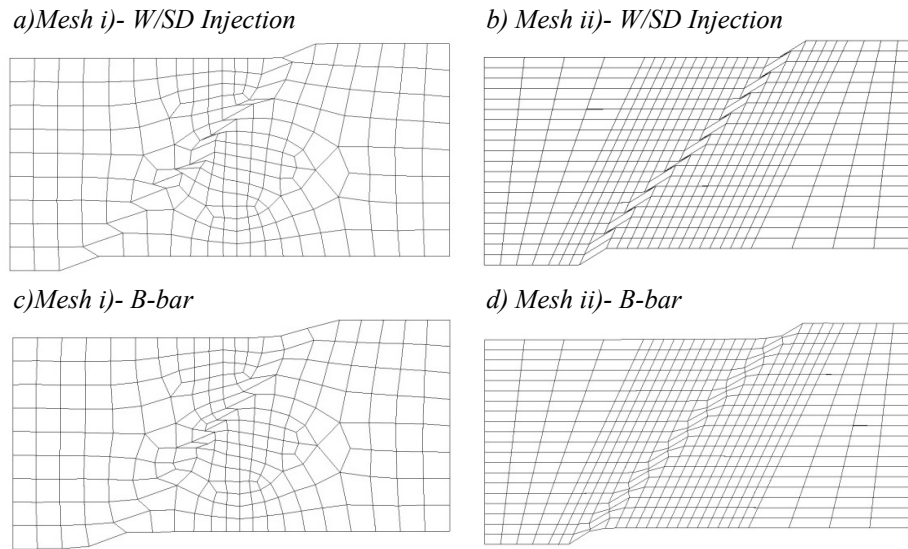


Figure 5.30 *Deformed finite element mesh (J_2 plasticity mode).*

In Figure 5.29 and Figure 5.30 it is clearly noticed that for the W/SD Injection (unlike in the B-bar formulation), the discontinuity band is sharply captured in a one-element-width band, without spurious stress transfer to the neighboring elements that unload elastically. In Figure 5.31, the mixed and the discontinuity domains are shown for the non-structured mesh.

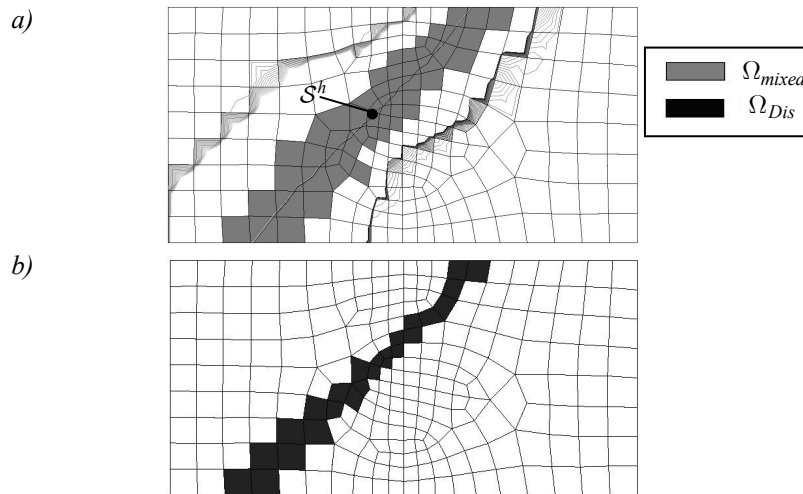


Figure 5.31 *Injection domains for two different times of analysis: a) time immediately after the bifurcation point (signalized with B at Figure 5.28-a), b) Time when the discontinuity injection threshold is attained .*

The first plot of Figure 5.31 corresponds to a time immediately after the bifurcation point (signalized with B at Figure 5.28-a)). The shaded elements symbolize the domain Ω_{mixed} where a constant strain mode is injected. The crack path \mathcal{S}^h where $\mu^h = 0$ is also shown in Figure 5.31-a). At this time, the discontinuity domain is an empty set of elements. As soon as the discontinuous modes are injected³⁸, the elements not containing the crack path automatically unload, leaving the injection domain, that collapses in a single layer of elements with all of them belonging to the discontinuity domain (Figure 5.31-b)).

5.5.3. Strip undergoing homogeneous uniaxial tensile stress – Mode I fracture modeling

The homogeneous strip is again analyzed, considering now a damage and a Rankine plasticity model. For both cases, the theoretical solution consists of a vertical discontinuity opening in mode I of fracture.

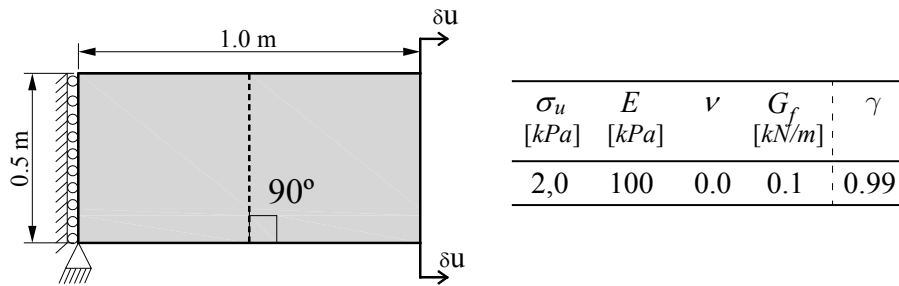


Figure 5.32 Strip stretching in the horizontal direction

The results computed at Section 3.1.6.2, 3.2.7.2 and 4.5.1 are now complemented by those obtained using a full injection procedure. In Section 5.5.2 results considering the three different enhanced modes are considered. Here, just the results obtained with the un-symmetric strong discontinuity injection are presented, since analogous results are obtained and no additional conclusions can be derived. The *CSM inj.*, case shown in Figure 5.33, stands for the case of Box 3.5, (where just the constant strain mode is injected and, then, no further enhanced injection is performed).

³⁸ Notice that this numerical example is a near-homogenous problem, where the propagation of the localization band is almost instantaneous.

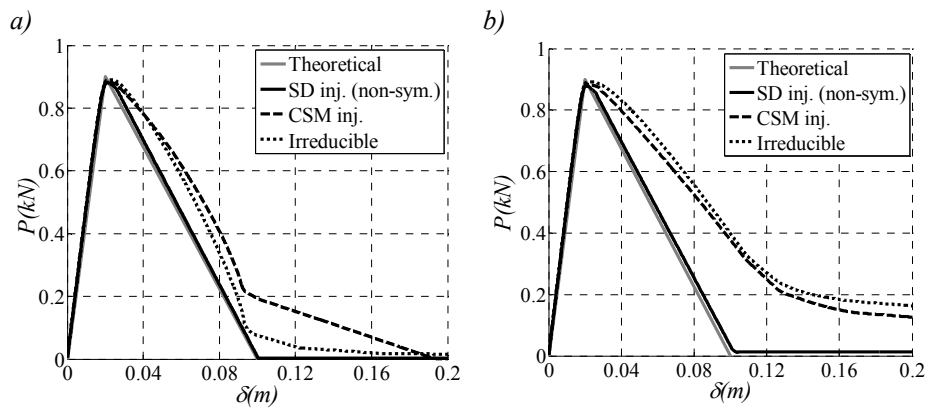
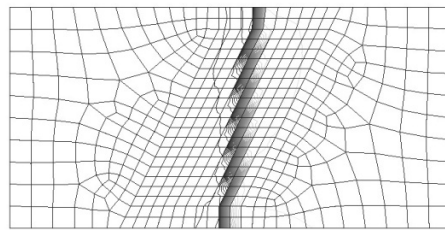


Figure 5.33 Force-displacement curves: a) Isotropic damage, b) Rankine plasticity model.

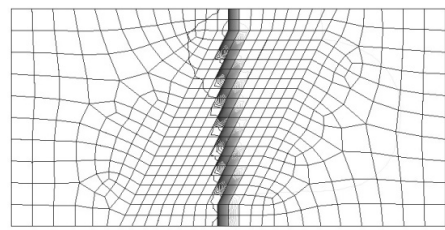
In terms of force-displacement curve, the benefits obtained by using the SD inj. are clear. For both constitutive models, the corresponding force-displacement curves perfectly matches the theoretical solution giving also a negligible residual load, this displaying that locking free results are attained.

5.5.3.1. Rankine plasticity model

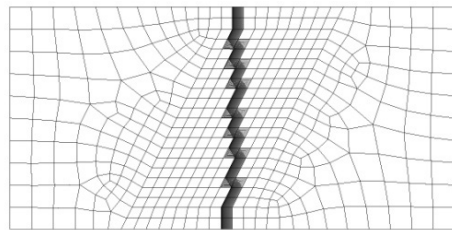
a) Irreducible formulation



b) CSM injection



c) SD Injection



d) SD Injection

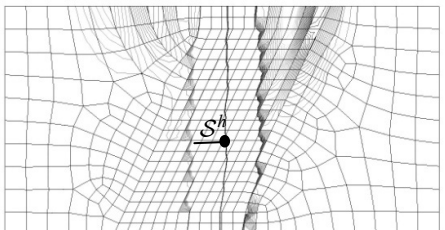


Figure 5.34 Rankine plasticity model: a), b) and c) Iso-displacement plots. d) Crack propagation path $S^h(\mu^h = 0)$.

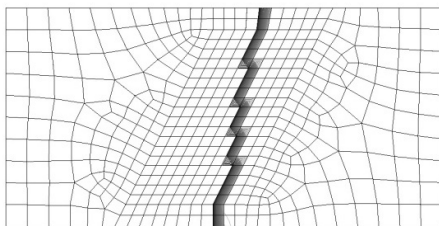
In terms of crack propagation, it is shown again that the irreducible formulation is strongly affected by mesh bias dependence (Figure 5.34-a)), whereas the constant strain and the strong discontinuity injection are much less affected

(Figure 5.34-b)). Given that the crack propagation obtained with the strong discontinuity injection is directly ruled by the previously injected constant strain mode (see Remark 5.4.1), its orientation (Figure 5.34-c)) almost coincides with that obtained by using just the CSM injection (Figure 5.34-b)).

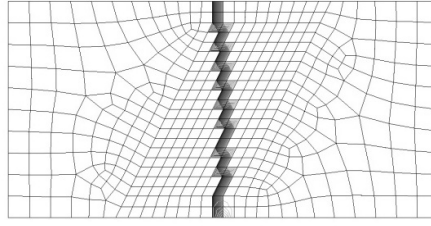
The relative improved behavior between both formulations (the SD and the CSM injection) is then related to the locking free results obtained by using the additional SD injection. Notice that, for this formulation, the deformations are sharply concentrated in a one-element-width band whereas for the CSM case they are smeared out over more than one element. In Figure 5.34-d) the obtained crack propagation path \mathcal{S}^h is depicted.

5.5.3.2. Damage constitutive model

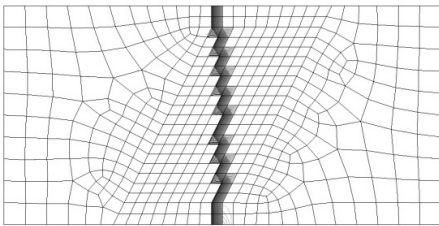
a) Irreducible formulation



b) CSM injection



c) SD Injection



d) SD Injection

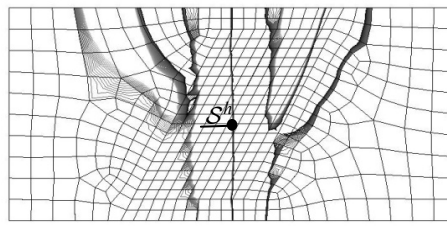


Figure 5.35 Damage model. a), b) and c) Iso-displacement plots. d) crack propagation path \mathcal{S}^h .

When damage models are used, as the damage variable tends to the unity, stress locking effects vanish and deformations tend to concentrate in a unique layer of elements even when standard irreducible formulations are used (see Figure 5.35-a)). Thus, for this constitutive model and independently of the formulation, residual loads also vanish (see Figure 5.33-a)). Nevertheless using the strong discontinuity injection, locking effects in earlier stages of localization are eliminated and the “bilinear” form of force-displacement curves (see Figure 5.33-a)), obtained when using the irreducible or the CSM injection, it is not noticeable. Here, it is also shown that results computed by using the SD and CSM injections are mesh bias independent (see vertical crack pattern of Figure 5.35 b) and c), and the vertical crack path \mathcal{S}^h , of Figure 5.35 c)).

5.5.4. Four point bending test

The classical four point bending test, of a concrete beam reported in [Arrea and Ingraffea 1982] is now tackled. The geometry of the problem is depicted in Figure 5.36-a). The post-critical behavior is modeled by a Rankine plasticity model. The material parameters are summarized in Figure 5.36-b). According to physical experiments a fracture with curved trajectory is expected to develop from the notch tip as it is sketched in Figure 5.36-a). The numerical analysis was held by controlling the Crack Mouth Sliding Displacement (CMSD) in plane stress conditions.

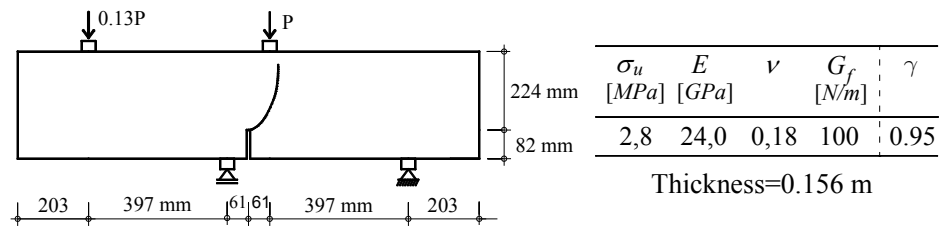


Figure 5.36 Four points bending test.

5.5.4.1. Kinematic crack locking

At this point, it is interesting to introduce the following discussion: it is well known, from strong discontinuity analysis, that the evolution of the displacement jump at the strong discontinuity regime is constrained by the so-called strong discontinuity conditions. These conditions imply, for a Rankine plasticity models, that just the normal component of the displacement jump $[[\dot{\mathbf{u}}_n]]$ can develop, whereas the tangential component has to be null $[[\dot{\mathbf{u}}_t]] = 0$ [Oliver, Cervera et al. 1999] (pure mode I fracture). This example shows a fracture with curved trajectory. Since the normal vector (to the discontinuity) changes from element to element along the localization band, the strong discontinuity, constrained to develop in mode I fracture, will not be compatible between elements and this issue will cause severe restrictions on the propagation of the crack. In other works, *the crack will be locked* in the finite element mesh being unable to progress along it, and this will be noticeable in extra energy dissipation, that can be appreciated in the force-displacement curve, as well as, in spurious cracking usually appearing transversally to the main crack.

This type of “kinematic crack locking” should not be confused with the classical stress locking of the traditional localization models, explained at Section 2.4.5, neither with the stress locking associated to fully integrated quads equipped with piece-wise constant jump embedded discontinuities, explained at Appendix B.

Notice that the strong discontinuity conditions are effective when the regularization parameter k is set to zero, and therefore, it can be expected that the restric-

tion on the displacement jump could be alleviated for increasing values of k , since mixed modes would be amenable to develop.

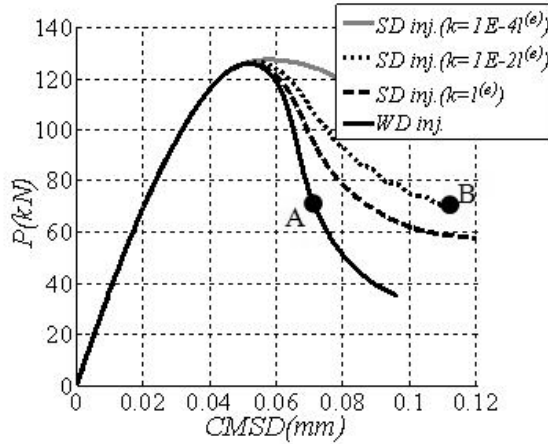


Figure 5.37 Force-displacement curves.

In Figure 5.37 the evolution of the Crack Mouth Sliding Displacement (CMSD) with the applied load P is depicted for several values of the regularizing parameter k . It is also shown the result obtained by using the Weak Discontinuity (WD) injection, considered in this case, as the reference solution. It is shown that for increasing values of k , the crack locking is alleviated, and the fracture can progress more through the finite element mesh dissipating less energy. Nevertheless, even for $k = l^{(e)}$ the result does not match the reference weak discontinuity solution.

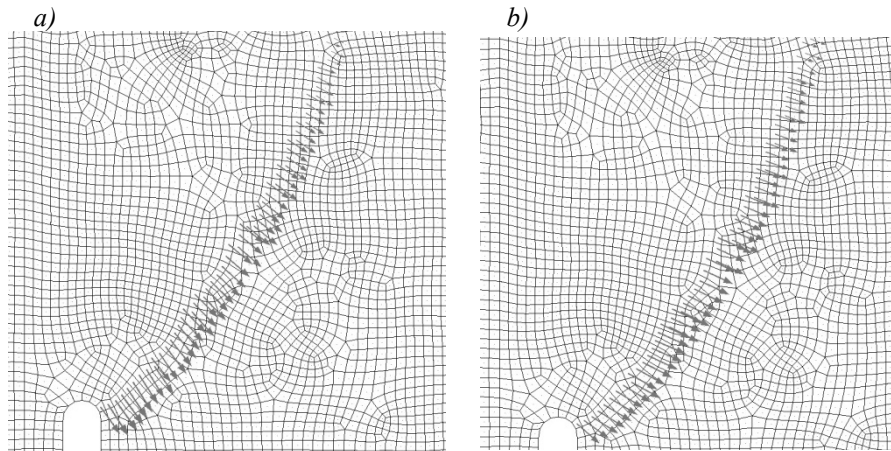


Figure 5.38 Displacement jump vector: a) $SD\ inj. (k=1E-2l^{(e)})$, b) $WD\ inj.$.

In Figure 5.38 it is shown that for the strong discontinuity case (Figure 5.38-a)) the displacement jump vector is orthogonal to the discontinuity, this translating a opening mode (mode I). On the other hand, for to the weak discontinuity case

(Figure 5.38-b)), it is noticeable a rotation on the displacement jump vector, that displays a mixed mode of fracture with opening and sliding.

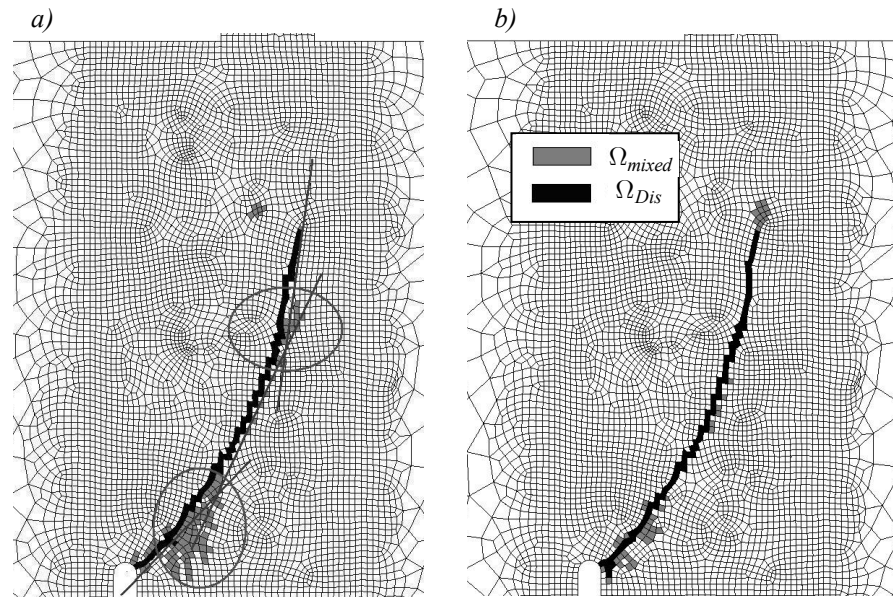


Figure 5.39 Evolution of the injection domains: a) SD inj. (plot corresponding to point B of Figure 5.38), b) WD inj. (plot corresponding to point A of Figure 5.38).

In Figure 5.39 the injection domains for a representative time of the analysis are compared. For the SD case it is noticeable that the mode I opening constrains the crack rotation. This issue is noticeable in Figure 5.39-a) by the spurious in-loading bifurcated elements in the bottom part of the localization band where spurious transversal cracking start developing. At the point of the analysis depicted in Figure 5.39-a), the crack is strictly locked (see horizontal slope of the curve computed with the SD inj. ($k = 1E - 2\ell^{(e)}$) - Figure 5.37) in the finite element mesh and the computation does not converge. For the weak discontinuity case (Figure 5.39-b)) the spurious in-loading elements are almost negligible and the crack can further progress.

This kinematic crack locking effect, appearing when strong discontinuities associated to some continuum constitutive models (or equivalent discrete models) are used, is often neglected in the literature since this type of examples (concrete beams with curved crack patterns) are generally modeled by damage models, and for that case, the strong discontinuity conditions do not imply any constraint on the displacement jump evolution, and mixed modes can develop without restriction (avoiding crack locking in the finite element mesh). Nevertheless, when modeling strong discontinuities, it is important to be well aware about this point, this being the reason that motivate the previous discussion.

For straight crack patterns this problem is not an issue since the mode I fracture can open without any geometrical constraint.

5.5.4.2. Comparison with experimental envelope

Due the kinematic crack locking effects associated with the Rankine plasticity model, the strong discontinuity injection is left aside (for this particular example) being the weak discontinuity solution considered as our reference solution to be compared with results out coming from physical experiments. To verify the improved behavior obtained with the weak discontinuity injection, results are also compared with those obtained by using the constant strain mode injection and with the irreducible formulation. The evolution of CMSD with the applied load P is depicted for the three different alternatives.

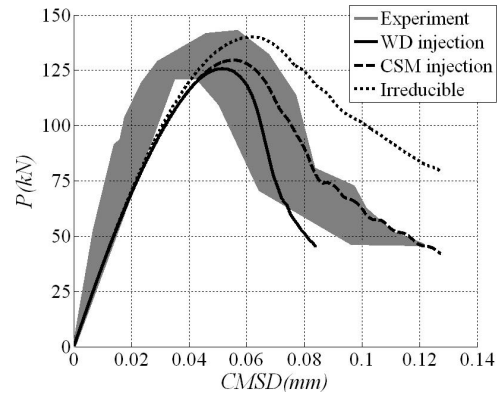


Figure 5.40 Force-displacement curves.

It is shown that when the irreducible formulation is used, due to stress locking, the post-critical behavior is excessively stiff, as it can be observed in the corresponding curve located outside the experimental envelope. On the other hand, when the weak discontinuity is used the post-critical behavior tends to better fit the experimental envelope.

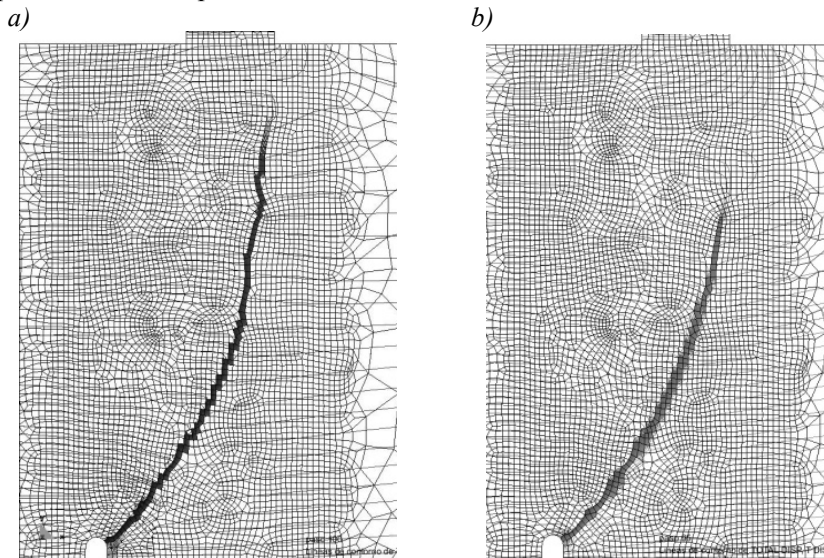


Figure 5.41 Iso-displacement plots: a) WD Injection, b) Irreducible formulation.

For the WD Injection case, it can be noticed that the iso-displacement field is sharply concentrated inside a one-element-width localization band whereas for the irreducible case the localization band is smeared out over more than one element (see Figure 5.41).

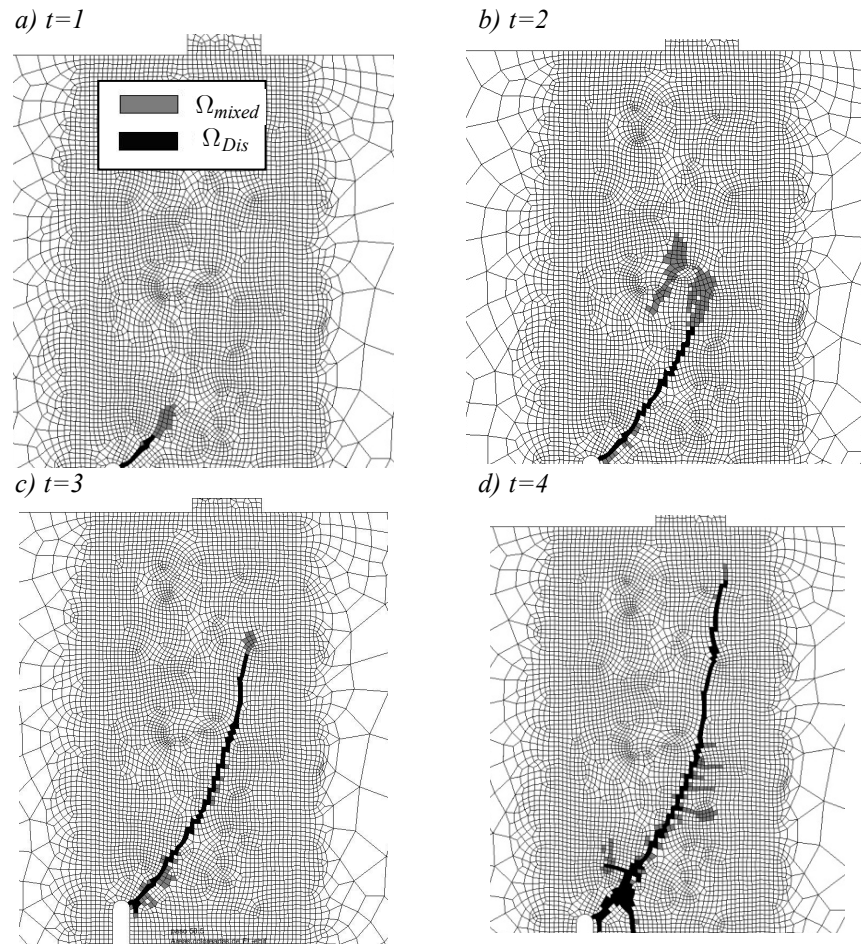


Figure 5.42 Evolution of the injection domains (WD. Injection) different times of the analysis.

In Figure 5.42 the evolution of the injection domains is depicted for several stages of the analysis. Stage 4 corresponds to the last stage of the analysis, just before the point where the computation stops to converge. At this point of analysis, when the crack approaches the top part of the beam, some spurious cracking is also noticed in the bottom of the localization band. Notwithstanding, this effect is considered small since it just happens in the very final stages of the analysis.

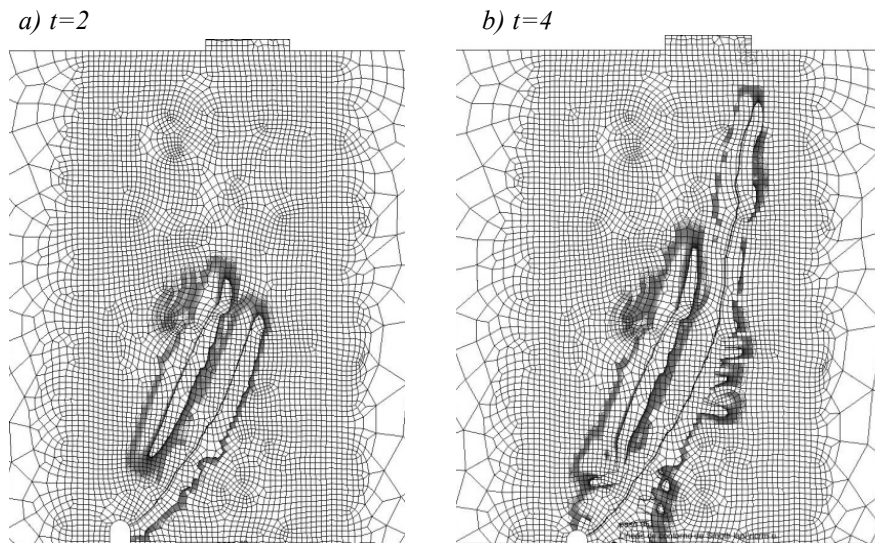


Figure 5.43 Crack propagation path S^h , at two different times of analysis (WD. Injection).

In Figure 5.43, the crack propagation path, obtained by using the weak discontinuity injection, is shown for two different times of analysis. It is noticed, that the crack path evolves from the notch tip reaching the top surface of the specimen just right to the loading platen, corresponding this to the localization band shown in Figure 5.41 a). It is also noticed a second line, corresponding to elements that in a first moment bifurcate (such that $\alpha > 0$), but in second stage unload elastically, so leaving the injection domain (this elements can be observed in Figure 5.42 b)).

5.5.4.3. Mesh refinement

To study mesh refinement influence, in Figure 5.44 and Figure 5.45, results obtained for three different degrees of mesh refinement³⁹, using the weak discontinuity injection, are presented. In terms of crack propagation, similar solutions are obtained whereas in terms of force deflection curves mesh a) produce higher dissipative results.

³⁹ The results presented in the previous Sections were obtained by using mesh c).

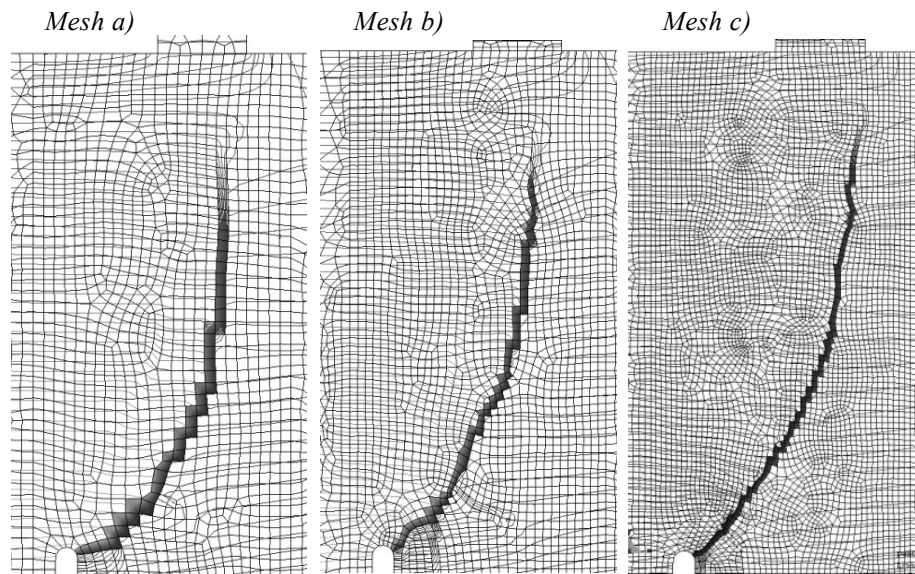


Figure 5.44 Iso-displacement contours for three different degrees of mesh refinement (results obtained using the weak discontinuity injection).

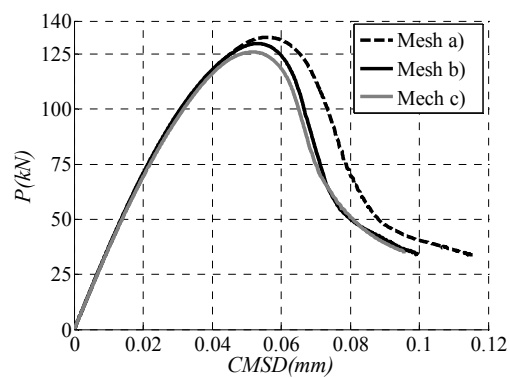


Figure 5.45 Force-displacement curves for three different degrees of mesh refinement (results obtained using the weak discontinuity injection).

5.5.5. Slope stability problem using a J_2 plasticity model

Let us consider now an interesting engineering practical case, as the slope stability problem already presented at Section 4.5.3. There, it was shown that using a misaligned mesh, the B-bar element fails in terms of providing results fully representative of a cohesive fracture.

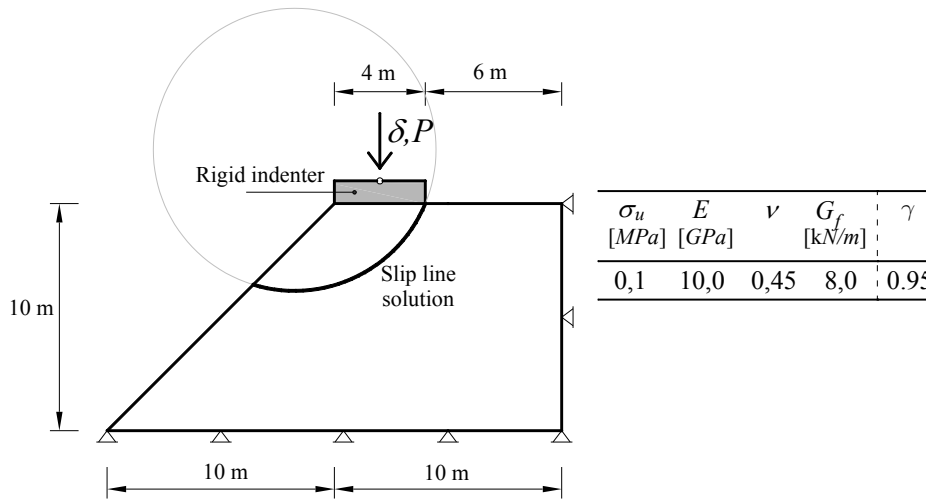


Figure 5.46 Slope stability problem.

Here the results obtained with the B-bar element at Section 4.5.3 are complemented by those obtained by the weak discontinuity injection (WD inj.). The result obtained with the aligned mesh (fully aligned with the slip line solution) is considered as the reference result⁴⁰ (see Figure 5.48).

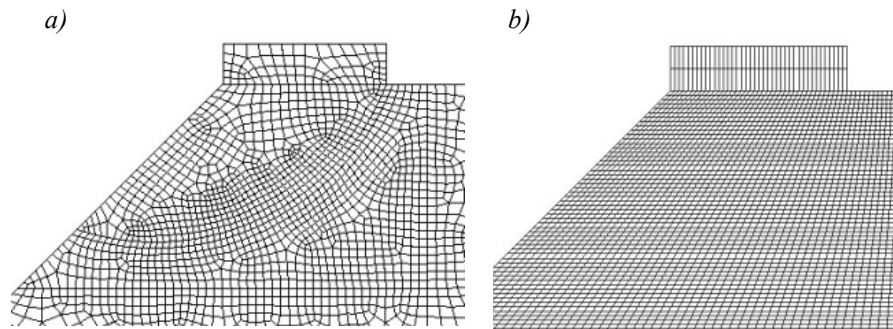


Figure 5.47 Finite element meshes: a) aligned mesh, b) miss-aligned mesh.

⁴⁰ Notice that results obtained with the aligned mesh are almost coincident independently of the formulation employed (either B-bar or weak discontinuity injection). For that reason, they are condensed under the name of “aligned mesh”.

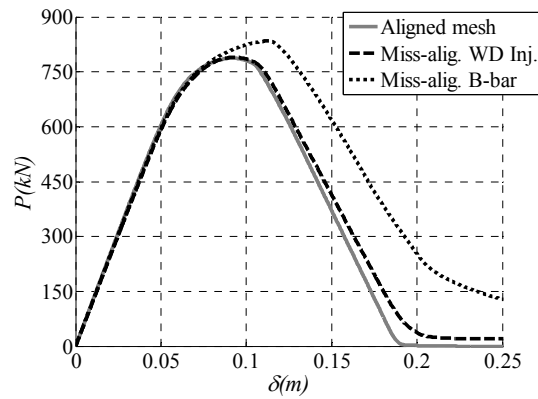


Figure 5.48 Force-displacement curves.

In Figure 5.48, force-displacement curves are shown for the different alternatives. Improved results when the weak discontinuity is injected are shown. Notice that the corresponding force-displacement curve almost match the result obtained with the aligned mesh (also a nearly zero residual load is obtained) this showing stress locking free results.

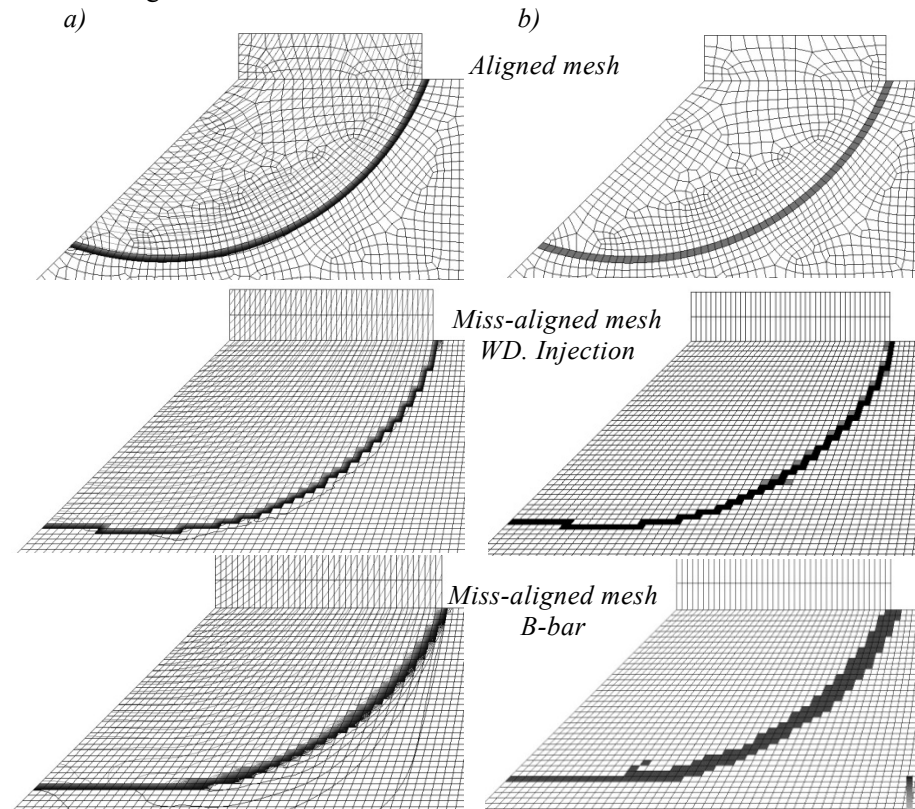


Figure 5.49 a) Iso-displacement contours, b) In-loading bifurcated elements at the final stage of the analysis.

In Figure 5.49, the iso-displacement contours and load patterns (elements in non-linear loading) are shown. For the WD Injection (miss-aligned mesh) it can be appreciated that the iso-displacement field is sharply concentrate inside a one-element-width localization band (as it happen when the aligned mesh is used), whereas for the B-bar case, the discontinuity is (due to stress locking) smeared out over several elements, this translating in the extra-dissipation of energy that can be appreciated in the corresponding force deflection curve of Figure 5.48.

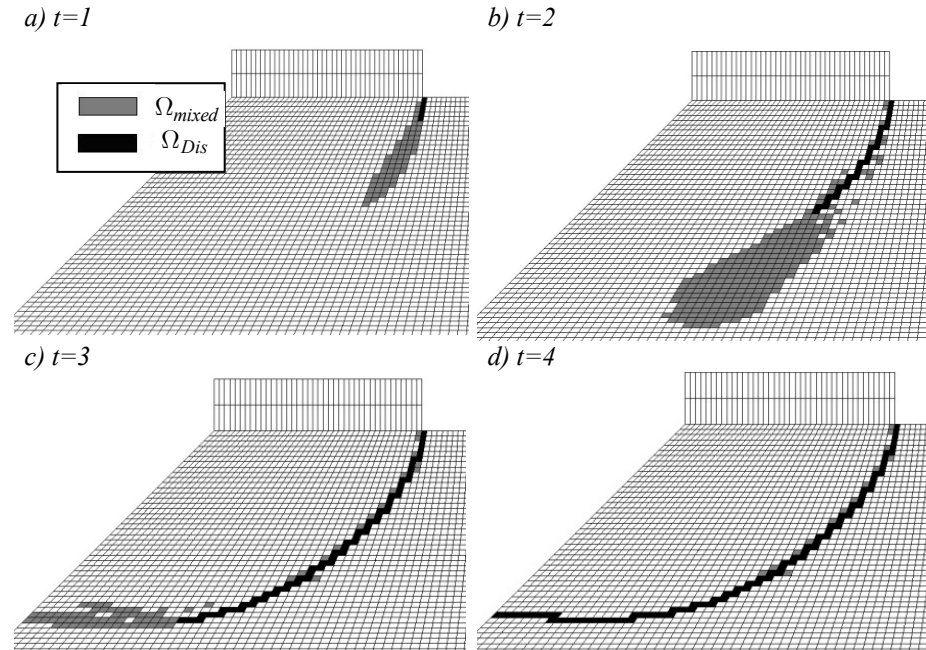


Figure 5.50 Evolution of the injection zones along different times of the analysis (Weak discontinuity injection).

Figure 5.51 shows the evolution of the injection domains, for four representative time steps of the analysis. It is observed, that once the discontinuity mode is injected, the neighboring “locked in” elements tend to unload, and finally, the non-linear loading tends to concentrate in just a layer of elements, corresponding to the band where the discontinuity is injected. In Figure 5.51, the crack propagation path \mathcal{S}^h , corresponding to time $t=2$ and $t=4$, is shown.

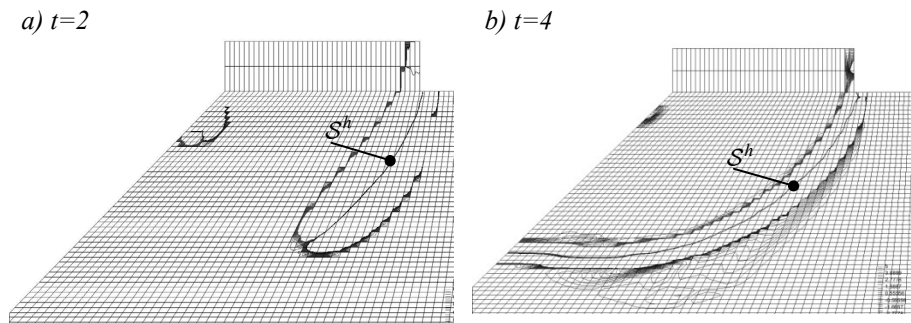


Figure 5.51 Crack propagation path S^h , at two different times of analysis. (Weak discontinuity injection).

5.5.6. Rigid strip footing using a J_2 plasticity model

The numerical example presented in this Section corresponds to the classical geo mechanical problem of an undrained soil layer subjected to a central loading (see Figure 5.52). The same problem was considered in references [Chen 1975; Oliver, Cervera et al. 1999]. Prandtl and Hill have proposed analytic solutions for this classical problem. When a rigid and rough surface footing is modeled, a Prandtl's mechanism is expected to develop (Figure 5.52).

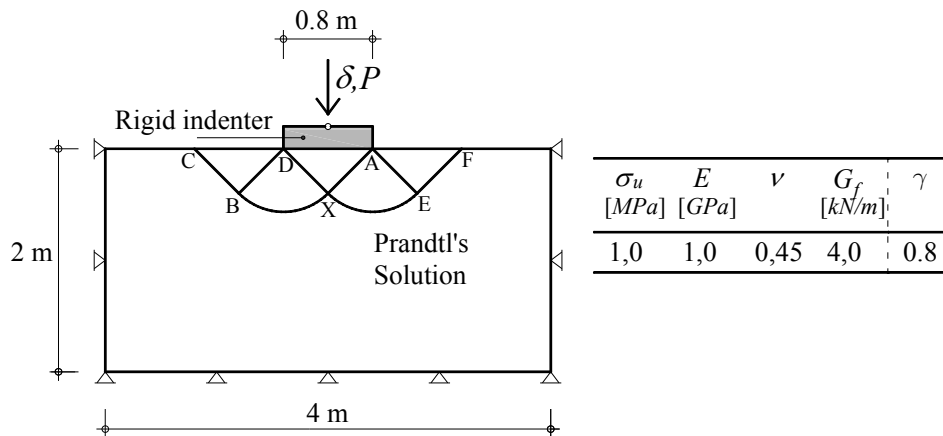


Figure 5.52 Rigid strip footing using a J_2 plasticity model.

In this example, in order to get additional robustness, the value for γ (that establishes the threshold from where the discontinuity is injected) was taken lower than in the previous numerical examples $\gamma = 0.8$. The principal inconvenient is that, some stress locking, at earlier stages of the localization process, can occur. In Figure 5.53, the force-displacement curves considering the

B-bar methodology and WD injection are plotted being the former more dissipative than the later.

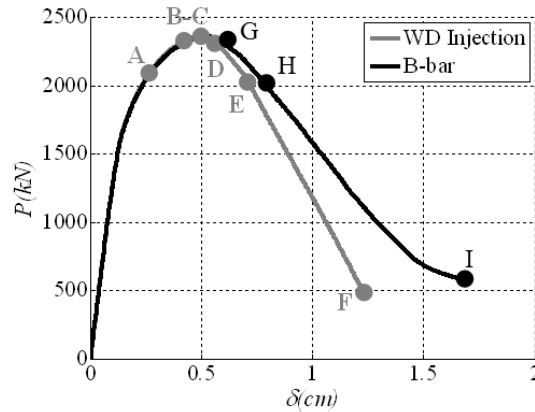


Figure 5.53 Force-displacement curves (The points plotted over the curve stand for the times depicted in Figure 5.53 to Figure 5.65).

5.5.6.1. Weak discontinuity solution

In the following pictures, a typical loading process obtained with the weak discontinuity injection procedure is described.

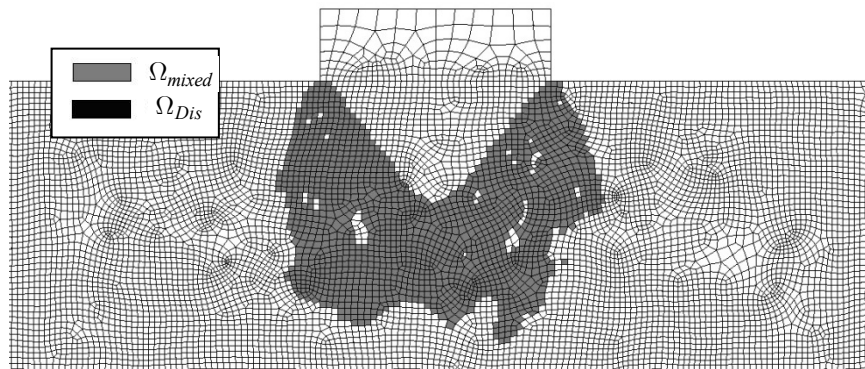


Figure 5.54 Evolution of the inj. domain (WD Injection Step-A of Figure 5.53).

In earlier stages of the non-linear loading, yielding initiates at the bottom corner of the footing spreading downwards and toward the centerline of the footing (see Figure 5.54 where the finite elements belonging to the injection domain are shown). At this point, triangular wedge of soil beneath the footing moving downwards, (jointly with the rigid footing) and remaining without any plastic deformation is displayed.

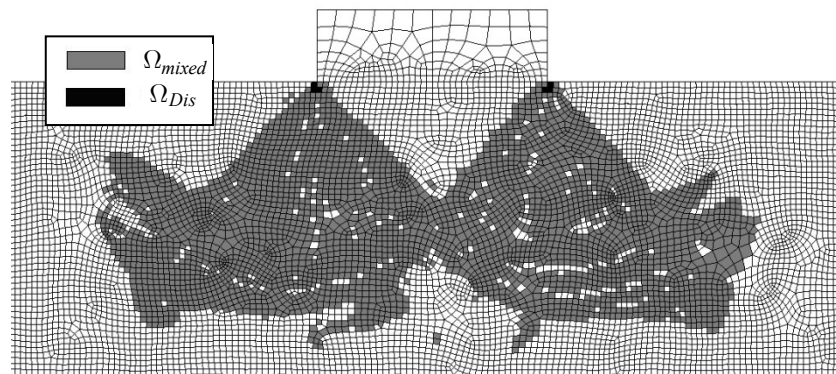


Figure 5.55 Evolution of the inj. domain (WD Injection, Step-B of Figure 5.53).

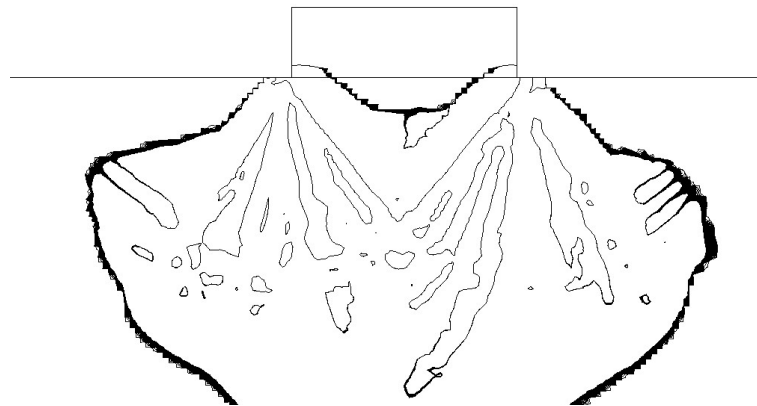


Figure 5.56 Crack propagation path $S^h(\mu^h = 0)$ (WD Inj. Step-B of Figure 5.53).

As loading progresses, the yielding zones remain spreading, now laterally, towards the sides of the footing (see Figure 5.55).

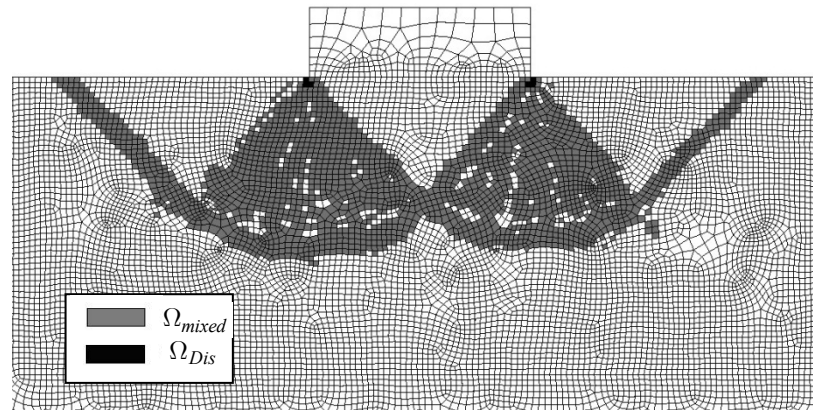


Figure 5.57 Evolution of the injection domain (WD Injection, Step-C of Figure 5.53).

In Figure 5.57 the Prandtl's mechanism, is already formed. In Prandtl's mechanism, the moving downwards triangular wedge of soil beneath the footing induces an upward movement of two lateral wedges that slide with respect to the adjacent soil layers. The triangle wedges moving upwards also remain without any plastic deformation as it can be seen in Figure 5.57. Notice that the symmetric mechanism shown in Figure 5.57 is numerically unstable, *i.e.* small numerical perturbations, as those coming out from numerical errors of the finite element computations (note that an un-symmetric mesh is used) will tend to collapse the solution in a single mechanism as effectively happens in the simulation displayed in Figure 5.59. Notice that the un-symmetric mechanism will dissipate less energy that the symmetric Prandtl's mechanism.

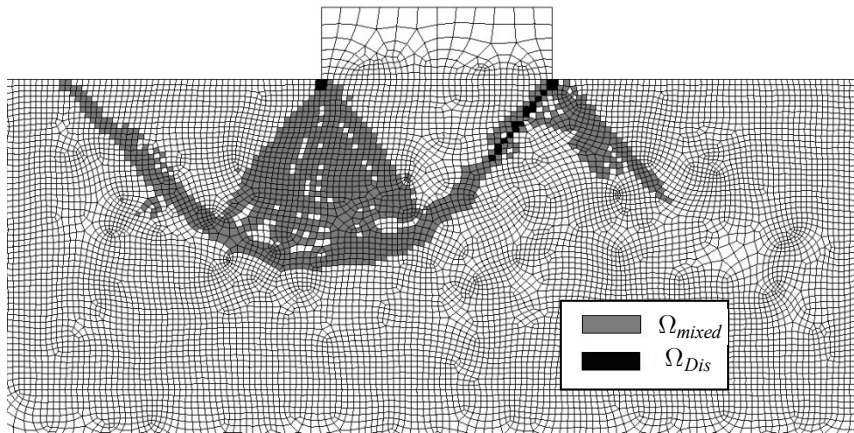


Figure 5.58 Evolution of the injection domain (WD Injection, Step-D of Figure 5.53).

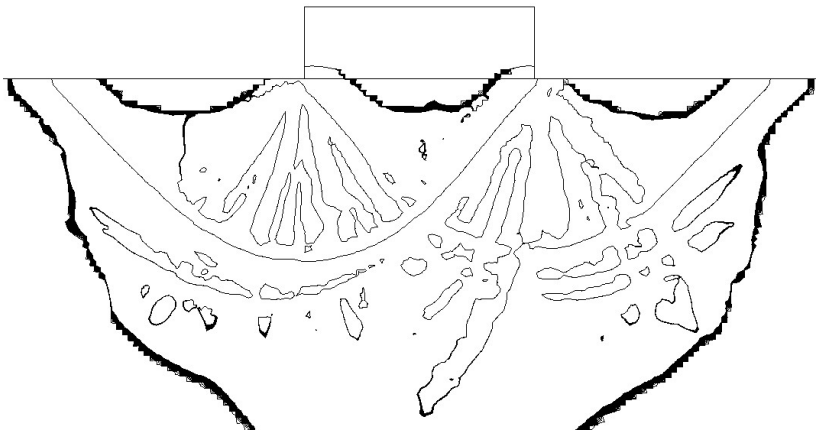


Figure 5.59 Crack propagation path $\mathcal{S}^h(\mu^h = 0)$ (WD Injection, Step-D of Figure 5.53).

At this point, when the Prandtl's mechanism collapses in the un-symmetric mechanism, the footing rotates and almost all the elements associated to mechanism D-X-F unload (see Figure 5.52). It is noticeable that the discontinuity domain Ω_{Dis} start to evolve. Point E of Figure 5.53 corresponds to the time when the discontinuity injection is performed along all the slip line length. At this time most of the elements outside the slip line unload (see Figure 5.60) and plastic deformations tend to concentrate in a unique layer of finite elements.

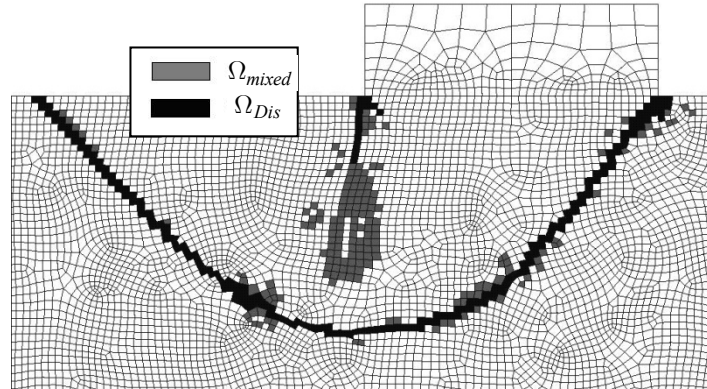


Figure 5.60 Evolution of the injection domain (WD Injection, Step – E of Figure 5.53).

In Figure 5.61 and Figure 5.62 the final step of the analysis The displacements contours and the deformed mesh at are shown, respectively

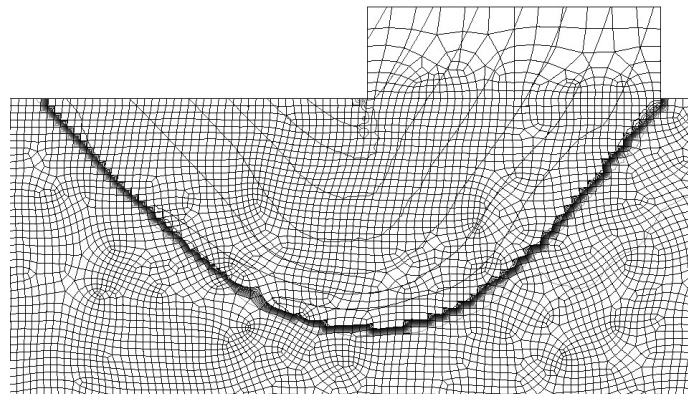


Figure 5.61 Iso-displacement contours (WD Injection, Step – F of Figure 5.53).

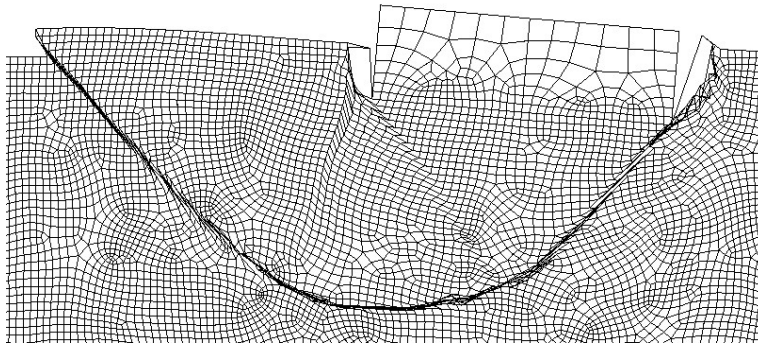


Figure 5.62 *Deformed meshes (WD Injection, Step - F of Figure 5.53).*

5.5.6.2. B-bar solution

In the next Figures, results obtained by using the B-bar method are presented for two steps of the analysis. It is shown that a higher number of bifurcated in-loading elements are noticed. In the final step of the analysis, Figure 5.65 displays that the iso-displacement contours encompass more than one finite element, this translating the extra dissipation already shown in Figure 5.53.

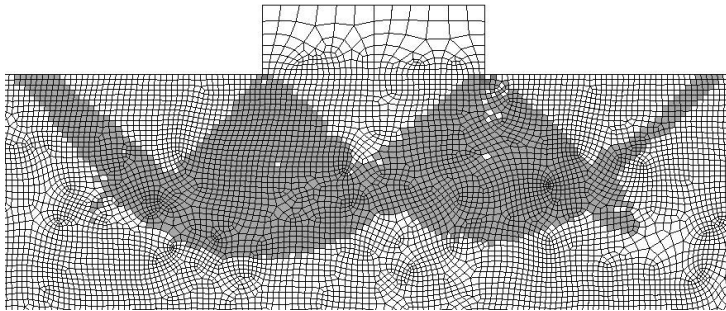


Figure 5.63 *Bifurcated in-loading elements (B-bar, Step-G of Figure 5.53).*

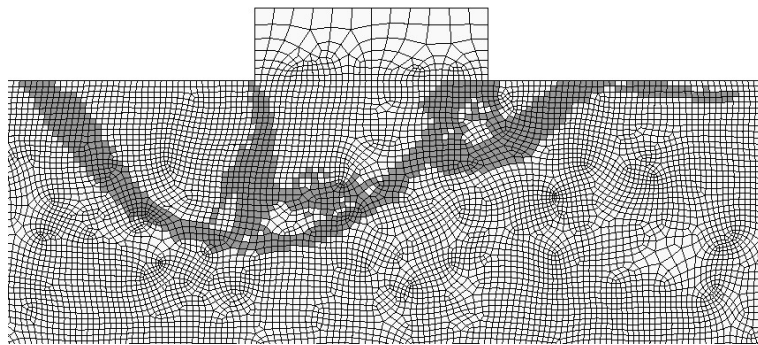


Figure 5.64 *Bifurcated in-loading elements (B-bar, Step-H of Figure 5.53).*

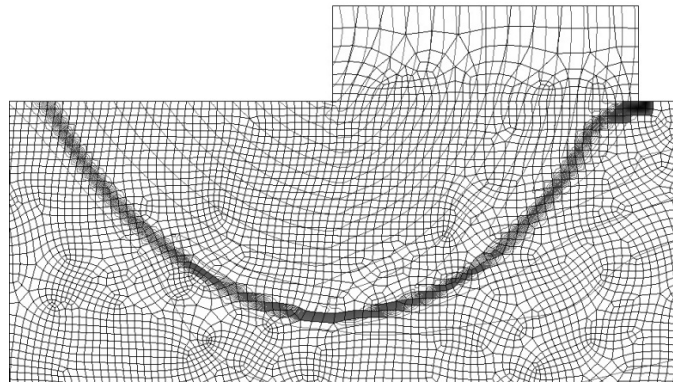


Figure 5.65 Iso-displacement contours (*B*-bar, Step-I of Figure 5.53).

5.5.6.3. Mesh refinement influence (using WD injection)

To study mesh refinement influence in next figures iso-displacement contours for three different degrees of mesh refinement are presented⁴¹. In terms of crack propagation, similar solutions are obtained (see Figure 5.66) whereas in terms of force deflection curves the coarse mesh produces higher dissipative results (see Figure 5.67).

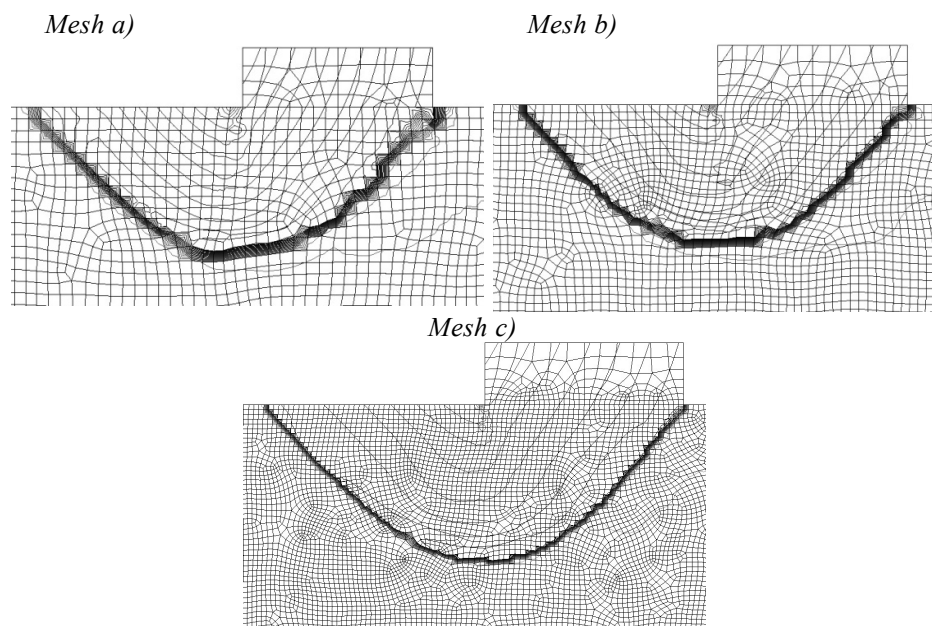


Figure 5.66 Iso-displacement contours for three different degrees of mesh refinement (results obtained by using the weak discontinuity injection).

⁴¹ The results presented in the previous Sections were obtained by using mesh c).

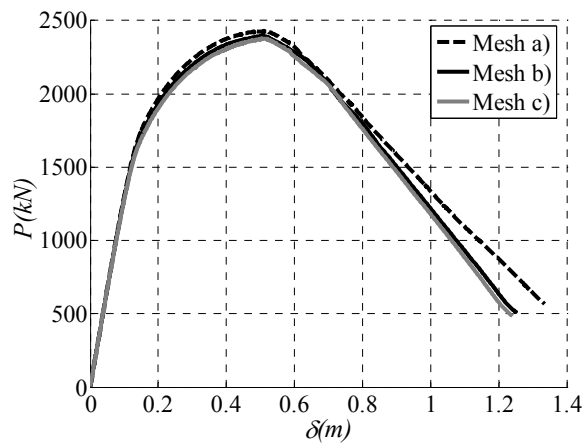


Figure 5.67 Force-displacement curves for three different degrees of mesh refinement (results obtained by using the weak discontinuity injection).

5.5.6.4. Symmetric solution (using WD injection)

It was shown that using a un-symmetric mesh, due to numerical perturbations, the Prandtl's mechanism collapses in a un-symmetric mechanism (as shown in Figure 5.61). On the other hand, by considering the structural symmetry conditions into the numerical analysis (see Figure 5.69-b)) a symmetric solution can be forced.

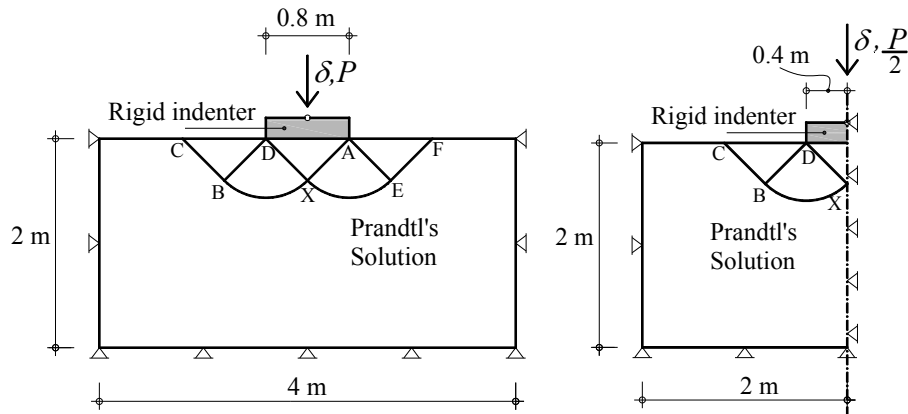


Figure 5.68 Rigid strip footing.

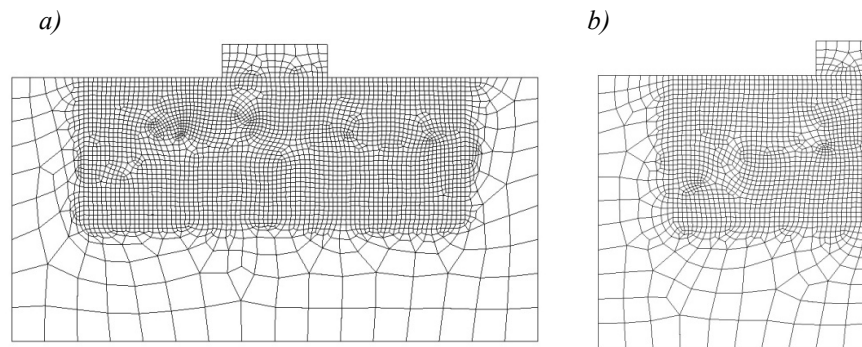


Figure 5.69 a) Un-symmetric mesh (mesh already used at Section 5.5.6.3 (see Figure 5.67-b)), b) Symmetric mesh.

In Figure 5.70, the force-displacement curves obtained by using the symmetric and un-symmetric meshes, are shown. Until point B (of Figure 5.70) both curves coincide. After that, for the un-symmetric mesh, the solution collapse in a lower dissipative un-symmetric mechanism (according to the analysis of Section 5.5.6.1 -see Figure 5.61), whereas, for the mesh b) of Figure 5.69, a symmetric mechanism is obtained (see Figure 5.71).

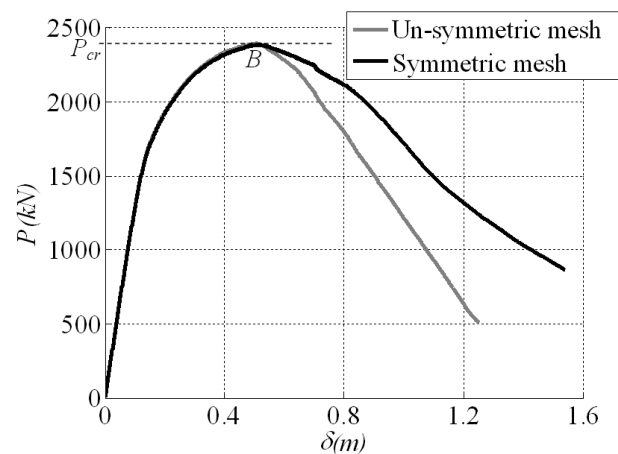
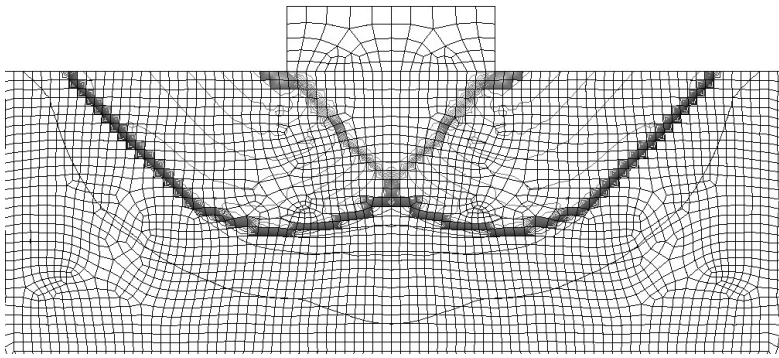
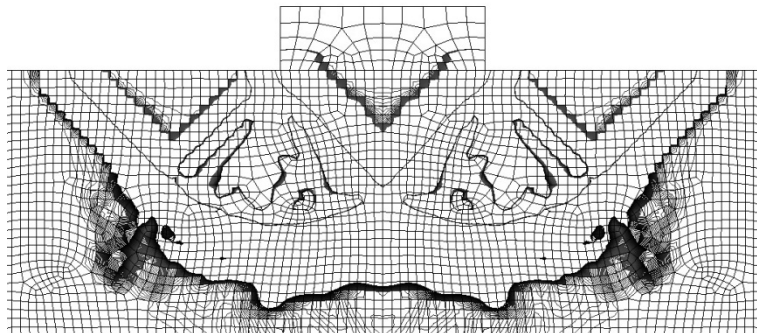
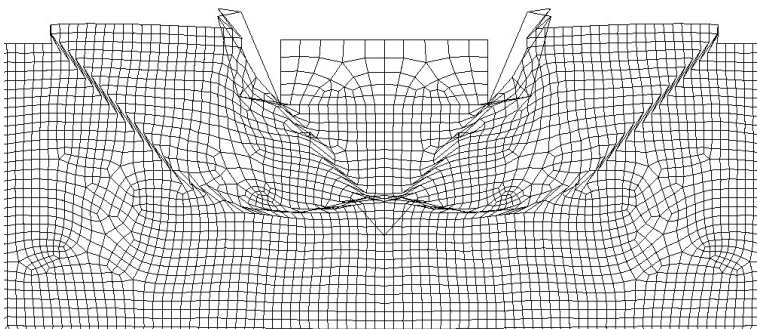


Figure 5.70 Force-displacement curves.
(results obtained using the weak discontinuity injection).

Notice that the theoretical critical load predicted by Prandtl $P_{cr}=2374$ kN match the numerical results.

In Figure 5.71, Figure 5.72 and Figure 5.73, for the symmetric mesh; the iso-displacement contours, the crack propagation path \mathcal{S}^h and the deformed mesh are shown.

Figure 5.71 *Iso-displacement contours.*Figure 5.72 *Crack propagation path S^h .*Figure 5.73 *Deformed mesh.*

Chapter 6

Conclusions

In the preceding Chapters, an exploratory work about the effects of some new techniques for material failure modelling has been presented.

The results presented at Chapter 3 show that, mixed formulations increase remarkably the failure propagation capabilities of the finite elements for capturing strain localization, overcoming the classical mesh bias dependence. Moreover, by restricting the mixed \mathbf{u}, ε formulation (in this work described as a constant strain mode injection for quadrilaterals) to that part of the domain where the fracture is being processed, instabilities related with hourglass modes do not appear.

On the other hand, despite the good information provided about crack propagation, mixed finite elements, still exhibit a limited capability to describe a strong discontinuity in a one-element finite element band, due to kinematic limitations in their deformation capabilities. In Chapter 4, this issue is studied in detail and several objective mismatch indicators were proposed to evaluate these limitations. These mismatch indicators allow arriving to some conclusions:

- The mismatch obtained for general unaligned meshes, is caused by the limited ability of standard finite element to reproduce strong discontinuity embedded into them. This kinematic flaw is here identified as the ultimate reason of stress locking.
- The proposed indicators, can be computed without a-priori knowledge of the exact fracture mechanics solution of the problem, and used as an objective tool for the quantitative evaluation of the performance of strain localization based methods in representing physical material fracture through discontinuous interfaces.

Application of those indicators to a set of benchmark problems, corroborates the limited capability of standard finite element formulations for representing material fracture. The aforementioned injection of a constant strain mode (CSM)

in quadrilateral elements was a first attempt to improve that capability. Apart from the obtained improvements, stress locking is still noticeable. By this reason, in Chapter 5, a second strain injection was proposed *i.e.*, soon after the CSM injection, the elemental kinematics is enhanced by means of the injection of a strong or weak discontinuity strain mode. This second injection is performed, by using the local information obtained from the previous injection (in this sense, the reduced integration quadrilateral is considered as a tracer element). To extract that information and locate the discontinuity into the finite element mesh, an auxiliary methodology was developed and termed as “the crack propagation problem”. The staggered resolution of the coupled problem allows us to regard the crack-propagation problem as a local smoothing technique (a post process) of the strain-like internal variable that can be locally and straightforwardly implemented in a finite element code in a non invasive manner.

The proposed strain injection method, tries to combine the best of two strategies (strain localization and strong discontinuities) for capturing material failure. The principal benefits are:

- The method keeps the simplicity of classical strain localization methods and global tracking algorithms can be circumvented. A pure local method for crack propagation was devised.
- Low computational cost. The computational cost is kept in the order of standard finite element methods (notice that, as a consequence of using finite elements with embedded strong discontinuities, the additional degrees of freedom are always condensed at the elemental level).
- The corresponding results show that the obtained crack patterns are independent on the mesh alignment.
- The benefits of embedded (or X-FEM) strong discontinuities are obtained (no stress locking and high accuracy).
- The methodology is applicable to any constitutive model (damage, elasto-plasticity, *etc.*) without apparent limitations.
- Coarse meshes can be used and local mesh refinement is not needed.
- Richer information about the propagating crack pattern in comparison with tracking based methods is obtained.
- The obtained results are encouraging in terms of the broadness of the application of the new techniques, developed in this work.

Appendix A

Rankine model IMPL-EX integration

In Section 2.2, the main mathematical relations of constitutive models were introduced. Additionally in Section 2.5, concepts related to the numerical integration of general constitutive equations via implicit or IMPL-EX algorithms were presented. Here attention is focused in the implementation aspects inherent to the IMPL-EX integration scheme for the Rankine constitutive model (presented in Section 2.2.1.1).

As it was previously mentioned, the main idea of IMPL-EX integration scheme is the extrapolation of the strain like internal variable (plastic multiplier) for the time step $n + 1$, from its implicit value computed in previous time step n . With this extrapolated variable an explicit evaluation of the stress tensor is performed and the momentum balance (equation (2.97)) is imposed in terms of these IMPL-EX stresses.

In Section A.1 of this appendix it is developed a procedure for the numerical computation of the implicit plastic multiplier. In Section A.2 expressions for the calculation of the IMPL-EX stresses and its consistent algorithmic tangent operator are developed. Finally in Section A.3 a step-by-step IMPL-EX algorithm of the Rankine constitutive model is summarized.

Following, in Box A.1, the main ingredients of Rankine constitutive model are summarized.

Additive decomposition	$\boldsymbol{\varepsilon} = \boldsymbol{\varepsilon}^e + \boldsymbol{\varepsilon}^p$	(A.1)
Constitutive equation	$\boldsymbol{\sigma} = \mathbf{C}^{el} : (\boldsymbol{\varepsilon} - \boldsymbol{\varepsilon}^p)$	(A.2)
Yield surface	$f^i(\boldsymbol{\sigma}, q) = \sigma^i - q, \quad i = I, II, III$	(A.3)
Flow rule	$\dot{\boldsymbol{\varepsilon}}^p = \sum_{i=I}^{III} \gamma^i \mathbf{m}^i \quad ; \quad \mathbf{m}^i(\boldsymbol{\sigma}) = \mathbf{p}^i \otimes \mathbf{p}^i$	(A.4)
Hardening law	$\dot{q}^p = H \sum_{i=I}^{III} \gamma^i$	(A.5)

Box A.1 Rankine constitutive model.

A.1. Implicit evaluation of the consistency parameter

According to the implicit backward-Euler difference the plastic strain $\boldsymbol{\varepsilon}_{n+1}^p$ is updated as follows:

$$\boldsymbol{\varepsilon}_{n+1}^p = \boldsymbol{\varepsilon}_n^p + \underbrace{\sum_{i=I}^{III} \Delta \gamma^i \mathbf{m}_{n+1}^i}_{\Delta \boldsymbol{\varepsilon}_{n+1}^p} \cdot \quad (\text{A.6})$$

By substituting the preceding equation into the constitutive relation (A.2), the expression for the stress tensor, at time step $n + 1$, reads:

$$\begin{aligned} \boldsymbol{\sigma}_{n+1} &= \mathbf{C}^{el} : \boldsymbol{\varepsilon}_n^e + \mathbf{C}^{el} : \Delta \boldsymbol{\varepsilon}_{n+1}^e = \underbrace{\mathbf{C}^{el} : (\boldsymbol{\varepsilon}_{n+1} - \boldsymbol{\varepsilon}_n^p)}_{\boldsymbol{\sigma}_{n+1}^{trial}} - \mathbf{C}^{el} : \Delta \boldsymbol{\varepsilon}_{n+1}^p, \\ \boldsymbol{\sigma}_{n+1} &= \boldsymbol{\sigma}_{n+1}^{trial} - \mathbf{C}^{el} : \sum_{i=I}^{III} \Delta \gamma^i \mathbf{m}_{n+1}^i \quad ; \quad \mathbf{m}_{n+1}^i(\boldsymbol{\sigma}_{n+1}) = \mathbf{p}_{n+1}^i \otimes \mathbf{p}_{n+1}^i. \end{aligned} \quad (\text{A.7})$$

Since the linear elastic fourth order tensor, \mathbf{C}^{el} is isotropic, the principal directions of $\boldsymbol{\sigma}_{n+1}$ are the same than the principal directions of $\boldsymbol{\sigma}_{n+1}^{trial}$, so $\mathbf{m}_{n+1}^i = \mathbf{m}_{n+1}^{i,trial}$, and the previous expression may be evaluated in a coordinate system with axes oriented in the principal directions of $\boldsymbol{\sigma}_{n+1}^{trial}$ and $\boldsymbol{\sigma}_{n+1}$.

Expression (A.7) may be written in the form:

$$\begin{bmatrix} \sigma^I \\ \sigma^{II} \\ \sigma^{III} \end{bmatrix}_{n+1} = \begin{bmatrix} \sigma^I \\ \sigma^{II} \\ \sigma^{III} \end{bmatrix}_{n+1}^{trial} - \underbrace{\begin{bmatrix} \lambda + 2\mu & \lambda & \lambda \\ \lambda & \lambda + 2\mu & \lambda \\ \lambda & \lambda & \lambda + 2\mu \end{bmatrix}}_{[\mathbf{C}_R^{el}]} \begin{bmatrix} \Delta\gamma^I \\ \Delta\gamma^{II} \\ \Delta\gamma^{III} \end{bmatrix}_{n+1}, \quad (\text{A.8})$$

$$\{\sigma_{n+1}^i\} = \left(\{\sigma_{n+1}^{i,trial}\} - [\mathbf{C}_R^{el}] \{\Delta\gamma_{n+1}^i\} \right).$$

And, to update the stress-like internal variable, from equation (A.5)

$$q_{n+1} = q_n + H \sum_{i=I}^{III} \Delta\gamma^i = q_n + H (\Delta\gamma^I + \Delta\gamma^{II} + \Delta\gamma^{III}),$$

$$\begin{bmatrix} q \\ q \\ q \end{bmatrix}_{n+1} = \begin{bmatrix} q \\ q \\ q \end{bmatrix}_n + \begin{bmatrix} H & H & H \\ H & H & H \\ H & H & H \end{bmatrix} \begin{bmatrix} \Delta\gamma^I \\ \Delta\gamma^{II} \\ \Delta\gamma^{III} \end{bmatrix}_{n+1}. \quad (\text{A.9})$$

where expression (A.9) was written in a matrix form in order to simplify the following algebraic manipulations.

The yield surface expression (A.3) at time step $n + 1$ reads,

$$\begin{aligned} f_{n+1}^I &= \sigma_{n+1}^I - (\sigma_y + q_{n+1}), \\ f_{n+1}^{II} &= \sigma_{n+1}^{II} - (\sigma_y + q_{n+1}), \\ f_{n+1}^{III} &= \sigma_{n+1}^{III} - (\sigma_y + q_{n+1}). \end{aligned} \quad (\text{A.10})$$

By substituting expression (A.8) and (A.9) into the yield surface expression, yields,

$$\begin{bmatrix} f^I \\ f^{II} \\ f^{III} \end{bmatrix}_{n+1} = \begin{bmatrix} f^I \\ f^{II} \\ f^{III} \end{bmatrix}_{n+1}^{trial} - \begin{bmatrix} \lambda + 2\mu + H & \lambda + H & \lambda + H \\ \lambda + H & \lambda + 2\mu + H & \lambda + H \\ \lambda + H & \lambda + H & \lambda + 2\mu + H \end{bmatrix} \begin{bmatrix} \Delta\gamma^I \\ \Delta\gamma^{II} \\ \Delta\gamma^{III} \end{bmatrix}_{n+1}, \quad (\text{A.11})$$

where:

$$\begin{bmatrix} f^I \\ f^{II} \\ f^{III} \end{bmatrix}_{n+1}^{trial} = \begin{bmatrix} \sigma^I \\ \sigma^{II} \\ \sigma^{III} \end{bmatrix}_{n+1}^{trial} - \begin{bmatrix} q \\ q \\ q \end{bmatrix}_n. \quad (\text{A.12})$$

Notice that, in loading state, it is possible to have just one, two or all the three surfaces active. Therefore the equation (A.11) is solved recursively through the following procedure in Box A.1:

- 1) Compute $f_{n+1}^{I\text{trial}}$ with $f_{n+1}^{I\text{trial}} = \sigma_{n+1}^{I\text{trial}} - q_n$
 $f_{n+1}^{I\text{trial}} < 0$ implies elastic behavior, then $\Delta\gamma_{n+1}^I = 0$, $\Delta\gamma_{n+1}^{II} = 0$ and
 $\Delta\gamma_{n+1}^{III} = 0$ & EXIT
- 2) If $f_{n+1}^{I\text{trial}} \geq 0$, it is assumed that just f_{n+1}^I is violated (then $\Delta\gamma_{n+1}^{II} = 0$ and
 $\Delta\gamma_{n+1}^{III} = 0$). Imposing $f_{n+1}^I = 0$, (A.11) yields $\Delta\gamma_{n+1}^I = \frac{f_{n+1}^{I\text{trial}}}{(\lambda + 2\mu + H)}$
- 3) Verify $f_{n+1}^{II} < 0$, with $f_{n+1}^{II} = f_{n+1}^{II\text{trial}} - (\lambda + H)\Delta\gamma_{n+1}^I$
 If $f_{n+1}^{II} < 0$ EXIT
- 4) If $f_{n+1}^{II} \geq 0$, is assumed that just f_{n+1}^I and f_{n+1}^{II} are violated ($\Delta\gamma_{n+1}^{III} = 0$),
 imposing in (A.11) $f^I = 0$ and $f^{II} = 0$:

$$f_{n+1}^{I\text{trial}} - (\lambda + 2\mu + H)\Delta\gamma_{n+1}^I - (\lambda + H)\Delta\gamma_{n+1}^{II} = 0$$

$$f_{n+1}^{II\text{trial}} - (\lambda + H)\Delta\gamma_{n+1}^I - (\lambda + 2\mu + H)\Delta\gamma_{n+1}^{II} = 0$$
 Solving analytically the previous system of equations, yields:

$$\Delta\gamma_{n+1}^I = \frac{af_{n+1}^{I\text{trial}} - bf_{n+1}^{II\text{trial}}}{a^2 - b^2} \quad \text{and} \quad \Delta\gamma_{n+1}^{II} = \frac{af_{n+1}^{II\text{trial}} - bf_{n+1}^{I\text{trial}}}{a^2 - b^2}$$
 where $a = \lambda + 2\mu + H$ and $b = \lambda + H$
- 5) Verify $f_{n+1}^{III} < 0$, with $f_{n+1}^{III} = f_{n+1}^{III\text{trial}} - (\lambda + H)\Delta\gamma_{n+1}^I - (\lambda + H)\Delta\gamma_{n+1}^{II}$
 If $f_{n+1}^{III} < 0$ EXIT
- 6) if $f_{n+1}^{III} \geq 0$, all the surfaces are active then $f_{n+1}^I = 0$, $f_{n+1}^{II} = 0$ and
 $f_{n+1}^{III} = 0$

System of equations to be solved:

$$\begin{bmatrix} \Delta\gamma^I \\ \Delta\gamma^{II} \\ \Delta\gamma^{III} \end{bmatrix}_{n+1} = \left(\begin{bmatrix} \lambda + 2\mu + H & \lambda + H & \lambda + H \\ \lambda + H & \lambda + 2\mu + H & \lambda + H \\ \lambda + H & \lambda + H & \lambda + 2\mu + H \end{bmatrix} \right)^{-1} \begin{bmatrix} f^I \\ f^{II} \\ f^{III} \end{bmatrix}_{n+1}^{\text{trial}}$$

Box A.2 Determination of the plastic multiplier

A.2. Explicit evaluation of the stress tensor

Considering a linear extrapolation for the plastic multiplier:

$$\Delta \tilde{\gamma}_{n+1} \stackrel{def}{=} \frac{\Delta t_{n+1}}{\Delta t_n} \Delta \gamma_n. \quad (\text{A.13})$$

Then the explicit evaluation of the IMPL-EX stresses is obtained as:

$$\tilde{\sigma}_{n+1} = \sigma_{n+1}^{trial} - \mathbf{C}^{el} : \sum_{i=1}^n \Delta \tilde{\gamma}_{n+1}^i \tilde{\mathbf{m}}_{n+1}^i, \quad \text{with } \tilde{\mathbf{m}}_{n+1}^i = \mathbf{m}_{n+1}^i(\tilde{\sigma}_{n+1}). \quad (\text{A.14})$$

Differentiating with respect to the strains, the tangent algorithmic operator reads:

$$\tilde{\mathbf{C}}_{n+1}^{alg} = \frac{\partial \tilde{\sigma}_{n+1}}{\partial \varepsilon_{n+1}} = \frac{\sigma_{n+1}^{trial}}{\partial \varepsilon_{n+1}} - \mathbf{C}^{el} : \sum_{i=1}^n \Delta \tilde{\gamma}_{n+1}^i \frac{\partial \tilde{\mathbf{m}}_{n+1}^i}{\partial \tilde{\sigma}_{n+1}} \frac{\partial \tilde{\sigma}_{n+1}}{\partial \varepsilon_{n+1}}. \quad (\text{A.15})$$

One of the most significant features, that one wants to attain, when using the IMPL-EX integration scheme, is the step-wise linear algorithm that emerges from the explicit extrapolation of the strain like internal variable (this aspect is important in order to minimize the computational cost). Nevertheless inspecting the previous expression can be noticed that the term $\partial \tilde{\mathbf{m}}_{n+1}^i / \partial \tilde{\sigma}_{n+1}$ is not constant during the time step, since $\tilde{\mathbf{m}}_{n+1}^i$ do not depend linearly on the stresses $\tilde{\sigma}_{n+1}$. In order to preserve that important property (step liner algorithm) Oliver suggests the linearization of the flow tensor around σ_n [Oliver et al. 2008b].

$$\begin{aligned} \tilde{\mathbf{m}}^i(\tilde{\sigma}_{n+1}) &= \tilde{\mathbf{m}}^i(\sigma_n + \Delta \tilde{\sigma}_{n+1}) = \\ &= \mathbf{m}^i(\sigma_n) + \frac{\partial \mathbf{m}^i(\sigma_n)}{\partial \sigma_n} \Delta \tilde{\sigma}_{n+1} + \mathcal{O}(\Delta \tilde{\sigma}_{n+1}). \end{aligned} \quad (\text{A.16})$$

Truncation up to the linear term yields,

$$\tilde{\mathbf{m}}_{n+1}^i = \mathbf{m}_n^i + \frac{\partial \mathbf{m}_n^i}{\partial \sigma_n} : (\tilde{\sigma}_{n+1} - \sigma_n). \quad (\text{A.17})$$

The flow tensor \mathbf{m} is a degree zero homogenous function of the stresses $\mathbf{m}(\lambda \sigma) = \mathbf{m}(\sigma)$ (note that there's no change on the principal directions when the stress tensor is multiplied by a factor λ). Therefore, applying the Euler's theorem for homogeneous functions [Apostol 1967], it turns out that :

$$\frac{\partial \mathbf{m}_n^i(\sigma_n)}{\partial \sigma_n} : \sigma_n = 0. \quad (\text{A.18})$$

Thus the linearized flow tensor reads:

$$\bar{\mathbf{m}}_{n+1}^i = \mathbf{m}_n^i + \frac{\partial \mathbf{m}_n^i}{\partial \boldsymbol{\sigma}_n} : \tilde{\boldsymbol{\sigma}}_{n+1}, \quad (\text{A.19})$$

and the IMPL-EX stresses:

$$\tilde{\boldsymbol{\sigma}}_{n+1} = \boldsymbol{\sigma}_{n+1}^{trial} - \mathbf{C}^{el} : \sum_{i=1}^n \Delta \tilde{\gamma}_{n+1}^i \left(\mathbf{m}_n^i + \frac{\partial \mathbf{m}_n^i}{\partial \boldsymbol{\sigma}_n} : \tilde{\boldsymbol{\sigma}}_{n+1} \right). \quad (\text{A.20})$$

After some algebraic manipulation,

$$\tilde{\boldsymbol{\sigma}}_{n+1} = \underbrace{\left(\mathbb{I} + \mathbf{C}^{el} : \sum_{i=1}^{III} \Delta \tilde{\gamma}_{n+1}^i \frac{\partial \mathbf{m}_n^i}{\partial \boldsymbol{\sigma}_n} \right)^{-1}}_{\mathbb{H}} : \left(\boldsymbol{\sigma}_{n+1}^{trial} - \mathbf{C}^{el} : \sum_{i=1}^{III} \Delta \tilde{\gamma}_{n+1}^i \mathbf{m}_n^i \right). \quad (\text{A.21})$$

Differentiating $\tilde{\boldsymbol{\sigma}}_{n+1}$ with respect to the strains $\boldsymbol{\varepsilon}_{n+1}$, the tangent algorithmic operator yields:

$$\frac{\partial \tilde{\boldsymbol{\sigma}}_{n+1}}{\partial \boldsymbol{\varepsilon}_{n+1}} = \tilde{\mathbf{C}}_{n+1}^{alg} = \mathbb{H}^{-1} : \mathbf{C}^{el}, \quad (\text{A.22})$$

where:

$$\mathbb{H} = \mathbb{I} + \mathbf{C}^{el} : \sum_{i=1}^{III} \Delta \tilde{\gamma}_{n+1}^i \frac{\partial \mathbf{m}_n^i}{\partial \boldsymbol{\sigma}_n}, \quad (\text{A.23})$$

where, now, the algorithmic tangent operator is constant during the time step $n+1$, *i.e.* the IMPL-EX integration scheme yield a step-wise linear problem and the iterative procedure will converge in just one iteration.

The above expressions entail the calculation of the eigenvectors derivative with respect to the tensor itself $\frac{\partial \mathbf{p}^i \otimes \mathbf{p}^i}{\partial \boldsymbol{\sigma}}$. Here, the expressions used in our implementation are presented [Banerjee and Norris 2007]. For alternative expressions interested readers may consult [Carlson and Hoger 1986].

$$\begin{aligned} \frac{\partial \mathbf{n}^I \otimes \mathbf{n}^I}{\partial \boldsymbol{\sigma}} &= \frac{1}{a_1} (a_2 \mathbb{J}_1 + a_3 (\mathbb{J}_2 - \mathbb{J}_3) - a_4 \mathbb{I} + 2\mathbb{I} * \boldsymbol{\sigma}), \\ \frac{\partial \mathbf{n}^{II} \otimes \mathbf{n}^{II}}{\partial \boldsymbol{\sigma}} &= \frac{1}{a_5} (a_6 \mathbb{J}_2 + a_7 (\mathbb{J}_1 - \mathbb{J}_3) - a_8 \mathbb{I} + 2\mathbb{I} * \boldsymbol{\sigma}), \\ \frac{\partial \mathbf{n}^{III} \otimes \mathbf{n}^{III}}{\partial \boldsymbol{\sigma}} &= \frac{1}{a_9} (a_{10} \mathbb{J}_3 + a_{11} (\mathbb{J}_1 - \mathbb{J}_2) - a_{12} \mathbb{I} + 2\mathbb{I} * \boldsymbol{\sigma}), \end{aligned} \quad (\text{A.24})$$

where:

$$\begin{aligned}
a_1 &= (\sigma^I - \sigma^{II})(\sigma^I - \sigma^{III}); a_2 = \sigma^{II} + \sigma^{III} - 2\sigma^I; a_3 = \sigma^{III} - \sigma^{II}; a_4 = \sigma^{II} + \sigma^{III}, \\
a_5 &= (\sigma^{II} - \sigma^I)(\sigma^{II} - \sigma^{III}); a_6 = \sigma^I + \sigma^{III} - 2\sigma^{II}; a_7 = \sigma^{III} - \sigma^I; a_8 = \sigma^I + \sigma^{III}, \\
a_9 &= (\sigma^{III} - \sigma^I)(\sigma^{III} - \sigma^{II}); a_{10} = \sigma^I + \sigma^{II} - 2\sigma^{III}; a_{11} = \sigma^{II} - \sigma^I; a_{12} = \sigma^I + \sigma^{II}, \\
\mathbb{J}^i &= \mathbf{n}^i \otimes \mathbf{n}^i \otimes \mathbf{n}^i \otimes \mathbf{n}^i,
\end{aligned}$$

and \mathbb{I} stands for fourth order unit tensor and the product $\mathbb{I}^* \boldsymbol{\sigma}$ is defined as

$$\mathbb{I}^* \boldsymbol{\sigma} = \frac{1}{2} (\mathbb{I}_{ijmp} \sigma_{pn} + \mathbb{I}_{ijnp} \sigma_{pm}) ; \mathbb{I}_{ijmp} = \frac{1}{2} (\delta_{im} \delta_{jp} + \delta_{ip} \delta_{jm}). \quad (\text{A.25})$$

For repeated eigenvalues, the derivative given by the previous expression is unbounded and the procedure for its calculation becomes quite cumbersome [Friswell 1996]. In practical computations this case rarely occurs. In our implementation this rare case is circumvented by the introduction of a small numerical perturbation on one of the repeated eigenvalues.

The fourth order tensor \mathbb{H} (see (A.23) appearing in expressions (A.21) and (A.22), may be easily evaluated in a coordinate system with axes oriented to the principal directions of $\boldsymbol{\sigma}_n$, and then transformed to the general Cartesian system by a transformation rule. In principal coordinates and using Voigt notation:

$$\{2\mathbb{I}^* \boldsymbol{\sigma}\} = \begin{bmatrix} p_1 & 0 & \dots & 0 \\ 0 & p_2 & & \\ & & p_3 & \vdots \\ \vdots & & & p_4 \\ & & & & p_5 & 0 \\ 0 & \dots & 0 & p_6 \end{bmatrix} ; \{\mathbb{H}\} = \begin{bmatrix} 1 & 0 & \dots & 0 \\ 0 & 1 & & \\ & & 1 & \vdots \\ \vdots & & & 0.5 \\ & & & & 0.5 & 0 \\ 0 & \dots & 0 & 0.5 \end{bmatrix}, \quad (\text{A.26})$$

where:

$$\begin{aligned}
p_1 &= \sigma^I ; p_2 = \sigma^{II} ; p_3 = \sigma^{III}, \\
p_4 &= \frac{1}{2} (0.5\sigma^{II} + 0.5\sigma^{III}) ; p_5 = \frac{1}{2} (0.5\sigma^I + 0.5\sigma^{III}), \\
p_6 &= \frac{1}{2} (0.5\sigma^I + 0.5\sigma^{II}),
\end{aligned}$$

With some trivial algebraic manipulation the term $\sum_{i=1}^{III} \Delta \tilde{\gamma}_{n+1}^i \frac{\partial \mathbf{m}_n^i}{\partial \boldsymbol{\sigma}_n}$ appearing in (A.23), can be written using Voigt notation as:

$$\left\{ \sum_{i=I}^{III} \Delta \tilde{\gamma}_{n+1}^i \frac{\partial \mathbf{m}_n^i}{\partial \boldsymbol{\sigma}_n} \right\} = \begin{bmatrix} D_1 & 0 & \dots & 0 \\ 0 & D_2 & & \\ & & D_3 & \vdots \\ \vdots & & & D_4 \\ & & & & D_5 & 0 \\ 0 & \dots & 0 & D_6 \end{bmatrix}, \quad (\text{A.27})$$

where

$$\begin{aligned} D_1 &= \Delta \tilde{\gamma}^I (a_2 - a_4 + p_1) + \Delta \tilde{\gamma}^{II} (a_7 - a_8 + p_1) + \Delta \tilde{\gamma}^{III} (a_{11} - a_{12} + p_1), \\ D_2 &= \Delta \tilde{\gamma}^I (a_3 - a_4 + p_2) + \Delta \tilde{\gamma}^{II} (a_6 - a_8 + p_2) + \Delta \tilde{\gamma}^{III} (-a_{11} - a_{12} + p_2), \\ D_3 &= \Delta \tilde{\gamma}^I (-a_3 - a_4 + p_3) + \Delta \tilde{\gamma}^{II} (-a_7 - a_8 + p_3) + \Delta \tilde{\gamma}^{III} (a_{10} - a_{12} + p_3), \\ D_4 &= \Delta \tilde{\gamma}^I (-0.5a_4 + p_4) + \Delta \tilde{\gamma}^{II} (-0.5a_8 + p_4) + \Delta \tilde{\gamma}^{III} (-0.5a_{12} + p_4), \\ D_5 &= \Delta \tilde{\gamma}^I (-0.5a_4 + p_5) + \Delta \tilde{\gamma}^{II} (-0.5a_8 + p_5) + \Delta \tilde{\gamma}^{III} (-0.5a_{12} + p_5), \\ D_6 &= \Delta \tilde{\gamma}^I (-0.5a_4 + p_6) + \Delta \tilde{\gamma}^{II} (-0.5a_8 + p_6) + \Delta \tilde{\gamma}^{III} (-0.5a_{12} + p_6), \end{aligned}$$

Finally, by using (A.27) in (A.23), the fourth order tensor \mathbb{H} , can be expressed in Voigt's notation as:

$$\{\mathbb{H}\} = \begin{bmatrix} 1+(\lambda+2\mu)D_1 & \lambda D_2 & \lambda D_3 & 0 & 0 & 0 \\ \lambda D_1 & 1+(\lambda+2\mu)D_2 & \lambda D_3 & 0 & 0 & 0 \\ \lambda D_1 & \lambda D_2 & 1+(\lambda+2\mu)D_3 & 0 & 0 & 0 \\ 0 & 0 & 0 & 0.5+2\mu D_4 & 0 & 0 \\ 0 & 0 & 0 & 0 & 0.5+2\mu D_5 & 0 \\ 0 & 0 & 0 & 0 & 0 & 0.5+2\mu D_6 \end{bmatrix} \quad (\text{A.28})$$

Moreover, the term $\sum_{i=I}^{III} \Delta \tilde{\gamma}_{n+1}^i \mathbf{m}_n^i$, appearing in equation (A.21) can be also evaluated in principal directions:

$$\left\{ \sum_{i=I}^{III} \Delta \tilde{\gamma}_{n+1}^i \mathbf{m}_n^i \right\} = \begin{bmatrix} \Delta \tilde{\gamma}^I \\ \Delta \tilde{\gamma}^II \\ \Delta \tilde{\gamma}^III \\ 0 \\ 0 \\ 0 \end{bmatrix}_{n+1}. \quad (\text{A.29})$$

Then, the explicit stress $\tilde{\boldsymbol{\sigma}}_{n+1}$ (A.21), can be, by using (A.28) and (A.29) computed in a the general coordinate system with the following expression:

$$\{\tilde{\boldsymbol{\sigma}}_{n+1}\} = \left([T][\mathbb{H}][T^t] \right)^{-1} \begin{bmatrix} \sigma_{xx} \\ \sigma_{yy} \\ \sigma_{zz} \\ \sigma_{xy} \\ \sigma_{xz} \\ \sigma_{yz} \end{bmatrix}_{n+1}^{trial} - [T_R] \begin{bmatrix} \lambda + 2\mu & \lambda & \lambda \\ \lambda & \lambda + 2\mu & \lambda \\ \lambda & \lambda & \lambda + 2\mu \end{bmatrix} \begin{bmatrix} \Delta \tilde{\gamma}^I \\ \Delta \tilde{\gamma}^II \\ \Delta \tilde{\gamma}^III \end{bmatrix}_{n+1} \begin{bmatrix} [\mathbf{C}_R] \\ \{\Delta \tilde{\gamma}_{n+1}\} \end{bmatrix}, \quad (\text{A.30})$$

$$\{\tilde{\boldsymbol{\sigma}}_{n+1}\} = \left([T(\boldsymbol{\sigma}_n)][\mathbb{H}][T(\boldsymbol{\sigma}_n)^t] \right)^{-1} \left(\{\tilde{\boldsymbol{\sigma}}_{n+1}^{trial}\} - [T_R(\boldsymbol{\sigma}_n)][\mathbf{C}_R^el] \{\Delta \tilde{\gamma}_{n+1}\} \right).$$

where $[T]$ is the full transformation matrix and $[T_R]$ is a reduced transformation matrix, introduced here to benefit from the zero values present on the Voigt's vector (A.29).

$$[T] = \begin{bmatrix} p_{(1)}^I p_{(1)}^I & p_{(1)}^II p_{(1)}^II & p_{(1)}^III p_{(1)}^III & 2p_{(1)}^I p_{(1)}^II & 2p_{(1)}^I p_{(1)}^III & 2p_{(1)}^II p_{(1)}^III \\ p_{(2)}^I p_{(2)}^I & p_{(2)}^II p_{(2)}^II & p_{(2)}^III p_{(2)}^III & 2p_{(2)}^I p_{(2)}^II & 2p_{(2)}^I p_{(2)}^III & 2p_{(2)}^II p_{(2)}^III \\ p_{(3)}^I p_{(3)}^I & p_{(3)}^II p_{(3)}^II & p_{(3)}^III p_{(3)}^III & 2p_{(3)}^I p_{(3)}^II & 2p_{(3)}^I p_{(3)}^III & 2p_{(3)}^II p_{(3)}^III \\ p_{(1)}^I p_{(2)}^I & p_{(1)}^II p_{(2)}^II & p_{(1)}^III p_{(2)}^III & p_{(1)}^I p_{(2)}^II + p_{(1)}^II p_{(2)}^I & p_{(1)}^III p_{(2)}^I + p_{(1)}^I p_{(2)}^III & p_{(1)}^III p_{(2)}^II + p_{(1)}^II p_{(2)}^III \\ p_{(1)}^I p_{(3)}^I & p_{(1)}^II p_{(3)}^II & p_{(1)}^III p_{(3)}^III & p_{(3)}^I p_{(1)}^II + p_{(3)}^II p_{(1)}^I & p_{(3)}^III p_{(1)}^I + p_{(3)}^I p_{(1)}^III & p_{(3)}^III p_{(1)}^II + p_{(3)}^II p_{(1)}^III \\ p_{(2)}^I p_{(3)}^I & p_{(2)}^II p_{(3)}^II & p_{(2)}^III p_{(3)}^III & p_{(3)}^I p_{(2)}^II + p_{(3)}^II p_{(2)}^I & p_{(3)}^III p_{(2)}^I + p_{(3)}^I p_{(2)}^III & p_{(3)}^III p_{(2)}^II + p_{(3)}^II p_{(2)}^III \end{bmatrix} \quad (\text{A.31})$$

$$[T_R] = \begin{bmatrix} p_{(1)}^I p_{(1)}^I & p_{(1)}^{II} p_{(1)}^{II} & p_{(1)}^{III} p_{(1)}^{III} \\ p_{(2)}^I p_{(2)}^I & p_{(2)}^{II} p_{(2)}^{II} & p_{(2)}^{III} p_{(2)}^{III} \\ p_{(3)}^I p_{(3)}^I & p_{(3)}^{II} p_{(3)}^{II} & p_{(3)}^{III} p_{(3)}^{III} \\ p_{(1)}^I p_{(2)}^I & p_{(1)}^{II} p_{(2)}^{II} & p_{(1)}^{III} p_{(2)}^{III} \\ p_{(1)}^I p_{(3)}^I & p_{(1)}^{II} p_{(3)}^{II} & p_{(1)}^{III} p_{(3)}^{III} \\ p_{(2)}^I p_{(3)}^I & p_{(2)}^{II} p_{(3)}^{II} & p_{(2)}^{III} p_{(3)}^{III} \end{bmatrix}. \quad (\text{A.32})$$

Also, the tangent algorithmic operator (A.22), can be computed in a the general coordinate system by using:

$$\{\tilde{\mathbf{C}}_{n+1}^{alg}\} = ([T(\boldsymbol{\sigma}_n)][\mathbb{H}(\boldsymbol{\sigma}_n, \tilde{\lambda}_{n+1})][T(\boldsymbol{\sigma}_n)^t])^{-1} : [\mathbf{C}]. \quad (\text{A.33})$$

A.3. Integration scheme

Data : $\{\varepsilon_{n+1}\}, \{\varepsilon_n^p\}, \Delta\gamma_n^i, q_n, \mathbf{p}_n^i, \sigma_n^i$	
1. Implicit stage	
1.1 Compute trial stress	$\{\boldsymbol{\sigma}_{n+1}^{trial}\} = \mathbf{C}^{el} : (\{\varepsilon_{n+1}\} - \{\varepsilon_n^p\})$
1.2 Compute principal directions of the stress tensor \mathbf{p}_{n+1}^i	Solve the eigenvalues problem: $\boldsymbol{\sigma}_{n+1}^{trial} \cdot \mathbf{p}_{n+1}^{i,trial} = \sigma_{n+1}^{i,trial} \mathbf{p}_{n+1}^{i,trial}$ (Recall that $\mathbf{p}^i(\boldsymbol{\sigma}_{n+1}) = \mathbf{p}^i(\boldsymbol{\sigma}_{n+1}^{trial})$)
1.3 Compute plastic multiplier	Solve procedure in Box A.1 for $\Delta\gamma_{n+1}^i$
1.4 Compute principal stresses σ_{n+1}^i	$\{\sigma_{n+1}^i\} = (\{\boldsymbol{\sigma}_{n+1}^{trial}\} - [\mathbf{C}_R])\{\Delta\gamma_{n+1}^i\}$
1.5 Update historical variables q_{n+1} and $\{\varepsilon_n^p\}$	$\varepsilon_{n+1}^p = \varepsilon_n^p + \sum_{i=I}^{III} \Delta\gamma_{n+1}^i \mathbf{p}_{n+1}^i \otimes \mathbf{p}_{n+1}^i$, $q_{n+1} = q_n + H \sum_{i=I}^{III} \Delta\gamma_{n+1}^i$

2. Explicit stage

- | | | |
|-----|--------------------------------------|---|
| 2.1 | Explicit extrapolation | $\Delta\tilde{\gamma}_{n+1}^i = \frac{\Delta t_{n+1}}{\Delta t_n} \Delta\gamma_n$ |
| 2.2 | Compute IMPL-EX stresses | $\{\tilde{\sigma}_{n+1}\}$ expression (A.30) |
| 2.3 | Compute algorithmic tangent operator | $\{\tilde{\mathbf{C}}_{n+1}^{alg}\}$ expression (A.33) |

Box A.3 Rankine model IMPL-EX integration scheme.

A.4. Alternatives for implementation

In this Section two alternatives to the one developed in Section A.2 are mentioned. These alternatives have not been used in this work, and thus, they are just mentioned as possible lines to explore.

A.4.1 Previous step flow

In the preceding development of the IMPL-EX algorithm, was performed a linearization of the flow tensor followed by a truncation up to the linear term (see (A.17)).

As a second alternative, expression (A.17) may be truncated in the first term, being this equivalent of using the flow tensor of the previous time step,

$$\bar{\mathbf{m}}_{n+1}^i = \mathbf{m}_n^i. \quad (\text{A.34})$$

This option provides less accuracy, implying a significant increase of time steps to achieve reasonable final results. On the other hand, implementation becomes easier since no eigenvectors derivatives appear on the IMPL-EX stresses expression:

$$\tilde{\sigma}_{n+1} = \sigma_{n+1}^{trial} - \mathbf{C}^{el} : \sum_{i=1}^n \Delta\tilde{\gamma}_{n+1}^i \mathbf{m}_n^i. \quad (\text{A.35})$$

Moreover the consistent algorithmic tangent operator turns out to be equal to the elastic tensor,

$$\tilde{\mathbf{C}}_{n+1}^{alg} = \frac{\partial \tilde{\sigma}_{n+1}}{\partial \varepsilon_{n+1}} = \mathbf{C}^{el}. \quad (\text{A.36})$$

A.4.2 Original flow

A second alternative procedure considers the original flow (without linearization):

$$\tilde{\boldsymbol{\sigma}}_{n+1} = \boldsymbol{\sigma}_{n+1}^{trial} - \mathbf{C}^{el} : \sum_{i=1}^n \Delta \tilde{\gamma}_{n+1}^i \tilde{\mathbf{m}}_{n+1}^i, \quad (\text{A.37})$$

recall $\tilde{\mathbf{m}}_{n+1}^i(\tilde{\boldsymbol{\sigma}}_{n+1}) = \mathbf{m}_{n+1}^i(\boldsymbol{\sigma}_{n+1}^{trial})$.

Differentiating in order to the strains, the tangent algorithmic operator reads

$$\tilde{\mathbf{C}}_{n+1}^{alg} = \frac{\partial \tilde{\boldsymbol{\sigma}}_{n+1}}{\partial \boldsymbol{\varepsilon}_{n+1}} = \mathbf{C}^{el} - \mathbf{C}^{el} : \sum_{i=1}^3 \Delta \tilde{\gamma}_{n+1}^i \frac{\partial \tilde{\mathbf{m}}_{n+1}^i}{\partial \tilde{\boldsymbol{\sigma}}_{n+1}} : \frac{\partial \tilde{\boldsymbol{\sigma}}_{n+1}}{\partial \boldsymbol{\varepsilon}_{n+1}}, \quad (\text{A.38})$$

and reorganizing terms:

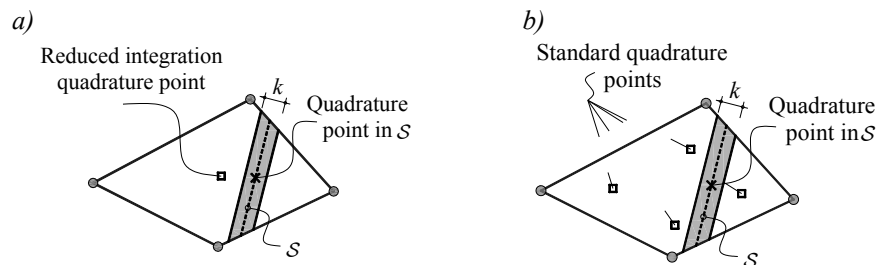
$$\tilde{\mathbf{C}}_{n+1}^{alg} = \left(\mathbb{I} + \mathbf{C}^{el} : \sum_{i=1}^3 \Delta \tilde{\gamma}_{n+1}^i \frac{\partial \tilde{\mathbf{m}}_{n+1}^i}{\partial \tilde{\boldsymbol{\sigma}}_{n+1}} \right)^{-1} : \mathbf{C}^{el}. \quad (\text{A.39})$$

As said previously, the tangent algorithmic operator is not constant during the time step since $\tilde{\mathbf{m}}_{n+1}^i$ do not depend linearly on the stresses $\tilde{\boldsymbol{\sigma}}_{n+1}$. The consequence is that the IMPL-EX integration will not give a step liner algorithm. Nevertheless the tangent operator preserves an important ‘‘IMPL-EX property’’, its semi-positive definiteness, which guarantees the robustness of the quadratic iterative procedure, *i.e.*, difficulties to get convergence are expected.

Appendix B

Stress locking in finite elements with embedded discontinuities

In this work a weak\strong discontinuity mode was proposed to be injected into quadrilateral elements. The main objective of this injection is to improve localization capabilities of the finite elements such that no spurious stress transfer occurs between the open discontinuity surfaces. The strong discontinuity was introduced via a three field $\hat{\mathbf{u}}, \hat{\boldsymbol{\varepsilon}}, [\hat{\mathbf{u}}]$ ⁴² mixed formulation and, as it was commented in Remark 5.1.4.3, this fact translates in a element-wise-constant regular strain field that can be integrated with only one quadrature point whereas in standard discontinuities approaches $\hat{\mathbf{u}}, [\hat{\mathbf{u}}]$ ⁴³ four quadrature points are required.



⁴² In the $\hat{\mathbf{u}}, \hat{\boldsymbol{\varepsilon}}, [\hat{\mathbf{u}}]$ formulation it is used standard bilinear interpolations for the **regular displacement** field and element-wise-constant discontinuous interpolations for the **regular strains** and **displacement jumps**

⁴³ In the $\hat{\mathbf{u}}, [\hat{\mathbf{u}}]$ case it is used standard bilinear interpolations for the **regular displacement** field and element-wise-constant interpolations just for the **displacement jumps**.

Figure B.1 *Quadrature rules a) $\hat{\mathbf{u}}, \hat{\mathbf{\epsilon}}, [\hat{\mathbf{u}}]$ formulation b) $\hat{\mathbf{u}}, [\hat{\mathbf{u}}]$ formulation.*

It is known that when a standard $\hat{\mathbf{u}}, [\hat{\mathbf{u}}]$ ⁴⁴ constant jump embedded discontinuities are used in combination with quadrilateral elements stress locking is noticeable, specifically when trying to reproduce non-constant separation modes along the element discontinuity. This issue was analysed in [Linder and Armero 2007] and [Manzoli and Shing 2006] where the authors propose elements with linear interpolation in the displacement jump to circumvent the problem.

The interesting practical property of using a $\hat{\mathbf{u}}, \hat{\mathbf{\epsilon}}, [\hat{\mathbf{u}}]$ constant jump constant strain formulation (associated to quadrilateral elements), is that the element (unlike the $\hat{\mathbf{u}}, [\hat{\mathbf{u}}]$ case) is stress locking free. In next sections an explanation for this improved behavior is given.

B.1. Motivation

We assume that for an element to be stress locking free its kinematics should allow rigid body motions of one part of the element with respect to the other, when the discontinuity is fully open (full softening state of the element).

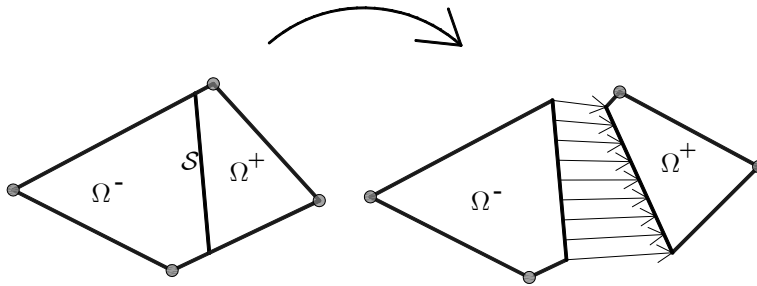


Figure B.2 *Quadrilateral element with a discontinuity inducing a rigid body motion in Ω^+ with respect to Ω^- .*

In a three dimensional setting this can be accomplished if the displacement jump along \mathcal{S} is described by six constant degrees of freedom: 3 displacements (translation) and 3 rotations.

Recalling the strong discontinuity kinematics of equation (4.1):

$$\dot{\mathbf{u}}(\mathbf{x}) = \dot{\bar{\mathbf{u}}}(\mathbf{x}) + \mathcal{H}_{\mathcal{S}} [\dot{\mathbf{u}}](\mathbf{x}), \quad (\text{B.1})$$

⁴⁴ The constant jump strong discontinuity formulation is usually used with triangular finite elements, and for these elements no stress locking is noticeable.

where $\dot{\bar{\mathbf{u}}}$ stands for the smooth part of the displacement field and \mathcal{H}_S stands for the Heaviside (step) function ($\mathcal{H}_S(\mathbf{x}) = 0 \forall \mathbf{x} \in \Omega^-$ and $\mathcal{H}_S(\mathbf{x}) = 1 \forall \mathbf{x} \in \Omega^+$).

For the stress-released case we assume $\dot{\bar{\mathbf{u}}} = \mathbf{0}$, thus:

$$\dot{\mathbf{u}}(\mathbf{x}) = \mathcal{H}_S[\![\dot{\mathbf{u}}]\!](\mathbf{x}) \begin{cases} \dot{\mathbf{u}}(\mathbf{x})|_{x \in \Omega^-} = 0 \\ \dot{\mathbf{u}}(\mathbf{x})|_{x \in \Omega^+} = [\![\dot{\mathbf{u}}]\!](\mathbf{x}) \end{cases}, \quad (\text{B.2})$$

where $\dot{\mathbf{u}}(\mathbf{x})$ reduce to a rigid body motion of Ω^+ ,

$$[\![\dot{\mathbf{u}}]\!] = \mathbf{c} + \boldsymbol{\theta} \wedge \mathbf{x}, \quad (\text{B.3})$$

being \mathbf{c} and $\boldsymbol{\theta}$ vectors of degree of freedom associated with translation and rotation respectively. Notice the displacement jump in (B.3) depends linearly with \mathbf{x} .

Writing expression (B.3) in a matrix form:

$$[\![\dot{\mathbf{u}}]\!]^{(e)}(\mathbf{x}) = \underbrace{\begin{bmatrix} 1 & 0 & 0 & 0 & x_3 & -x_2 \\ 0 & 1 & 0 & -x_3 & 0 & x_1 \\ 0 & 0 & 1 & x_2 & -x_1 & 0 \end{bmatrix}}_{\mathbf{G}(\mathbf{x})} \underbrace{\begin{bmatrix} c_1 \\ c_2 \\ c_3 \\ \theta_1 \\ \theta_2 \\ \theta_3 \end{bmatrix}}_{\boldsymbol{\gamma}^{(e)}}, \quad (\text{B.4})$$

where c_1 , c_2 and c_3 are degrees of freedom associated to the translation and θ_1 , θ_2 and θ_3 are the degrees of freedom associated to the rotation.

$$[\![\dot{\mathbf{u}}]\!]^{(e)}(\mathbf{x}) = \mathbf{G}(\mathbf{x})\boldsymbol{\gamma}. \quad (\text{B.5})$$

In a two-dimensional framework, equation (B.5) simplifies as follows:

$$[\![\dot{\mathbf{u}}]\!]^{(e)}(\mathbf{x}) = \underbrace{\begin{bmatrix} 1 & 0 & -x_2 \\ 0 & 1 & x_1 \end{bmatrix}}_{\mathbf{G}(\mathbf{x})} \underbrace{\begin{bmatrix} c_1 \\ c_2 \\ \theta \end{bmatrix}}_{\boldsymbol{\gamma}}. \quad (\text{B.6})$$

Considering the additional rotational degrees of freedom of the displacement $[\![\dot{\mathbf{u}}]\!]^{(e)} = \mathbf{G}\boldsymbol{\gamma}^{(e)}$, a symmetric Galerkin formulation can be introduced, likewise was done Section 5.1.5.

$$\sum_{e \in \Omega} \int_{\Omega^{(e)}} \nabla^s \hat{\boldsymbol{\eta}}^h : \dot{\boldsymbol{\Sigma}}(\dot{\boldsymbol{\varepsilon}}^{(e)}) d\Omega = \dot{\mathbf{f}}^{ext}, \quad \forall \hat{\boldsymbol{\eta}}^h \in \hat{\mathcal{N}}^h, \quad (\text{B.7})$$

$$\sum_{e \in \Omega} \int_{\Omega^{(e)}} \nabla^s \tilde{\boldsymbol{\eta}}^h : \dot{\boldsymbol{\Sigma}}(\dot{\boldsymbol{\varepsilon}}^{(e)}) d\Omega = 0, \quad \forall \tilde{\boldsymbol{\eta}}^h \in \tilde{\mathcal{N}}^h, \quad (\text{B.8})$$

where the spaces $\hat{\mathcal{N}}^h$ and $\tilde{\mathcal{N}}^h$ are defined at Section 5.1.5 being (being now $[\![\dot{\mathbf{u}}]\!]^{(e)} = \mathbf{G}\boldsymbol{\gamma}^{(e)}$)

After some algebraic manipulation of expression (B.8), a symmetric formulation is summarized in Box 5.3.

<p>Given $\hat{\mathbf{u}}^* : \Gamma_u \rightarrow \mathbb{R}^N$, $\hat{\mathbf{t}}^* : \Gamma_\sigma \rightarrow \mathbb{R}^N$ and $\hat{\mathbf{b}} : \Omega \rightarrow \mathbb{R}^N$ find $\hat{\mathbf{u}}^h \in \mathcal{U}^h$ such that for all $\hat{\boldsymbol{\eta}}^h \in \mathcal{N}^h$</p> $\sum_{e \in \Omega} \int_{\Omega^{(e)}} \nabla^s \hat{\boldsymbol{\eta}}^h : \dot{\boldsymbol{\Sigma}}(\dot{\boldsymbol{\varepsilon}}^{(e)}) d\Omega = \hat{\mathbf{f}}^{ext}, \quad \forall \hat{\boldsymbol{\eta}}^h \in \mathcal{N}^h \quad (\text{B.9})$ $\int_{\Omega^{(e)} \setminus \mathcal{S}} \mathbf{G}^T \cdot \nabla \varphi^h \cdot \dot{\boldsymbol{\Sigma}}(\dot{\boldsymbol{\varepsilon}}^{(e)}) d\Omega = \int_{\mathcal{S}^{(e)}} \mathbf{G}^T \cdot \mathbf{n}^{(e)} \cdot \dot{\boldsymbol{\Sigma}}(\dot{\boldsymbol{\varepsilon}}^{(e)}) d\Omega^{(e)}, \quad \forall e \in \Omega_{\mathcal{M}} \quad (\text{B.10})$ <p>where:</p> $\dot{\boldsymbol{\varepsilon}}^{(e)} = \nabla^s \hat{\mathbf{u}}^h - \left(\nabla \varphi^h \otimes [[\hat{\mathbf{u}}]]^{(e)} \right)^S + \frac{\mu_{\mathcal{S}}}{k} \left(\mathbf{n}^{(e)} \otimes [[\hat{\mathbf{u}}]]^{(e)} \right)^S$ $[[\hat{\mathbf{u}}]]^{(e)} = \mathbf{G} \boldsymbol{\gamma}^{(e)}$
--

Box B.1 Mixed $\hat{\mathbf{u}}, [[\hat{\mathbf{u}}]]$ symmetric formulation considering rotation degrees of freedom (linear displacement along \mathcal{S}).

B.2. Specification for 2D elements

The linear jump formulation summarized in Box 5.3 should be stress locking free for any finite element (triangles, quadrilaterals, higher order elements, *etc.*) since rigid body modes are allowed for the full soft state. Following specific elements are analyzed, and conclusions about stress locking of piece-wise constant jump formulations are derived.

B.2.1 Linear triangles, $(\hat{\mathbf{u}}, [[\hat{\mathbf{u}}]])$ formulation

For linear triangular elements, equations in Box 5.3 can be integrated with two sampling points: one⁴⁵ associated to $\Omega^{(e)} \setminus \mathcal{S}(\mathbf{x}_\Omega)$ and a second associated to $\mathcal{S}^{(e)}(\mathbf{x}_{\mathcal{S}})$.

⁴⁵ Notice that for the triangle finite elements the integrals in equations (B.9) and (B.10) are constant or linear and thus, they can be exactly integrated with a single quadrature point.

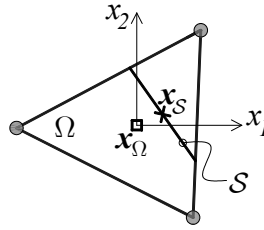


Figure B.3 Linear triangle.

Taking $\mathbf{x}_\Omega \equiv \mathbf{x}_S$, as it is usually done in the ambit of the embedded discontinuity approach, and taking the local coordinate system of axes in \mathbf{x}_Ω , such that $\mathbf{x}_\Omega = \mathbf{x}_S = \mathbf{0}$, the third column of the operator $\mathbf{G}(\mathbf{x})$ is null and expression (B.6) reads:

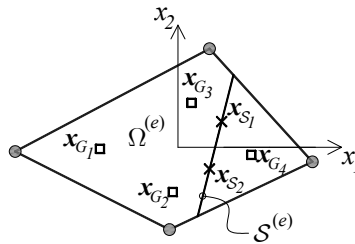
$$\llbracket \dot{\mathbf{u}} \rrbracket^{(e)}(\mathbf{x}) = \begin{bmatrix} 1 & 0 & 0 \\ 0 & 1 & 0 \end{bmatrix} \begin{bmatrix} c_1 \\ c_2 \\ \theta \end{bmatrix} = \begin{bmatrix} c_1 \\ c_2 \\ 0 \end{bmatrix}, \quad (\text{B.11})$$

where the degree of freedom θ associated to the rotation “does not appear in the formulation”, this allow us to conclude, that the element is stress locking free by considering uniquely 2 displacement degrees of freedom (constant jump in \mathcal{S}), as it is usually done when linear triangles associated with finite element formulation with embedded discontinuities are used.

$$\llbracket \dot{\mathbf{u}} \rrbracket^{(e)}(\mathbf{x}) = \begin{bmatrix} c_1 \\ c_2 \end{bmatrix}. \quad (\text{B.12})$$

B.2.2 Bilinear quadrilateral elements, $(\dot{\mathbf{u}}, \llbracket \dot{\mathbf{u}} \rrbracket)$ formulation (fully integrated quads)

For bilinear quadrilateral elements, integration of equations in Box 5.3 requires, due the quadratic character of the integrals in (B.9) and (B.10), a 2×2 quadrature rule in $\Omega^{(e)} \setminus \mathcal{S}$ and two quadrature points in $\mathcal{S}^{(e)}(\mathbf{x}_S)$.


 Figure B.4 Quadrilateral element associated to a $\dot{\mathbf{u}}, \llbracket \dot{\mathbf{u}} \rrbracket$ formulation.

For an element to be considered stress locking free, the kinematics of equation (B.6) should be fulfilled for all sampling points. Notice that, for this element (unlike for the triangle element of Section B.2.1), the degree of freedom associated to the rotation, θ , explicitly appears in the formulation (the third column of the operator $\mathbf{G}(\mathbf{x})$ is different from zero in almost all gauss points).

Therefore, finite element formulations that do not consider the rotation degree of freedom (as it happens in the $\hat{\mathbf{u}}, [\hat{\mathbf{u}}]$ constant jump formulation) can potentially suffer from stress locking, since it is not guaranteed that the rigid body modes can develop for general deformation cases.

B.2.3 Bilinear quadrilateral elements, $(\hat{\mathbf{u}}, \hat{\mathbf{e}}, [\hat{\mathbf{u}}])$ formulation (reduced integration)

In this work, an embedded discontinuity finite element formulation based in a mixed $\hat{\mathbf{u}}, \hat{\mathbf{e}}, [\hat{\mathbf{u}}]$ formulation was proposed. The main practical consequence is that strains $\hat{\mathbf{e}}^{(e)}$ are constant inside the quadrilateral element and the kernels of the integrals appearing in expressions (B.9) and (B.10) become constant, being therefore exactly integrated with just one gauss point for both domains (one associated to $\Omega^{(e)} \setminus \mathcal{S}$ and other \mathcal{S}) as it happens for the triangular element of Section B.2.1.

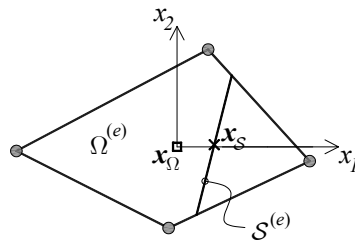


Figure B.5 *Quadrilateral element associated to $\hat{\mathbf{u}}, \hat{\mathbf{e}}, [\hat{\mathbf{u}}]$ formulation.*

Thus, taking $\mathbf{x}_\Omega \equiv \mathbf{x}_\mathcal{S}$, as it is usually done in the ambit of finite elements with embedded discontinuities, and placing the local coordinate system of axes in \mathbf{x}_Ω (without loss of generality), such that $\mathbf{x}_\Omega = \mathbf{x}_\mathcal{S} = \mathbf{0}$, the third column of the operator $\mathbf{G}(\mathbf{x})$ (in equation (B.6)), when evaluated at this point, is null.

$$\mathbf{G}(\mathbf{x}) = \begin{bmatrix} 1 & 0 & 0 \\ 0 & 1 & 0 \end{bmatrix} \Rightarrow [\hat{\mathbf{u}}]^{(e)} = \begin{bmatrix} c_1 \\ c_2 \\ 0 \end{bmatrix}. \quad (\text{B.13})$$

Therefore, the rotation degree of freedom does not appear in the formulation, this meaning that the element it is stress locking free without considering rotation degrees of freedom, as it was the case of the mixed $\hat{\mathbf{u}}, \hat{\boldsymbol{\varepsilon}}, [\hat{\mathbf{u}}]$ formulation proposed in this work.

B.3. Numerical example

In this section, we consider a simple numerical example to illustrate how quadrilaterals elements with constant jump embedded discontinuities are affected by stress locking.

We consider here the one element bending test (see Figure B.6) already used in [Linder and Armero 2007] and [Manzoli and Shing 2006] for analyze the same stress locking issue. The test consists of a square block with imposed displacement at the top δ_{top} and bottom δ_{bot} , with δ_{bot} increasing twice as fast as the top displacement in the loading pseudo-time $t(s)$.

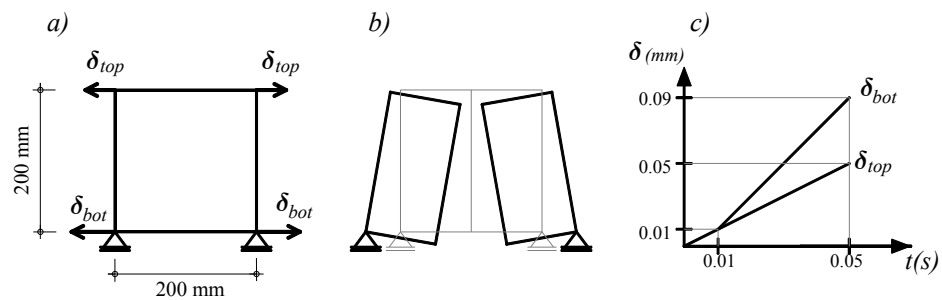


Figure B.6 *Bending one element test: a) geometrical data, b) theoretical deformed shape, c) loading data.*

This bending test will strongly challenge the constant displacement jump strong discontinuity formulations, since the theoretical solution of the problem involves both, a rigid body translation and a rigid body rotation.

Figure B.7 compares results obtained with the standard $\hat{\mathbf{u}}, [\hat{\mathbf{u}}]$ and the proposed $\hat{\mathbf{u}}, \hat{\boldsymbol{\varepsilon}}, [\hat{\mathbf{u}}]$ strong discontinuity formulations, with the analytical solution⁴⁶ in terms of reaction vs. displacement curves. We remark that both formulations consider uniquely constant (translation) displacement jumps.

⁴⁶ The analytical solution is taken from [Linder and Armero 2007].

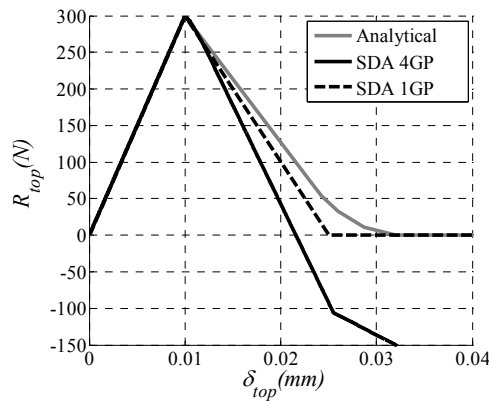


Figure B.7 Reaction force vs. imposed displacement at the top comparing the analytical solution with solutions computed with the standard $\hat{\mathbf{u}}, [\hat{\mathbf{u}}]$ strong discontinuity formulation that is integrated with 4 gauss points (SDA 4GP) and with the proposed $\hat{\mathbf{u}}, \hat{\mathbf{e}}, [\hat{\mathbf{u}}]$ formulation integrated with just 1 gauss point (SDA 1GP).

From Figure B.7 it can be concluded that the proposed $\hat{\mathbf{u}}, \hat{\mathbf{e}}, [\hat{\mathbf{u}}]$ (1 GP) is stress locking free in the sense that no spurious stress is transferred by the discontinuity after fully softened state. In the other hand the standard quadrilateral element $\hat{\mathbf{u}}, [\hat{\mathbf{u}}]$ (4 GP) is affected by stress locking⁴⁷ that prevents the relaxation of the resisting forces this corresponding to the undesirable behavior already reported by other authors in [Manzoli and Shing 2006; Linder and Armero 2007].

Notice that the result obtained with the $\hat{\mathbf{u}}, \hat{\mathbf{e}}, [\hat{\mathbf{u}}]$ formulation does not exactly match the analytical solution since the theoretical solution exhibits a linear displacement jump through the discontinuity, whereas the proposed formulation considers element-wise constant jumps. Therefore, in order to better approximate the analytical solution more finite elements would be required

Remark B.3.1: In references [Manzoli and Shing 2006; Linder and Armero 2007] to avoid stress locking problems associated to constant jump embedded formulations (for quads), the authors propose a linear description of jump along the discontinuity by using 4 displacement (translation) degrees of freedom (in 2D). This additional degrees of freedom can become excessive (in front of the 3 exactly required by (B.6)) and that, can lead in some cases, to singular equations that need specific stabilization treatment.

⁴⁷ Notwithstanding the severe stress locking found for this simple problem, it is expected with mesh refinement, the stress locking effects to be alleviated, since the rigid body motion of Ω^+ with respect to Ω^- is then approximated by more element-wise discontinuous displacement jumps.

In our proposal, a constant element displacement jump is considered, no additional degrees of freedom are need and therefore, the computational cost and the complexity of the formulation remain low.

Appendix C

Weak/strong discontinuity injection: Element matrices

Independently of the chosen formulation, the element-wise constant degrees of freedom $[[\dot{\mathbf{u}}]]^{(e)}$ have elemental support, and thus, they can be solved, at the element level, by a standard condensation procedure that is summarized here (this procedure is restricted to those elements belonging to the injection domain).

The residual equilibrium forces $\dot{\mathbf{R}}^{(e)}$, and that of the additional equation $\dot{\mathbf{r}}^{(e)}$ (e.g. traction continuity) can be expressed in the following form:

$$\begin{Bmatrix} \dot{\mathbf{R}}^{(e)} \\ \dot{\mathbf{r}}^{(e)} \end{Bmatrix} = \begin{bmatrix} \mathbf{K}_{uu}^{(e)} & \mathbf{K}_{u[u]}^{(e)} \\ \mathbf{K}_{[u]u}^{(e)} & \mathbf{K}_{[u][u]}^{(e)} \end{bmatrix} \begin{Bmatrix} \{\dot{\mathbf{u}}\}^{(e)} \\ [[\dot{\mathbf{u}}]]^{(e)} \end{Bmatrix}, \quad (\text{C.14})$$

where $\{\dot{\mathbf{u}}\}^{(e)}$ stands for the elemental vector $\{\dot{\mathbf{u}}\}^{(e)} = \{\dot{\mathbf{u}}_1^T, \dot{\mathbf{u}}_2^T, \dot{\mathbf{u}}_3^T, \dot{\mathbf{u}}_4^T\}^T$ composed

by the $\dot{\mathbf{u}}_i = \{\dot{u}_x, \dot{u}_y\}_i^T$ degrees of freedom, and $\mathbf{K}_{uu}^{(e)} = \frac{\partial \dot{\mathbf{R}}^{(e)}}{\partial \dot{\mathbf{u}}^{(e)}}$, $\mathbf{K}_{u[u]}^{(e)} = \frac{\partial \dot{\mathbf{R}}^{(e)}}{\partial [[\dot{\mathbf{u}}]]^{(e)}}$,

$\mathbf{K}_{[u]u}^{(e)} = \frac{\partial \dot{\mathbf{r}}^{(e)}}{\partial \dot{\mathbf{u}}^{(e)}}$ and $\mathbf{K}_{[u][u]}^{(e)} = \frac{\partial \dot{\mathbf{r}}^{(e)}}{\partial [[\dot{\mathbf{u}}]]^{(e)}}$ are the elemental stiffness matrixes.

Solving the second equation of (C.14) for $[[\dot{\mathbf{u}}]]^{(e)}$:

$$[[\dot{\mathbf{u}}]]^{(e)} = \left(\mathbf{K}_{[u][u]}^{(e)} \right)^{-1} \left(\dot{\mathbf{r}}^{(e)} - \mathbf{K}_{[u]u}^{(e)} \{\dot{\mathbf{u}}\}^{(e)} \right), \quad (\text{C.15})$$

by substituting $[[\dot{\mathbf{u}}]]^{(e)}$ in the first equation of (C.14) and reorganizing terms:

$$\underbrace{\dot{\mathbf{R}}^{(e)} - \mathbf{K}_{u[u]}^{(e)} \left(\mathbf{K}_{[u][u]}^{(e)} \right)^{-1} \dot{\mathbf{r}}^{(e)}}_{\hat{\mathbf{R}}^{(e)}} = \underbrace{\left(\mathbf{K}_{uu}^{(e)} - \left(\mathbf{K}_{[u][u]}^{(e)} \mathbf{K}_{[u]u}^{(e)} \right)^{-1} \right)}_{\hat{\mathbf{K}}^{(e)}} \{\dot{\mathbf{u}}\}^{(e)}, \quad (\text{C.16})$$

where $\hat{\mathbf{K}}^{(e)}$ and $\hat{\mathbf{R}}^{(e)}$ are the elemental condensed stiffness matrix and residual vector respectively. Once the condensed element matrices are computed, the global entities $\hat{\mathbf{K}}$ and $\hat{\mathbf{R}}$ can be assembled and then $\{\hat{\mathbf{u}}\}$ can be solved at the global level in a standard manner:

$$\hat{\mathbf{R}} = \hat{\mathbf{K}} \{\hat{\mathbf{u}}\},$$

where :

$$\hat{\mathbf{K}} = \mathcal{A}_{e \in \Omega_{mf}} \left(\hat{\mathbf{K}}^{(e)} \right), \quad \hat{\mathbf{R}} = \mathcal{A}_{e \in \Omega_{mf}} \left(\hat{\mathbf{R}}^{(e)} \right), \quad (\text{C.17})$$

where $\{\hat{\mathbf{u}}\}$ stands for the global vector composed by the $\hat{\mathbf{u}}_i$ degrees of freedom $\{\hat{\mathbf{u}}\} = \{\hat{\mathbf{u}}_1, \hat{\mathbf{u}}_2, \dots, \hat{\mathbf{u}}_{nnodes}\}^T$, being $nnodes$ the total number of nodes of the finite element mesh).

Once equation (C.17) is solved for $\{\hat{\mathbf{u}}\}$, $[[\hat{\mathbf{u}}]]^{(e)}$ can be computed at the element level, by using expression (C.15).

For the proposed formulations, expressions for the entities in equation (C.14) are following summarized.

C.1. Symmetric strong discontinuity formulation

$$\begin{aligned}
\dot{\mathbf{R}}^{(e)} &= \int_{\Omega^{(e)}} \bar{\mathbf{B}}^{(e)} \cdot \{ \dot{\boldsymbol{\Sigma}}(\dot{\boldsymbol{\varepsilon}}^{(e)}) \} d\Omega - \dot{\mathbf{F}}_{ext}^{(e)} \\
\dot{\mathbf{r}}^{(e)} &= \int_{\mathcal{S}^{(e)}} [\mathbf{n}^{(e)}] \cdot \{ \dot{\boldsymbol{\Sigma}}(\dot{\boldsymbol{\varepsilon}}_S^{(e)}) \} d\mathcal{S} - \int_{\Omega^{(e)}} \left[\overline{\nabla \varphi^h}^{(e)} \right] \cdot \{ \dot{\boldsymbol{\Sigma}}(\dot{\boldsymbol{\varepsilon}}^{(e)}) \} d\Omega \\
&\text{where:} \\
\dot{\boldsymbol{\varepsilon}}_S^{(e)} &= \bar{\mathbf{B}}^{(e)} \cdot \{ \dot{\hat{\mathbf{u}}} \}^{(e)} - \left[\overline{\nabla \varphi^h}^{(e)} \right] \cdot [\dot{\hat{\mathbf{u}}}]^{(e)} + \frac{1}{k} [\mathbf{n}^{(e)}] \cdot [\dot{\hat{\mathbf{u}}}]^{(e)} \\
\dot{\boldsymbol{\varepsilon}}^{(e)} &= \bar{\mathbf{B}}^{(e)} \cdot \{ \dot{\hat{\mathbf{u}}} \}^{(e)} - \left[\overline{\nabla \varphi^h}^{(e)} \right] \cdot [\dot{\hat{\mathbf{u}}}]^{(e)} \\
\mathbf{K}_{uu}^{(e)} &= \int_{\Omega^{(e)}} \bar{\mathbf{B}}^{(e)} \cdot \{ \mathbf{C}_{\Omega^{(e)} \setminus \mathcal{S}} \} \cdot \bar{\mathbf{B}}^{(e)} d\Omega \\
\mathbf{K}_{u[u]}^{(e)} &= - \int_{\Omega^{(e)}} \bar{\mathbf{B}}^{(e)} \cdot \{ \mathbf{C}_{\Omega^{(e)} \setminus \mathcal{S}} \} \cdot \left[\overline{\nabla \varphi^h}^{(e)} \right] d\Omega \\
\mathbf{K}_{[u]u}^{(e)} &= \underbrace{\int_{\mathcal{S}} [\mathbf{n}^{(e)}] \cdot \{ \mathbf{C}_S \} \cdot \bar{\mathbf{B}}^{(e)} d\mathcal{S}}_{\rightarrow 0} - \int_{\Omega^{(e)}} \left[\overline{\nabla \varphi^h}^{(e)} \right] \cdot \{ \mathbf{C}_{\Omega^{(e)} \setminus \mathcal{S}} \} \cdot \bar{\mathbf{B}}^{(e)} d\Omega \\
\mathbf{K}_{[u][u]}^{(e)} &= - \underbrace{\int_{\mathcal{S}} [\mathbf{n}^{(e)}] \cdot \{ \mathbf{C}_S \} \cdot \left[\overline{\nabla \varphi^h}^{(e)} \right] d\mathcal{S}}_{\rightarrow 0} + \int_{\mathcal{S}} [\mathbf{n}^{(e)}] \cdot \{ \mathbf{C}_S \} \cdot \frac{1}{k} [\mathbf{n}^{(e)}] d\mathcal{S} \\
&+ \int_{\Omega^{(e)}} \left[\overline{\nabla \varphi^h}^{(e)} \right] \cdot \{ \mathbf{C}_{\Omega^{(e)} \setminus \mathcal{S}} \} \cdot \left[\overline{\nabla \varphi^h}^{(e)} \right] d\Omega
\end{aligned} \tag{C.18}$$

$$\begin{aligned}
\mathbf{K}_{[u]u}^{(e)} &= \underbrace{\int_{\mathcal{S}} [\mathbf{n}^{(e)}] \cdot \{ \mathbf{C}_S \} \cdot \bar{\mathbf{B}}^{(e)} d\mathcal{S}}_{\rightarrow 0} - \int_{\Omega^{(e)}} \left[\overline{\nabla \varphi^h}^{(e)} \right] \cdot \{ \mathbf{C}_{\Omega^{(e)} \setminus \mathcal{S}} \} \cdot \bar{\mathbf{B}}^{(e)} d\Omega \\
\mathbf{K}_{[u][u]}^{(e)} &= - \underbrace{\int_{\mathcal{S}} [\mathbf{n}^{(e)}] \cdot \{ \mathbf{C}_S \} \cdot \left[\overline{\nabla \varphi^h}^{(e)} \right] d\mathcal{S}}_{\rightarrow 0} + \int_{\mathcal{S}} [\mathbf{n}^{(e)}] \cdot \{ \mathbf{C}_S \} \cdot \frac{1}{k} [\mathbf{n}^{(e)}] d\mathcal{S} \\
&+ \int_{\Omega^{(e)}} \left[\overline{\nabla \varphi^h}^{(e)} \right] \cdot \{ \mathbf{C}_{\Omega^{(e)} \setminus \mathcal{S}} \} \cdot \left[\overline{\nabla \varphi^h}^{(e)} \right] d\Omega
\end{aligned} \tag{C.19}$$

Box C.1 Symmetric strong discontinuity formulation.

Notice that for strong discontinuity case of Box C.1, when $k \rightarrow 0$, the strain field is unbounded, whereas the stress field remains bounded. For this to be possible, as previously mentioned, the continuum softening modulus is reinterpreted in a distributional sense, *i.e.*:

$$\frac{1}{H} = \delta_S \frac{1}{\bar{H}}, H = k\bar{H}. \tag{C.20}$$

Thus for $k \rightarrow 0$, $H \rightarrow 0$ and by equation (2.21) and (2.64) also $\{ \mathbf{C}_S \} \rightarrow 0$, meaning this that the terms where $\{ \mathbf{C}_S \}$ appear, vanish, except the one divided by k , since k also tends to zero. For $k \rightarrow 0$ the formulation is symmetric since $\mathbf{K}_{uu}^{(e)} = (\mathbf{K}_{uu}^{(e)})^T$, $\mathbf{K}_{u[u]}^{(e)} = (\mathbf{K}_{[u]u}^{(e)})^T$ and $\mathbf{K}_{[u][u]}^{(e)} = (\mathbf{K}_{[u][u]}^{(e)})^T$. If the regularizing parameter k , is not tending to zero (for example to make the transition described in Remark 5.1.6.1), the terms indicated in equation (C.19) as tending to zero, will tend to break the symmetry of the formulation.

C.2. Un-symmetric strong discontinuity formulation.

$$\begin{aligned}
\dot{\mathbf{R}}^{(e)} &= \int_{\Omega^{(e)}} \bar{\mathbf{B}}^{(e)} \cdot \{ \dot{\boldsymbol{\Sigma}}(\dot{\boldsymbol{\varepsilon}}^{(e)}) \} d\Omega - \dot{\mathbf{F}}_{ext}^{(e)} \\
\dot{\mathbf{r}}^{(e)} &= \int_{\mathcal{S}^{(e)}} [\mathbf{n}^{(e)}] \cdot \{ \dot{\boldsymbol{\Sigma}}(\dot{\boldsymbol{\varepsilon}}_S^{(e)}) \} d\mathcal{S} - \frac{1}{\ell^{(e)}} \int_{\Omega^{(e)}} [\mathbf{n}^{(e)}] \cdot \{ \dot{\boldsymbol{\Sigma}}(\dot{\boldsymbol{\varepsilon}}^{(e)}) \} d\Omega \\
&\text{where:} \\
\dot{\boldsymbol{\varepsilon}}_S^{(e)} &= \bar{\mathbf{B}}^{(e)} \cdot \{ \dot{\boldsymbol{\mathbf{u}}} \}^{(e)} - \left[\overline{\nabla \varphi^h}^{(e)} \right] \cdot [\dot{\boldsymbol{\mathbf{u}}}]^{(e)} + \frac{1}{k} [\mathbf{n}^{(e)}] \cdot [\dot{\boldsymbol{\mathbf{u}}}]^{(e)} \\
\dot{\boldsymbol{\varepsilon}}^{(e)} &= \bar{\mathbf{B}}^{(e)} \cdot \{ \dot{\boldsymbol{\mathbf{u}}} \}^{(e)} - \left[\overline{\nabla \varphi^h}^{(e)} \right] \cdot [\dot{\boldsymbol{\mathbf{u}}}]^{(e)} \\
\mathbf{K}_{uu}^{(e)} &= \int_{\Omega^{(e)}} \bar{\mathbf{B}}^{(e)} \cdot \{ \mathbf{C}_{\Omega^{(e)} \setminus \mathcal{S}} \} \cdot \bar{\mathbf{B}}^{(e)} d\Omega \\
\mathbf{K}_{u[u]}^{(e)} &= - \int_{\Omega^{(e)}} \bar{\mathbf{B}}^{(e)} \cdot \{ \mathbf{C}_{\Omega^{(e)} \setminus \mathcal{S}} \} \cdot \left[\overline{\nabla \varphi^h}^{(e)} \right] d\Omega \\
\mathbf{K}_{[u]u}^{(e)} &= \underbrace{\int_{\mathcal{S}} [\mathbf{n}^{(e)}] \cdot \{ \mathbf{C}_S \} \cdot \bar{\mathbf{B}}^{(e)} d\mathcal{S}}_{\rightarrow 0} - \frac{1}{\ell^{(e)}} \int_{\Omega^{(e)}} [\mathbf{n}^{(e)}] \cdot \{ \mathbf{C}_{\Omega^{(e)} \setminus \mathcal{S}} \} \cdot \bar{\mathbf{B}}^{(e)} d\Omega \\
\mathbf{K}_{[u][u]}^{(e)} &= - \underbrace{\int_{\mathcal{S}} [\mathbf{n}^{(e)}] \cdot \{ \mathbf{C}_S \} \cdot \left[\overline{\nabla \varphi^h}^{(e)} \right] d\mathcal{S}}_{\rightarrow 0} + \int_{\mathcal{S}} [\mathbf{n}^{(e)}] \cdot \{ \mathbf{C}_S \} \cdot \frac{1}{k} [\mathbf{n}^{(e)}] d\mathcal{S} \\
&+ \frac{1}{\ell^{(e)}} \int_{\Omega^{(e)}} [\mathbf{n}^{(e)}] \cdot \{ \mathbf{C}_{\Omega^{(e)} \setminus \mathcal{S}} \} \cdot \left[\overline{\nabla \varphi^h}^{(e)} \right] d\Omega
\end{aligned} \tag{C.21}$$

Box C.2 Un-symmetric strong discontinuity formulation.

The non-symmetric character of this formulation is clearly observed since, $\mathbf{K}_{u[u]}^{(e)} \neq \left(\mathbf{K}_{[u]u}^{(e)} \right)^T$ and $\mathbf{K}_{[u][u]}^{(e)} \neq \left(\mathbf{K}_{[u]u}^{(e)} \right)^T$. Note that for $k \rightarrow 0$ the formulation become symmetric for the special case where:

$$\frac{\text{meas}(\mathcal{S}^{(e)})}{\text{meas}(\Omega^{(e)})} [\mathbf{n}^{(e)}] = \left[\overline{\nabla \varphi^h}^{(e)} \right]. \tag{C.23}$$

C.3. Weak discontinuity formulation.

$$\begin{aligned}
\dot{\mathbf{R}}^{(e)} &= \int_{\Omega^{(e)}} \bar{\mathbf{B}}^{(e)} \cdot \left\{ \dot{\boldsymbol{\Sigma}}(\dot{\boldsymbol{\varepsilon}}_{\Omega_S}^{(e)}) \right\} d\Omega - \dot{\mathbf{F}}_{ext}^{(e)} \\
\dot{\mathbf{r}}^{(e)} &= [\mathbf{n}^{(e)}] \cdot \left\{ \dot{\boldsymbol{\Sigma}}(\dot{\boldsymbol{\varepsilon}}_{\Omega_S}^{(e)}) \right\} - [\mathbf{n}^{(e)}] \cdot \left\{ \dot{\boldsymbol{\Sigma}}(\dot{\boldsymbol{\varepsilon}}_{\Omega \setminus \Omega_S}^{(e)}) \right\} \\
\text{where:} & \\
\dot{\boldsymbol{\varepsilon}}_{\Omega_S}^{(e)} &= \bar{\mathbf{B}}^{(e)} \cdot \left\{ \dot{\mathbf{u}} \right\}^{(e)} + [\mathcal{M}^{(e)}] \llbracket \dot{\mathbf{u}} \rrbracket^{(e)} ; \quad [\mathcal{M}^{(e)}] = \frac{1}{\ell^{(e)}} [\mathbf{n}^{(e)}] - \left[\overline{\nabla \varphi^h}^{(e)} \right] \\
\dot{\boldsymbol{\varepsilon}}_{\Omega \setminus \Omega_S}^{(e)} &= \bar{\mathbf{B}}^{(e)} \cdot \left\{ \dot{\mathbf{u}} \right\}^{(e)} - \left[\overline{\nabla \varphi^h}^{(e)} \right] \cdot \llbracket \dot{\mathbf{u}} \rrbracket^{(e)} \\
\mathbf{K}_{uu}^{(e)} &= \int_{\Omega^{(e)}} \bar{\mathbf{B}}^{(e)} \cdot \left\{ \mathbf{C}_{\Omega_S^{(e)}} \right\} \cdot \bar{\mathbf{B}}^{(e)} d\Omega \\
\mathbf{K}_{u[u]}^{(e)} &= \int_{\Omega^{(e)}} \bar{\mathbf{B}}^{(e)} \cdot \left\{ \mathbf{C}_{\Omega_S^{(e)}} \right\} \cdot [\mathcal{M}^{(e)}] d\Omega \\
\mathbf{K}_{[u]u}^{(e)} &= [\mathbf{n}^{(e)}] \cdot \left\{ \mathbf{C}_{\Omega_S^{(e)}} \right\} \cdot \bar{\mathbf{B}}^{(e)} - [\mathbf{n}^{(e)}] \cdot \left\{ \mathbf{C}_{\Omega^{(e)} \setminus \Omega_S} \right\} \cdot \bar{\mathbf{B}}^{(e)} \\
\mathbf{K}_{[u][u]}^{(e)} &= [\mathbf{n}^{(e)}] \cdot \left\{ \mathbf{C}_{\Omega_S^{(e)}} \right\} \cdot [\mathcal{M}^{(e)}] + [\mathbf{n}^{(e)}] \cdot \left\{ \mathbf{C}_{\Omega^{(e)} \setminus \Omega_S} \right\} \cdot \left[\overline{\nabla \varphi^h}^{(e)} \right]
\end{aligned} \tag{C.24}$$

$$\tag{C.25}$$

Box C.3 *Weak discontinuity formulation.*

References

- Alfaiate, J. "New developments in the study of strong embedded discontinuities in finite elements." *Advances in Fracture and Damage Mechanics* **251-2**: 109-114,2003.
- Alfaiate, J., A. Simone and L. J. Sluys. "Non-homogeneous displacement jumps in strong embedded discontinuities." *International Journal of Solids and Structures* **40**(21): 5799-5817,2003.
- Alfaiate, J., G. N. Wells and L. J. Sluys. "On the use of embedded discontinuity elements with crack path continuity for mode-I and mixed-mode fracture." *Engineering Fracture Mechanics* **69**(6): 661-686,2002.
- Apostol, T. M. *Calculus*. New York, J. Wiley,1967.
- Argyris, J. H. and K. J. Willam. "Some considerations for the evaluation of finite element models." *Nuclear Engineering and Design* **28**(1): 76-96,1974.
- Armero, F. and K. Garikipati. "An analysis of strong discontinuities in multiplicative finite strain plasticity and their relation with the numerical simulation of strain localization in solids." *Int.J. Solids and Structures* **33**(20-22): 2863-2885,1996.
- Armero, F. and J. Kim. "Three-dimensional finite elements with embedded strong discontinuities to model material failure in the infinitesimal range." *International Journal for Numerical Methods in Engineering*: n/a-n/a,2012.
- Arrea, M. and A. R. Ingraffea. *Mixed-mode Crack Propagation in Mortar and Concrete*, Dept. Struct. Eng. Cornell Univ. New York,1982.
- Azevedo, N. M. and J. V. Lemos. "Hybrid discrete element/finite element method for fracture analysis." *Computer Methods in Applied Mechanics and Engineering* **195**(33-36): 4579-4593,2006.
- Azevedo, N. M., J. V. Lemos and J. R. de Almeida. "Influence of aggregate deformation and contact behaviour on discrete particle modelling of fracture of concrete." *Engineering Fracture Mechanics* **75**(6): 1569-1586,2008.
- Babuska, I., J. T. Oden and J. K. Lee. "Mixed-hybrid finite element approximations of second-order elliptic boundary-value problems." *Computer Methods in Applied Mechanics and Engineering* **11**(2): 175-206,1977.
- Babuška, I., T. Strouboulis, C. S. Upadhyay and S. K. Gangaraj. "Computer-based proof of the existence of superconvergence points in the finite element method; superconvergence of the derivatives in finite element solutions of Laplace's, Poisson's, and the elasticity equations." *Numerical Methods for Partial Differential Equations* **12**(3): 347-392,1996.
- Banerjee, B. and A. N. Norris. A spectral decomposition problem. <http://imechanica.org/node/1091>. iMechanica, Computational Mechanics Forum,2007.
- Barlow, J. "Optimal stress locations in finite element models." *International Journal for Numerical Methods in Engineering* **10**(2): 243-251,1976.
- Barlow, J. "More on optimal stress points—reduced integration, element distortions and error estimation." *International Journal for Numerical Methods in Engineering* **28**(7): 1487-1504,1989.

- Bathe, K. J. *Finite element procedures in engineering analysis*, Prentice-Hall,1982.
- Bazant, Z. and B. Oh. "Crack band theory for fracture of concrete." *Materials and Structures* **16**(93): 155-177,1983.
- Bazant, Z. and J. Planas. *Fracture and size effect in concrete and other quasibrittle materials*, CRC Press,1998.
- Bazant, Z., M. Tabbara, M. Kazemi and G. Pijaudier-Cabot. "Random Particle Model for Fracture of Aggregate or Fiber Composites." *Journal of Engineering Mechanics* **116**(8): 1686-1705,1990.
- Bazant, Z. P. *Crack band theory for fracture of concrete*. Materiaux et Constructions,1983.
- Belytschko, T. and W. E. Bachrach. "Efficient implementation of quadrilaterals with high coarse-mesh accuracy." *Comput. Methods Appl. Mech. Eng.* **54**(3): 279-301,1986.
- Belytschko, T., H. Chen, J. X. Xu and G. Zi. "Dynamic crack propagation based on loss of hyperbolicity and a new discontinuous enrichment." *International Journal for Numerical Methods in Engineering* **58**(12): 1873-1905,2003.
- Belytschko, T., S. Loehnert and J.-H. Song. "Multiscale aggregating discontinuities: A method for circumventing loss of material stability." *International Journal for Numerical Methods in Engineering* **73**(6): 869-894,2008.
- Belytschko, T., N. Moes, S. Usui and C. Parimi. "Arbitrary discontinuities in finite elements." *International Journal for Numerical Methods in Engineering* **50**(4): 993-1013,2001.
- Blanco, S., A. E. Huespe, J. Oliver and M. D. G. Pulido. "Modeling material failure in large concrete structures: Recent computational developments." *Computational Modelling of Concrete Structures*: 129-138
930,2006.
- Bochev, P. and M. Gunzburger. "An Absolutely Stable Pressure-Poisson Stabilized Finite Element Method for the Stokes Equations." *SIAM J. Numer. Anal.* **42**(3): 1189-1207,2004.
- Brezzi, F. and M. Fortin. *Mixed and hybrid finite element methods*, Springer-Verlag New York, Inc.,1991.
- Caleyron, F., A. Combescure, V. Faucher and S. Potapov. "Dynamic simulation of damage-fracture transition in smoothed particles hydrodynamics shells." *International Journal for Numerical Methods in Engineering* **90**(6): 707-738,2012.
- Carlson, D. E. and A. Hoger. "The derivative of a tensor-valued function of a tensor." *Quarterly Appl. Math.*: 409-423,1986.
- Cervera, M. and M. Chiumenti. "Mesh objective tensile cracking via a local continuum damage model and a crack tracking technique." *Computer Methods in Applied Mechanics and Engineering* **196**(1-3): 304-320,2006.
- Cervera, M., M. Chiumenti and C. Agelet de Saracibar. "Softening, localization and stabilization: capture of discontinuous solutions in J2 plasticity." *International Journal for Numerical and Analytical Methods in Geomechanics* **28**(5): 373-393,2004.
- Cervera, M., M. Chiumenti and R. Codina. "Mixed stabilized finite element methods in nonlinear solid mechanics. Part I: Formulation." *Computer Methods in Applied Mechanics and Engineering* **199**(37-40): 2559-2570,2010.

- Cervera, M., M. Chiumenti and R. Codina. "Mesh objective modeling of cracks using continuous linear strain and displacement interpolations." *International Journal for Numerical Methods in Engineering* **87**(10): 962-987,2011.
- Coleman, B. D. and W. Noll. "The thermodynamics of elastic materials with heat conduction and viscosity." *Arch. Rational Mech. Anal.* **13**: 167-178,1963.
- Crisfield, M. "LOCAL INSTABILITIES IN THE NON-LINEAR ANALYSIS OF REINFORCED CONCRETE BEAMS AND SLABS." *Proc. Instn. Civ. Engrs.* **73**(1): 135-145,1982.
- Crisfield, M. A. "Snap-through and snap-back response in concrete structures and the dangers of under-integration." *International Journal for Numerical Methods in Engineering* **22**(3): 751-767,1986.
- Crisfield, M. A. *Non-Linear Finite Element Analysis of Solids and Structures: Advanced Topics, 1st edition* New York, NY, USA John Wiley & Sons, Inc,1997.
- Crisfield, M. A. *Non-linear Finite Element Analysis of Solids and Structures Volume 2: Advanced Topics*, John Wiley & Sons,1998.
- Chen, J. F. *Limit Analysis and Soil Plasticity*, Elsevier,1975.
- de Borst, R. Non-linear analysis of frictional materials., Ph.D. Thesis, Delft Univ. of Technology,1986.
- de Borst, R. "Damage processes in solids and structures and their numerical computations." *Topics in applied mechanics : integration of theory and applications in applied mechanics*: 89,1993.
- de Borst, R., L. J. Sluys, H. B. Mühlhaus and J. Pamin. "Fundamental issues in finite element analyses of localization of deformation." *Engineering Computations* **10**: 99-121,1993.
- de Borst, R. and H.-B. Mühlhaus. "Gradient-dependent plasticity: Formulation and algorithmic aspects." *International Journal for Numerical Methods in Engineering* **35**(3): 521-539,1992.
- Dohrmann, C. R. and P. B. Bochev. "A stabilized finite element method for the Stokes problem based on polynomial pressure projections." *International Journal for Numerical Methods in Fluids* **46**(2): 183-201,2004.
- Dugdale, D. S. "Yielding of steel sheets containing slits." *Journal of the Mechanics and Physics of Solids* **8**(2): 100-104,1960.
- Dvorkin, E. N., A. M. Cuitino and G. Gioia. "Finite elements with displacement embedded localization lines insensitive to mesh size and distortions." *Int.J.Num.Meth.Engng.* **30**: 541-564,1990.
- Flanagan, D. P. and T. Belytschko. "A uniform strain hexahedron and quadrilateral with orthogonal hourglass control." *International Journal for Numerical Methods in Engineering* **17**(5): 679-706,1981.
- Francfort, G. A. and J. J. Marigo. "Revisiting brittle fracture as an energy minimization problem." *Journal of the Mechanics and Physics of Solids* **46**(8): 1319-1342,1998.
- Friswell. *The derivatives of repeated eigenvalues and their associated eigenvectors.* New York, NY, ETATS-UNIS, American Society of Mechanical Engineers,1996.
- Gallagher, R. H. *Survey and evaluation of the finite element method in fracture mechanics analysis.* Proceedings of the First International Conference on Structural Mechanics in Reactor Technology, Berlin,1971.

- Gerstle, W. e. a. Finite Element Analysis of Fracture in Concrete Structures, American Concrete Institute,1997.
- Griffith, A. A. "The Phenomena of Rupture and Flow in Solids." *Philosophical Transactions of the Royal Society of London. Series A, Containing Papers of a Mathematical or Physical Character* **221**,1921.
- Gumbsch, P. "An Atomistic Study of Brittle Fracture: Towards Explicit Failure Criteria from Atomistic Modelling." *J.~Mater.\ Res.* **10**: 2897-2907,1995.
- Hadamard, J. "Sur les problèmes aux dérivés partielles et leur signification physique." *Princeton University Bulletin* **13**: 49-52,1902.
- Hadamard, J. *Leçons sur la propagation des ondes et les équations de l'hydrodynamique*. Paris, A. Hermann,1903.
- Hernández, J. A., J. Oliver, A. E. Huespe and M. Caicedo. *high-performance model reduction procedures in multiscale simulations*. Barcelona, International Center for Numerical Methods in Engineering,2012.
- Herrmann, H. J. and S. Roux. Modelization of fracture in disordered systems. *Statistical Models for the Fracture of Disordered Media*. S. R. H. J. Hemmann. Amsterdam, North-Holland: 159-188,1990.
- Herrmann, L. R. "Elasticity equations for nearly incompressible materials by a variational theorem." *AIAA Journal* **3**: 1896 -1900,1965.
- Hill, R. "Acceleration waves in solids." *Journal Mech. Phys. Solids* **16**: 1-10,1962.
- Hillerborg, A. *Numerical methods to simulate softening and fracture of concrete*. Fracture Mechanics of Concrete: Structural Application and Numerical Calculation,1985.
- Hillerborg, A., M. Modeer and P. E. Petersson. "Analysis of crack formation and crack growth in concrete by means of fracture mechanics and finite elements." *Cement and concrete research* **6**(6): 773-782,1976.
- Huespe, A. E., A. Needleman, J. Oliver and P. J. Sánchez. "A finite thickness band method for ductile fracture analysis." *International Journal of Plasticity* **25**(12): 2349-2365,2009.
- Huespe, A. E. and J. Oliver. Crack models with embedded discontinuities. *Numerical Modeling of Concrete Cracking*. G. M. Hofstetter, Guenther (Eds.), Springer: 1-67,2011.
- Hughes, T. J. R. "Generalization of selective integration procedures to anisotropic and nonlinear media." *International Journal for Numerical Methods in Engineering* **15**(9): 1413-1418,1980.
- Hughes, T. J. R. *The Finite Element Method*. Englewood Cliffs, N.J., Prentice-Hall, Inc.,1987.
- Hughes, T. J. R. *The finite element method*. New York, Dover,2000.
- Inglis, C. "Stress in a plate due to the presence of cracks and sharp corners." *Proc. Int. Naval Architect* **60**,1913.
- Irwin, G. "Fracture Dynamics. In Fracturing of Metals." *American Society of Metals: Cleveland*,1948.
- Jenq, Y. S. and S. P. Shah. "A Fracture toughness criterion for concrete." *Engineering Fracture Mechanics* **21**(5): 1055-1069,1985.
- Jirásek, M. "Analysis of Rotating Crack Model." *J. Eng. Mech.* **124**(8): 842,1998.
- Jirasek, M. and P. Grassl. "Evaluation of directional mesh bias in concrete fracture simulations using continuum damage models." *Engineering Fracture Mechanics* **75**(8): 1921-1943,2008.

- Johnson, C. and J. Pitkäranta. "Analysis of Some Mixed Finite Element Methods Related to Reduced Integration." *Mathematics of Computation* **38**(158): 375-400,1982.
- Ju, J. W. DAMAGE MECHANICS OF COMPOSITE MATERIALS: CONSTITUTIVE MODELING AND COMPUTATIONAL ALGORITHMS. Princeton, Department of Civil Engineering and Operations Research, Princeton University,1991.
- Kachanov, L. M. "Time of the rupture process under creep conditions." *Izv. Akad. Nauk. {S.S.R.} Otd. Tech. Nauk.* **8**: 26-31,1958.
- Khan, A. S. *Continuum Theory of Plasticity*, John Wiley & Sons Inc.,1995.
- Klaas, O., A. Maniatty and M. S. Shephard. "A stabilized mixed finite element method for finite elasticity.: Formulation for linear displacement and pressure interpolation." *Computer Methods in Applied Mechanics and Engineering* **180**(1-2): 65-79,1999.
- Knops, R. J. and L. E. Payne. *Uniqueness theorems in linear elasticity*. Berlin, Springer-Verlag,1971.
- Kobayashi, A. S., M. N. Hawkins, D. B. Barker and B. M. Liaw. Fracture Process Zone of Concrete. *Application of Fracture Mechanics to Cementitious Composites*. S. P. Shah, Editor. Dordrecht, Marinus Nuijhoff, Publications: 25-50,1985.
- Kosloff, D. and G. A. Frazier. "Treatment of hourglass patterns in low order finite element codes." *International Journal for Numerical and Analytical Methods in Geomechanics* **2**(1): 57-72,1978.
- Kozicki, J. and J. Tejchman. "2D Lattice Model for Fracture in Brittle Materials." *Arch. Hydro-Engrg. Environ. Mech* **53**(2): 137-154,2006.
- Kraft, J. M., A. M. Sullivan and R. W. Boyle *Effect of dimensions on fast fracture instability of notched sheets*. Proceedings of the Crack Propagation Symposium, Cranfield,1961.
- Lemaitre, J. *A course on damage mechanics*, Springer-Verlag,1992.
- Linder, C. and F. Armero. "Finite elements with embedded strong discontinuities for the modeling of failure in solids." *International Journal for Numerical Methods in Engineering* **72**(12): 1391-1433,2007.
- Linder, C. and F. Armero. "Finite elements with embedded branching." *Finite Elements in Analysis and Design* **45**(4): 280-293,2009.
- Linero, D. L., J. Oliver, A. E. Huespe and M. D. G. Pulido. "Cracking modeling in reinforced concrete via the strong discontinuity approach." *Computational Modelling of Concrete Structures*: 173-182 930,2006.
- Lofti, H. R. and P. B. Shing. "Embedded Representation of Fracture in Concrete with Mixed Finite-Elements." *International Journal for Numerical Methods in Engineering* **38**(8): 1307-1325,1995.
- Lubliner, J. *Plasticity Theory*, Mcmillan Publishing Company,1990.
- Lubliner, J., J. Oliver, S. Oller and E. Onate. "A Plastic-Damage Model for Concrete." *International Journal of Solids and Structures* **25**(3): 299-326,1989.
- Malkus, D. S. "A finite element displacement model valid for any value of the compressibility." *International journal of solids and structures* **12**: 731-738,1976.

- Malkus, D. S. and T. J. R. Hughes. "Mixed finite element methods - reduced and selective integration techniques: a unification of concepts." *Comp. Meth. Appl. Mech. Eng.* **15**: 63-81,1978.
- Manzoli, O. L. and P. B. Shing. "A general technique to embed non-uniform discontinuities into standard solid finite elements." *Computers & Structures* **84**(10-11): 742-757,2006.
- Marsden, J. E. and T. J. R. Hughes. *Mathematical foundations of elasticity*, Prentice-Hall,1983.
- Meguro, K. and M. Hakuno. "Fracture analyses of concrete structures by the modified distinct element method." *Structural Engineering/Earthquake Engineering* **6**(2): 283-294,1989.
- Miehe, C., M. Hofacker and F. Welschinger. "A phase field model for rate-independent crack propagation: Robust algorithmic implementation based on operator splits." *Computer Methods in Applied Mechanics and Engineering* **199**(45-48): 2765-2778,2010a.
- Miehe, C., F. Welschinger and M. Hofacker. "Thermodynamically consistent phase-field models of fracture: Variational principles and multi-field FE implementations." *International Journal for Numerical Methods in Engineering* **83**(10): 1273-1311,2010b.
- Mora, D. F., J. Oliver and A. E. Huespe. COMPUTATIONAL MODELING OF FIBER REINFORCED CEMENT COMPOSITES AS A COMPLEX MATERIAL. *Congress on Numerical Methods in Engineering*. APMTAC. Coimbra, Portugal,2011.
- Mosler, J. and G. Meschke. "3D modelling of strong discontinuities in elastoplastic solids: fixed and rotating localization formulations." *International Journal for Numerical Methods in Engineering* **57**(11): 1553-1576,2003.
- Mosler, J. and G. Meschke. "Embedded crack vs. smeared crack models: a comparison of elementwise discontinuous crack path approaches with emphasis on mesh bias." *Computer Methods in Applied Mechanics and Engineering* **193**(30-32): 3351-3375,2004.
- Muhlhaus, H. B. and I. Vardoulakis. "The thickness of shear bands in granular materials." *Geotechnique* **37**(3): 271-283,1987.
- Nagtegaal, J. C., D. M. Parks and J. C. Rice. "On numerically accurate finite element solutions in the fully plastic range." *Comput. Methods Appl. Mech. Eng.*: 153-177,1990.
- Neto, E. S. d., D. Peric and D. Owen. *Computational Methods for Plasticity: Theory and Applications*, John Wiley & Sons Ltd,2008.
- Oliver, J. "A Consistent Characteristic Length for Smeared Cracking Models." *International Journal for Numerical Methods in Engineering* **28**(2): 461-474,1989.
- Oliver, J. "Modelling strong discontinuities in solid mechanics via strain softening constitutive equations. Part 1. Fundamentals." *International Journal for Numerical Methods in Engineering* **39**(21): 3575-3600,1996a.
- Oliver, J. "Modelling strong discontinuities in solid mechanics via strain softening constitutive equations. Part 2. Numerical simulation." *International Journal for Numerical Methods in Engineering* **39**(21): 3601-3623,1996b.

- Oliver, J. "On the discrete constitutive models induced by strong discontinuity kinematics and continuum constitutive equations." *International Journal of Solids and Structures* **37**(48-50): 7207-7229,2000.
- Oliver, J. Topics on failure mechanics, International Center for Numerical Methods in Engineering (CIMNE),2002.
- Oliver, J., M. Cervera and O. Manzoli. "Strong discontinuities and continuum plasticity models: the strong discontinuity approach." *International Journal of Plasticity* **15**(3): 319-351,1999.
- Oliver, J., M. Cervera, S. Oller and J. Lubliner. *Isotropic damage models and smeared crack analysis of concrete*. Proc. SCI-C Computer Aided Analysis and Design of Concrete Structures,1990.
- Oliver, J. and A. Huespe. "Theoretical and computational issues in modelling material failure in strong discontinuity scenarios." *Computer Methods in Applied Mechanics and Engineering* **193**(27-29): 2987-3014,2004a.
- Oliver, J., A. Huespe, S. Blanco and D. Linero. "Stability and robustness issues in numerical modeling of material failure with the strong discontinuity approach." *Computer Methods in Applied Mechanics and Engineering* **195**(52): 7093-7114,2006.
- Oliver, J., A. Huespe and J. Cante. "An implicit/explicit integration scheme to increase computability of non-linear material and contact/friction problems." *Computer Methods in Applied Mechanics and Engineering* **197**(21-24): 1865-1889,2008a.
- Oliver, J. and A. E. Huespe. "Continuum approach to material failure in strong discontinuity settings." *Computer Methods in Applied Mechanics and Engineering* **193**(30-32): 3195-3220,2004b.
- Oliver, J., A. E. Huespe and J. C. Cante. "An implicit/explicit integration scheme to increase computability of non-linear material and contact/friction problems." *Computer Methods in Applied Mechanics and Engineering* **197**(21-24): 1865-1889,2008b.
- Oliver, J., A. E. Huespe, J. C. Cante and G. Díaz. "On the numerical resolution of the discontinuous material bifurcation problem." *International Journal for Numerical Methods in Engineering* **83**: 786–804,2010.
- Oliver, J., A. E. Huespe, M. D. G. Pulido and E. Chaves. "From continuum mechanics to fracture mechanics: the strong discontinuity approach." *Engineering Fracture Mechanics* **69**(2): 113-136,2002.
- Oliver, J., A. E. Huespe, E. Samaniego and E. W. V. Chaves. "Continuum approach to the numerical simulation of material failure in concrete." *International Journal for Numerical and Analytical Methods in Geomechanics* **28**(7-8): 609-632,2004.
- Oliver, J., D. F. Mora, A. E. Huespe and R. Weyler. "A micromorphic model for steel fiber reinforced concrete." *International Journal of Solids and Structures*,2012.
- Ortiz, M., Y. Leroy and A. Needleman. "A finite element method for localized failure analysis." *Comp.Meth.Appl.Mech.Eng.* **61**: 189-214,1987.
- Pastor, M., M. Quecedo and O. C. Zienkiewicz. "A mixed displacement-pressure formulation for numerical analysis of plastic failure." *Computers & Structures* **62**(1): 13-23,1997.
- Pijaudier Cabot, G. and Z. Bazant. "Nonlocal damage theory." *Journal Engineering Mechanics ASCE* **113**: 1512-1533,1987.

- Potyondy, D. O. and P. A. Cundall. Modelling Rock Using Bonded Assemblies of Circular Particles. *2nd North American Rock Mechanics Symposium*. Montreal, American Rock Mechanics Association: 1937–1944,1996.
- Prabel, B., A. Combescure, A. Gravouil and S. Marie. "Level set X-FEM non-matching meshes: application to dynamic crack propagation in elastic-plastic media." *International Journal for Numerical Methods in Engineering* **69**(8): 1553-1569,2007.
- Rashid, Y. "Analysis or prestressed concrete pressure vessels." *Nuclear Engineering and Design* **7**: 773-782,1968.
- Reddy, B. D. and J. C. Simo. "Stability and Convergence of a Class of Enhanced Strain Methods." *SIAM Journal on Numerical Analysis* **32**(6): 1705-1728,1995.
- Rice, J. R. The Localization of Plastic Deformation. *Theoretical and Applied Mechanics*. W. T. Koiter, North-Holland Publ. Co.: 207-220,1976.
- Rice, J. R. and J. W. Rudnicki. "A note on some feature of the theory of localization of deformation." *International Journal of Solid and Structures* **16**: 597-605,1980.
- Rots, J. G. Computational Modeling of Concrete Fracture, Delft University of Technology. **Ph.D. Thesis**,1988.
- Rudnicki, J. W. and J. R. Rice. "Conditions for the localization of deformation in pressure-sensitive dilatant materials." *Journal of the Mechanics and Physics of Solids* **23**(6): 371-394,1975.
- Runesson, K., N. S. Ottosen and D. Peric. "Discontinuous bifurcations of elastic-plastic solutions at plane stress and plane strain." *Int. J. of Plasticity* **7**: 99-121,1991.
- Saether, E., V. Yamakov, D. R. Phillips and E. H. Glaessgen. An Overview of the State of the Art in Atomistic and Multiscale Simulation of Fracture NASA/TM-2009-215564,2009.
- Samaniego, E. Contributions to the Continuum Modelling of Strong Discontinuities in two-dimensional Solids institution ETSCCP Technical University of Barcelona. *Dept. of Material Strength and Struct. in Eng.* Barcelona, Technical University of Catalonia (UPC),2003.
- Sánchez, P. J., V. E. Sonzogni and A. E. Huespe. "Study of a stabilized mixed finite element with emphasis on its numerical performance for strain localization problems." *Communications in numerical methods in engineering* **24**: 297–320,2008.
- Schlangen, E. and E. J. Garboczi. "Fracture simulations of concrete using lattice models: Computational aspects." *Engineering Fracture Mechanics* **57**(2–3): 319-332,1997.
- Simó, J. and J. Ju. "Strain and stress based continuum damage models. I. Formulation." *International Journal of Solid and Structures* **23**: 821-840,1987.
- Simo, J., J. Oliver and F. Armero. "An analysis of strong discontinuities induced by strain-softening in rate-independent inelastic solids." *Computational Mechanics* **12**: 277-296,1993.
- Simo, J. C. and T. J. R. Hughes. *Computational Inelasticity*, Springer,1998.
- Simo, J. C. and S. Rifai. "A class of mixed assumed strain methods and the method of incompatible modes." *Int. Journ. Num. Meth. Engng.* **29**: 1595-1638,1990.
- Stakgold, I. *Green's functions and boundary value problems*. New York, Wiley,1998.

- Steinmann, P. and K. Willam. "Finite elements for capturing localized failure." *Archive of Applied Mechanics* **61**(4): 259-275,1991a.
- Steinmann, P. and K. Willam. "Performance of enhanced finite element formulations in localized failure computations." *Computer Methods in Applied Mechanics and Engineering* **90**(1-3): 845-867,1991b.
- Wilson, E. L., R. L. Taylor and W. P. Doherty. *Incompatible displacement models. Numerical and Computer Models in Structural Mechanics*, New York, Academic Press,1973.
- Zienkiewicz, O. C., R. L. Taylor and J. M. Too. "Reduced integration technique in general analysis of plates and shells." *International Journal for Numerical Methods in Engineering* **3**(2): 275-290,1971.
- Zienkiewicz, O. C. and J. Z. Zhu. "The superconvergent patch recovery and a posteriori error estimates. Part 1: The recovery technique." *International Journal for Numerical Methods in Engineering* **33**(7): 1331-1364,1992.

